



HAL
open science

Investigation of the electrochromic properties of V₂O₅ thin films deposited by sputtering: comparison of High Power Impulse Magnetron Sputtering (HiPIMS) vs conventional Radio Frequency Magnetron Sputtering (RFMS)

Giljoo Song

► **To cite this version:**

Giljoo Song. Investigation of the electrochromic properties of V₂O₅ thin films deposited by sputtering: comparison of High Power Impulse Magnetron Sputtering (HiPIMS) vs conventional Radio Frequency Magnetron Sputtering (RFMS). Material chemistry. Université de Bordeaux, 2019. English. NNT : 2019BORD0062 . tel-03221282

HAL Id: tel-03221282

<https://theses.hal.science/tel-03221282>

Submitted on 8 May 2021

HAL is a multi-disciplinary open access archive for the deposit and dissemination of scientific research documents, whether they are published or not. The documents may come from teaching and research institutions in France or abroad, or from public or private research centers.

L'archive ouverte pluridisciplinaire **HAL**, est destinée au dépôt et à la diffusion de documents scientifiques de niveau recherche, publiés ou non, émanant des établissements d'enseignement et de recherche français ou étrangers, des laboratoires publics ou privés.

THÈSE PRÉSENTÉE
POUR OBTENIR LE GRADE DE
DOCTEUR DE
L'UNIVERSITÉ DE BORDEAUX

ÉCOLE DOCTORALE
SPÉCIALITÉ : PHYSICO-CHIMIE DE LA MATIÈRE CONDENSÉE

Giljoo SONG

Investigation of the electrochromic properties of V_2O_5 thin films deposited by sputtering : comparison of High Power Impulse Magnetron Sputtering (HiPIMS) vs conventional Radio Frequency Magnetron Sputtering (RFMS)

Sous la direction de : Aline Rougier

Soutenance prévue le 7 Mai 2019

Membres du jury :

Mme. BADDOUR Rita, Directrice de Recherche, CNRS-ICMPE, Thiais	Rapportrice
M. KIM Jongwook, Maître de Conférences, Ecole Polytechnique, Palaiseau	Examineur
Mme. LEE Caroline Sunyong, Professeure, Université de Hanyang, Corée du sud	Examinatrice
M. MAGLIONE, Mario, Directeur de Recherche, CNRS-ICMCB, Pessac	Directeur
M. PIERSON, Jean-François, Professeur, Université de Lorraine, Nancy	Rapporteur
Mme. ROUGIER, Aline, Directrice de Recherche, CNRS-ICMCB, Pessac	Directrice de thèse

Acknowledgments

First of all, I would like to express my sincere gratitude to Dr. Mario Maglione, Director of ICMCB-CNRS, for welcoming me at ICMCB and also providing a great scientific environment.

Many thanks to my supervisor Dr. Aline ROUGIER for wonderful guidance. There is no doubt that she did teach me based on not only their great scientific knowledge but also their sincere care and love.

I would like to thank all the jury members for their efforts to review and judge this work.

I would like to thank very much to my company SK Hynix and Hyunyul PARK, Sungmin HWANG, Ilyoung LIM in SK Hynix for great support and help.

My deep gratitude to my dear friends for the support and encouragements, Khawla ZRIKEM, Shian GUAN, Romain FUTSCH, Dr. Issam MJEJRI and Dr. Mathias DA ROCHA.

I am thankful to all the following people from the ICMCB and PLACAMAT for the help, experiments they did or the effective discussions: Lionel TEULE-GAY and Dominique MICHAU, Sonia BUFFIÉRE, Eric LEBRAUD, Christine LABRUGERE, Alexandre FARGUES and Nicola PENIN.

My deep gratitude to Hyungjin PARK and his family, Dr. Eungjang LEE, Dr. Kayoung KIM and Dr. Daehoon PARK for their encouragements during my Ph.D. period.

Finally, this thesis is dedicated to my wife Youngeun and to my daughter, Hyojin and Hyowon and to my parents and parents-in-law.

Caractérisation des propriétés électrochromes de couches minces de V_2O_5 déposées par pulvérisation cathodique : comparaison de la méthode HiPIMS et de la méthode RFMS

Les matériaux et dispositifs électrochromes sont capables de modifier leurs propriétés optiques sous l'application d'une tension. De plus en plus présents dans notre vie quotidienne, leur domaine d'application s'étend des rétroviseurs automobiles (Première commercialisation fin des années 80 par Gentex sur une technologie à base de viologènes pour une production aujourd'hui de plus de 80 Millions par an), aux fenêtres intelligentes (bâtiments, toits de voiture, augmentation prévue de 13%/ans, soit un coût de \$2.6 billions en 2020 pour les vitrages) à l'affichage. Parmi les différents matériaux électrochromes, les oxydes de métaux de transition ont suscité un vif intérêt suite aux travaux de Deb à la fin des années 60, montrant la commutation réversible de couches minces d'oxyde de tungstène WO_3 . WO_3 , de coloration cathodique, reste aujourd'hui l'état de l'art des matériaux électrochromes, il est communément associé à l'oxyde de nickel NiO dans les dispositifs commercialisés. Toutefois l'association de ces deux oxydes souffre de certaines limitations telles qu'une incompatibilité acido-basique. L'oxyde de Vanadium, V_2O_5 , est un candidat de choix pour substituer NiO.

Ce travail de thèse, dédié à la comparaison des propriétés électrochromes de couches minces de V_2O_5 déposées par pulvérisation cathodique utilisant la méthode conventionnelle et la méthode HiPIMS (High Power Impulse Magnetron Sputtering) est divisé en quatre grandes parties. La première partie, découpée en trois chapitres, précise l'état de l'art des matériaux et dispositifs électrochromes avec des détails concernant les applications actuelles (Chapt. 1), introduit les caractéristiques notamment structurales de l'oxyde étudié V_2O_5 (Chapt. 2) et se conclut par une description de la technique de dépôt utilisée, la pulvérisation cathodique (Chapt. 3). Les résultats expérimentaux font l'objet des trois parties suivantes et concernent dans un premier temps, la caractérisation physico-chimique et les propriétés électrochromes (Electrochimique et optique) des couches minces V_2O_5 . La partie C s'attache plus précisément à la compréhension du mécanisme électrochrome mis en jeu, tandis que l'intégration des couches de V_2O_5 en dispositifs complets est rapportée dans la dernière partie.

La première étape de ce travail de thèse a consisté en l'optimisation des paramètres de dépôt. Majoritairement trois paramètres ont été étudiés : la puissance, la pression totale et la pression partielle en oxygène à partir de l'utilisation de deux cibles, du Vanadium métallique V, et de l'oxyde V_2O_5 . La détermination des conditions optimums a été effectuée en

caractérisant électrochimiquement et optiquement les films déposés. Visuellement, les films frais de dépôt sont de couleur orange. Les conditions de dépôt sélectionnées sont regroupées dans le tableau I.

Tableau I : Conditions de dépôt de films V_xO_y , Puissance, Pression totale et Pression partielle en oxygène, à partir d'une cible métallique ou d'une cible d'oxyde.

	Cible V	Cible V_2O_5
Puissance (W)	200	150
P_{Tot} (Pa)	2	2
PO_2 (%) (Pa)	20	2

La caractérisation structurale des films, menée en diffraction des rayons X en configuration en angle rasant montre des films cristallisés en symétrie orthorhombique (G.E. $Pmmn$) pour les films déposés à partir d'une cible métallique, tandis qu'ils sont amorphes à partir d'une cible d'oxyde (Fig. 1a). Les clichés de microscopie électronique à balayage mettent en évidence des états de surface assez perturbés (Fig. 1b).

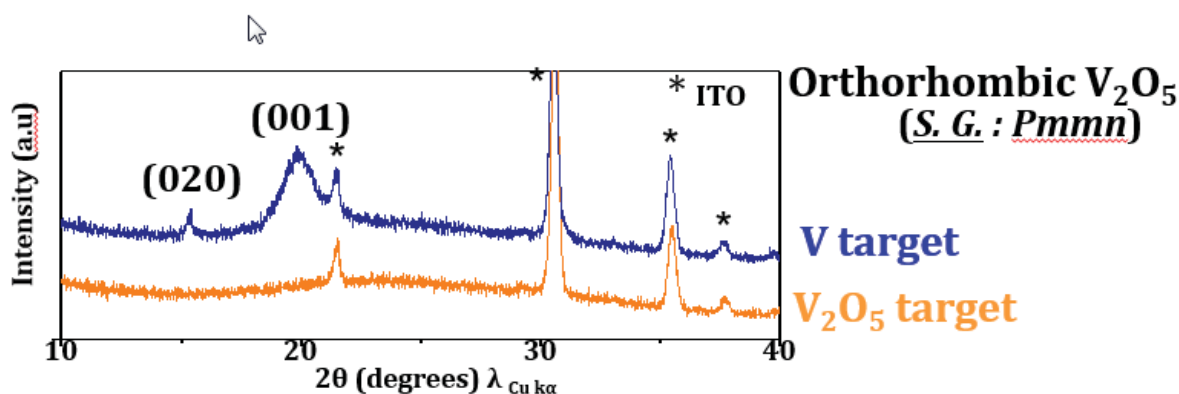
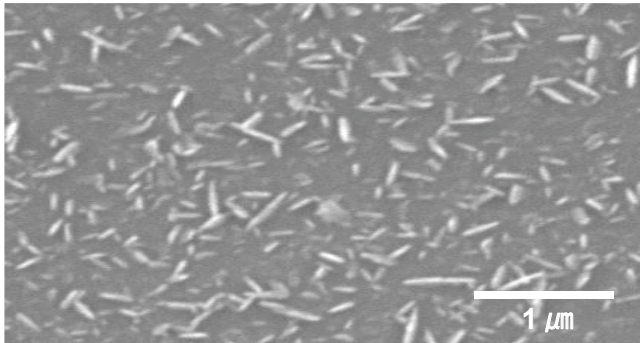
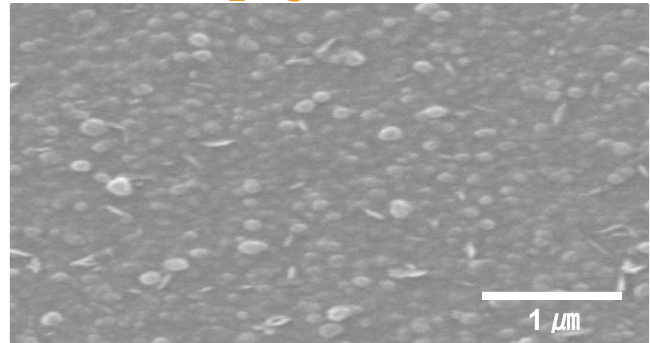


Figure 1 : a) Diffractogrammes de Rayons X des films V_2O_5 déposés à partir d'une cible métallique (Bleu) et d'une cible oxyde (V_2O_5), b) Morphologie associée.

V target



V₂O₅ target



La caractérisation électrochimique des films a été menée par voltampérométrie cyclique pour l'évaluation de la durabilité et par chronoampérométrie pour l'évaluation de la cinétique. Les films ont été cyclés en cellule à trois électrodes en milieu électrolyte lithié et sodé suivant la chaîne électrochimique V_2O_5/Li (Na) électrolyte /Pt vs ECS (Fig. 2). La signature des voltampérogrammes montre la présence de deux pics réversibles en milieu lithié tandis que la forme du voltampérogramme est beaucoup plus écrasée en milieu sodé. Toutefois, dans les deux milieux, les films commutent de façon réversible d'orange à vert et bleu en cyclage. Ce multichromisme, propre à l'oxyde V_2O_5 , est associé à une modulation en transmittance de l'ordre de 40 % à 450 nm avec un déplacement du seuil de transmittance vers les plus faibles longueurs d'onde en réduction.

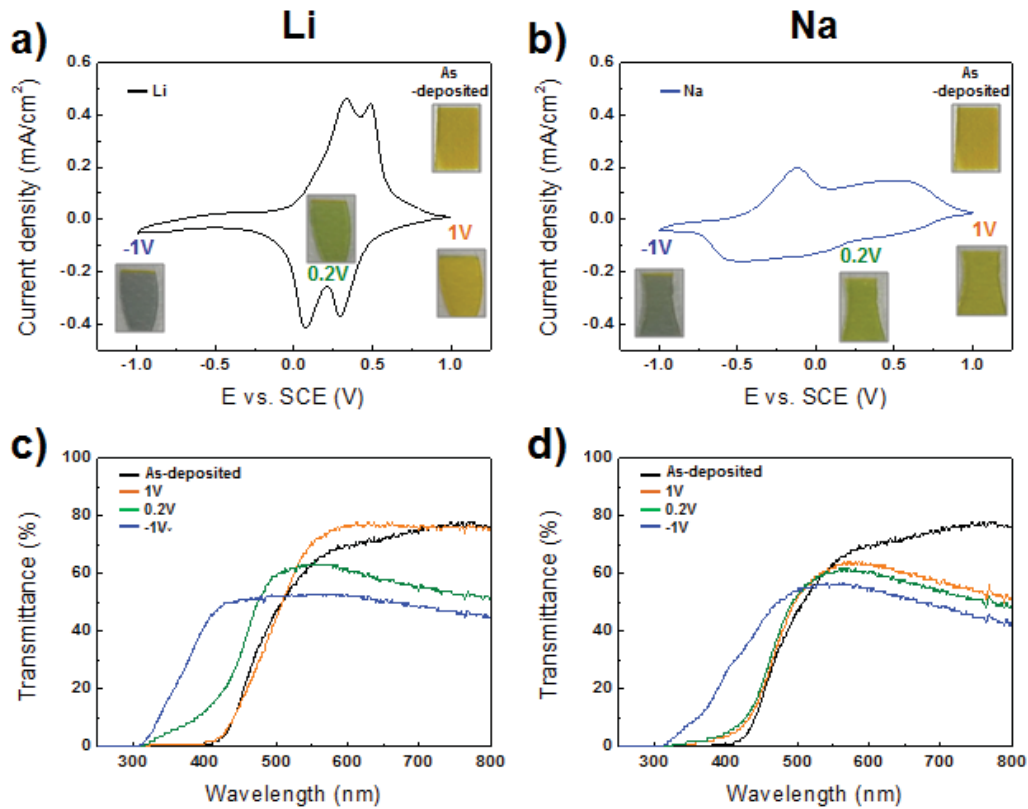


Figure 2 : Voltampérogrammes en cellule à trois électrodes, V_2O_5/Li (Na) électrolyte /Pt vs ECS pour une vitesse de balayage de 10 mV/s et transmittances associées dans les 4 états (frais de dépôt, réduit à 0.2 V et -1 V et oxydé à 1 V). (a, c) correspondent aux films déposés à partir d'une cible métallique et (b, d) aux films déposés à partir d'une cible oxyde.

Des caractéristiques électrochromes similaires, pour les films déposés à partir d'une cible oxyde sont observées, avec toutefois une tenue en cyclage beaucoup plus faible associée à une « dé-cohésion » des films très rapide. Afin de pallier à cette durabilité limitée liée majoritairement à une morphologie de mauvaise qualité, des films ont été déposés par HiPIMS. Cette méthode ayant été mise en place pour la première fois au laboratoire, un travail d'optimisation a dû être mené. Amorphes et denses, les films déposés par HiPIMS dans des conditions optimisées de durée de pulsation de 45 μ s et un taux de répétition de 1200 Hz adoptent un comportement électrochrome très proche des films déposés de façon conventionnelle. Toutefois, ils montrent une meilleure durabilité associée à une morphologie qui évolue peu en cyclage (Fig. 3).

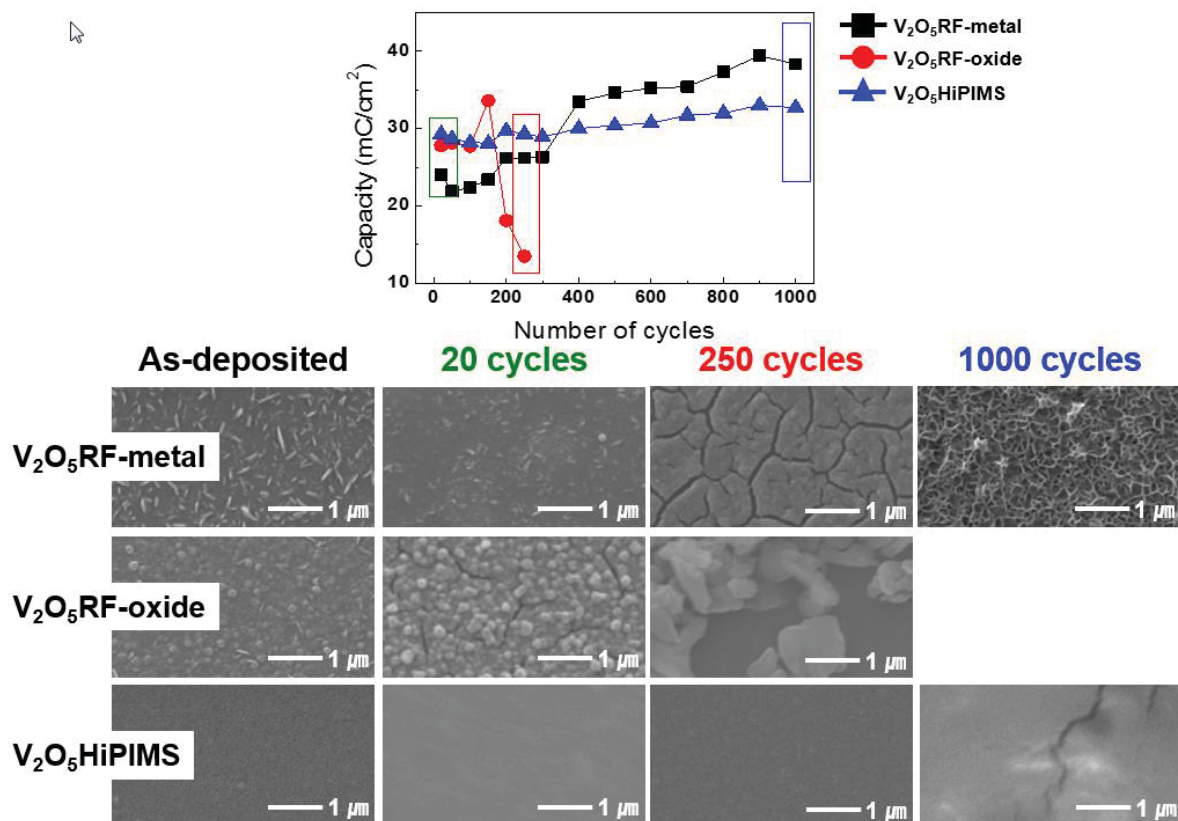


Figure 3 : Capacité en cyclage pour les cellules $V_2O_5/Li (Na)$ électrolyte /Pt vs ECS (Électrode au Calomel Saturé) à partir de films V_2O_5 déposés à partir d'une cible métallique, d'une cible d'oxyde ou par la méthode HiPIMS ; Evolution des morphologies associées.

La détermination du mécanisme électrochrome fait l'objet de la partie C. Cette étude a été menée sur les films cristallisés déposés à partir d'une cible métallique. Avant de débiter les caractérisations *ex-situ* sur les films réduits leur effet mémoire a été évalué par comparaison des transmittances optiques après réduction à 0,2 V et -1,0 V pour 120 s et après une période d'un mois sans potentiel appliqué. Dans ces conditions, aucune modification des propriétés optiques n'est enregistrée. La combinaison d'un nombre important de techniques de caractérisation, telles, la diffraction des rayons X, la Spectroscopie de Photoelectrons, La Spectrométrie de Masse d'Ions Secondaires à Temps de Vol TOFSIMS et de mesures électrochimiques conclut à un mécanisme électrochrome complexe basé sur un mélange de contributions faradique et capacitive et une distribution inhomogène du Li dans l'épaisseur du film. La compréhension plus fine du mécanisme mis en jeu fera l'objet de perspectives.

La partie D est dédiée à l'intégration des couches minces dans les dispositifs complets. Deux types de configuration ont été testés en parallèle. Une première configuration de type "vitrage

intelligent” associant un film de V_2O_5 pré-cyclé ($Li_xV_2O_5$) et un film de WO_3 conduit à une modulation de transmittance de près de 50 % à 650 nm et une bonne cyclabilité. Toutefois, l’absence d’un état transparent non coloré limite l’utilisation de V_2O_5 pour cette application. Dans ce travail, l’utilisation d’un électrolyte de couleur blanche entre deux couches de films de V_2O_5 , dont l’un est initialement pré-cyclé conduit à une configuration originale permettant une modulation de couleur simultanée sur les deux faces du dispositif (Fig. 4).

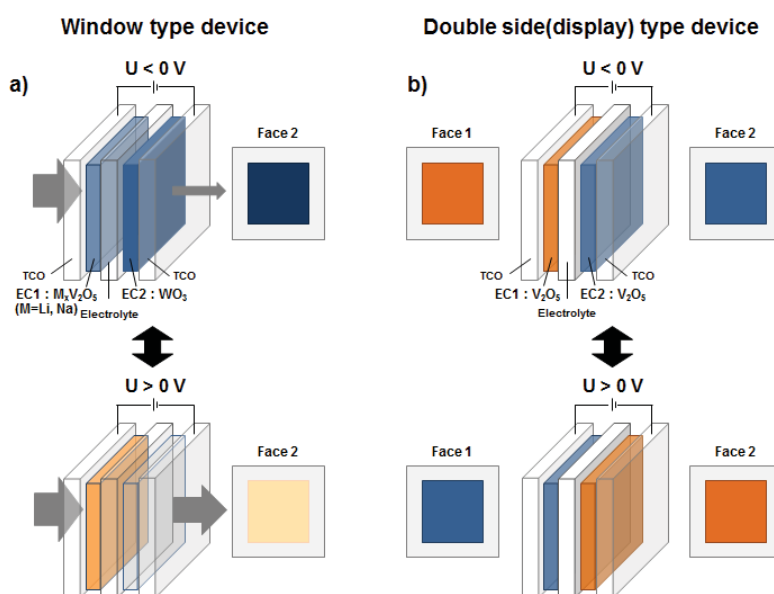


Figure 4 : Deux types de configuration “Vitrage” et “Afficheurs” pour des dispositifs à base de Films V_2O_5 .

En conclusion dans ce travail, l’optimisation des conditions de dépôt de couches minces d’oxyde de vanadium a permis de démontrer l’apport de la technique HiPIMS à la réalisation de films de haute qualité présentant des propriétés électrochromes améliorées. Le multichromisme, orange, vert, bleu, a été corrélé à un mécanisme électrochrome complexe s’appuyant sur une distribution inhomogène du Li dans la couche et un processus redox de “bulk” et de surface. L’intégration des films unitaires dans des dispositifs aux architectures variées a conforté l’intérêt pour ces matériaux.

Table of contents

General introduction	1
Reference	3
PART A : STATE OF THE ART	5
Chapter 1. Electrochromism	6
1. Overview	6
1.1. Context of smart windows	6
1.2. Principle of operation of an electrochromic device	7
1.3. Applications	9
1.3.1. Smart windows	9
1.3.2. Display, mirror and wearable devices.	11
1.3.3. The Market	12
1.4. Performance criteria	13
1.5. Light-matter interaction	15
2. Origins and role of the layers composition in the electrochromic device	16
2.1. Electrochromic materials	16
2.1.1. Conductive polymers	17
2.1.2. Viologen and Prussian blue compounds	18
2.1.2.1. Viologen	18
2.1.2.2. Prussian blue (PB)	19
2.1.3. Metal oxides	20
2.2. Electrolytes	22
2.2.1. Metal oxides	23
2.2.2. Ion conductive membranes	23
2.2.3. Ionic liquids	23
2.3. Transparent Conductive Oxides (TCOs)	25
2.4. Substrates	26

3. Characterization technique : electrochemistry	26
3.1. Some notions	26
3.2. Experimental techniques.	29
3.2.1. Electrode cell	29
3.2.2. Electrochemical characterization methods	30
3.2.3. <i>In-situ</i> optical characterizations	31
Chapter 2. Vanadium oxide (V₂O₅)	32
1. Vanadium oxide	32
2. Structure of V₂O₅	33
3. Electrochromism of V₂O₅	35
Chapter 3. Deposition method : sputtering	37
1. General overview of sputtering	37
1.1. Principle of sputtering	37
1.2. Structure zone models	39
2. Radio frequency magnetron sputtering (RFMS)	41
2.1. Radio frequency sputtering	41
2.2. Principle of the self-biasing voltage	42
2.3. Magnetron effect	43
2.4. Reactive plasma sputtering	44
PART B : SINGLE LAYER DEPOSITION	46
Chapter 1. Deposition of vanadium oxide by RFMS with V metal and V₂O₅ oxide target	
1. Deposition condition	47
1.1. Equipment	47
1.2. Experimental protocol	47
1.3. Deposition settings	48

2. Deposition of V₂O₅ Thin film with V metallic target	50
2.1. Thin film deposition at various RF power and total pressure conditions	50
2.2. Thin film deposition at various P(O ₂) conditions	51
2.2.1. The self-biasing voltage	51
2.2.2. Optical Characteristics	52
2.2.2.1. Visual aspect	53
2.2.2.2. Optical transmittance	53
2.2.3. Morphology	55
2.2.4. Structural characterization	55
2.2.5. Electrochemical properties	57
2.2.6. Optical properties	58
3. Electrochromic properties of V₂O₅RF-metal in Li and Na based electrolytes	59
3.1. V ₂ O ₅ RF-metal thin films	59
3.1.1. Thickness and morphology	59
3.1.2. Characterization	60
3.1.3. Electrochemical properties	63
3.2. Electrochromic properties of V ₂ O ₅ films	65
3.3. Durability	68
3.4. Switching time	70
4. Deposition of V₂O₅ thin film with V₂O₅ target	72
4.1. Thin film deposition at various power and pressure conditions	73
4.2. Thin film deposition at various P(O ₂) conditions	74
4.2.1. Optical Characteristics	75
4.2.1.1. Visual aspect	75
4.2.1.2. Optical transmittance	75
4.2.2. Morphology	76
4.2.3. Structural characterization	77
4.2.4. Electrochemical properties	77

4.2.5. Optical properties	78
5. Electrochromic properties of V₂O₅RF-oxide in Li and Na based electrolytes	79
5.1. Structural and textural characterizations	79
5.1.1. Thickness and morphology	79
5.1.2. EELS characterization	80
5.2. Electrochromic properties	81
5.3. Durability	84
5.4. Switching time	86
Chapter 2. Deposition of vanadium oxide by HiPIMS	88
1. High Power Impulse Magnetron Sputtering (HiPIMS)	88
1.1. Principle of HiPIMS	88
1.2. Advantages of HiPIMS	90
2. Deposition conditions : experimental methodology	92
3. Thin film deposition of V₂O₅ with HiPIMS at various pulse durations and a repetition rate conditions	92
3.1. Using various pulse durations and a repetition rate conditions	92
3.2. Using various oxygen partial pressure conditions	93
3.2.1. Visual aspect	94
3.2.2. Optical transmittance	94
3.2.3. Morphology	94
3.2.4. Structural characterization	95
3.2.5. Electrochemical properties	97
3.2.6. Optical properties	97
3.2.7. Cycling stability	98
4. Electrochromic properties of V₂O₅HiPIMS in Li and Na based electrolytes	99

4.1. V ₂ O ₅ HiPIMS thin films	99
4.1.1. Thickness and morphology	99
4.1.2. Composition.	101
4.2. Electrochromic properties	103
4.2.1. Electrochemical and optical properties	103
4.3. Durability	105
4.4. Switching time	107
Conclusion	108
PART C : ELECTROCHROMIC MECHANISM	110
Chapter 1. Comparison of the EC behavior of V₂O₅ thin films : capacitive to faradic contributions	111
Chapter 2. EC mechanism in V₂O₅RF-Metal thin films	116
1. Structural modification upon cycling by XRD	117
2. XPS analysis	122
3. Depth profile using TOF-SIMS	128
4. Depth profiles using Auger Electron Spectroscopy (AES)	131
5. Li content analysis using RBS/NRA(AIFIRA)	131
Conclusion	133
PART D : ELECTROCHROMIC DEVICES (ECDs)	134
Chapter 1. Full devices of V₂O₅/WO₃ films for smart window application	136
1. V₂O₅/WO₃ with Li and Na based electrolytes	136
1.1. Fabrication method	136
1.1.1. EC behavior of WO ₃ single thin films	136
1.1.2. Pre-cycling of single thin films	137
1.1.3. Fabrication of V ₂ O ₅ /Li and Na gel liquid electrolytes/WO ₃	138

1.2. Electrochromic properties of V ₂ O ₅ /Li and Na gel liquid electrolytes/WO ₃	139
1.2.1. Electrochemical and optical properties	139
1.2.2. Switching time	141
Chapter 2. Full devices of V₂O₅/V₂O₅ films for display application	143
1. V₂O₅/V₂O₅ with Li and Na based electrolytes	143
1.1. Fabrication method	143
1.1.1. Preparation of white-opaque gel electrolyte	143
1.1.1.1. Transmittance and reflectance of white-opaque gel electrolyte	143
1.1.1.2. Conductivity of white-opaque gel electrolyte	144
1.1.2. Fabrication of V ₂ O ₅ /Li and Na- white-opaque gel electrolyte/V ₂ O ₅	144
1.2. Electrochromic properties of V ₂ O ₅ /Li and Na-white-opaque gel electrolyte/V ₂ O ₅ .	145
1.2.1. Electrochemical properties	145
1.2.2. Optical properties	146
1.2.3. Switching time	148
Conclusion	150
General conclusion and perspectives	151
Appendix	156
1. X-ray diffraction (XRD)	156
2. Grazing Incidence X-Ray Diffraction (GIXRD)	157
3. X-ray photoelectron spectroscopy (XPS)	159
4. Spectroscopy of energy loss of electrons (EELS).	160
5. Rutherford Backscattering Spectrometry (RBS).	161
Reference	164

General introduction

Over the last decades, there has been tremendous research on electrochromic materials because of their wide range of applications such as smart windows, displays, rearview mirrors, and so forth [1-9]. Electrochromic (EC) materials have been of great academic and commercial interest and recognized as one of the key “green” technologies for sustainability and energy savings in building environments [10, 11]. For electrochromic materials, molybdenum oxide, niobium oxide, tungsten oxide, etc. are regarded as cathodic colored materials (i.e. colored in the reduced state) whereas iridium oxide, cobalt oxide, nickel oxide, and ruthenium oxide are classified as anodic colored materials (i.e. colored in the oxidized state).

Vanadium pentoxide (V_2O_5) has come up as a promising electrochromic material for device application because of its multicolor electrochromism. Vanadium oxide (V_2O_5) is one of the only materials that clearly show both anodic and cathodic colorations as a result of the occurrence of various oxidation states associated with different colors. Thus it offers the possibility of obtaining multicolor displays. Besides, as powder its abundance and layered structure facilitate the exchange of a large amount of Li cations.

V_2O_5 thin films can be fabricated by a wide range of methods such as sol-gel [12, 13], radio frequency magnetron sputtering [14, 15, 16], chemical vapor deposition [17, 18] etc. The deposition parameters utilized in each deposition technique strongly influence the film characteristics such as structure, crystallinity, and morphology, all being directly responsible for the resulting electrochemical and electrochromic performance of the grown materials.

This Ph.D thesis deals with the characterization of V_2O_5 thin films deposited by Radio Frequency Magnetron Sputtering (RFMS) and High Power Impulse Magnetron Sputtering (HiPIMS) as well as the investigation and understanding of their electrochromic properties in respect of different structure and morphology depending on the deposition methods and conditions.

The part A describes the general concepts associated to this work. It is splitted in 3 chapters. After an introduction of general comments on electrochromism, including materials and applications, the characteristics of V_2O_5 are described. The third chapter introduces the deposition technique used in this work, that is to say the sputtering technique. The part B will

focus on the deposition and electrochromic characterization of single layers of V_2O_5 thin films deposited by Radio frequency magnetron sputtering (RFMS) and High Power Impulse Magnetron Sputtering (HiPIMS). In chapter 1, V_2O_5 thin films deposited by RFMS with V metal target and V_2O_5 oxide target are optimized. The relationship between the V_2O_5 thin film characteristics such as structure, crystallinity, and morphology and the deposition condition in RFMS is investigated. The electrochromic properties of V_2O_5 thin films are characterized by cyclic voltammetry in Li and Na based electrolytes combined with *ex-situ* optical measurements and compared. In chapter 2, V_2O_5 thin films deposited by HiPIMS with V metal target are optimized. The characteristics and electrochromic properties of V_2O_5 thin films are studied by cyclic voltammetry in Li and Na based electrolytes combined with *ex-situ* optical measurements and compared.

Better understanding on the involved mechanism at the origin of the multi-chromism of V_2O_5 thin films is investigated in part C. In chapter 1, initial comparisons in between the three different types of films, namely V_2O_5 RF-metal, V_2O_5 RF-oxide and V_2O_5 HiPIMS, are discussed in terms of faradic and capacitive contributions. In the second chapter, focusing on the V_2O_5 RF-metal, several characterizations including, XRD, XPS, TOFSIMS, AES and RBS/NRA are combined.

In Part D, EC devices are fabricated using deposited V_2O_5 thin films and their performance evaluation and applicability are described. In chapter 1, V_2O_5 thin film is combined to WO_3 thin film, using an ionic liquid transparent electrolyte, both in Li and Na based media. In chapter 2, double side type EC devices using two V_2O_5 thin films separated by a white opaque transparent electrolyte are fabricated and their EC properties are evaluated. Finally, the physico-chemical characteristics and electrochromic properties of V_2O_5 thin films deposited by RFMS and HiPIMS are summarized in "conclusion and perspectives" section.

Reference

- [1] C.G. Granqvist, *Handbook of Inorganic Electrochromic Materials*, Elsevier, Amsterdam (1995).
- [2] K.C. Ho, C.B. Greenberg, D.M. Macarthur, *Electrochem. Soc. Proc*, Electrochromic Materials and their Applications III PV (1996) 96.
- [3] C.G. Granqvist, E. Avendano, A. Azens, *Thin Solid Films*, 442 (2003) 210.
- [4] A. Azens, G.G. Granqvist, *J. Appl. Electrochem*, 7 (2003) 64.
- [5] C.G. Granqvist, E. Avendaño, A. Azens, *Thin Solid Films*, 442 (2003) 201.
- [6] F. Michalak, K. von Rottkay, T. Richardson, J. Slack, M. Rubin, *Electrochim. Acta*, 44 (1999) 3085.
- [7] E. Avendaño, A. Azens, G.A. Niklasson, C.G. Granqvist, *Sol. Energy Mater. Sol. Cells*, 84 (2004) 337.
- [8] S.J. Wen, J. Kerr, M. Rubin, J. Slack, K. von Rottkay, *Sol. Energy Mater. Sol. Cells*, 56 (1999) 299.
- [9] M. Martini, G.E.S. Brito, M.C.A. Fantini, A.F. Craievich, A. Gorenstein, *Electrochim. Acta*, 46 (2001) 2275.
- [10] V.R. Buch, A.K. Chawla, S.K. Rawal, *Mater. Today: Proceedings*, 3 (2016) 1429-1437.
- [11] C.G. Granqvist, *Sol. Energy Mater. Sol. Cells*, 99 (2012) 1-13.
- [12] D. Yu, C. Chen, S. Xie, Y. Liu, K. Park, X. Zhou, Q. Zhang, J. Li, G. Cao, *Energy Environ. Sci*, 4 (2011) 858.
- [13] D. Liu, Y. Liu, B.B. Garcia, Q. Zhang, A. Pan, Y.H. Jeong, G. Cao, *J. Mater. Chem*, 19 (2009) 8789.
- [14] N. Kumagai, H. Kitamoto, M. Baba, S. Durand-Vidal, D. Devilliers, H. Groult, *J. Appl. Electrochem*. 28 (1998) 41.
- [15] C. Navone, R. Baddour-Hadjean, J.P. Pereira-Ramos, R. Salotb, *J. Electrochem. Soc*, 156

(2009) A763-A767.

[16] I. Quinzeni, S. Ferrari, E. Quartarone, P. Mustarelli, *J. Power Sources*, 196 (2011) 10228-10233.

[17] N.K. Nandakumar, E.G. Seebauer, *Thin Solid Films*, 519 (2011) 3663-3668.

[18] H. Yin, K. Yu, H. Peng, Z. Zhang, R. Huang, J. Travas-Sejdic, Z. Zhua, *J. Mater. Chem*, 22 (2012) 5013-5019.

PART A : STATE OF THE ART

In order to address the various aspects of our work, this part is separated in four chapters. Electrochromism is described in chapter 1, vanadium oxide (V_2O_5) is described in chapter 2 and sputtering deposition method is described in chapter 3, respectively.

Chapter 1. Electrochromism

1. Overview

1.1 Context of smart windows

It is now essential to pay special attention to buildings, consumers of 30 to 40% of primary energy [1]. This energy is mainly used to heat, cool, light or even ventilate our habitat. The window should no longer simply be used for its main function, which is to let the light enter a room, but go beyond and plays a much more significant role in our daily lives. It can be used in various forms and formats to satisfy the visual appearance, but must also isolate external noise, retain heat and prevent cold to enter a room. In recent years, the purchase of air conditioners to improve our comfort has become indispensable following the record-breaking temperatures every year. In return, it has become the main source of expenditure following their intensive use in summer. In addition, a person spends an average of 80 to 90% of their time in a closed room, with only contact with the outside the window. It is a way to take advantage of the external view, while benefiting from the sunlight. The latter is also known for these health benefits. Small windows have been shown to have a negative impact on the quality of work provided. To remedy this, architects favor larger windows. Therefore, our habitat will have to evolve technologically and it will undoubtedly pass through the use of so-called smart high-tech windows, also called "Smart Windows". These smart windows have the ability to block the thermal effects induced by infrared radiation from the sun, and therefore limit the use of air conditioning systems while continuing to contribute to the well-being of people working or residing in these buildings. Smart windows have existed since 1984 [2] and rely on one of the chromogenic technologies including thermochromics, gasochromics and electrochromics [3]. Electrochromism is defined by the ability of a system to modify its optical properties in response to an applied voltage. Thus in the visible field, electrochromic materials can change color. This phenomenon results from a double injection of ion and electron. Currently, several companies market smart electrochromic windows, such as Suntuive [4], SageGlass [5], ChromoGenics AB [6], Viewglass [7] or EControl-Glas GmbH [8]. Figure 1 is an example of the concept of smart windows proposed by EControl-Glas GmbH.



Figure 1. Illustration of a smart window proposed by the EControl-Glas GmbH. The left part is colored blue-gray and blocks some of the visible light and IR while the right part is colorless and transmissive to light [8].

1.2. Principle of operation of an electrochromic device (ECD)

The structure of an electrochromic device (ECD) is essentially based on 5 layers as shown in Figure 2 :

- two transparent and conductive oxide (TCOs), located at the extreme parts of the ECD, ensuring the conduction of electrons from one electrode to the other via an external circuit.
- two electrochromic materials (EC1 and EC2) located between the TCOs and separated by the electrolyte.
- an electrolyte, located between EC1 and EC2, allowing the diffusion of ions from one material to the other.

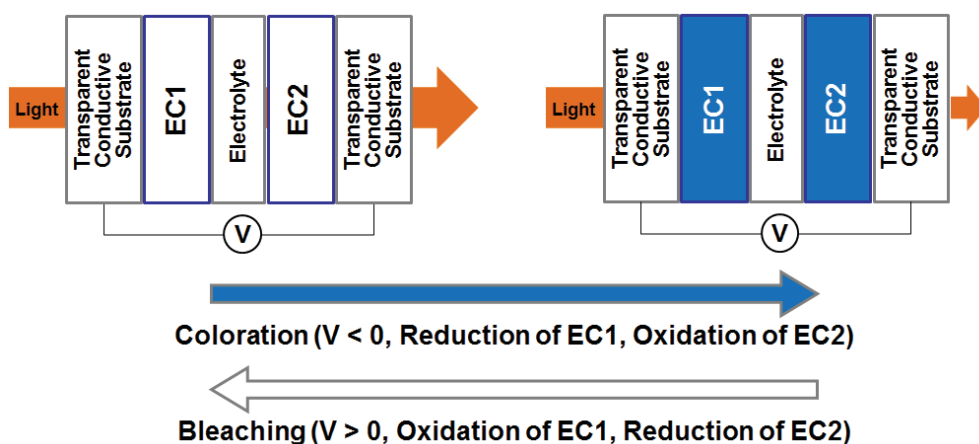


Figure 2. Principle of operation of an electrochromic device composed of 5 layers according to the

electrochemical chain: TCO / EC1 / electrolyte / EC2 / TCO. When a voltage greater than 0 V is applied, the device will be colored. When a voltage less than 0 V is applied, the device will be bleached. This example device corresponds to NiO and WO₃.

The operating principle of an ECD, schematized in Figure 2, is often compared to an optical battery. When a voltage (> 0 V for example) is applied between the two TCOs, the electrons will move from EC1 to EC2 via the external circuit, while the ions will travel the path that separates EC1 from EC2 via the electrolyte. Oxidation-reduction reactions will thus be performed at each electrochromic layer. When the first electrochromic layer is reduced, simultaneously the second electrochromic layer is oxidized.

Since the electrochromic layers are colored simultaneously, there are two categories of electrochromic materials:

- the electrochromic materials with anodic coloration, the latter are colored in oxidation.
- the electrochromic materials with cathodic coloration, the latter are colored in reduction.

There are mainly two types of ECDs (Figure 3). The transmissive ECD will be passed incident light through the device. The reflective ECD will be reflected the incident light and released to the opposite side. When the ECD is in the colored state, the intensity of the transmitted or reflected light is less than the intensity of the incident light.

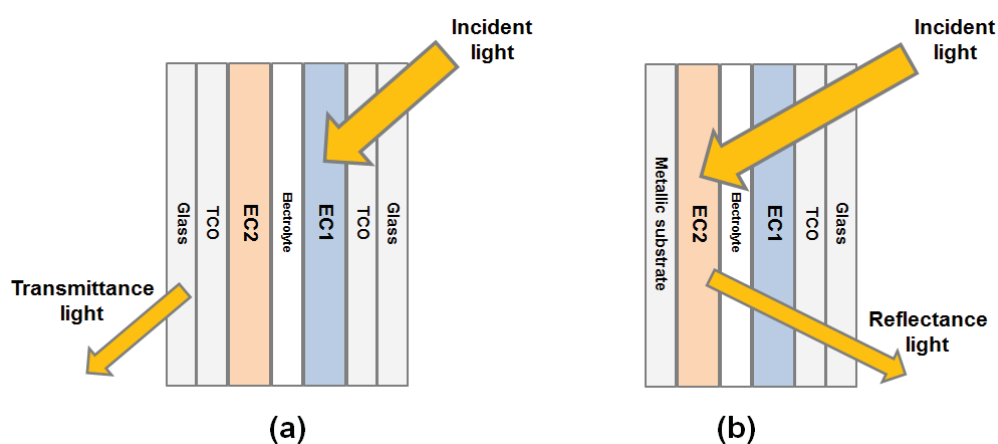


Figure 3. Two operating modes for the ECD: (a) Transmissive, Glass/TCO/EC1/electrolyte/EC2/ TCO/Glass, (b) Reflective, reflective substrate/EC1/electrolyte/EC2/TCO/Glass.

1.3. Applications

1.3.1 Smart window

The classic window is a center of exchange of light and heat between the outside and the inside, which is necessary to regulate with the help of air-conditioning systems so that our comfort is optimal. The smart window is today the flagship application in the field of electrochromism for the benefits it offers. It aims to improve human comforts in our habitats, but also to reduce our electricity bills related mainly to the use of air conditioning and lighting systems. Even if there are some models already on the market, it is still difficult to obtain information on the exact composition of ECDs. This fear of disclosing information on the composition of ECDs, shows that it is a technology still maturing, which requires the lifting of some technological locks.

The sunlight has wavelengths between 300 and 3000 nm. The region of visible (Vis) is between 380 and 780 nm, that of ultraviolet (UV) and infrared (IR) is at wavelengths lower and higher than the visible region respectively. Infrared light makes us feel warm, while visible light allows us to see the color. Figure 4 represents the solar spectrum (1.5G irradiance in black) and the percentage of optical transmission in the color state (sky blue) and color (red) of the ECD. The green zone corresponds to the visible light that we perceive. This figure shows that when the ECD is in the colored state, the IR radiation and visible part is totally blocked by the ECD. In the bleached state, EDC is transmissive to the visible part and infrared radiation.

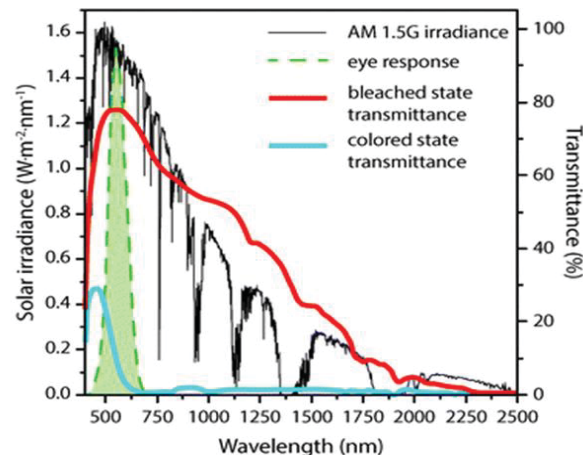


Figure 4. Representation of the solar spectrum (black curve) and optical transmission spectra of ECD at colored state (light blue) and bleached state (red) [9].

Figure 5a is an example of the colored and bleached state of a smart window marketed by SageGlass and Gentex Corporation. An occupant has the ability to regulate the temperature inside a room and its visibility on the outside by controlling the coloration state of the smart window. Figure 5b shows the airplane windows in their four states.



Figure 5. Example of two color states of an intelligent window commercialized by SageGlass (a). Two intermediate levels of tint are also available between the transparent and colored state allowing to adjustable at its convenience the shade of the window [4]. Instead of window shades, these airplane passenger windows incorporate an electrochromic device that can progressively darken the window (left to right) as the passenger desires. Gentex Corporation (b) [10].

Smart windows can provide the following advantages.

- Possibility of regulating the internal temperature of a room.
- Decrease in the price of the electricity bill, through the decrease (see removal) of the use of cooling systems, especially in times of high heat (the California Energy Board, believes that smart windows can reduce the energy peak associated with cooling systems by 19-26% [11]).
- Decrease in the price of the electricity bill, related to the decrease in the use of lighting

systems (energy savings related to lighting, can be from 48 to 67% when windows are controlled for improve visual comfort [11]).

- . Opening on the outside thanks to the removal of the shutters. Human well-being accentuated by the benefits of sunlight.
- . Possibility of creating houses all glazed. Building constructions are increasingly focused on fully glazed facades, giving the occupants a panoramic view of the outdoors.
- . Suppression of glare on computer screens or televisions.
- . Possibility to control smart windows individually to adapt to the position of the sun.
- . Possibility to control smart windows thanks to cell phones, tablets etc ...

1.3.2 Displays, mirrors and wearable devices

Electrochromic devices have been applied to various fields besides Smart Windows. Figure 6 shows examples applied to displays, mirrors and wearable devices. A Portugal company called Ynvisible is using electrochromic materials to create cards, store displays and even advertisements in print (Figure 6a) [12]. In this example, a touch on a promotion for an airline ticket switches an electrochromic panel and displays the fare. Figure 6b is Gentex Night Vision Safety (NVS) glare elimination mirrors, which are equipped several million cars [10]. When switched on (bottom), electrochromic dyes produce a blue-green color that reduces glare by both removing some of the light intensity and absorbing some of the wavelengths. Electrochromic polymers can be printed onto spandex, which can be treated to act as an electrode (Figure 6c). Switching from its neutral (top left) to its oxidized state (top right) turns the polymer green. A prototype, stenciled design shows the same change from top to bottom (below) [13].

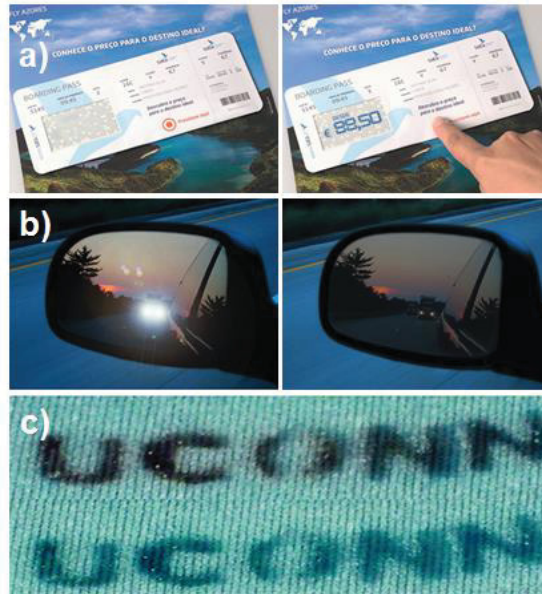


Figure 6. ECD applications for displays (a) [12], mirrors (b) [10] and wearable devices (c) [13].

1.3.3 The Market

According to the latest n-tech reports (Figure 7), it is estimated that the market for electrochromic glasses (smart windows and electrochromic mirrors) could reach \$ 3 billions by 2020. By 2019, the smart window market would reach \$ 500 millions while it was only \$ 40 millions in 2016. Smart windows, for the moment, are present in a wide variety of buildings, such as those related to education, hospitals or shopping malls, airports. But, individuals and regions with strong sunshine are high potential markets and are still little exploited. A recent policy of using energy in an efficient way in relation to building development is a prerequisite for the exponential growth of smart window sales.

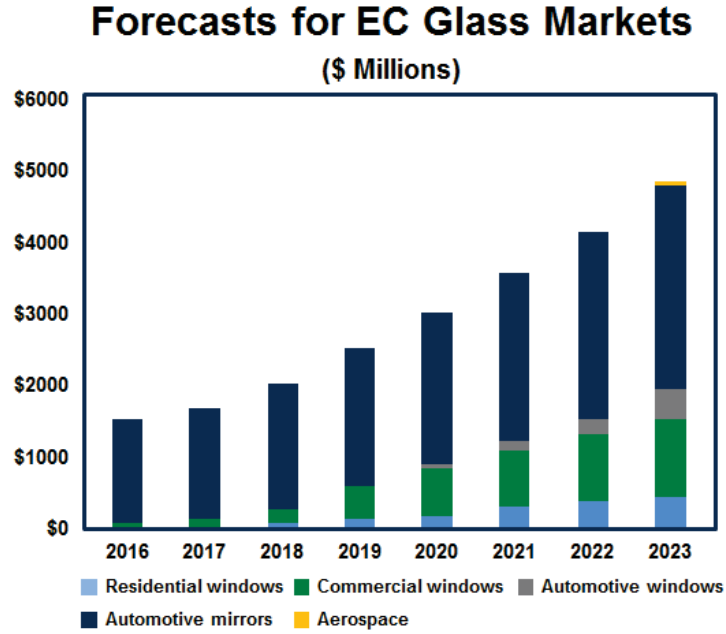


Figure 7. Market for electrochromic glass estimated by n-tech [14].

1.4. Performance criteria

The performances of electrochromic material and ECD are evaluated according to several criteria.

-. Optical contrast and density (OC, OD) : The difference in transmittance between the bleached and colored state can be expressed ΔT as equation 1. The optical contrast is defined by the ratio of optical transmission between the bleached (T_b) and colored (T_c) states, equation 2. The OC is classically calculated for the wavelength λ corresponding to the maximum sensitivity of the eye. ($\lambda = 550 \text{ nm}$)

$$\Delta T = T_b - T_c \quad (1)$$

$$OC = \frac{T_b}{T_c} \quad (2)$$

The OC is calculated via the ratio of the transmittance in the bleached and the transmittance in colored state. The larger the OC, the more the difference between the bleached and colored

state will be marked. Higher value of OC indicates larger difference in transmittance. Therefore, we could evaluate a given electrochromic device with its OC, together with its optical density, $\Delta OD(\lambda)$. The optical density can also be expressed as equation 3.

$$\Delta OD = \log \frac{T_b}{T_c} \quad (3)$$

- **Coloration efficiency (CE)** : This corresponds to the optical density (ΔOD) on the quantity of charges provided (Q), (equation 4). A high CE is often associated with good electrochromic performance.

$$CE = \frac{\Delta OD}{Q} \quad (4)$$

- **Life time** : this corresponds to the ability of an ECD to bleach and then color without altering its optical and electrochemical performance.

- **Switching time** : this is the time required by the material or ECD to change from a color state to a second color state and vice versa. A switching time of the order of ten minutes is accepted for smart windows as it leaves to adapt to the color change, while this order of magnitude decreases to a few seconds for displays in order to obtain information as quickly as possible. The switching time for coloration and bleaching is generally different and also depends on the active surface of the device.

- **Operating temperature** : the ECD must be able to maintain good electrochemical and optical performance in a temperature range of -40 to 100 ° C.

- **Memory effect** : it corresponds to the ability of ECD to retain in its bleached or colored state when the voltage is no more applied.

The economic criterion is not addressed in this section, but it is obviously an essential criterion to hope for a large commercialization. These criteria are numerous and make it possible to ensure the proper functioning of an electrochromic material or device.

1.5 Light-matter interaction

During the light-matter interaction, the light will be transmitted (T), absorbed (A) or reflected (R) (Figure 8). Part of the radiation can be used except for light that is redistributed into space after it has been in contact with the material. If we do not consider the diffusion, the total energy of the light will obey the following relation (equation 5)

$$T + A + R = 1 \quad (5)$$

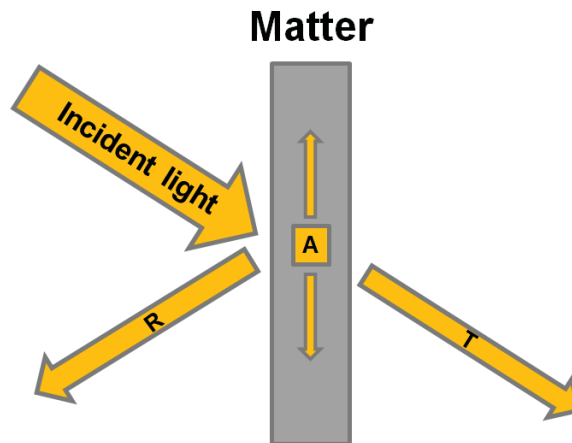


Figure 8. Interaction between incident light matter, T transmission, A absorption, and R reflection.

Figure 8 is a simple model with a single interface between air and material, but this model can be much more complex in an ECD. The interactions will depend on the wavelength (λ) of the incident light, the angle of incidence and the optical properties of the material. An ECD is composed of 7 layers (Substrate / TCO / EC1 / Electrolyte / EC2 / TCO / Substrate). Each layer will interact with light in a way that can lead to multiple transmission, reflection and absorption. An example of the multiple interactions of light with ECD (3 layers: EC1 / electrolyte / EC2) is shown in Figure 9. In this example, the fractional indices are not taken into account, but at the interface between two different materials, the light follows the Snell-Descartes law, equation 6 :

$$n_1 \sin i_1 = n_2 \sin i_2 \quad (6)$$

n_1 and n_2 , correspond to the refractive indices of each material and i_1 and i_2 correspond to the

2.1.1 Conductive polymers

The electrochromic properties of a conductive polymer were first described in 1981 by Diaz et al. for poly-N-methylpyrrole [15]. Since then, intense work has been done on conductive polymers, and today the most commonly used are polyaniline (PANI) [16], polypyrrole (PPy) [15], polythiophene (PTh) [17, 18, 19] and many derivatives. Conductive polymers are generally synthesized by electropolymerization. The polymers are insulator in the neutral state, but are generally doped by reaction with an oxidizing agent or reducing making them conductive. The optical properties of these materials can be modified by controlling the doping, thus playing on the band gap between the HOMO energy level and the LUMO energy level [20]. The p-type conductive polymers are the most common in the literature due to their better stability compared to the n-type conductive polymers. The conductivity of these materials can reach 10^2 - 10^5 S/cm [21]. Conductive polymers are able to carry a charge through alternating single and double bonds π - π . The main mechanism involves a coupling between radical cations, or a reaction between a radical cation with a neutral monomer (a neutral monomer becoming a radical cation by oxidizing (loss of electron)). Much research has been done on derived materials such as aromatics and aromatic heterocyclic structures. The electrochemical oxidation of aromatic molecules, such as pyrrole, thiophene, aniline, furan, etc., leads to electroactive conductive polymers (oxidation / reduction).

Polythiophene [17, 18, 19], polypyrrole [15] and polyaniline [16] have received the most attention with regard to their electrochromic properties. Polythiophene (PTh) is particularly stable and easy to synthesize. The PTh is blue when it is doped (oxidized) and red when it is in its undoped form. Color modification is possible by judiciously choosing the thiophene monomer. For example, the colors available with a polymer prepared with 3-methylthiophene will depend on the position of the methyl groups on the main chain of the polymer. The available colors in the oxidized form are pale blue, blue, violet and in reduced form, pink, yellow, red or orange [22]. The colors also depend on the length of the polymer chain. Materials based on poly (3,4-(ethylenedioxy) thiophene) (PEDOT) have a smaller band gap than polythiophenes, giving them greater absorbance in the near-infrared region. The doped PEDOT is transparent (sometimes slightly bluish) in the visible region and the neutral polymer is blue-black [17, 23, 24, 25]. Polypyrrole (PPy) is blue-violet when doped then yellow-green when electrochemically reduced. Polyaniline can change from a yellow-to-green state when oxidized, but can also be colored dark blue, purple, or brown when even

more positive potentials are applied. However, too high potentials can suppress the reversibility property. Table 1 gathers some electrochromic conductive polymers.

Table 1. Some examples of electrochromic conductive polymers [26].

Material	Anion	Electrolyte	
		Oxidation state	Reduction state
Polypyrrole (PPy)	ClO_4^-	Brown	Yellow
Polythiophene (PTh)	ClO_4^-	Brown	Green
Polymethylthiophene (PMT)	BF_4^-	Blue	Red
Poly-3,4-dimethylthiophene	ClO_4^-	Dark blue	Blue
Poly-2,2-bithiophene (PBTh)	CF_3^- , SO_3^-	Bule/gray	Red
Polyaniline (PANI)		Green-blue	Yellow-transparent

The main advantages of conductive polymers are their short response times and the possibility of obtaining a large color panel. The main disadvantage is their limited life time and UV instability compared to metal oxides.

2.1.2 Viologen and Prussian blue compounds

2.1.2.1 Viologen

The most studied viologen is : 1,1-dimethyl-4,4'-bipyridilium (MV) (Figure 10). It is mainly known in 3 states, in neutral form, with a positive charge (radical cation) and with two positive charges (dication). Dication is the most stable form and is colorless, whereas viologen with a radical cation is the compound with the most intense color. The maximum wavelength of the compound can vary according to the substituent nitrogen as shown in table 2. Viologen is particularly used in the electrochromic mirrors of the Gentex company [27].

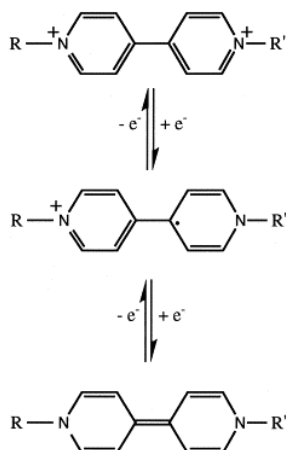


Figure 10. Viologen : 1,1-disubstituted -4,4-bipyridilium in its neutral form, with a positive charge (radical cation) and two positive charges (dication).

Table 2. Different substituents, anions and solvents that can alter the optical properties of viologen [28].

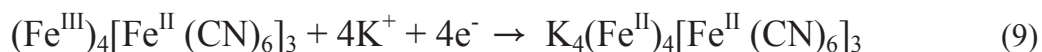
Substituent	Anion	Solvent	λ_{\max} nm
Methyl	Cl ⁻	H ₂ O	605
Methyl	I ⁻	H ₂ O-MeCN	605
Methyl	Cl ⁻	MeOH	609
Methyl	Cl ⁻	EtOH	611
Ethyl	ClO ₄ ⁻	DMF	603
Heptyl	Br ⁻	H ₂ O	545
Benzyl	Cl ⁻	H ₂ O	604
P-CN-Ph	BF ₄ ⁻	PC	674
P-CN-Ph	Cl ⁻	H ₂ O	535

2.1.2.2 Prussian blue (PB)

Prussian blue $\text{Fe}^{\text{III}}[\text{Fe}^{\text{II}}(\text{CN})_6]$, or ferrocyanate, was discovered in 1704 [29]. Prussian Blue (PB) is often deposited on a conductive substrate by electroreduction from aqueous solutions of soluble salts of Fe^{3+} and ions $[\text{Fe}^{\text{III}}(\text{CN})_6]^{3-}$ and according to the following reaction (equation 8):



In an acidic aqueous electrolyte such as KCl, the K^+ ions balance the charges but do not interfere with the electrochromic properties [28, 30]. The reaction is written (equation 9):



blue

colourless

2.1.3 Metal oxides

It is accepted that a metal oxide changes color as a result of a change in the oxidation state of the metal cation. Table 3 shows some examples of inorganic electrochromic metal oxides with cathodic and anodic coloration. The oxides of iridium [31], rhodium [32], ruthenium [33], tungsten [34], manganese [35], cobalt [36] or nickel [37] are some examples of metal oxides having electrochromic properties. Vanadium oxide has the particularity of being both a material with cathodic and anodic coloration [38]. There are many deposition techniques to obtain these oxides in thin layers such as : thermal evaporation, sputtering, electro-deposition, sol-gel, etc. The thin layers can be deposited with a low thickness and made in large size. However, although they are stable under UV radiation, the oxide films can have the disadvantages of being sensitive to moisture and resistant to shocks and lead to cracks.

The most studied of inorganic EC is tungsten oxide. WO_3 is an oxide which has the optical property of switching in thin layers between colorless and the blue color [39]. The reversible modification of the optical properties, induced by the variation of the degree of oxidation of the tungsten cations, is due to the insertion (deinsertion) of positively charged ions associated with the injection (extraction) of electrons into the material. The blue color is related to the oxidation state of the tungsten cations ($\text{W}^{6+}/\text{W}^{5+}$), and can be modified reversibly by polarization inversion. The x in $\text{M}_x\text{W}_x^{5+}\text{W}_{1-x}^{6+}\text{O}_3^{2-}$ is the number of levels d1 just below the conduction band (CB) of the tungsten oxide (Figure 11). It also reflects the W^{5+} cation. The inter-band electronic transfer is accompanied by the absorption of less energetic photons (1.4 V) in the red, giving rise to the blue color in the visible. The band gap of WO_3 (E_g) is generally equal to 2.7 eV. It can vary from 2.4 eV (cubic structure) to 3.12 eV (orthorhombic),

leading to a high transparency of WO_3 [40, 41].

Table 3. The main inorganic electrochromic metal oxides of anodic and cathodic coloration with the associated colors in the oxidized and reduced states.

	Metal	Oxidation form	Reduction form
Cathodic coloration	Bismuth [42]	Bi_2O_3 Transparent	$\text{Li}_x\text{Bi}_2\text{O}_3$ Black-brown
	Molybdenum [43]	MoO_3 Transparent	M_xMoO_3 Intense blue
	Niobium [44]	Nb_2O_5 Transparent	$\text{M}_x\text{Nb}_2\text{O}_5$ Blue
	Titanium [45]	TiO_2 Transparent	M_xTiO_2 Blue-gray
	Tungsten [46]	WO_3 Transparent	M_xWO_3 Intense blue
Anodic coloration	Nickel [37]	NiOOH Brown	$\text{Ni}(\text{OH})_2$ Transparent
	Iridium [47]	$\text{IrO}_2\cdot\text{H}_2\text{O}$ Blue-gray	$\text{Ir}(\text{OH})_3$ Transparent
	Cobalt [36]	Co_3O_4 Black-brown	$\text{M}_x\text{Co}_3\text{O}_4$ Light-yellow
	Manganese [48]	MnO_2 Black-brown	MnOOH Light-yellow
Cathodic/anodic coloration	Vanadium [49]	V_2O_5 Brown-yellow	$\text{M}_x\text{V}_2\text{O}_5$ Light-blue

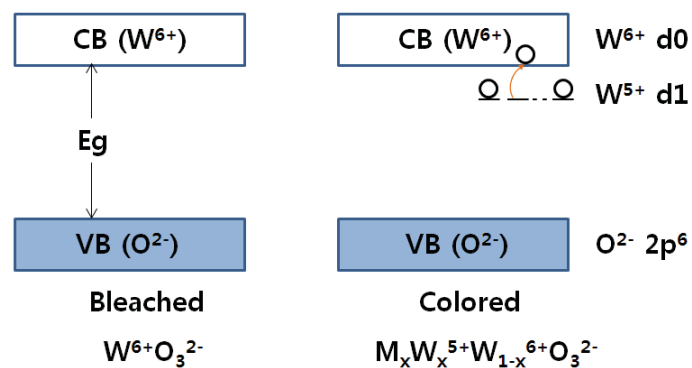
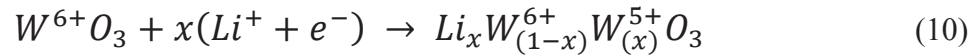


Figure 11. Diagram of the conduction (CB) and valence (VB) bands in the colorless (left) and colored (right) state of tungsten oxide, WO_3 .

WO₃ is conventionally cycled in an electrolyte having small cations such as H⁺ (H₃PO₄ or H₂SO₄) or Li⁺ (LiClO₄-PC or ionic liquid with a lithium salt). The mechanisms involving these cations are equivalent. The electrochemical reaction of WO₃ in a lithium-based electrolyte is described (equation 10). x is the number of Li⁺ cations inserted into the WO₃.



WO₃ is most often present in its amorphous form [50, 51] even if the crystallized and / or hydrated forms of WO₃ also possess interesting electrochromic properties [52, 53]. The bonds are mainly ionic and the stoichiometry can be illustrated as being composed of ions W⁶⁺ and O²⁻ [54, 55, 56]. Each W⁶⁺ ion is surrounded by 6 O²⁻ ions, ideally forming an octahedron. Each O²⁻ ion is bound to 2 tungsten ions in a linear configuration.

2.2 Electrolytes

The electrolyte is the central part of an ECD and should meet a set of criteria:

- It must be a good ionic conductor to obtain fast kinetics.
- It must not be degraded in the window of optimized potential for coloration and bleaching ECD.
- It must be transparent for the application of smart windows.
- It must be chemically inert.
- It must be an electrical insulator.
- It must not break down, freeze or evaporate under temperature.
- It must be mechanically resistant.
- It must be manufactured at low cost and non-polluting for the environment.
- It must ensure adhesion between the two electrochromic layers.

For ECDs, there are essentially two types of electrolytes: solid films (metal oxides), polymeric membranes. Laminated ECDs can be obtained from polymeric membranes using or not ionic liquids while solid ECDs contain solid films.

2.2.1 Metal oxides

The metal oxides Ta₂O₅ [57], ZrO₂ [58], LiTaO₃ [59], LiNbO₃ [60], are some examples of solid electrolyte meeting many of the criteria. The thin layers are generally porous and the pre-insertion of H⁺ and Li⁺ cations is carried out by co-spraying, chemically, electrochemically or by exposure to moisture.

2.2.2 Ion conductive membranes

The ionic conductive membranes consist mainly of a polymer (solid or gel) that acts as a host matrix and an ionic salt that provides the ions. The viscosity of the membrane and the concentration of ions present will play a role in the overall kinetics of the system. These membranes contain monovalent cations such as H⁺, Li⁺, Na⁺ and K⁺ [61, 62]. The solid polymers are generally composed of a lithium salt, such as LiClO₄ or LiPF₆, dissolved in a polymer such as poly (methylmethacrylate) (PMMA), polyvinylidene diouride (PVDF) or poly (ethylene oxide) (PEO). The membranes can be gelled, and are composed of a large amount of liquid electrolyte in a host polymer. They have a better ionic conductivity but less interesting mechanical properties than solid polymers. The most widely used polymers are PEO, poly (acrylonitrile) (PAN), poly (vinylidene-uoroide hexa-uoropropylene) (PVDF-HFP), PVDF, PMMA.

2.2.3 Ionic liquids

Ionic liquids are defined as salts with a melting temperature below 100 °C, acting both as a solvent and as a salt. Ionic liquids offer several advantages in terms of ionic conductivity, transference number, electrochemical window, as well as physical and chemical properties such as non-volatility, melting point, density, viscosity and observed temperature of solidification. The non-volatility of the ionic liquid also makes it possible to operate in temperature ranges higher than those used for aqueous solvents. They are non-flammable, have a high ionic conductivity of between 10⁻² and 10⁻⁵ S.cm⁻¹ and are stable in a large window of electrochemical potential (about 4 V) [63, 64, 65, 66, 67]. There are many combinations of anions and cations to adjust the properties of ionic liquids. The most used cations are imidazolium, ammonium, phosphonium, triazolium, pyrrolidinium and

pyridinium and are presented in Figure 12.

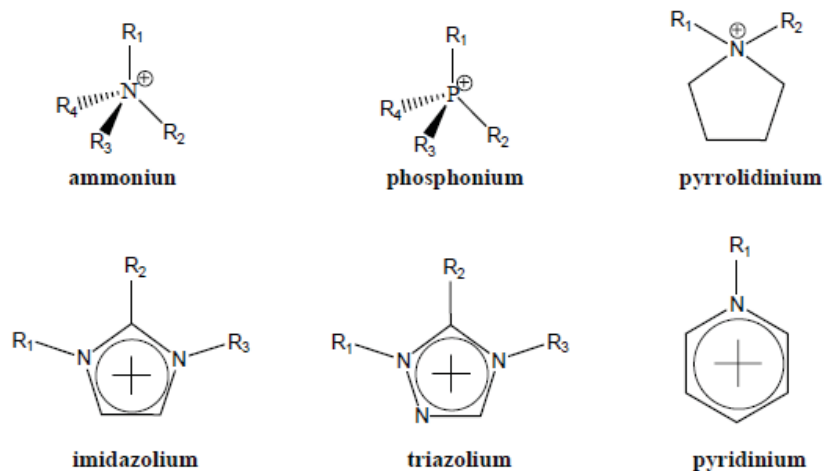


Figure 12. The most commonly used cations in ionic liquids.

There are also numerous anions such as bis((tri-uromethyl)-sulfonyl)imide (TFSI), perchlorate (ClO_4^-), tetra uoborate (BF_4^-), hexa uorophosphate (PF_6^-), tri-uoroacetate (CF_3CO_2^-) etc. During this work, ionic liquids composed of an imidazolium cation and a bis((trioromethyl)sulfonyl)imide anion were mainly used. They are presented in Figure 13. $\text{Li}_3\text{NaTFSI-EMITFSI}$ electrolyte used in this work and are presented in Table 4 and Figure 14.

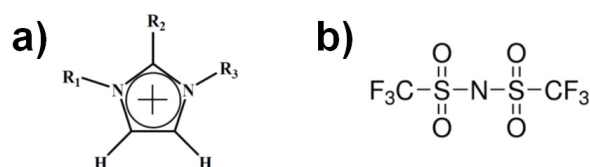


Figure 13. (a) cation of imidazolium and (b) anion bis((trifluoromethyl)sulfonyl) imide

Table 4. The electrolytes used in this work.

Ion	Cation [Acronym]	Anion [Acronym]	R1	R2	R3
Li / Na	1-ethyl-3-methylimidazolium [EMI ⁺]	bis((trifluoromethyl)sulfonyl) imide [TFSI]	CH ₃	H	C ₂ H ₅
	1-butyl-3-methylimidazolium [BMI ⁺]		CH ₃	H	C ₄ H ₉

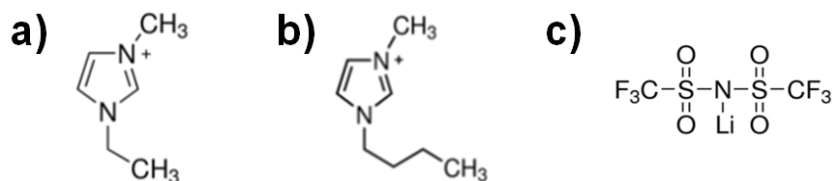


Figure 14. (a) 1-ethyl-3-methylimidazolium(EMI), (b) 1-butyl-3-methylimidazolium (BMI) and (c) bis(trifluoromethane)sulfonimide lithium salt (LiTFSI).

2.3 Transparent Conductive Oxides (TCOs)

The main role of the conductive transparent oxide layer is to provide electrons to the electrochromic layer. As its name implies, a TCO must be as transparent as possible while having the characteristic of being a good electronic conductor. The first report on transparent conductor oxides dates from 1907 by Badeker, who showed that a thin layer of cadmium (Cd) could become transparent while remaining conductive when oxidized [68]. Thin layers of strongly doped oxides with a wide band gap (> 3.3 eV) are commonly used. Indium oxide doped with tin (In_2O_3 : Sn, ITO) has a n-type conductivity and is the state of the art [69]. Thin ITO films are generally deposited on a glass substrate. Their visible absorption is generally less than 2% and average reflection in IR region reaches about 90%. They combine low resistivity ($\sim 1 \times 10^{-4}$ Ωcm) with excellent transmission (over 85-90%) and good durability. The deposition on flexible substrates can introduce risks of cracking and delamination, inducing a decrease of the electrical conductivity. The fluorine doped tin oxide (SnO_2 :F, FTO) [70], zinc oxide doped with aluminum (ZnO :Al) [71] or zinc oxide doped with gallium (ZnO :Ga) [72] are also good transparent conductive oxides. Highly metallic films with high transparency, electrical conductivity and resistance to mechanical pressure higher than the oxide layers can also be considered like TCOs. Lansaker et al. [73] reported about a transparent conductive material consisting of a very thin (< 10 nm) gold films sandwiched between two films of TiO_2 . This multilayer possessed a transmission of 80% and a resistivity of about 10^{-4} Ωcm . Leftheriotis et al reported [74] a transparent conductive material of ZnS/ Ag/ ZnS type also providing good transmission ($> 70\%$) at a wavelength of 550 nm.

2.4 Substrates

The substrates are positioned at both ends of the EDC. Glass substrates (substrates) are generally used for the application of smart windows. For the application of the electrochromic mirrors, one of the two substrates is metallic to ensure the device's re-arrangement. In order to diversify the applications, the use of paperboard, plastic or tissue substrates is becoming more and more frequent.

In this study, ITO coated glass was used as substrate. The ITO substrate, with a thickness of 80 nm, coated glass (25 mm x 25 mm) was purchased from SOLEMS and had a sheet resistance of 30 Ω /sq.

3. Characterization technique : electrochemistry

3.1 Some notions

Electrochemistry is defined as a science dealing with the relation between electrical and chemical phenomena. During an electrochemical reaction, a cation of the reactive species changes its degree of oxidation following a reduction or oxidation reaction, thus generating electrons and a current I (mA). The electrochemical reaction is not spontaneous but results from the application of a voltage U (V), higher than the equilibrium voltage of the material to oxidize or lower than the equilibrium voltage to reduce. By convention, a positive current characterizes an oxidation and a negative current a reduction.

In 3-electrode system without agitation, the ions move mainly through migration and diffusion. Migration corresponds to the displacement of the charged species under the influence of an electric field diffusion associated to the displacement of the charged species under the influence of a concentration gradient. The electrolyte is an ion source composed of cations and anions. Under the state of the electric field, the anions and cations will migrate in the opposite direction from one electrode to the other.

Depending on the nature of the working electrode and the ions present in the electrolyte, intercalation / insertion and / or adsorption mechanisms at the electrode-electrolyte interface can be evidenced by methods such as cyclic voltammetry (CV) and chronoamperometry (CA)

(these techniques will be described in more detail later in the manuscript).

The signature of the current-potential curves of a cyclic voltammetry is characteristic of the reaction that occurs at the electrode, and may be faradic or capacitive in nature. Figure 15 shows the two forms of voltammograms corresponding to the two main electrochemical mechanisms. The presence of a peak in oxidation and reduction on a voltammogram is associated with faradic behavior while a voltammogram of rectangular shape reflects a capacitive behavior.

- A faradic current corresponds to a redox reaction.

- A capacitive current corresponds to an accumulation of charges on the surface of the electrode which does not result in a change in the chemical composition of the electrode

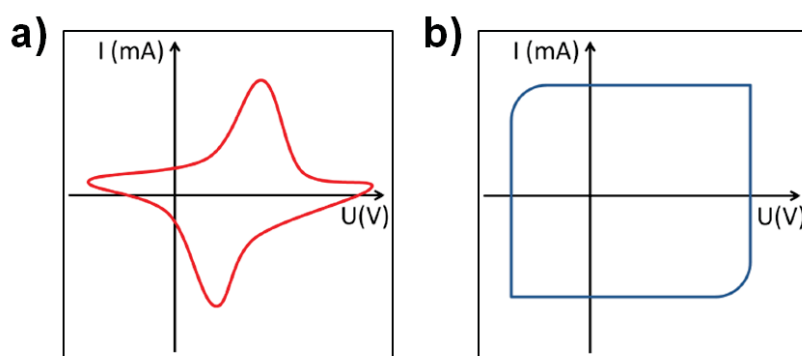


Figure 15. Simplified diagram of a voltammogram corresponding to (a) faradic behavior and (b) capacitive behavior.

When a current of instantaneous intensity $I(t)$ passes through an electrochemical cell for a time t , the capacitance involved is denoted by Faraday's law as being the integral :

$$Q = \int_0^t I(t) dt \quad (11)$$

The unit of electrochemical capacity is Coulomb (C) or A.s. The electrochemical capacity

corresponds to the consumption (for a reduction reaction) or the production (for an oxidation reaction) of Q/F moles of electrons during a reaction (Faraday is the electric charge carried by a mole of electron) and taking into account the stoichiometry of the reaction, the production or consumption of n moles:

$$n = Q/nF \quad (12)$$



The voltage of an electrochemical cell, notated U , denotes the potential difference between the two electrodes and is expressed in volts (V).

$$U = U_{WE} - U_{CE} \quad (14)$$

WE is the acronym for the working electrode and CE stands for the counter electrode.

The passage of current in an electrode is not always associated physically with a transfer of electrons through the interface. Indeed, the displacement of the charges can lead to the constitution of a double electric layer whose charge and discharge imply a current of capacitive nature. This capacitive current is distinguished from a faradic current implicated in an electrochemical reaction that obeys Faraday's law.

Table 5 presents some factors that influence the electrochemical response of a material in a given electrolyte. For example, a porous material will provide better electrolytic penetration and a greater surface area than a dense material. An electrolyte with a poorly adapted pH can degrade the material.

Table 5. Some characteristics of the materials / electrolytes impacting the current response.

Material	Electrolyte
Morphology	Viscosity
Structure	pH
Chemical composition	Nature of ions
Active surface	Ion size

3.2 Experimental techniques

3.2.1 Electrodes cell

Figure 16 shows the three-electrode cell used to characterize the electrochemical behavior of an electrochromic material. Three electrodes connected to a potentiostat are immersed in an electrolyte.

The three electrodes used are:

- a working electrode (WE) : a thin layer of electrochromic material on ITO glass substrate
- a counter-electrode (CE) : platinum plate (Pt)
- a reference electrode (REF) : a saturated calomel electrode (Hg / Hg₂Cl₂ / saturated aqueous solution of KCl), 0.248 V vs ENH

The electrolyte can be an acid, a base or an ionic liquid.

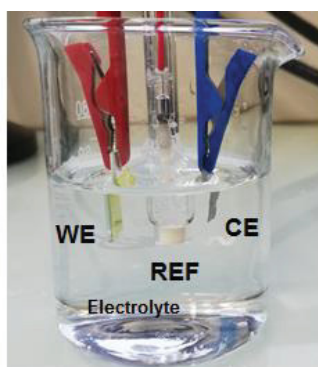


Figure 16. 3 electrodes cell, with a Platinum electrode as counter electrode, a saturated calomel reference electrode and a working electrode (thin electrochromic layer).

Note : For ECD, the voltage is applied between the two electrochromic layers.

3.2.2. Electrochemical characterization methods

The cyclic voltammetry and chronoamperometry are the two main methods for assessing the majority of performance criteria. They are presented in figure 17.

- Cyclic voltammetry (CV) : a current is recorded according to a linear variation of the potential in time, $I = f(U)$. When the potential reaches a given value, the direction of variation is reversed to a second value and so on. The scanning speed (mV/s) can be modified to favor surface or insertion phenomena.

- Chronoamperometry (CA) : alternatively, two potentials (U) are applied each for a time (t) and the current response as a function of time is recorded, $I = f(t)$. At $I = 0$ mA, for a given potential, the reaction of reduction or oxidation is then considered complete, the material is in equilibrium.

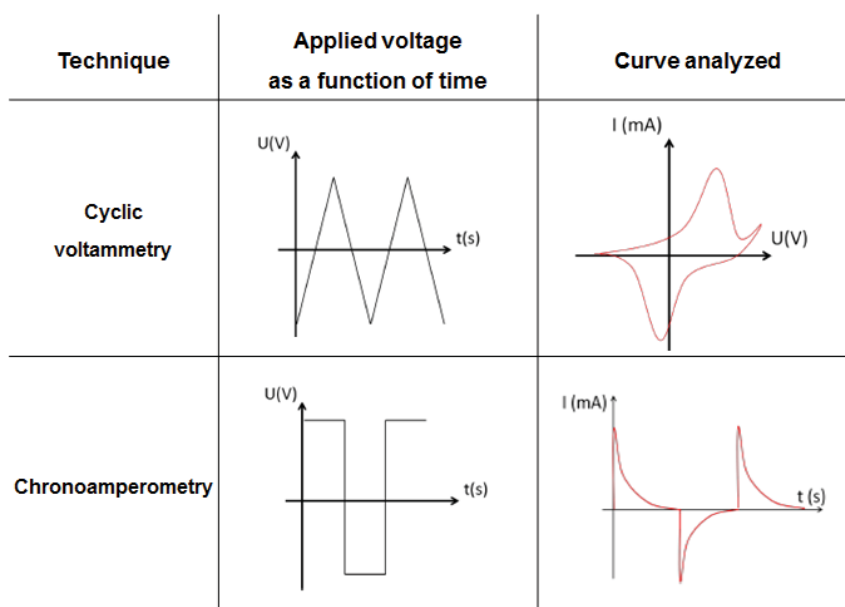


Figure 17. The figure shows the applied voltage versus time and the curve analyzed for the two main electrochemical techniques, the cyclic voltammetry and the chronoamperometry.

3.2.3. *In-situ* optical characteristics

The optical measurements were performed in a cell positioned within a VARIAN Cary 5000 dual beam spectrophotometer, providing the possibility of recording transmission spectra from ultraviolet to infrared. A beam of one or more wavelengths is focused on the material, then a detector at the output of the sample in the light transmitted. The sample must be in equilibrium during the measurement. In this study, the optical transmission of the thin film during a cyclic voltammetry or a chronoamperometry to evaluate the memory is recorded at a wavelength $\lambda = 650$ nm. For most electrochromic materials, it is usually measured at a wavelength of 550 nm. However, the vanadium oxide thin film used in this study exhibits an absorption edge near 550 nm. The electrochemical cell containing the electrolyte is used as a baseline for *in-situ* measurements whereas air is used as a reference for *ex-situ* measurements. The transmittance corresponds to the ITO coated glass substrate covered by the electrochromic thin film.

Chapter 2. Vanadium oxide (V_2O_5)

1. Vanadium oxide

Vanadium oxide has been one of the most extensively studied materials employed in different technological applications such as Li-ion batteries [75-85], Na-ion batteries [86], sensors [87, 88, 89], electrochromism [90-101], thermochromism [101-106] and photochromism [107]. Vanadium element exists in several oxidation states, including V^{3+} , V^{4+} and V^{5+} , allowing the formation of several oxides with exciting properties combining structural transformations with various V–O coordination geometries and optical, magnetic or electronic modifications [108, 109]. As examples, both vanadium dioxide (VO_2) and vanadium pentoxide (V_2O_5) undergo reversible semiconductor-metal phase transformation at specific temperatures of 68 °C and 280 °C, [110] respectively. This structural transformation brings about a great change both in electrical and optical properties. [111, 112, 113]

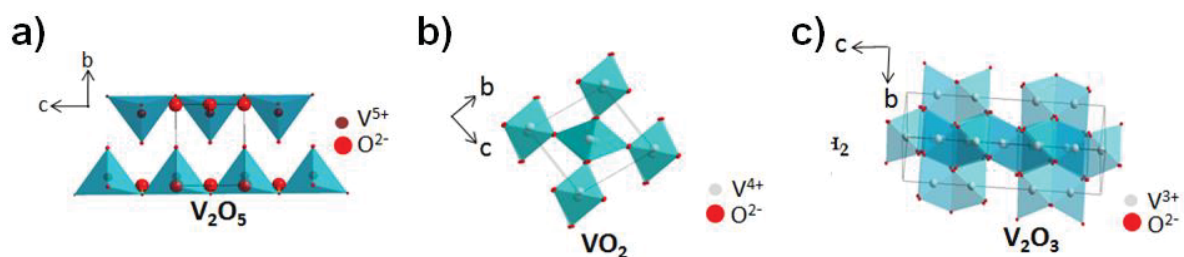


Figure 18. V_2O_5 , VO_2 and V_2O_3 [109].

Vanadium pentoxide (V_2O_5) is known for its most promising electrochromic properties. Other oxides with mixed valence oxidation states like V_6O_{13} where both V^{5+} and V^{4+} are present are also possible along with oxides with stoichiometry between VO_2 and V_2O_3 where V^{4+} and V^{3+} are present. These mixed valence oxides are possible due to oxygen vacancy defects. If enough vacancies are present, they can bind together along a lattice plane by reorganising the V–O coordination units. The wide range of possible primary and mixed oxides and their associated formation temperatures can be seen in the phase diagram in Figure 19.

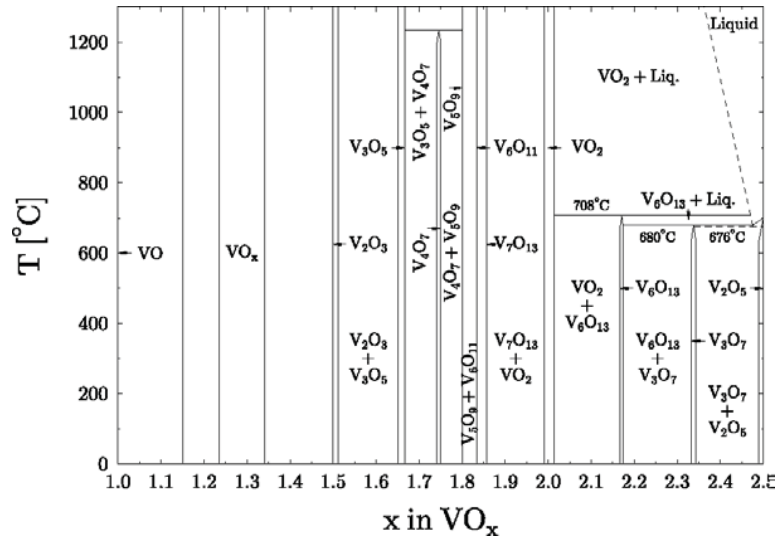


Figure 19. Phase diagram of the VO_x system [114, 115].

2. Structure of V₂O₅

Vanadium pentoxide (V₂O₅) has the highest oxidation state and is the most stable of all the oxides. It has a layered orthorhombic unit cell structure in the stoichiometry of VO_{2.458} ~ VO_{2.5} belonging to the Pmmn space group with lattice parameters $a=11.516 \text{ \AA}$, $b=3.565 \text{ \AA}$ and $c=4.372 \text{ \AA}$. [116, 117]. The V₂O₅ layered structure is made up of chains of edge sharing VO₅ square pyramids whose chains are linked together via corner sharing as seen in Figure 20.

The layered structure of V₂O₅ is constructed by the layers of series of VO₅ pyramids with distorted apices. These pyramids are in series in the planes of (00*l*). In every pyramid, a vanadium atom is embedded by five oxygen atoms, five V–O single bonds connect the vanadium atom to oxygen atoms. Among pyramids in the same layer, every oxygen atom is bonded by two or three vanadium atoms depending on its position. Within a series of the pyramids, positions of the oxygen atoms at the apices of pyramids alternate in the sequence of up-up-down-down. Furthermore, there is a weak V–O interaction between the oxygen atom at the apices of a pyramid and the vanadium atom within that in the adjacent layer [118]. This interlayered interaction that perpendicular to the *c*-axis maintain the layered character of the V₂O₅. After introducing the lithium ions into the interlayered spaces of V₂O₅, a series of the phase transformations will occur leading to the change of the crystalline structure as well

as electrochemical energy storage.

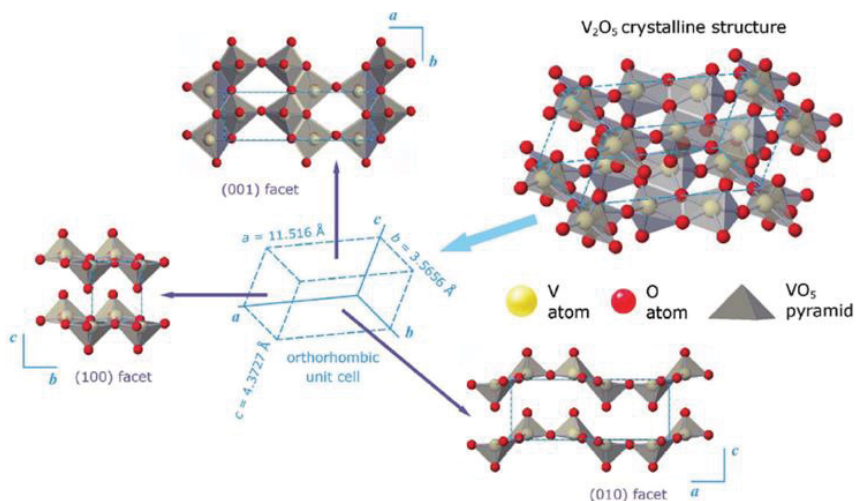


Figure 20. The crystalline structure of V_2O_5 within one unit cell. The orthorhombic unit cell of V_2O_5 is marked as blue dashed lines. The crystal structure of pristine V_2O_5 is built by square pyramids sharing edges and corners. The 3D view and the projected views of (100), (010), and (001) facets are depicted as well [119-123].

The polyhedra thus form double zig-zag chains along the axis b . These chains are connected laterally to each other by vertices along the axis a . This structure can also be described using irregular VO_6 octahedra where the sixth oxygen are at a greater distance of about 2.79 \AA (Figure 21). This link is a Van Der Waals bond perpendicular to the plane (a, b) thus ensuring the cohesion between the sheets.

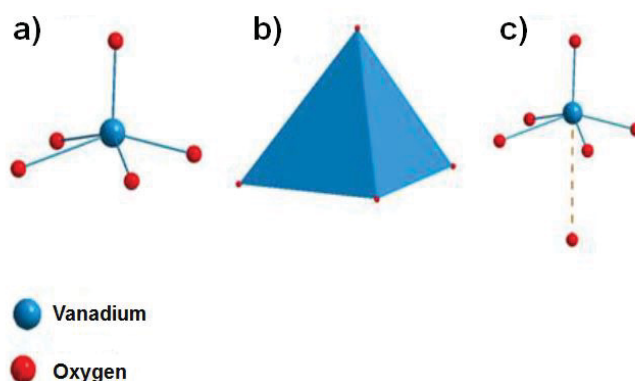


Figure 21. Vanadium coordination in V_2O_5 : square-based pyramid (a,b) and pseudo-octahedron (c).

3. Electrochromism of V₂O₅

As earlier mentioned, there are two main kinds of electrochromic oxides: ‘cathodic’ ones colouring under reduction and ‘anodic’ ones colouring under oxidation. Figure 22 indicates metals capable of forming oxides of these two categories and also points out that oxides based on vanadium are intermediate [124]. Vanadium oxide (V₂O₅) has a characteristic of showing different colors in the cathodic and anodic state. V₂O₅ is one of the only materials that clearly show both anodic and cathodic colorations as a result of the occurrence of various oxidation states associated with different colors. Thus offering the possibility of obtaining multicolor displays.

Electrochromic oxides

H																			He
Li	Be											B	C	N	O	F	Ne		
Na	Mg											Al	Si	P	S	Cl	Ar		
K	Ca	Sc	Ti	V	Cr	Mn	Fe	Co	Ni	Cu	Zn	Ga	Ge	As	Se	Br	Kr		
Rb	Sr	Y	Zr	Nb	Mo	Tc	Ru	Rh	Pd	Ag	Cd	In	Sn	Sb	Te	I	Xe		
Cs	Ba	La	Hf	Ta	W	Re	Os	Ir	Pt	Au	Hg	Tl	Pb	Bi	Po	At	Rn		
Fr	Ra	Ac																	

	Cathodic coloration
	Anodic coloration

Figure 22. Periodic system of the elements (except the lanthanides and actinides). Differently shaded boxes indicate transition metals with oxides capable of giving cathodic and anodic electrochromism [124].

Orthorhombic vanadium pentoxide (V₂O₅) is the “oxygen saturated state” (highest oxidation state for vanadium) in the VO_x system, and consequently the most stable one. It has attracted a considerable interest due to its interesting physical properties. Because of its anisotropic structural framework based on penta-coordinated vanadium (with square pyramid geometry), forming a “lamellar” structure (planes of edge sharing pyramids isolated from each other with a interlayer length about 4 Å), V₂O₅ is one of the most popular material for electrochromic applications. [125-132]. Indeed, facile intercalation of Li⁺ ions into the V₂O₅ interlayer spaces leads to redox phenomena associated with reversible changes of the optical

properties. Lithium intercalation and deintercalation in V_2O_5 can be described by equation 15:



There are three paths for lithium diffusion in the orthorhombic V_2O_5 (Figure 23)[133]. Path A and path B propagate along the b -axis and the c -axis, respectively. Both of them are one-dimensional spatial diffusion tunnels. Path C is a two-dimensional diffusion route, which approximately goes along the diagonal of the a and b -axis. Path A is the easiest direction for lithium ions to diffuse in the lattice of V_2O_5 .

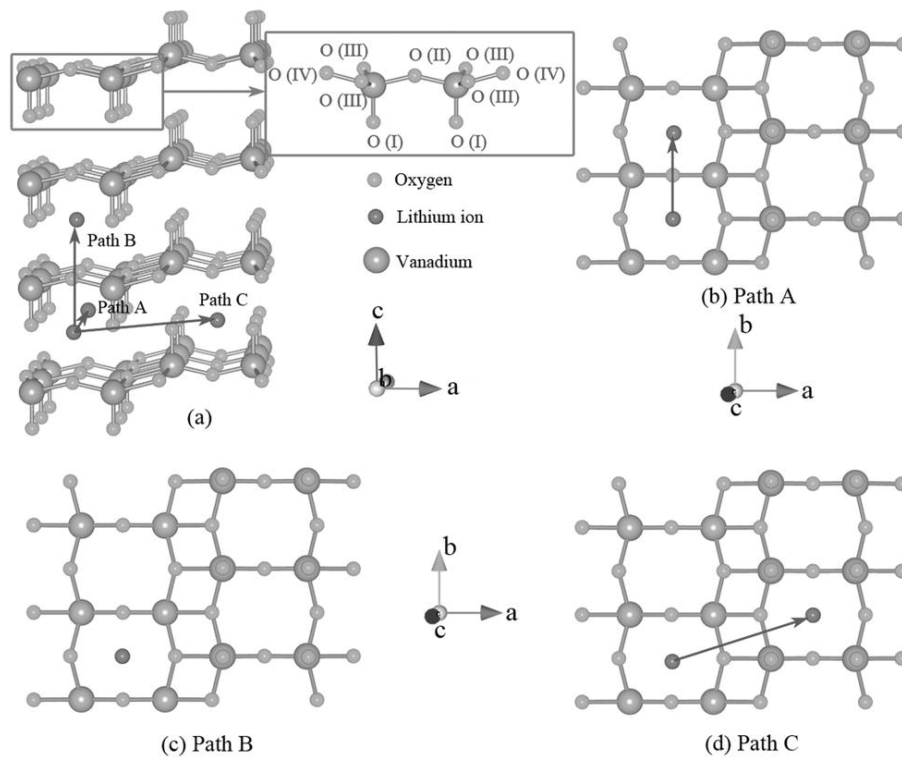


Figure 23. Schematic diagram of (a) possible Li^+ diffusion paths in the crystal lattice of the orthorhombic V_2O_5 viewed along the $[010]$ direction; (b) path A, path B, and path C viewed along the $[001]$ direction. Path A and path B propagate along the b -axis and the c -axis, respectively. Path C goes approximately along the diagonal of the a - and b -axis [133].

Chapter 3. Deposition method : sputtering

In our study, the deposition technique chosen to deposit thin films of vanadium oxide is sputtering. This work was performed in the service collective thin films with the help of Lionel TEULE-GAY and Dominique MICHAU. This deposition method was discovered in 1852 by Grove. It is part of the family of physical deposition techniques that includes thermal evaporation, laser ablation and sputtering. It is a technique developed on an industrial scale to make large surface deposits with a wide variety of materials. This technique allows a deposition of a large range of materials including metal oxide or nitride (ZnO, NiO, FeON, VN, NbON, CuO etc) [134-142]. The basic concepts of sputtering will be described in this section.

1. General overview of sputtering

1.1. Principle of sputtering

Figure 24 is an illustration of the basic principle of cathodic sputtering. In an atmosphere composed of neutral argon atoms, a sufficiently high potential difference is applied between a cathode and an anode to initiate a glow discharge : the plasma. The application of a negative voltage to the cathode (also called target), will generate positively charged argon ions that will be attracted to the target. These ions, possessing kinetic energy, come to bombard the target and cause collisions with the matter of the target. The atoms of the target acquire enough energy to be ejected towards the substrate facing the cathode and to condense therein. Under ion bombardment, the cathode will induce secondary electrons that will maintain the plasma. The cathode and the anode are conventionally positioned face-to-face in a chamber where a minimum vacuum of 10^{-7} mbar is achieved by pumping. The pressure of the gas is generally between 1 and tens of Pa.

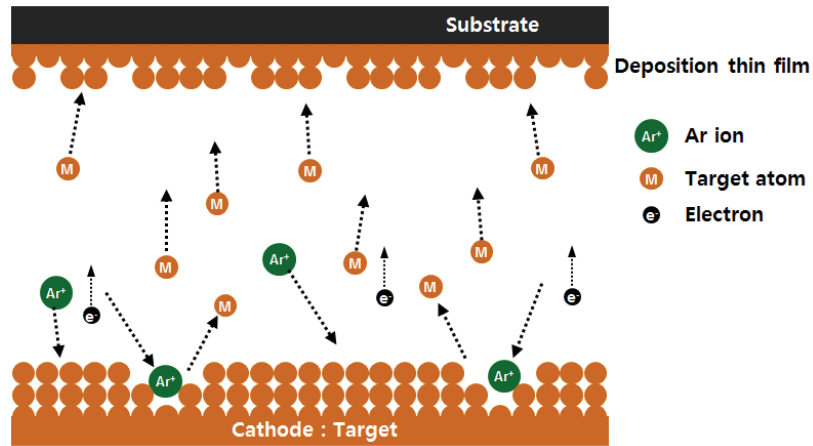


Figure 24. Basic principle of cathodic sputtering with Ar gas.

The structure and texture of the deposited thin film will depend on several parameters such as [142]:

- the nature of the target,
- the kinetic energy of the ions that bombard the target,
- the evolution of the target during the deposition,

A sputtering yield can be defined as the ratio of the number of sputtered atoms of the target to that of the number of ions that bombard it. The accumulation of atoms that condense on the substrate will form a thin layer. This growth takes place in several stages:

1. adsorption of atoms on the surface,
2. diffusion of atoms with sufficient energy before binding to the substrate,
3. the adsorbed atoms will react and bind to each other,
4. nucleation,
5. the layer becomes thicker and develops its structure, morphology etc ...

The distance between the substrate and the target and the pressure of the gas, the number of collisions that can play on the kinetic energy and the direction of the atoms passing through the plasma. An average free path greater than the distance between the target and the

substrate, leads to a low kinetic energy loss, and therefore a thinner, denser layer. An average free path lower than the distance between the target and the substrate, induces a greater loss of kinetic energy, therefore a porous thin layer. The properties of adhesion, internal stresses or crystalline orientation are related to the kinetics of growth, the nature and the energy of the atoms arriving on the substrate. The process of growth of the thin layer can take place in three different modes as shown in figure 25 :

- Frank-van der Merwe (2D): strong bond between the film and the substrate, the layers will settle one after the other.
- Volmer-Weber (3D): the bonds are stronger between the atoms than with the substrate, clusters will form on the substrate and associate with each other.
- Stranski-Krastanov (2D / 3D): intermediate mode between the first two, a first monolayer will be created then islands will be formed.

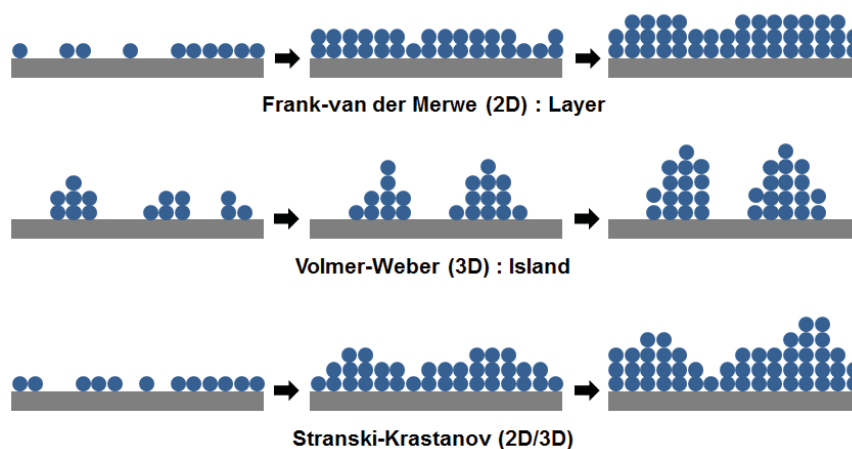


Figure 25. Thin film growth mode of 2D, 3D and 2D/3D.

1.2. Structure zone models

The optical and mechanical properties of a thin film depend in part on its morphology. The cathodic sputtering makes it possible to obtain different morphologies that depend essentially on the kinetic and thermal energy of the atoms arriving on the substrate. In 1969, Movchan et al. have reported a model of structural zones by correlating the morphology of the deposited

thin film with the ratio of the substrate temperature to the substrate melting temperature [143]. Thornton, in 1977, takes the previous model taking into account this time the value of the argon pressure. Figure 26 presents the models proposed by Movchan et al and Thornton. Four areas are mainly identified [144]:

- Zone 1: the kinetic energy of the atoms is weak. The deposits have a columnar structure with low compactness. The diameter of the columns increases with temperature. The grains lengthen in the direction of the plasma and do not displace in the lateral directions. The deposits have a low lateral resistance. As the argon pressure increases, the kinetic energy of the atoms decreases.

- Zone T: it is a transitory zone between zone 1 and zone 2. It is characterized by compact granular grains next to each other. The voids diminish due to a greater kinetic energy of the atoms allowing a greater diffusion in the lateral directions.

- Zone 2: this zone is characterized by grains in the form of columns contiguous to each other. Thin films do not exhibit porosity. Thermal energy is predominant and the microstructure no longer depends on argon pressure. The mechanical properties are similar to those of massive materials.

- Zone 3: the grains can be used in all directions. The grains are equiaxial, which is characteristic of massive materials, treated at high temperature. The grain surface is smooth.

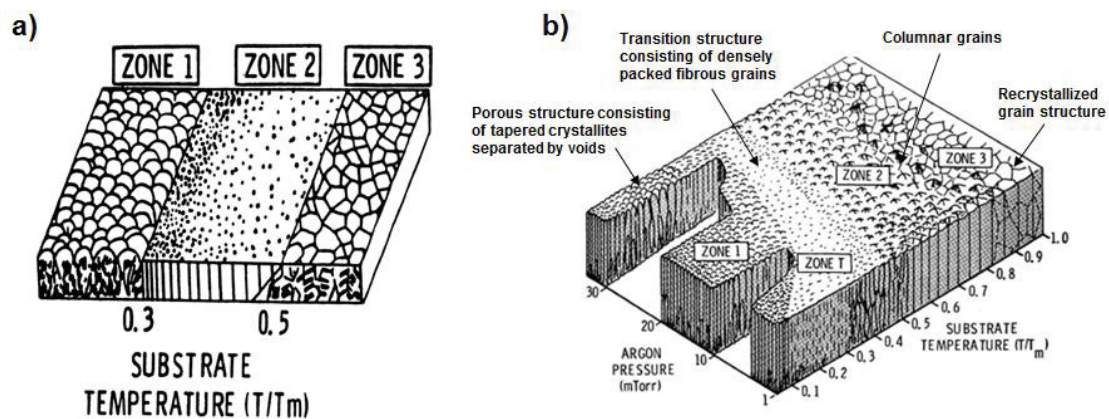


Figure 26. Structure models for thin-film growth, (a) the model proposed by Movchan and Demchishin, and (b) Thornton's proposed model for sputtered life [143, 144].

Anders proposes in 2010 [145] an adaptation of the previous models with the model of zones of following structure (figure 27):

- the ratio of the substrate temperature to the substrate melting temperature ($T_h = T / T_m$) by T^* , which takes into account T_h and T_{pot} which is the characteristic temperature that allows mobility atoms. $T^* = T_h + T_{pot}$ and $T_{pot} = E_{pot} / (kN_{moved})$ (k is the boltzman constant, E_{pot} is the potential energy of the particles arriving on the surface and N the number of atoms (particles) arriving at the surface).

- the linear axis of the pressure by a logarithmic axis of the normalized energy, E^* , describing displacement and heating effects caused by the kinetic energy of bombarding particles.

- the axis z by the thickness of the film, t^* .

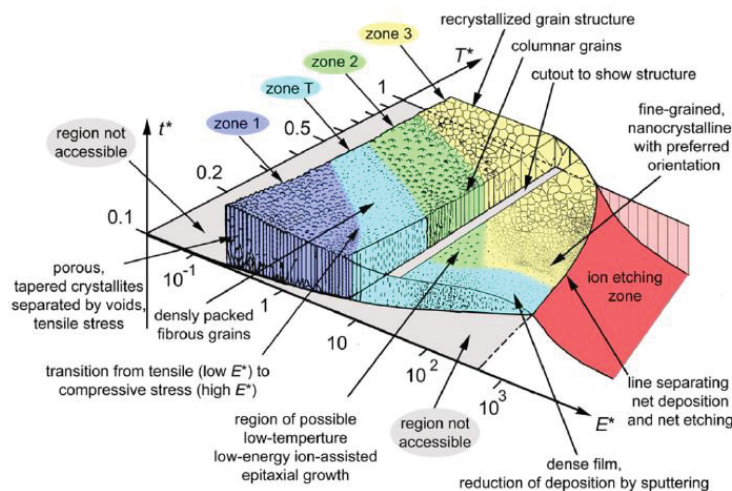


Figure 27. Structure area model proposed by Anders [145].

2. Radio frequency magnetron sputtering (RFMS)

2.1. Radio frequency sputtering

Radio frequency sputtering is a technique based on the alternation of electric field, suitable for insulating materials, to avoid the accumulation of charges on the target or the appearance of arcs that may damage the target. Traditional DC Sputtering is a cost effective way of applying metal target coatings that are electrical conductors like gold. However, DC

Sputtering is limited when it comes to dielectric target materials coatings which are non-conducting insulating materials that can take on a polarized charge. Over time, positive ions are produced which accumulate on the surface of the target face giving it a positive charge. At a certain point this charge can build up and lead to a complete secession of sputtering atoms being discharged for coating. By alternating the electrical potential with RF Sputtering, the surface of the target material can be “cleaned” of a charge buildup with each cycle. On the positive cycle electrons are attracted to the target material or cathode giving it a negative bias. RF Sputtering can sustain a plasma throughout the chamber at a lower pressure (1-15 mTorr). The result is fewer ionized gas collisions equaling more efficient line-of-site deposition of the coating material. Because with RF Sputtering the target material is being “cleaned” with each cycle from building up a charge it helps reduce arcing. Arcing is where there is an intensely focused and localized discharge emanates from the target material or cathode into the plasma that creating droplets and problems with non-uniform film deposition. RF Sputtering greatly reduces the buildup of a charge in a specific location on the surface of the target material that leads to the sparks that creates the arc which causes numerous quality control issues. On the negative portion of the cycle which is occurring at the radio frequency of 13.56 MHz used internationally for RF power supply equipment ion bombardment of the target to be sputtered continues. RF Sputtering offers several advantages depending upon your specific application. RF plasmas tend to defuse throughout the entire chamber rather than concentrating around the cathode or target material as with DC Sputtering.

2.2. Principle of the self-biasing voltage

Electrons lighter than argon ions have a much higher mobility. Thus, the electrons arrive at the electrodes faster than the ions, and the neutrality of the charges is not maintained. At initiation, the voltage is close to 0 V and the concentration (the current) of electrons is greater than that of the ions. As a result, the self-biasing voltage shifts to negative values until the equilibrium between the electron and ion currents is reached. The value of the self-bias voltage is characteristic of the deposition conditions of the thin layer. A self-biasing voltage then ensures the balance of the positive and negative charges. Figure 28 shows the curves $I = f(V)$ of the plasma at the initiation of the discharge and when the self-biasing voltage is reached.

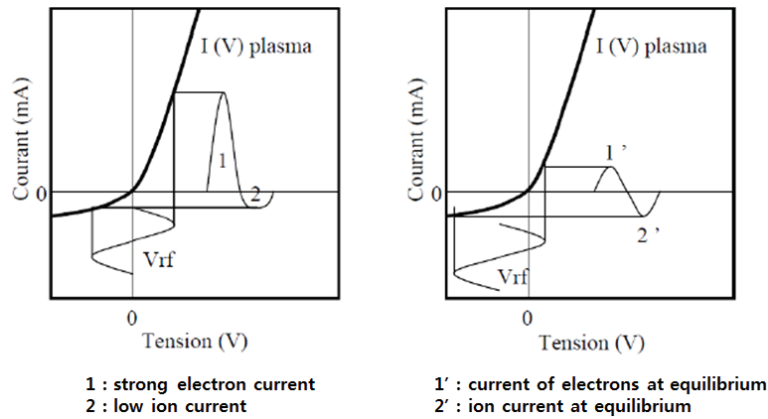


Figure 28. Curves $I = f(V)$ of the plasma.

2.3. Magnetron effect

The magnetron allows one to trap the electrons and to concentrate the plasma close to the surface of the target thanks to the magnets placed at the back of the target (Figure 29). These magnets make the electron beam to work at lower pressures and thus have atomized atoms that experience fewer collisions before reaching the substrate. These atoms possessing greater kinetic energy can thus be used on the surface. For a circular target, the central magnetic pole and the annular pane, create magnetic field lines between these poles. This geometry induces a cycloidal trajectory of the electrons along the target which will not be able to escape this magnetic capsule unless they are struck by the atoms of the gas. However, the erosion of the target does not occur uniformly over the entire target and the latter is widened according to the geometry of the magnetic field.

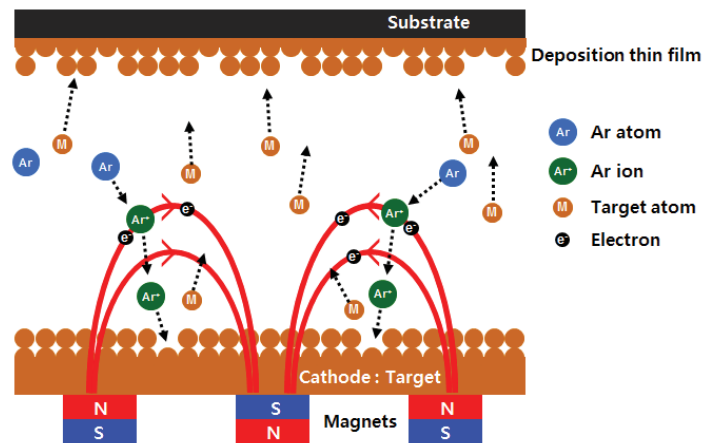


Figure 29. Principle of magnetron effect.

2.4. Reactive plasma sputtering

Sputtering in a reactive atmosphere makes it possible to vary the composition / stoichiometry of a material or to obtain an oxide (or nitride, hydride, etc.) from a metal target. In this work, oxygen (O_2) is introduced into the sputtering chamber to combine with the material from the target to form a thin layer of metal oxide on the substrate as shown in figure 30. The oxygen flow rate leads to different sputtering regimes, as shown in figure 31. The reactive gas (lower flow in reactive gas) interacts with the sputtered material of the metal target. This regime makes it possible to obtain fast deposition rates. An oxidized sputtering regime occurs when an oxide is formed on the surface of the target (higher flow in reactive gas) and acts as the target. Deposition rates decrease and the overall composition at the surface of the substrate will vary very little. The surplus of oxygen will be evacuated by a pumping system. A transition zone exists between these two regimes.

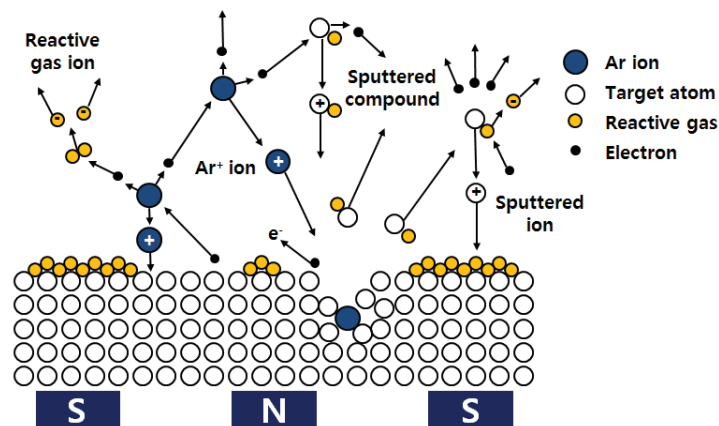


Figure 30. The reactive sputtering process with Ar and reactive gas. Reactive molecules are dissociated through an electron impact.

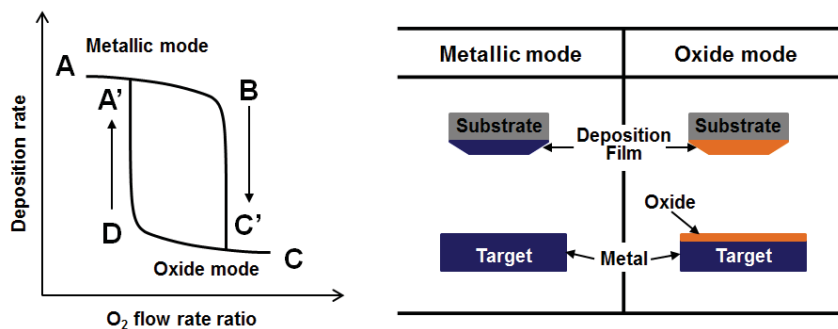


Figure 31. Sputtering regimes : metallic or oxide.

The possible presence of oxides on the surface of the target, the evolution of the morphology, the erosion of the target during the deposits and the accumulation of implanted ions are all factors that can affect the reproducibility of the deposits. .

Electrochromic devices are already used around our life. Electrochromism is one of the most remarkable technologies. Among the electrochromic materials, metal oxides have cathodic coloration and anodic coloration. Vanadium is the only metal element possessing two properties. More precisely it is vanadium oxide. Sputtering has many advantages for thin film deposition. The part B of this thesis will be devoted single layer deposition.

PART B : SINGLE LAYER DEPOSITION

During the past decades, V_2O_5 thin films have attracted significant attention in secondary lithium ion batteries [146, 147, 148], electrochemical supercapacitors [149, 150], chemical sensors, solar cell windows. Especially, many attempts have been made to apply vanadium oxide films for electrochromic devices [124, 151, 152]. The electrochromic performance of vanadium oxide depends on several parameters including film thickness, morphology and porosity and the deposition method. Various physical and chemical techniques, such as thermal evaporation, electron beam evaporation, sol-gel, electrochemical deposition, and pulsed laser ablation, have been used for the deposition of vanadium oxide films [153, 154].

Most studies on the electrochromism of vanadium oxide have been performed on Li electrolytes. To our knowledge, vanadium oxide thin films have never been tested in Na electrolyte for electrochromism even though reports exist on vanadium oxide for Na batteries [155, 156].

This part concerns the investigation for electrochromic properties of V_2O_5 thin films deposited by Radio frequency magnetron sputtering (RFMS) and High Power Impulse Magnetron Sputtering (HiPIMS). In chapter 1, V_2O_5 thin films deposited by RFMS with V metal target and V_2O_5 oxide target are characterized and optimized. The electrochromic properties of V_2O_5 thin films are characterized by cyclic voltammetry in Li and Na based electrolytes combined with *ex-situ* optical measurements and compared. In chapter 2, V_2O_5 thin films deposited by HiPIMS with V metal target were characterized and optimized. The electrochromic properties of V_2O_5 thin films are characterized by cyclic voltammetry in Li and Na based electrolytes combined with *ex-situ* optical measurements and compared.

Chapter 1. Deposition of vanadium oxide by RFMS with V metal and V₂O₅ oxide target

1. Deposition conditions

1.1 Equipment

As introduced previously, vanadium oxide thin films have been deposited by sputtering. The apparatus used is a 1985 Leybold model, which has a 75 mm cathode, 4 positions substrates and a hot substrate holder (700 °C). The apparatus also has a radio frequency generator (13.56 MHz) and a magnetron. Vanadium oxide films were only deposited at room temperature. (however, heat is generated when plasma is turned on). The targets have a diameter of 75 mm, to obtain a homogeneity of the deposition area of 3 cm². A reactive atmosphere was created by introducing a 99.999% pure oxygen gas inside the enclosure. Targets of vanadium metal (99.99%) and vanadium oxide (99.99%) were purchased from Neyco. Glass substrates coated with ITO were purchased from SOLEMS. These substrates have a sheet resistance of 30 Ω/sq, thickness of 80 nm and optical transmission greater than 90%.

1.2. Experimental protocol

Substrate cleaning

The substrates were glass covered with an ITO thin film. Before each sputtering deposition, the substrates were cleaned with ethanol and then with isopropanol vapor.

Preparation of the target and deposition of the thin film.

Once the substrate is positioned in the chamber, residual pressure below $2\sim 3 \times 10^{-7}$ mbar minimum is required to prevent any contamination. To clean the target surface, pre-sputtering of the target was carried out for 5 min prior to the films deposition. The protocol then takes place mainly in 3 steps.

- **1st step**: pre-sputtering

The surface condition of the target must be the same before the beginning of each deposition to ensure the reproducibility of deposition. However, it is impossible to avoid the erosion of the target as deposition occurs, which can lead to differences, but in these conditions, they are estimated to be minimal between two depositions. During the pre-press step, a cover (shutter) is positioned between the substrate and the target to prevent the material from settling on the substrate. This step may vary depending on the nature of the target:

* Metal vanadium target : the target is reduced under an argon atmosphere for a duration of 30 min, in order to remove the oxide layer that was formed during the previous deposition.

* Vanadium oxide target : the target is oxidized under a oxygen partial pressure of 10%, because the target tends to be reduced during the sputtering with oxygen partial pressure.

The color of the target and the self-biasing voltage are the only two parameters that can indicate whether the target's original state has been recovered.

- **2nd step** : stabilization of the plasma

A plasma stabilization step is performed at the chosen deposition conditions. The duration chosen for this step is 40 min.

- **3rd step**: the deposition of the thin layer

1.3. Deposition settings

The physicochemical and mechanical properties of thin films deposited by magnetron sputtering essentially depend on the following parameters:

- nature of the target
- total pressure
- power
- target-substrate distance
- reactive gas in the enclosure
- partial pressure of the reactive gas

- Substrate bias
- kinds of power supply (RF, DC, pulsed-DC, HiPIMS)

The optimization of these parameters is essential for the growth of a thin layer with the desired properties, but this step can be complicated because the interdependence of some parameters complicates the systematic optimization approach of the thin layers that consists in only changing one parameter at a time. The characteristics sought for the thin layer of vanadium oxide are initially:

- good adhesion between the substrate and the thin layer
- chemical stability
- good electrochromic properties

The electrochromic properties will depend on the morphology, structure and composition of the thin layer. The morphology can be varied by varying the kinetic energy of the atoms while the composition of the thin layer depends mainly on the oxygen flux introduced into the chamber and the power applied to the target.

The deposition parameters are shown in Table 6. The oxygen partial pressure defined as $\frac{P(O_2)}{P(Ar)+P(O_2)}$. In this formula, P(O₂) is the oxygen partial pressure. Thus, It will be replaced later in the manuscript by P(O₂) to simplify the writing.

Table 6. Summary of the various deposition parameters.

Parameters	Metallic target	Oxide target
Power (W)	100, 150, 200	100, 150
Total pressure (Pa)	1, 2, 3	1, 2, 3
P(O₂) %	2, 10, 20	2, 5, 10
Distance of target-substrate (mm)	80	80

In order to quickly evaluate the quality of thin films, a structural characterization by X-ray

diffraction and an electrochemical characterization in a 3 electrodes cell (V_2O_5/Li electrolyte/Pt vs SCE), associated with optical measurements have been conducted. The first depositions were made from a vanadium metallic target.

2. Deposition of V_2O_5 Thin film with V metallic target.

The power, total pressures and the $P(O_2)$ used are 100, 150, 200 W and 1, 2, 3 Pa and 2, 10, 20% respectively. Vanadium oxide films by RF magnetron sputtering with V metallic target will be replaced later in the manuscript by V_2O_5 RF-metal to simplify the writing.

2.1 Thin film deposition at various RF power and total pressure conditions

At 2 Pa pressure and 20% $P(O_2)$, thin films were deposited under different RF powers (100, 150, 200 W). Thin films deposited at 100 and 150 W lead to film that faster degrade and show poor adhesion with substrate during cycling using cyclic voltammetry at a fixed scanning rate of 10 mV / sec in the voltage range of -1.0 to 1.0 V in Li (LiTFSI-EMITFSI) electrolyte (Figure 32). We increased the RF power until 200 W in consideration of the damage of the equipment and the target. Thin films deposited at 200 W show no degradation and good adhesion with the substrate during cycling (Figure 32).

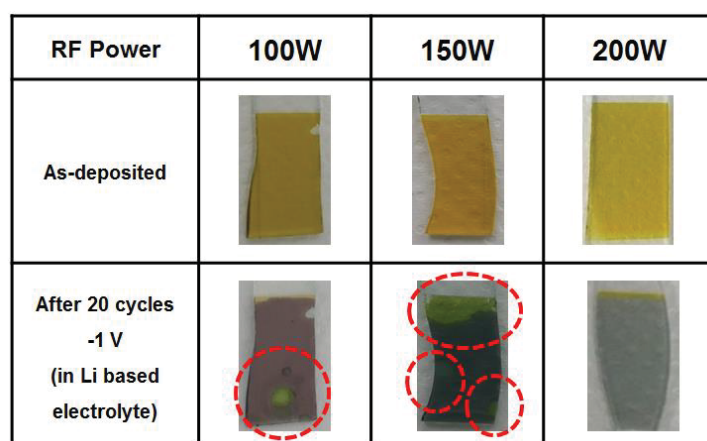


Figure 32. The surface of V_2O_5 RF-metal at RF power of 100, 150, 200 W after 20 cycles in the voltage range of -1.0 to 1.0 V in LiTFSI-EMITFSI electrolyte. The electrochemical chain is V_2O_5 /electrolyte/Pt vs SCE.

At 200 W RF power and 20% P(O₂), thin films were deposited under different total pressures (1, 2, 3 Pa). Figure 33 gathers the *ex-situ* transmittance in the as-deposited state and at various potentials, namely in reduction at -1V and in oxidation at +1 V after 20 cycles in the voltage range of -1 to 1 V in LiTFSI-EMITFSI electrolyte. However, thin films deposited at 2 Pa pressure showed the largest ΔT at 650 nm wavelength and color switch from orange to blue during cycling using cyclic voltammetry in Li electrolyte (Figure 33).

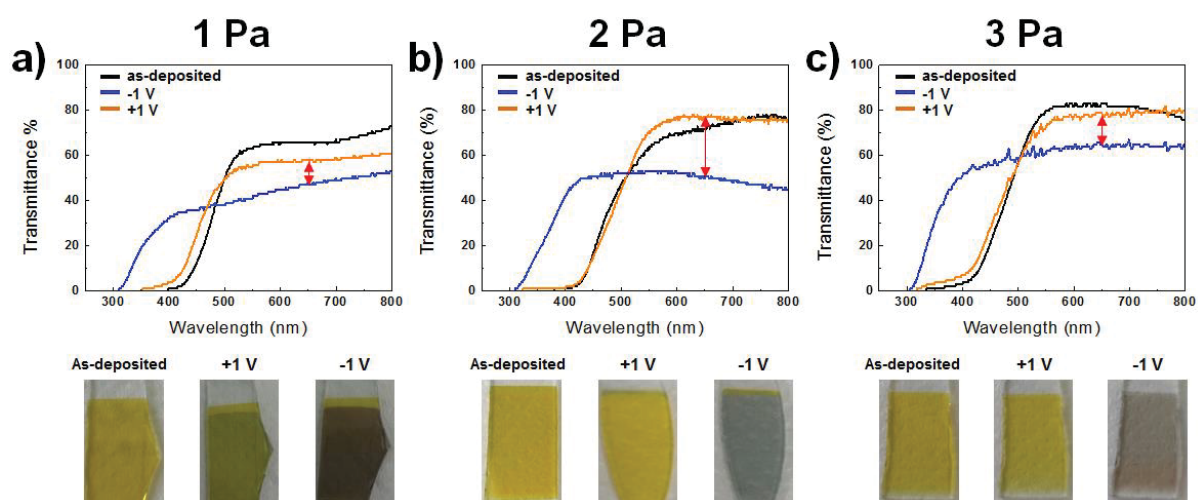


Figure 33. Optical properties of V₂O₅RF-metal at total pressure of 1 (a), 2 (b), 3 (c) Pa after 20 cycles in the voltage range of -1 to 1 V in LiTFSI-EMITFSI electrolyte. The electrochemical chain is V₂O₅/electrolyte/Pt vs SCE.

From the above results, RF power and total pressure were chosen as 200 W and 2 Pa, respectively.

2.2 Thin film deposition at various P(O₂) conditions

Parameters with the best properties in the previous part were mostly conserved (power 200 W, total pressure of 2 Pa, target distance-substrate 8 cm). We further study the influence of the oxygen partial pressure on the thin film growth and electrochromic properties.

2.2.1 The self-biasing voltage

The evolution of the values of self-bias voltages as a function of $P(O_2)$ is presented in Figure 34.

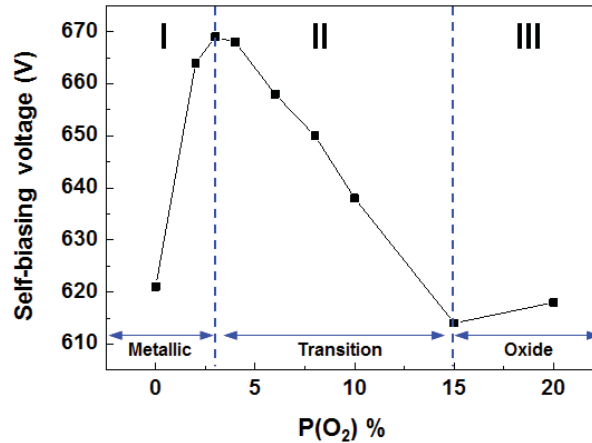


Figure 34. Evolution of the self-biasing voltage as a function of $P(O_2)$ of the deposition of V_2O_5 RF-metal thin films.

Depending on $P(O_2)$, three regimes are observed, named I between 0 and 3% $P(O_2)$, II between 3 and 15% $P(O_2)$ and III between 15 and 20% of $P(O_2)$.

- Zone I corresponds to the metallic regime.
- Zone II corresponds to the transition regime.
- Zone III corresponds to the oxidized regime.

In the metallic regime, there is not enough oxygen to the oxidized target. In oxidized regime, the deposition rate decreases following the formation of an insulating vanadium oxide layer on the surface of the vanadium target which will act as the target. The intrinsic characteristics of the thin films produced under the conditions of zone III will be close to each other. This evolution is comparable with the work of Hollands et al. from 1968 on thin films of tantalum oxide deposited from a metal tantalum target [157] and with the work of H. Miyazaki et al. of the deposition of vanadium oxide from a metallic vanadium target [158].

We selected the $P(O_2)$ for each of the three different regions for Zone I : $P(O_2)$ 2%, Zone II : $P(O_2)$ 10% and Zone III : $P(O_2)$ 20%, respectively, V_2O_5 RF-metal thin films were deposited

under these conditions and their characteristics were analyzed.

2.2.2 Optical Characteristics

2.2.2.1. Visual aspect

Figure 35 shows the visual appearance of the V₂O₅RF-metal thin films in their initial states as a function of P(O₂). Thickness of thin films deposited under a P(O₂) of 2%, 10% and 20% were 226 ± 20 nm, 218 ± 20 nm and 210 ± 20 nm, respectively. At a P(O₂) of 2%, thin films are yellow-dark greenish. At a P(O₂) of 10%, 20%, thin films are yellow-orange color. The yellow/orange color is characteristic of V₂O₅.

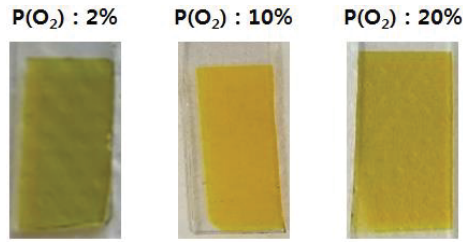


Figure 35. Visual image of as-deposited V₂O₅RF-metal thin films of 200 nm thickness with different P(O₂).

2.2.2.2. Optical transmittance

Figure 36 describes the evolution of the optical transmittance spectra and optical band gap of V₂O₅RF-metal thin films as a function of P(O₂). The transmittance of the thin films slightly differs depending on the P(O₂) conditions. The thin film deposited under P(O₂) of 20% show the highest transmittance at 650 nm wavelength.

The optical band gap corresponds to the minimum energy difference between the valence and conduction bands in electronic transition. According to the inter-band absorption theory, the optical band gap of film can be evaluated by the relations as follows [159]:

$$T = (1 - R)^2 \exp(-\alpha d) / 1 - R^2 \exp(-2\alpha d) \quad (16)$$

$$(\alpha h\nu) = B(h\nu - E_g)^n \quad (17)$$

where T is the transmittance, R the reflectance, α the absorption coefficient, d the film thickness, $h\nu$ the incident photon energy, B the edge width parameter, E_g the optical band gap, n the exponent, and n can take values of 2, 3, 1/2, 3/2 for different electronic transitions as indirect allowed, indirect forbidden, direct allowed and direct forbidden, respectively. Figure 36 (b) shows the plot of $(\alpha h\nu)^{1/2}$ versus $h\nu$ of V_2O_5 RF-metal thin films. We found that experimental data fit better when n took value of 2, suggesting the indirect allowed transition. The calculated value of the E_g is 2.18 eV at P(O₂) 2%, 2.30 eV at P(O₂) 10% and 2.35 eV at P(O₂) 20%, respectively. The optical band gap increases with increasing P(O₂). The band gap of V_2O_5 was reported to be 2.02 to 2.50 eV according to the thin film preparation method (Table 7).

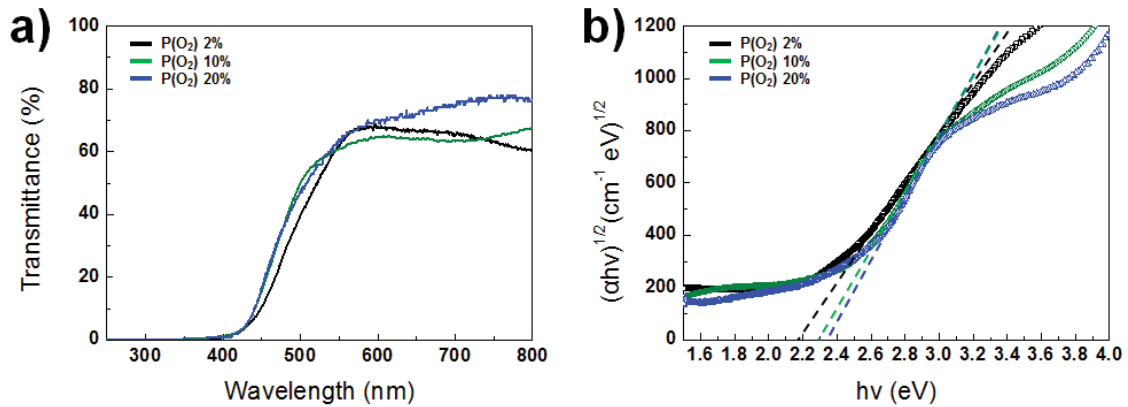


Figure 36. Transmittance (a) and Plot of $(\alpha h\nu)^{1/2}$ versus $h\nu$ (b) of as-deposited V_2O_5 RF-metal thin films of 200 nm thickness with different P(O₂).

Table 7. Value and type of the optical band gap of V_2O_5

Method of preparation	Structure	E_g direct (eV)	E_g indirect (eV)	Ref
Sol-gel	Orthorhombic	2.42 - 2.49	-	[160]
Spray pyrolysis	Orthorhombic	2.44 - 2.50	2.33	[161, 162]
Vacuum evaporation	Orthorhombic	2.03	-	[163]
Electron beam evaporation	Orthorhombic	-	2.18 - 2.36	[164]
DC sputtering	Orthorhombic	-	2.02-2.29	[165]
RF sputtering	Orthorhombic	-	2.30-2.36	[166, 167]

2.2.3 Morphology

Figure 37 shows the SEM image of the V_2O_5 RF-metal thin films deposited according to the oxygen partial pressures. At a 2% oxygen partial pressure, the film shows very smooth and homogeneous surface. At a 10% oxygen partial pressure, the film surface becomes rougher. At a 20% oxygen partial pressure, thin films exhibit different morphologies. The film shows a needle or flake shape surface. The V_2O_5 RF-metal thin films appears to be more rough and porous as the oxygen partial pressure increases.

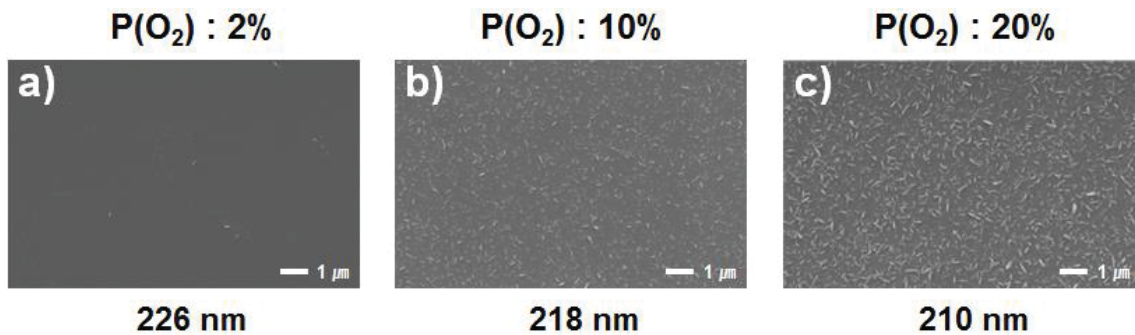


Figure 37. SEM images of surface for V_2O_5 RF-metal thin films deposited by $P(O_2)$ of 2% (a), 10% (b) and 20% (c).

2.2.4 Structural characterization

In order to analyze the structure of thin films more precisely, grazing incidence x-ray diffraction (GIXRD) with $CuK\alpha$ (wavelength, $\lambda=1.5417 \text{ \AA}$) incident radiation was used (D8 DISCOVER, BRUKER). The initial step consisted in optimizing the recording of the X-ray pattern by considering various grazing angles, namely 0.5, 1 and 2 degree. As a result of adjusting the incidence angle, 0.5 degree angle was the most suitable giving higher intensity and facilitates the analysis of the thin films of this study (Figure 38).

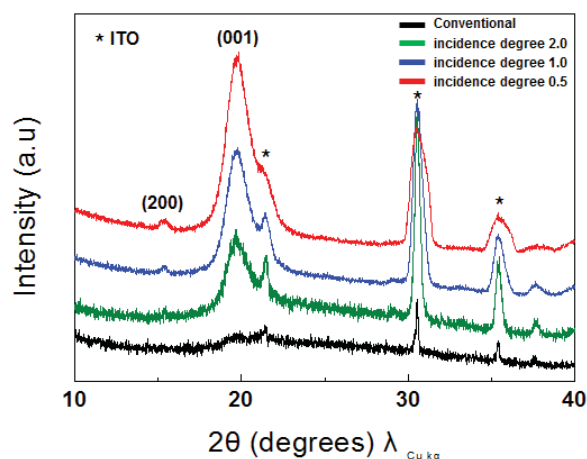


Figure 38. GIXRD patterns using different incidence angles of as-deposited V_2O_5 RF-metal thin films of 200 nm thickness with $P(O_2)$ 20%.

Figure 39 shows the grazing incidence X-ray diffraction pattern GIXRD (incidence degree 0.5 degree) of V_2O_5 RF-metal thin film prepared on ITO coated glass substrate at room temperature according to oxygen partial pressures. No diffraction patterns at the exception of the ITO peaks are visible, for the oxygen partial pressure of 2%. When the oxygen partial pressure increases to 10%, the XRD pattern shows (001) and (200) orientation of V_2O_5 orthorombic structure (S.G : Pmmn, JCPDS 41-1426). When the oxygen partial pressure is 20%, the intensities of the (001) and (200) peaks increase. It indicates that the crystallinity of the thin film increases as the oxygen partial pressure increases. Oxygen promotes crystallization, and by adjusting the flow rate of oxygen and Ar during the magnetron sputtering deposition, crystalline V_2O_5 films can be prepared at low substrate temperatures [167, 168, 170] and even at room temperature [171-174]. Crystallization may also come for a composition closer to the one of V_2O_5 . Various cristallinity levels should induce different electrochemical and optical properties.

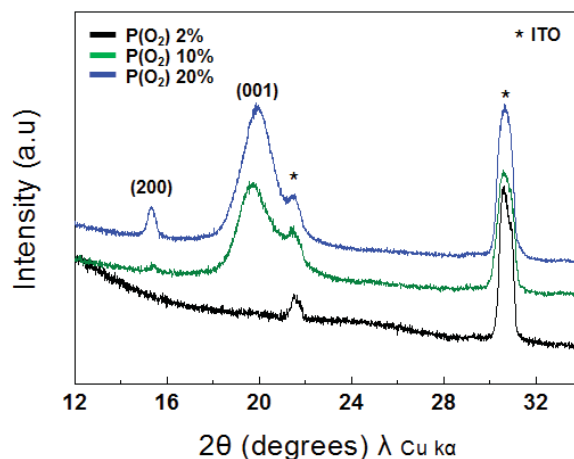


Figure 39. GIXRD pattern of as-deposited 200 nm V_2O_5 RF-metal thin films deposited by 2%, 10% and 20% oxygen partial pressure.

2.2.5 Electrochemical properties

Figure 40 shows the 20th cyclic voltammograms of the V_2O_5 RF-metal thin film deposited according to the different oxygen partial pressures. V_2O_5 thin films were electrochemically characterized using V_2O_5 /electrolyte/Pt vs SCE. The current - potential curve was measured at a fixed scanning rate of 10 mV / sec in the range of -1.0 V to 1.0 V in Li (LiTFSI-EMITFSI) electrolyte. Depending on the polarity of the applied voltage, the film repeats various coloring steps. In first approximation as the voltage is lowered, the V_2O_5 RF-metal thin film is reduced and lithium ions are injected. Conversely, Li ions are extracted as the voltage rises in conjunction with oxidation.

All three films show reversible characteristics. The CV of V_2O_5 RF-metal thin film deposited by 2% oxygen partial pressure shows a single peak located at -0.2 V in the reduction and 0.2 V in oxidation, while a shoulder at higher potential is visible. The CVs of the V_2O_5 RF-metal thin film deposited using 10% oxygen partial pressure consist of three pair of peaks. CV curve of the film deposited by 20% oxygen partial pressure shows better resolution with the presence of two well defined peaks located at 0.3 V and 0.1 V in reduction and at 0.3 V and 0.5 V in oxidation. From the above XRD results, amorphous film (2% oxygen partial pressure) the CV shows one broad peak. For crystalline film (20% oxygen partial pressure) the CV shows two sharp characteristic peaks. For films deposited by 10% oxygen partial pressure, two sharp peaks and one broad peak are mixed.

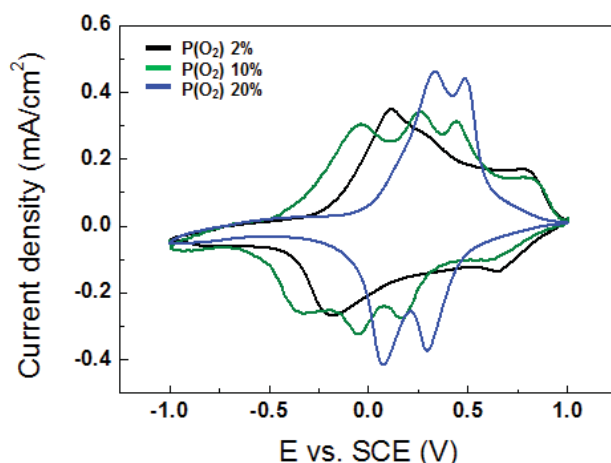


Figure 40. Cyclic voltammograms of 200 nm V_2O_5 RF-metal thin films deposited in 2%, 10% and 20% oxygen partial pressure cycled in Li based electrolyte after 20 cycles. The electrochemical chain is V_2O_5 /electrolyte/Pt vs SCE.

2.2.6 Optical properties

Thin films deposited with 2%, 10%, and 20% oxygen partial pressure show dark green, yellow, and yellow colors, respectively. The optical properties of the thin film were measured after 20 cycles. Figure 41 shows *ex-situ* optical transmittance data under applied potential. In Li based electrolyte, the films turn to gray in the reduced state (-1 V) and orange in the oxidized state (+1 V). The transmittance modulation, ΔT , of films at gray color (-1 V) and orange color (+1 V) is measured at 650 nm. A ΔT of films deposited at 2%, 10% and 20% oxygen partial pressures are 25%, 22% and 26%, respectively, indicating a rather similar contrast whatever the oxygen partial pressure.

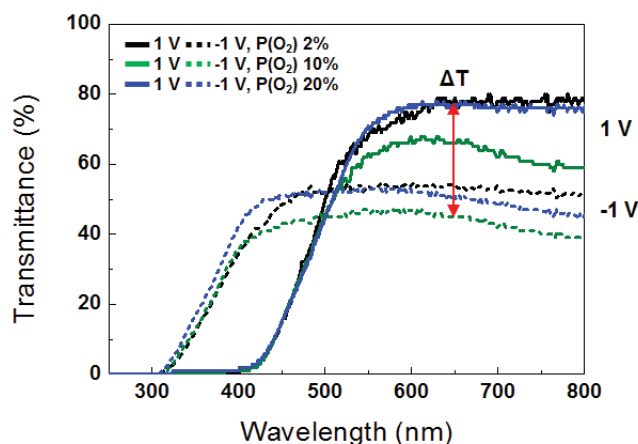


Figure 41. *Ex-situ* optical transmittance spectra of V_2O_5 RF-metal thin films by deposited by 2%, 10% and 20%

oxygen partial pressure in Li based electrolyte after 20 cycles. The electrochemical chain is V_2O_5 /electrolyte/Pt vs SCE.

From the above results, the thin films deposited at RF power of 200 W, total pressure of 2 Pa and $P(O_2)$ of 20% by RFMS with metallic target showing crystalline V_2O_5 and “better” electrochromic properties were chosen for deeper studies.

3. Electrochromic properties of V_2O_5 RF-metal in Li and Na based electrolytes

3.1 V_2O_5 RF-metal thin films

3.1.1 Thickness and morphology

We fabricated thin films of various thicknesses using the previously selected optimized deposition conditions. Figure 42 shows the surface morphology and GIXRD pattern of 210 nm, 409 nm and 682 nm of V_2O_5 RF-metal thin film deposited with a $P(O_2)$ of 20%. Fibrous texture of needles or flakes becomes more and more visible on the surface as the thickness increases. This result is similar to the one of S. Oukassi et al [175]. GIXRD patterns of Figure 42 (d) shows that the (001) and (200) peak intensity increase as increasing of film thickness. Thinner films show strong (001) orientation, suggesting a layer consisting of closely compact grains grown with the (001) parallel to the substrate. In particular, the (200) orientation is more pronounced for thicker films. The ratio in intensities $I(200)/I(001)$ for 210 nm, 409 nm and 682 nm thickness increases from 0.27 to 0.66 and 1.23, respectively (Table 7).

Table 8. Ratio of (200) and (001) intensity of V_2O_5 RF-metal thin films at different thickness.

Thickness	$I(200) / I(001)$
210 nm	0.27
409 nm	0.66
682 nm	1.23

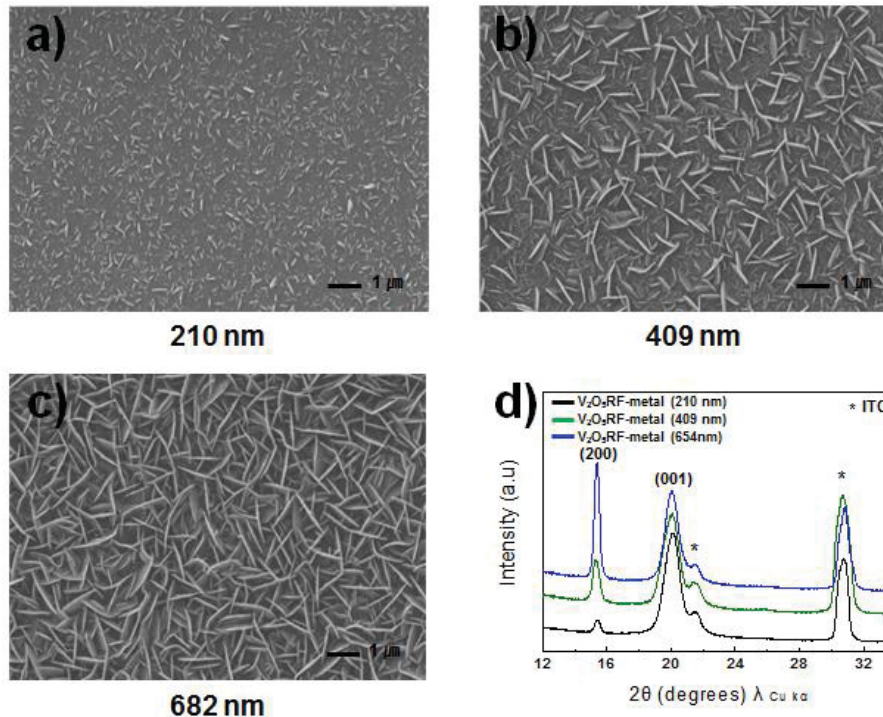


Figure 42. SEM images and GIXRD pattern for 210 nm (a, d), 409 nm (b, d) and 682 nm (c, d) of V₂O₅RF-metal thin films

3.1.2 Characterization

In order to better characterize the film composition, X-ray photoelectron spectroscopy and Electron Energy loss spectroscopy (EELS) were investigated. The former being further used on cycled films will be better described in the next part, devoted to mechanism (Part C, Chapter 2, p 124). Shortly, the XPS study confirms the single presence of V⁵⁺ in V₂O₅RF-metal as-deposited films (Figure 93, p 134).

The EELS study was performed at UMS Placamat in collaboration with Sonia Buffière. To conduct the experiments, the scratched film mixed with ethanol was deposited on copper grids (200 mesh) coated with carbon. Two calibration powders of home made V₂O₅ and VO₂ were utilized [176]. In order to stabilize the measurement, a cryogenic sample holder (Gatan) was used (at N₂ liq. temperature : -165 °C). Measurements were performed on high-resolution (gun field emission) transmission electron microscope (HRMET) JEOL 2200FS, operated at 200kV with a punctual resolution of 1.9 Å, as well as an “Omega” in-column energy filter (from GATAN) for EEL spectra with an energy resolution of 1 eV. The following conditions

were chosen for the EEL spectra acquisition : Illumination semi-angle $\alpha = 1.4$ mrad and collection semi-angle $\beta = 6.6$ mrad, dispersion = $60 \mu\text{m}/\text{eV}$. The 0-loss was acquired in 0.02 s and the $V(L_3-L_2) / O(K)$ were acquired in 3 s (energy shift of +550 eV)

An average of 5 or 6 different locations were recorded for each sample leading to homogeneous results (for $V(L_3/L_2)$ and $O(K)$ edges).

Figure 43 (a) presents the observed energy loss spectra of the 200 nm V_2O_5 RF-metal thin film. Since intra-atomic correlations are pre-eminent, EELS $VL_{2,3}$ edges correspond to excitations from the $2p^63d^n$ V ground state towards the $2p^53d^{n+1}$ V states [177]. The two major features of these edges are the strong white lines L_3 and L_2 , due to the spin orbit splitting of the $2p$ core hole, and separated by about 6.5 eV [168]. In V_2O_5 RF-metal thin film, the peaks of VL_3 and VL_2 edge are located at 514.1 eV and at 520.7 eV. The peak of O_k edge is located at 571.1eV

The relative distance between the vanadium (VL_3) and oxygen (O_k) edges are suggested as a characteristic measurement of the chemical shift of the V absorption edges. The corresponding energy intervals are marked by ΔE in the figure 43 (a). From literature, we choose the shift of the VL_3 edge relative to the O_k peak as a measurement of the oxidation state [178, 179].

The calibration points of the powder materials (pure VO_2 , V_2O_5) is used for quantitative evaluation (Figure 43 b). Having determined the chemical shifts of the vanadium oxide thin films, their oxidation state can be derived directly from the position at this calibration line as demonstrated in the figure 43 (b). V_2O_5 RF-metal thin film shows oxidation state of 4.5 ± 0.2 of V. A similar value was found for Ion Beam sputtered films [180]. Table 9 summarizes the respective quantitative data on the chemical shift and the derived oxidation states.

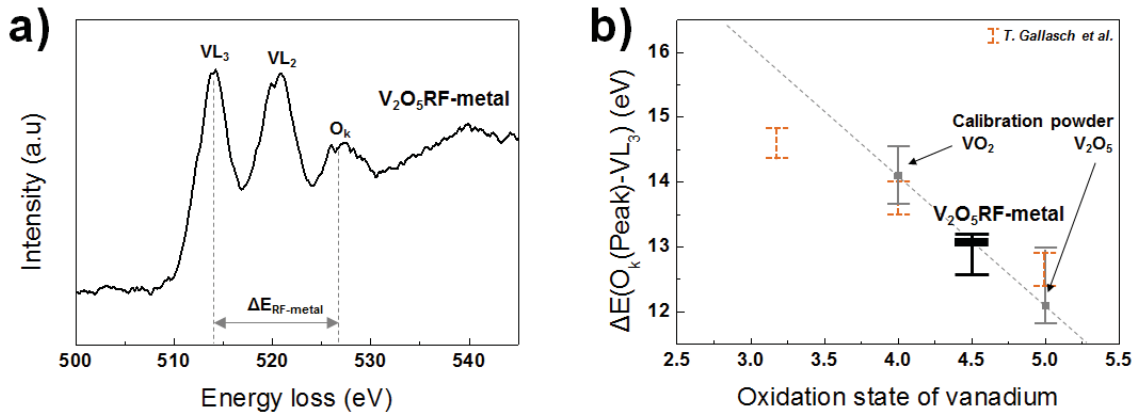


Figure 43. EELS data (a) and quantitative determination of the V-oxidation state (b) of 200 nm V_2O_5 RF-metal thin films. For comparison literature data by T. Gallasch et al. are also shown [179].

Table 9. Quantitative determination of the V-oxidation state of 200 nm V_2O_5 RF-metal thin films.

Sample	O_k Peak (eV)	VL_3 Peak (eV)	ΔE (O- VL_3) (eV)	V-oxidation state
V_2O_5 Powder	526.7	514.6	12.1	5
VO_2 Powder	527.9	513.8	14.1	4
V_2O_5 RF-metal	527.2	514.1	13.1	4.5 ± 0.2

Elemental composition analyses of the films were carried out using RBS (Rutherford backscattering spectroscopy) / NRA (Nuclear reaction analysis). Analysis were carried on AIFIRA facility (CENBG, France) with a 2.8 MeV proton beam in collaboration with Stéphanie Sorieul. RBS and NRA were both performed with the same Si-detector (PIPS, Canberra) mounted at 140° with a solid angle of 25 msr. PIXE analysis were done with a HPGe detector (GUL0110P, Canberra) mounted at 135° and equipped with a Funny Filter (180 μ m polyester, hole : 500 μ m). The beam current was adjusted in order to keep the dead time below 10%. Data treatment was done respectively with SIMNRA and its add-on MultiSIMNRA for RBS/NRA, and GUPIX for PIXE. RBS and PIXE results were used in order to have a proper characterization of the samples [180].

As this technique required thicker films, 400 nm V_2O_5 RF-metal thin films deposited on ITO substrates were analyzed. The concentration of V and O found by RBS/NRA was 21.1 at.%

and 56.8 at.% on ITO. Table 10 summarizes the respective quantitative data of V₂O₅RF-metal thin films.

Table 10. V₂O₅RF-metal thin films (400 nm) and oxygen to vanadium atomic ratio.

Thickness	Atomic %				Stoichiometry V _x O _y
	V	O	H	C	
400 nm	21.2	56.8	21.6	0.5	V _{1.87} O ₅

To explain the deviation V_{1.87}O₅ from the V₂O₅ composition, we may suggest three explanations; (i) the roughness of the layer being quite high some ratio diffused ions may have a modified trajectory with distorted signals. The roughness is indeed particular important for the few tenth nanometer of the layers, (ii) the density of the layer is well below the one of the theoretical one of 3.36 g/cm³ V₂O₅; this results in the decrease of the V and O peaks. Indeed, upon fitting the data, an invisible elements for RBS was added to compensate that effect. (iii) hydrogen was detected in a non-negligible contribution in the RBS spectra while it was not considered for the calculation assuming a V_xO_y formula. In addition, some carbon content was determined as contaminant.

3.1.3 Electrochemical properties

Figure 44 (a) shows the 20th cyclic voltammograms of the V₂O₅RF-metal thin film deposited according to the different oxygen partial pressures. V₂O₅ thin films were electrochemically characterized using V₂O₅/electrolyte/Pt vs SCE. The current - potential curve was measured at a fixed scanning rate of 10 mV / sec in the range of -1.0 to 1.0 V in Li (LiTFSI-EMITFSI) electrolyte. All three different thickness films show reversible characteristics. The 200 nm thin film shows two well defined peaks located at 0.3 V and 0.1 V in reduction and at 0.3 V and 0.5 V in oxidation. The CV of 400 nm thin film exhibits three paired of peaks at 0.3 V, 0.1 V and -0.2 V in reduction and at -0.1 V, 0.4 V and 0.6 V in oxidation. The CV of 600 nm thin film shows three paired peaks at 0.1 V, -0.2 V and -0.5 V in reduction and at -0.1 V, 0.4 V

and 0.6 V in oxidation. Charge capacity increases as the thickness increases with a slight deviation from a pure linear evolution (Figure 44 b). The charge capacity of V_2O_5 films are 23.9 mC/cm^2 at 210 nm, 45.2 mC/cm^2 at 409 nm, and 90.5 mC/cm^2 at 682 nm, respectively. The increase in capacity is more than the increase in thickness. This may be correlated to the fact that V_2O_5 film shows a (h00) preferred orientation with increasing thickness. Indeed, C. Navone et al. reported that (h00) preferentially oriented films have higher capacity than the crystalline thin films of other preferential orientations [181]. If the surface roughness of the electrode is large, the surface area capable of reacting with Li ions is large, which is suitable for implementation of a large capacity. However, since the insertion of a large amount of Li can accelerate deterioration of the electrode material, an optimized surface area is required.

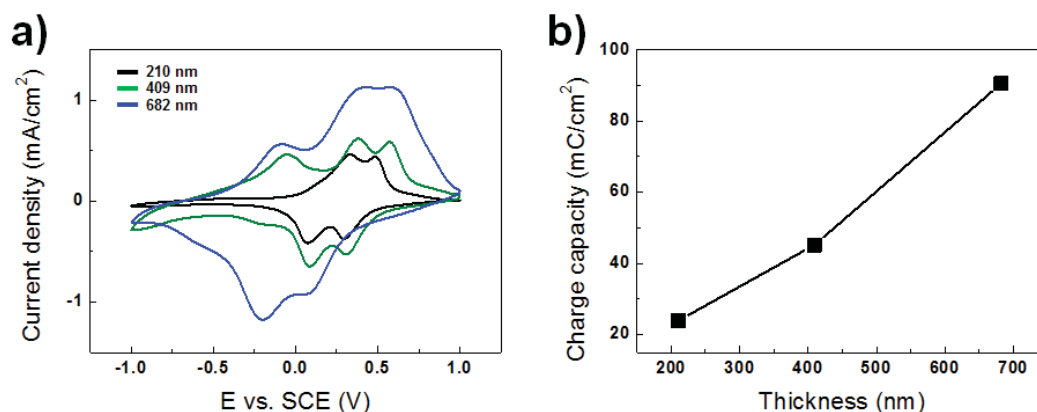


Figure 44. Cyclic voltammograms (a) and charge capacity (b) of V_2O_5 RF-metal thin films of 210 nm, 409 nm and 682 nm thickness in Li based electrolyte after 20 cycles. The electrochemical chain is V_2O_5 /electrolyte/Pt vs SCE.

In our study, the surface of V_2O_5 RF-metal thin films tends to be easily removed by contact with gloves or paper over 400 nm thickness films (Figure 45) meaning that the adhesion of the thin film to the substrate becomes rather poor. Hereafter, the analysis and evaluation were performed using **200 nm thickness V_2O_5 RF-metal thin films**.



Figure 45. Surface scratch of V_2O_5 RF-metal thin film of 409 nm

3.2 Electrochromic properties of V_2O_5 films

V_2O_5 RF-metal thin films of 200 nm thickness were electrochemically and optically characterized using V_2O_5 /electrolyte/Pt vs SCE galvanostatic chain. Figures 46 (a) and (c) show the 20th typical cyclic voltammograms in Li(LiTFSI-EMITFSI) and Na(NaTFSI-EMIFTSI) based electrolytes, respectively with a sweep rate of 10 mV/s. In Li electrolyte, cyclic voltammogram shows better resolution with the presence of two well defined peaks located at 0.3 V and 0.1 V in reduction and at 0.3 V and 0.5 V in oxidation, while a rather rectangular shape is observed in Na electrolyte. Significant lower current density is shown in Na electrolyte (corresponding to lower capacity). The V_2O_5 RF-metal film, initially yellow, goes through distinct color changes as green at 0.2 V, blue at -0.4 V and gray at -1 V upon reduction/oxidation. The orange color is recovered at 1 V at the end of the oxidation. The reversible electrochromism with 4 color states is demonstrated for both electrolytes. However, the color of the thin film remains slightly green at 1 V in Na electrolyte suggesting a limited reversibility. We will discuss this in the mechanism part (Part C). Figures 46 (c) and (d) show *ex-situ* optical transmittance data under applied potential. In Li electrolyte, reduced gray state (-1 V) and the oxidized orange state (+1 V) are associated with transmittance values of T_G 48% and T_O 3% at 420 nm and T_G 73% and T_O 52% at 650 nm, corresponding to a transmittance modulation ΔT of 44% at 420 nm and of 21% at 650 nm, respectively (Table 11). In Na electrolyte, transmittance modulation ΔT are 24% and 8% at 420 nm and 650 nm respectively (Table 11). The absorption edge is shifted to lower wavelength in both electrolytes. In conclusion, V_2O_5 RF-metal thin films exhibited reversible multi-color electrochromic characteristics under applied voltage in Li and Na electrolytes. On the other hand, they showed higher capacity and ΔT in Li electrolyte than in Na electrolyte. And the color of the thin film was slightly green at 1 V the end of the oxidation in Na electrolyte. We think that the insertion/deinsertion reaction of Na ions with larger size than Li is more difficult in the

thin film. More details on mechanism will be discussed later in Part C.

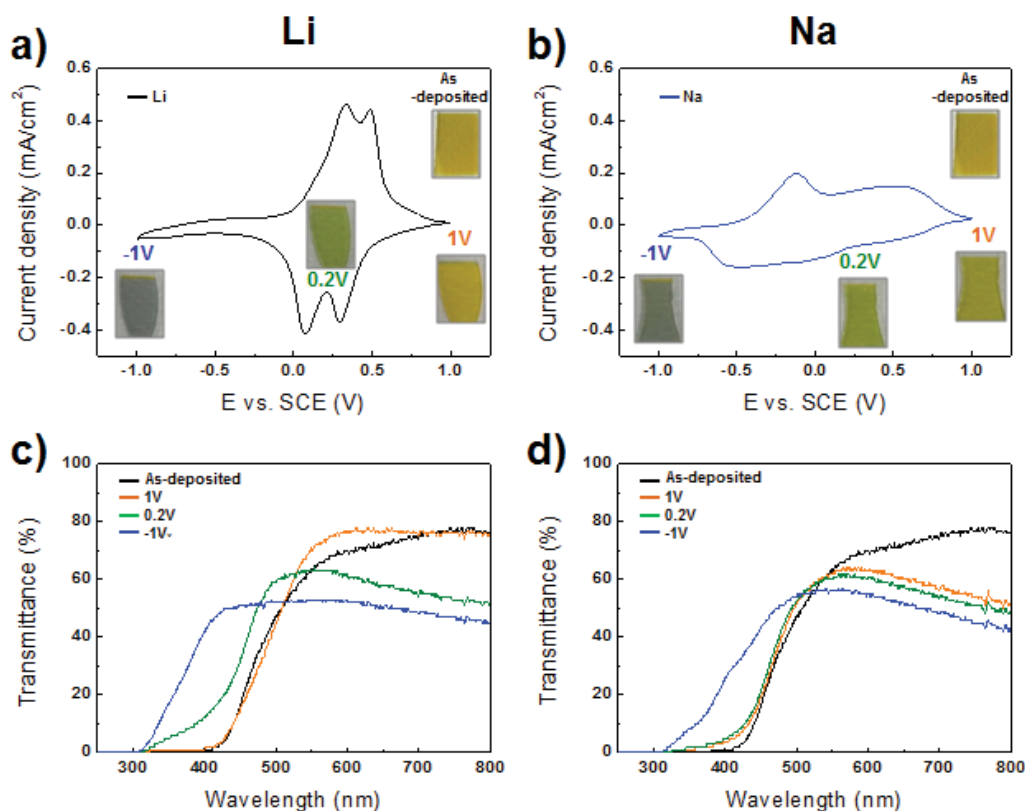


Figure 46. Cyclic voltammograms and *ex-situ* optical transmittance spectra of V_2O_5 RF-metal thin films in Li (a, c) and Na (b, d) based electrolytes after 20 cycles. V_2O_5 /electrolyte/Pt vs SCE chain is cycled with a scan rate of 10 mV/s.

Table 11 summarizes the coloration efficiency (Part A, chapter 1, equation 4, p 22) of the films in two wavelengths corresponding to 420 nm and 650 nm, exhibiting value of 50.4 cm^2/C and 7.5 cm^2/C in Li electrolyte. In Na electrolyte, the coloration efficiency of the films exhibit value of 35.0 cm^2/C and 3.6 cm^2/C 10 times lower than in Li electrolyte.

Table 11. Coloration efficiency, transmittance variation ΔT , and optical density ΔOD of V_2O_5 RF-metal thin films in Li and Na based electrolytes (Part A, chapter 1, 1.4, equation 1, 3 and 4, p 14)

Electrolyte	Charge density (mC/cm ²)	$\lambda = 420\text{nm}$			$\lambda = 650\text{nm}$		
		ΔT	ΔOD	CE(cm ² /C)	ΔT	ΔOD	CE(cm ² /C)
Li	23.9	44	1.20	50.4	26	0.18	7.5
Na	17.2	24	0.60	35.0	8	0.06	3.6

In comparison to our values, coloration efficiencies of vanadium oxide films were reported in the range 5.9~12.5 cm²/C by sol-gel deposition [182-185], of 19.3 cm²/C by electrodeposition [186], in the range 13.0~26.2 cm²/C by thermal evaporation [187, 188], and of 13.0 cm²/C by pulsed spray pyrolysis [189] (Table 12). The coloration efficiency of the vanadium oxide films by sputtering was quite spread in the range 5.2~110.0 cm²/C [190-193] (Table 12). In case of the doped-vanadium oxide films, the coloration efficiency of Mo-doped V_2O_5 by electrochemical deposition was 42.7 cm²/C [194] and W-doped V_2O_5 by pulsed spray pyrolysis and RF magnetron sputtering were 49.0 cm²/C [195] (Table 12).

Table 12. Coloration efficiency of V_2O_5 films with various deposition methods.

	Charge capacity (mC/cm ²)	Electrolyte	Wavelength (nm)	CE (cm ² /C)	Deposition technique	Ref
V_2O_5	-	1 M LiClO ₄ /PC (propylene carbonate)	633	5.9	sol-gel	[182]
	43.3		636	9.3		[183]
	-		800	14.0		[184]
	20		630	12.5	[185]	
	-		780	19.3	electrodeposition	[186]
	-	0.5 M LiClO ₄ /PC	415	13.0	thermal evaporation	[187]
	12.5		550	26.2		[188]
	-		630	13.0	pulsed spray pyrolysis	[189]
	6.2	1 M LiClO ₄ /PC	630	5.2	reactive RF sputtering	[190]
	-		440	24.2		
	3.3	1 N LiClO ₄ /PC	400	110		[191]
	4.0	0.1 M LiClO ₄ /PC	400	100.5		[192]
	-	1 M LiClO ₄ /PC	400	84.5		[193]
Mo-doped V_2O_5	-	0.1 M LiClO ₄ /PC	850	42.7	electrodeposition	[194]
WO ₃ -doped V_2O_5	19.3	0.5 M LiClO ₄ /PC	630	49.0	pulsed spray pyrolysis	[195]

3.3 Durability

Cyclic voltammetry (CV) measurements were performed with a scan rate of 10 mV/s at potential range of -1V to +1V over 1000 cycles in Li and Na electrolytes. The cyclic voltammograms in figure 48 revealed that the films possessed sustainability and limitations. In Li electrolyte, the evolution of CV shape starts after 100 cycles followed by a gradual change after 250 cycles. After 1000 cycles, the two characteristic peaks shown in the first 20 cycles are greatly reduced and new peaks located at -0.2 V and -0.5 V in reduction state and -0.25 V and -0.1 V in oxidation state become clearly visible. In addition, the capacity of the thin film increases as increasing cycling (figure 47 c). After 1000 cycles, the increase of capacity is of 50% as compared to the first 20 cycles (Figure 47 d). This increase can be attributed to a modification of the morphology and an increase in film porosity. Figure 48 (a,b,c,d) shows SEM images of V_2O_5 RF-metal in Li electrolyte after 20, 250 and 1000 cycles. The surface of the thin film after 20 cycles is similar to the one of as-deposited film. After 250 cycles, several cracks are observed prior to a drastic change after 1000 cycles. Indeed, after 1000 cycles, the surface seems to be covered with “filaments” and appears rather porous.

In the Na electrolyte, the cyclic voltammograms show no significant modification in comparison with the Li electrolyte as increasing cycles (Figure 47 b). Figure 47 (d) shows that the capacity trend remains constant as increasing cycles. After 1000 cycles, the capacity of thin film corresponds to 90% of the capacity in the first few 20 cycles. Figure 48 (a,e,f,g) gathers SEM images of V_2O_5 RF-metal in Na electrolyte after 20, 250 and 1000 cycles. The surfaces of the film after 20 cycles and after 250 cycles are similar to the one of the as-deposited film. Several cracks are observed after 1000 cycles. The stable capacity trend in Na based electrolytes seems to be closely related to morphology.

In conclusion and in first approximation, the higher capacity in Li electrolyte as compared to Na electrolyte, indicates that a larger quantity of Li ions are involved in the insertion/de-insertion reaction within the thin film upon cycling (Figure 47 c,d). The good stability in Na based electrolyte is also consistent with a non-evolution of the CV shape. However, depending on the electrolyte nature, thin films show very different evolution of the morphology on cycling (Figure 48). The increased “interaction” of Li ions with the thin film accelerates its degradation. Upon cycling, cracks and holes are generated on surface leading to more porous films. The increase of capacity is closely related to a modification of the

morphology.

For both electrolytes, during the 250 cycles, GIXRD analysis was carried out. This result will be discussed in the mechanism part (Part C).

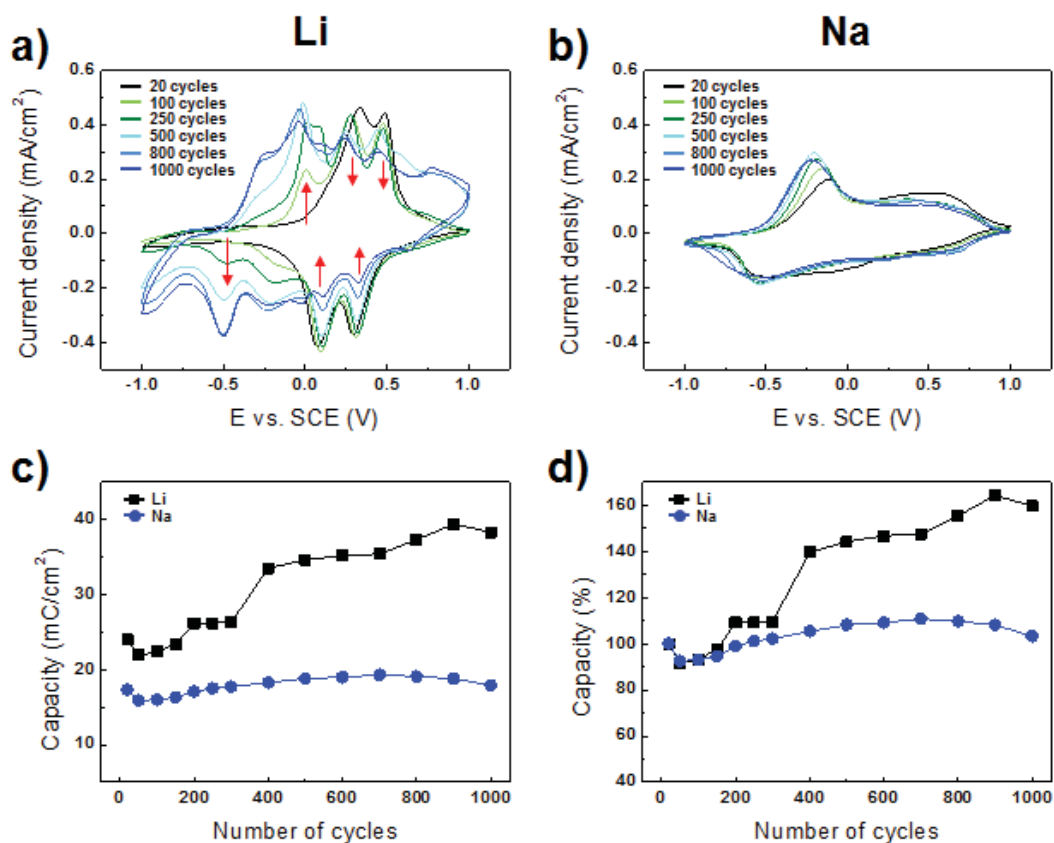


Figure 47. Cyclic voltammograms and evolution of the capacity versus the number of cycles of V₂O₅RF-metal in Li (a, c, d) and Na (b, c, d) electrolyte until 1000 cycles. The electrochemical chain is V₂O₅/electrolyte/Pt vs SCE.

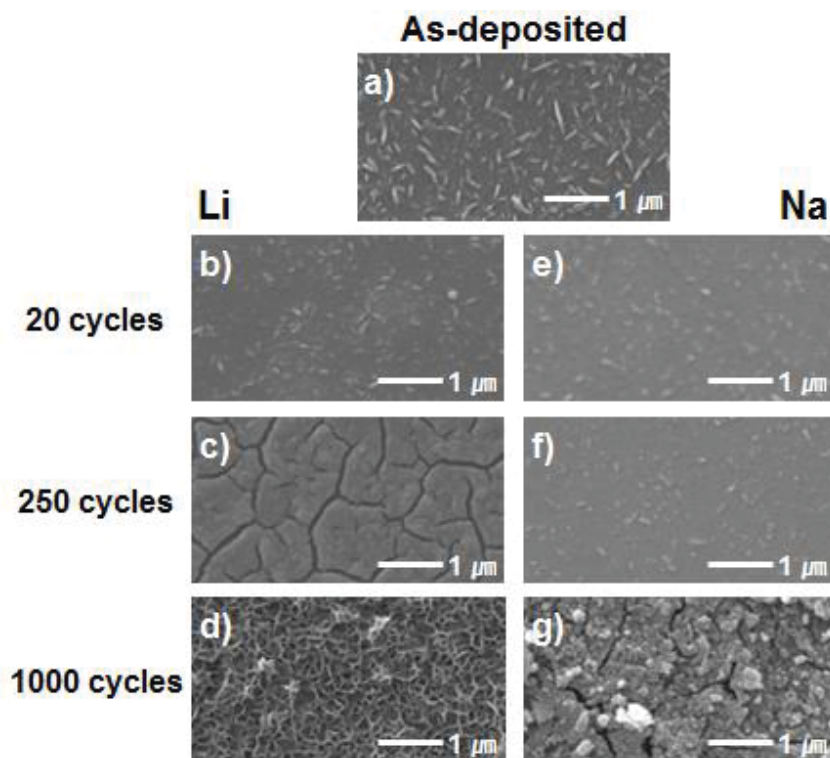


Figure 48. SEM images of V_2O_5 RF-metal in Li (b, c, d) and Na (e, f, g) based electrolyte after 20, 250 and 1000 cycles.

3.4 Switching time

Chronoamperograms of V_2O_5 RF-metal films, recorded applying voltage in reduction of -1 V and in oxidation of +1 V with a pulse duration of 40 s in Li and Na electrolytes, are shown in figure 49. The switching time for the insertion and deinsertion of V_2O_5 films is defined as the time interval for the value to reach 90% of its full contrast. In Li electrolyte, switching time is 13.0 s in insertion and 16.8 s in deinsertion (Figure 49 a). In Na electrolyte, switching time is 2.5 s in insertion and 4.5 s in deinsertion (Figure 49 b). Insertion reaction is faster than deinsertion reaction in both electrolytes. It is considered that deinsertion reaction in which ions are deinserted from thin films is more difficult than insertion reaction in which ions are inserted into thin films. In reduction (insertion) it also corresponds to the evolution from a non-conductive (only V^{5+}) to a conductive state (V^{5+} and V^{4+}) while it is the opposite in oxidation (deinsertion). In addition, switching time in Na is about 5 times faster than in Li. Above the difference in kinetics, the striking feature is the difference in shape. The shape of the chronoamperograms in Li electrolyte is rather complex showing more than one step

while the one in Na based electrolyte consists of a single step. In the literature, similar rather unusual behavior, was reported by P. Gimenez and T.F. Otero group on carbon nanotubes. Those authors published that carbon nanotubes electrode show the three kinetic controlling processes according to the three processes described by the electrochemically stimulated conformational relaxation (ESCR) model [196, 197, 198] for the responses of conducting polymer films. At any oxidation time, each of the three components describes the fraction of current consumed to charge the EDL (Electrical Double Layer), by oxidation-relaxation of the compacted structure or for the oxidation of the relaxed material under diffusion kinetic control of the counterions, respectively. In conclusion, the charge consumed by the capacitive component (the charge of the EDL) and the charge consumed by the two Faradaic components (oxidation-relaxation and oxidation-diffusion) of the electrochemical response can be identified and quantitatively separated [199, 200].

We measured chronoamperograms using a non-ions electrolyte (EMITFSI) and compared electrochemical response behavior in Li and Na electrolytes. Figure 49 (c) shows the Anodic chronoamperogram for EMITFSI (non-ions), Li and NaTFSI-EMITFSI electrolytes. In EMITFSI electrolyte, electrochemical response corresponding to electrical double layer charge is shown. In the Na based electrolyte, anodic chronoamperogram corresponding to electrical double layer charge and oxidation-relaxation are detected. On the other hand, electrochemical response corresponding to oxidation-relaxation and oxidation-diffusion for a very long time is shown in Li based electrolyte. As a result, non-ions electrolytes exhibit very fast switching time due to capacitive components, while Li based electrolytes exhibit very slow switching time due to faradic components. In the case of the Na based electrolyte, the switching time is intermediate between the two electrolytes, and the oxidation-diffusion reaction is shorter than Li and show more capacitive component characteristics. Those explanations are based on observed similarities in CA shapes between V_2O_5 RF-metal thin films and carbon nanotubes and remain a first interpretation. More details on the determination of the capacitive and faradic contributions upon cycling will be discussed in Part C (Chapter 1).

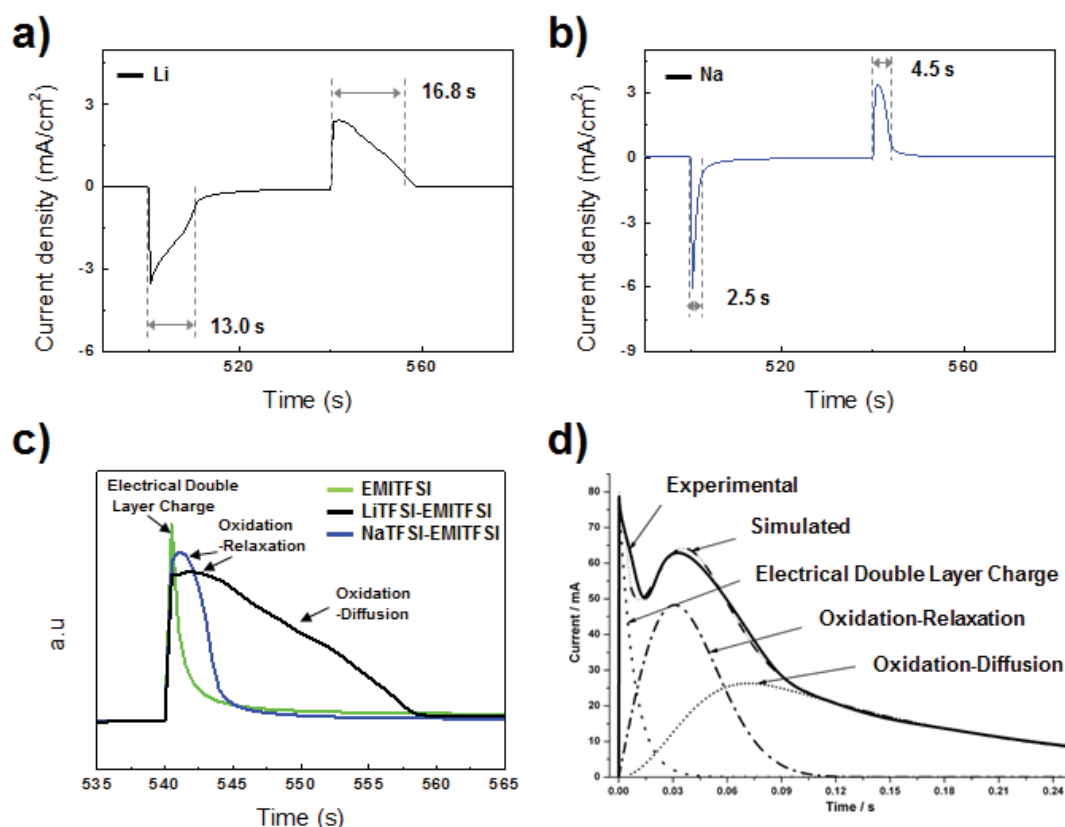


Figure 49. Chronoamperograms of V_2O_5 /RF-metal thin films in Li (a), Na (b) based and non-ions (EMITFSI) (c) electrolyte at potential range of -1 V to 1 V after 10 cycles. The electrochemical chain is V_2O_5 /electrolyte/Pt vs SCE. Experimental anodic chronoamperometric responses from SG-SWNT (single walled carbon nano tubes) when the actuator was submitted to ± 2 V square potential waves at a frequency of 2 Hz. Dotted line: capacitive charge of the electrical double layer (EDL). Dash-dotted line: oxidation under relaxation-nucleation kinetic control. Short dotted line: oxidation under diffusion kinetic control of the balancing counterions through the nanotube film. Dashed line: simulated responses obtained by addition of the three components [199, 200].

In order to determine the influence of film crystallinity on the film behavior, deposition of amorphous films was performed using an oxide V_2O_5 target instead of a metallic one. Their study takes place in the next paragraph.

4. Deposition of V_2O_5 thin film using V_2O_5 target.

The amorphous state of an electrode is usually associated with an open structure. Such open structure adequately prevents lattice expansion and favors large diffusion path of lithium ions

into the electrode because there is no interference of lithium motion at the grain boundaries. Generally, the amorphous material is suitable for production by thin film processes such as sputtering or vacuum evaporation. We used RF magnetron sputtering to fabricate amorphous V_2O_5 thin films and studied their electrochromic properties.

The power, total pressures and the $P(O_2)$ used are 100, 150 W and 1, 2, 3 Pa and 2, 5, 10% respectively. The commercial V_2O_5 targets were 75 mm diameter (99.99 %, Neyco). Vanadium oxide films by RF magnetron sputtering with V_2O_5 oxide target will be replaced later in the manuscript by V_2O_5 RF-oxide to simplify the writing. Electrochromic characterization in lithium based electrolyte was used to determine the “optimized” condition.

4.1 Thin film deposition at various powers and pressure conditions

At 2 Pa pressure and 2% $P(O_2)$, thin films were deposited under two RF powers (100, 150 W). Thin films deposited at 100 W lead to degradation and show poor adhesion to the substrate during cycling using chronoamperometry at -1 V to 1 V in Li electrolyte (Figure 51 a). We increase the RF power to 150 W. At higher power than 150 W, some damage (crack) may occur to the target. Thin films deposited at 150 W show no degradation and good adhesion to the substrate during cycling (Figure 50).

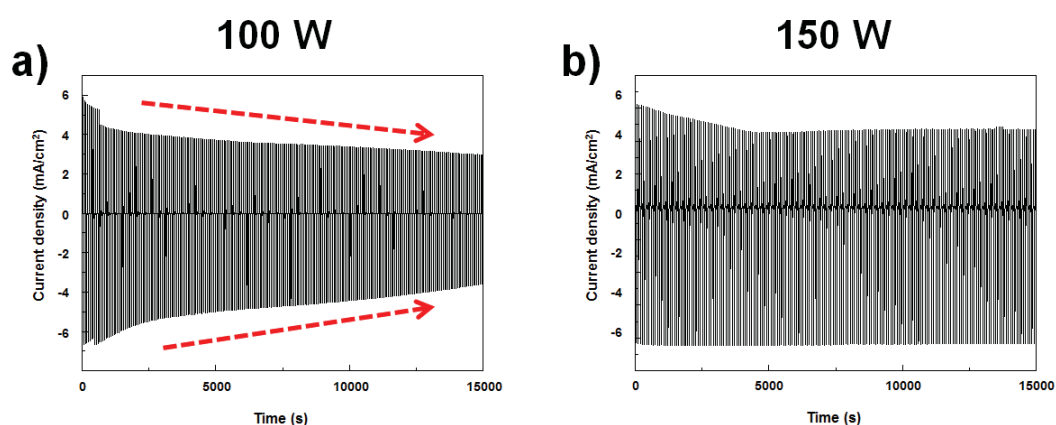


Figure 50. Chronoamperograms of V_2O_5 RF-oxide thin films by deposited with RF power of 100 W (a), 150 W (b) in Li based electrolyte at potential range of -1 V to 1 V during 15000 s (187 cycles). The electrochemical chain is V_2O_5 /electrolyte/Pt vs SCE.

At 150 W RF power and 2% P(O₂), thin films were deposited under different total pressures (1, 2, 3 Pa). Thin films were yellowish-orange in all conditions. However, thin films deposited at 1 Pa pressure showed poor adhesion with substrate after 20 cycles using cyclic voltammetry at -1 to 1V in Li electrolyte. The thin film deposited at 3 Pa pressure showed only 2 colors (yellow-violet) at the applied potential during cycling. The thin film deposited at 2 Pa pressure showed 3 colors (yellow-green-blue/gray) at the applied potential during cycling (Figure 51).

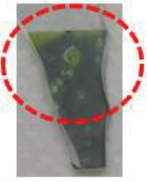
Total pressure	1 Pa	2 Pa	3 Pa
As-deposited			
After 20 cycles -1 V (in Li based electrolyte)			

Figure 51. Images of V₂O₅RF-oxide thin films by deposited under different total pressures of 1, 2 and 2 Pa after 20 cycles in Li based electrolyte at potential range of -1 V to 1 V. The electrochemical chain is V₂O₅/LiTFSI-EMITFSI/Pt vs SCE.

From the above results, **RF power and total pressure** were chosen as **150 W and 2 Pa**, respectively.

4.2 Thin film deposition under various P(O₂)

Parameters with the best properties in the previous part were mostly conserved (RF power 150 W, total pressure of 2 Pa, target distance-substrate 8 cm). Deposition of thin films were further proceed under P(O₂) conditions of 2, 5, 10%. Whatever the deposition conditions, the

thin films show a good adhesion to the ITO substrate. They don't degrade as a result of daily handling and don't show any visible evolution under ambient atmosphere. Between each deposit, a pre-sputtering is carried out under a P(O₂) atmosphere of 10% for a period of 30 min to recover the initial state of the target.

4.2.1 Optical Characteristics

4.2.1.1. Visual aspect

Figure 52 shows the visual appearance of the thin layers in their initial states as a function of P(O₂). All thin films are 200 nm thickness in order to compare them. All thin films exhibit yellow color at P(O₂) of 2, 5% and dark yellow at P(O₂) of 10%. The yellow/orange color is characteristic of V₂O₅.

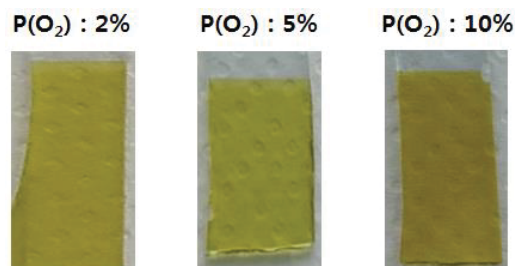


Figure 52. Visual image of as-deposited V₂O₅RF-oxide thin films with different P(O₂) of 2% (190 nm), 5% (199 nm) and 20% (203 nm).

4.2.2.2. Optical transmittance

Figure 53 describes the evolution of the optical transmission spectra and optical band gap of V₂O₅RF-oxide thin films as a function of P(O₂). The transmittance is slightly different depending on the P(O₂) condition. The thin film deposited under P(O₂) of 5% show the highest transmittance at 650 nm wavelength, whereas the transmittance decreases for P(O₂) of 2% and 10%. There is also a shift of the overall transmittance towards higher wavelength for the films deposited under P(O₂) of 10%. The optical band gap of film can be evaluated by the relations equation 16 and 17. Figure 53 (b) shows the plot of $(\alpha h\nu)^{1/2}$ versus $h\nu$ of

V₂O₅RF-oxide thin films. We found that experimental data fit better when n took value of 2, suggesting the indirect allowed transition. The calculated value of the E_g are 2.25 eV at P(O₂) 2%, 2.28 eV at P(O₂) 5% and 2.16 eV at P(O₂) 10%, respectively.

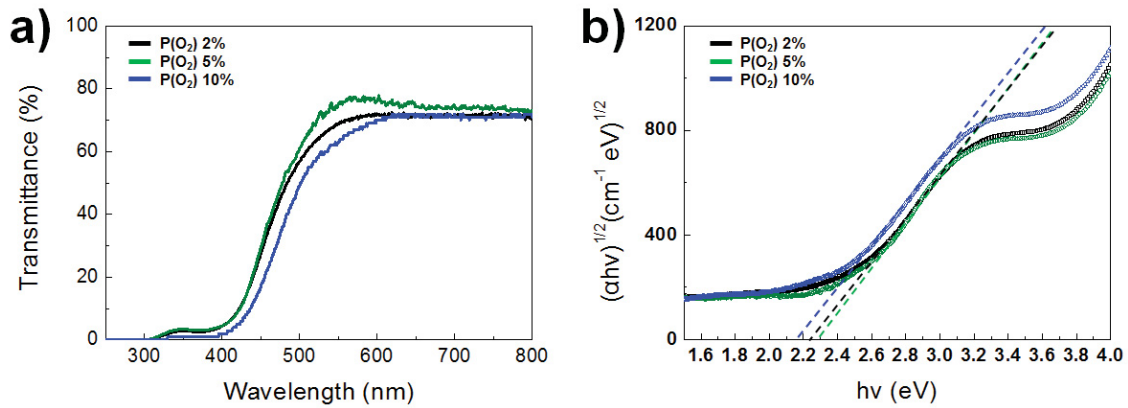


Figure 53. Transmittance (a) and Plot of $(\alpha h\nu)^{1/2}$ versus $h\nu$ (b) of as-deposited V₂O₅RF-oxide thin films of 200 nm thickness with different P(O₂).

4.2.2 Morphology

Figure 54 shows the SEM image of the vanadium oxide thin film deposited according to the oxygen partial pressures. At a 2% oxygen partial pressure, the film shows small particles on the surface. At a 5% oxygen partial pressure, those extra features appear more visible. At a 10% oxygen partial pressure, thin film exhibit very rough morphology. The film shows a needle or flake shape surface. The vanadium oxide thin film appears to be more rough and porous as the oxygen partial pressure increases. These results are similar to the surface phenomenon observed for V₂O₅RF-metal thin films (Figure 37).

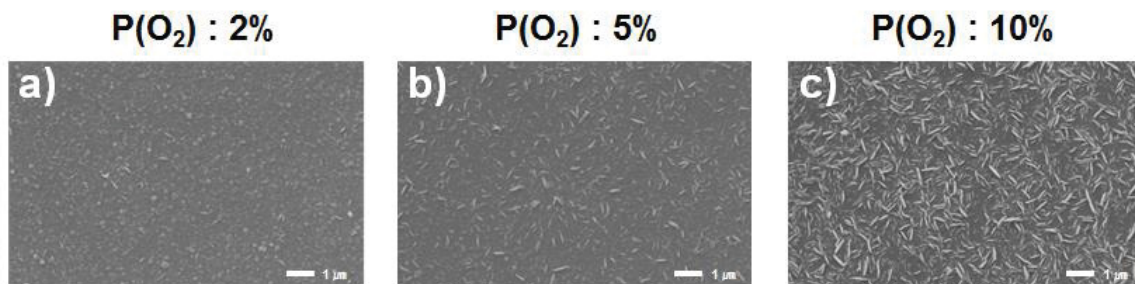


Figure 54. SEM images of surface of V₂O₅RF-oxide thin films of 200nm thickness deposited under P(O₂) of (a) 2%, (b) 5% and (c) 10%.

4.2.3 Structural characterization

Figure 55 shows the grazing incidence X-ray diffraction pattern (incidence degree 0.5 degree) of 200 nm V_2O_5 RF-oxide thin film according to oxygen flow rate. No diffraction peaks except the ITO crystal peaks are visible for the V_2O_5 RF-oxide thin films at the 2% oxygen partial pressure. When the oxygen flow ratio increases to 5%, a peak located at 19.9° starts to be distinguished. Its intensity increases for the $P(O_2)$ of 10% film. This peak can be assigned to the (001) peak and preferred orientation of V_2O_5 orthorhombic structure (S.G : Pmmn). The increase in (001) and (200) peaks intensity show an increase in film crystallinity as the oxygen partial pressure increases. These results are similar to phenomenon of V_2O_5 RF-metal thin films (Figure 39).

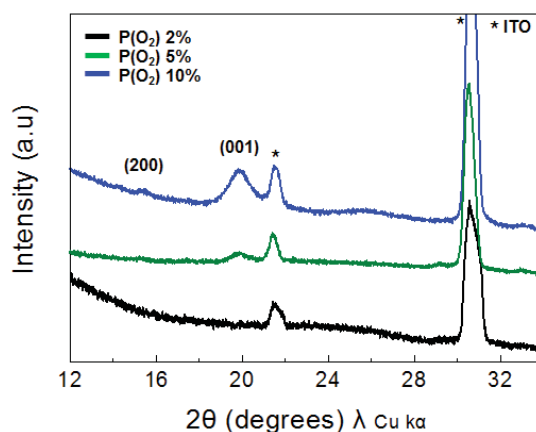


Figure 55. GIXRD pattern of 200 nm V_2O_5 RF-oxide thin films deposited under $P(O_2)$ of 2, 5 and 10%

4.2.4 Electrochemical properties

Figure 56 shows the the 20th typical cyclic voltammograms of the V_2O_5 RF-oxide thin films deposited according to the $P(O_2)$ of 2, 5 and 10% using $V_2O_5/LiTFSI-EMITFSI/Pt$ vs SCE, cycled using scan rate of 10 mV / sec in the range of -1.0 to 1.0 V.

Independently of the oxygen partial pressure, the CVs show reversible characteristics. The V_2O_5 RF-oxide thin film deposited by 2% oxygen partial pressure shows a single peak located at -0.3 V in the reduction and 0 V in oxidation. When the oxygen partial pressure increases to 5 and 10%, three paired peaks are observed. For the 5% oxygen partial pressure, peaks are

located at 0.3 V, 0.1 V and -0.25 V in reduction and 0 V, 0.2 V and 0.4 V in oxidation. CV curve of the film deposited by 20% oxygen partial pressure shows peaks located 0.25 V, 0.1 V and -0.2 V in reduction and -0.1 V, 0.2 V and 0.35 V in oxidation. The CV shape at 5 and 10% oxygen partial pressure is better defined but rather complex with this presence and of three pairs of peaks.

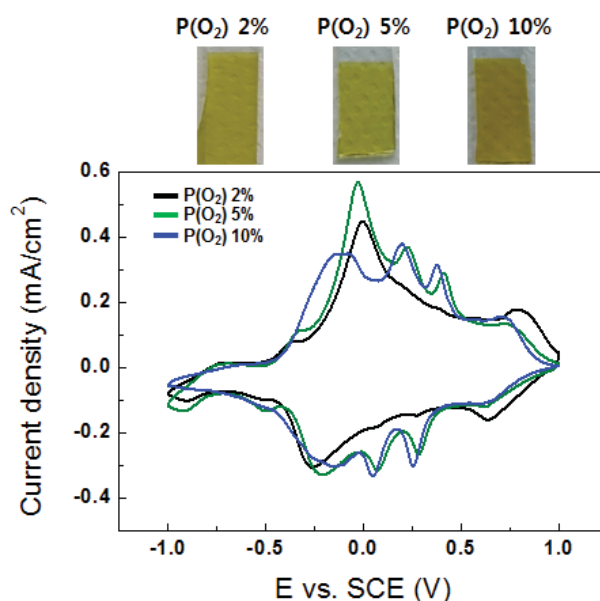


Figure 56. Cyclic voltammograms of 200 nm V_2O_5 RF-oxide thin films by deposited under $P(O_2)$ 2, 5, 10% in Li based electrolyte after 20 cycles. The electrochemical chain is V_2O_5 /electrolyte/Pt vs SCE.

4.2.5 Optical properties

Thin Films deposited by 2%, 5%, and 10% oxygen partial pressure show yellowish color. The optical properties of the thin film were measured upon cycling. Figure 57 shows *ex-situ* optical transmittance data under applied potential. In Li based electrolyte, films were gray/blue in the reduced state (-1 V) and orange in the oxidized state (+ 1 V). ΔT of films at gray color (-1V) and orange color (+ 1V) was measured at 650 nm. The difference in transmittance of films deposited at 2%, 5% and 10% oxygen partial pressure are very close of 24%, 24% and 25%, respectively.

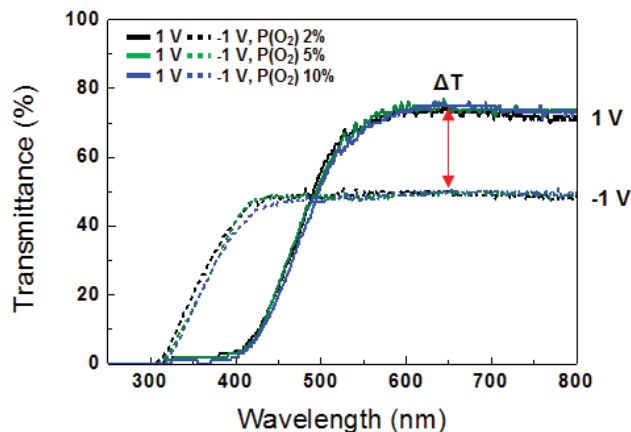


Figure 57. *Ex-situ* optical transmittance spectra 200 nm V_2O_5 RF-oxide thin films by deposited under $P(O_2)$ 2, 5, 10% in Li based electrolyte at -1V to 1V potential range after 20 cycles. The electrochemical chain is V_2O_5 /electrolyte/Pt vs SCE.

From the above results, the V_2O_5 RF-oxide thin film deposited at RF power of 150 W, total pressure of 2 Pa and $P(O_2)$ of 2% with V_2O_5 target is amorphous and show better electrochromic properties. We have conducted deeper studies using this film.

5. Electrochromic properties of V_2O_5 RF-oxide in Li and Na based electrolytes

5.1 Structural and textural characterizations

5.1.1 Thickness and morphology

V_2O_5 RF-oxide thin films of various thicknesses were deposited using the previously selected optimized conditions. Figure 58 shows the SEM image and GIXRD pattern for each thickness. As the thickness increases, the surface morphology becomes more fibrous texture of needles or flakes type. GIXRD pattern of Figure 58 (d) shows that the (001) peak increases and (200) peak appear as increasing film thickness. It is concluded an amorphous growth step up to a 200 nm thickness followed by a fibrous and porous crystalline film.

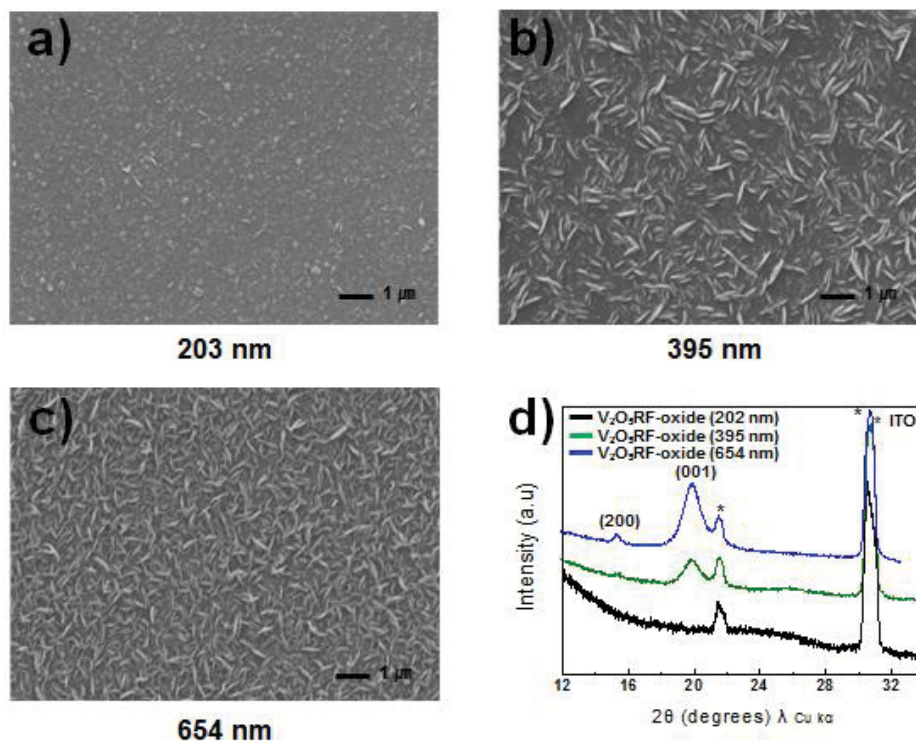


Figure 58. SEM images and GIXRD pattern for 203 nm (a, d), 395 nm (b, d) and 654 nm (c, d) of V_2O_5 RF-oxide thin films.

5.1.2 EELS characterization

EELS was carried out to characterize the 200 nm V_2O_5 RF-oxide thin film. Figure 59 (a) presents the observed energy loss spectra of the V_2O_5 RF-oxide thin film. It is seen that the characteristic edges of V (VL_3) shift significantly towards lower values comparison with V_2O_5 RF-metal. The value of ΔE , which is the distance between the vanadium (VL_3) and oxygen (Ok) edges, was measured. Oxidation state of V_2O_5 RF-oxide can be derived directly from the position at this calibration line using VO_2 and V_2O_5 pure powder as demonstrated in the figure 59 (b). V_2O_5 RF-oxide thin film shows oxidation state of +4.3. Table 13 summarizes the respective quantitative data on the chemical shift and the derived oxidation states.

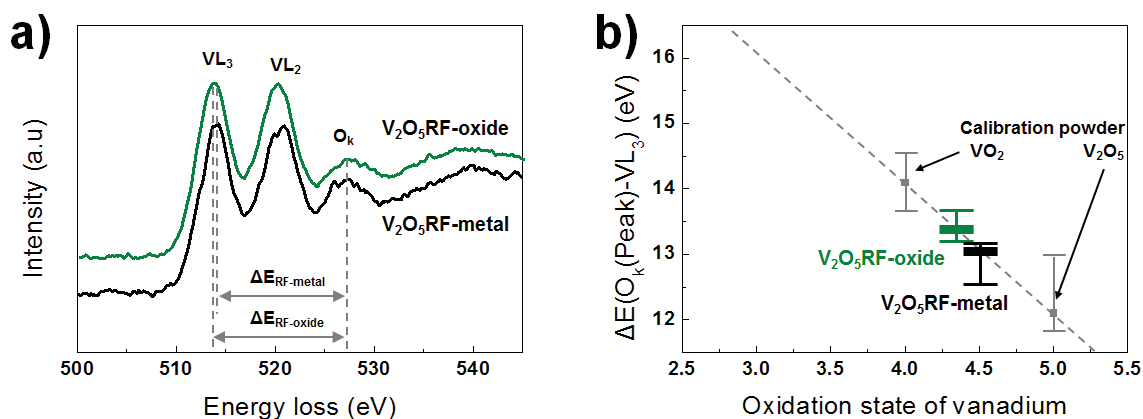


Figure 59. EELS spectra (a) and quantitative determination of the V-oxidation state (b) of 200 nm V_2O_5 RF-oxide thin films.

Table 13. Quantitative determination of the V-oxidation state of 200 nm V_2O_5 RF-oxide thin films.

Sample	O_k Peak (eV)	VL_3 Peak (eV)	ΔE (O- VL_3) (eV)	V-oxidation state
V_2O_5 Powder	526.7	514.6	12.1	5
VO_2 Powder	527.9	513.8	14.1	4
V_2O_5 RF-oxide	527.1	513.6	13.5	4.3 ± 0.2
V_2O_5 RF-metal	527.2	514.1	13.1	4.5 ± 0.2

The surface of V_2O_5 RF-oxide thin films shows to be easily removed by contact with gloves over 400 nm thickness films. This is same situation with previous V_2O_5 RF-metal thin film (Figure 45). It seems that the porous surface of the flake or needle types are significantly less adherent to the surface. Hereafter, the analysis and evaluation were performed using 200 nm thickness V_2O_5 RF-oxide thin films.

5.2 Electrochromic properties

V_2O_5 RF-oxide thin films of 203 nm thickness were electrochemically and optically characterized using V_2O_5 /electrolyte/Pt vs SCE cell. Figure 60 (a) and (c) shows the 20th

typical cyclic voltammograms in Li (LiTFSI-EMITFSI) and Na (NaTFSI-EMIFTSI) based electrolytes, respectively with a sweep rate of 10 mV/s. Independently of the electrolyte, both CV curve show similarities with a major peak located in oxidation at 1 V. The V₂O₅RF-oxide thin film, initially yellow, goes through distinct color changes as green at 0.2 V, blue at -0.4 V and gray at -1 V upon reduction/oxidation. The orange color is recovered at the end of the oxidation. The reversible electrochromism with 4 color states was demonstrated for both electrolytes. Figure 60 (c) and (d) show *ex-situ* optical transmittance data under applied potential. In Li electrolyte, reduced gray state (-1 V) and the oxidized orange state (+1 V) are associated with transmittance values of T_G 47% and T_O 8% at 420 nm and T_G 48% and T_O 71% at 650 nm, corresponding to a transmittance modulation ΔT of 39% at 420 nm and 27% at 650 nm, respectively (Table 14). In Na electrolyte, the transmittance modulations ΔT are 41% and 23% at 420 nm and 650 nm respectively (Table 14). The absorption edge is shifted to lower wavelength at insertion reaction in both electrolytes. In conclusion, V₂O₅RF-oxide thin films exhibit reversible multi-color electrochromic characteristics under applied voltage in Li and Na electrolytes. In addition, the value of modulation in transmittance ΔT in Na electrolyte is very similar with Li. Another surprising thing is that the value of current density in Na electrolyte is very similar with the one in Li. This is a very different phenomenon from the results seen in previous crystalline V₂O₅RF-metal thin films probably associated with the amorphous character of the films.

As a result, the amorphous V₂O₅RF-oxide thin films deposited by RF magnetron sputtering with V₂O₅ target show good electrochromic properties not only in Li based electrolyte but also in Na based electrolyte, noneless of the size difference between the two ions.

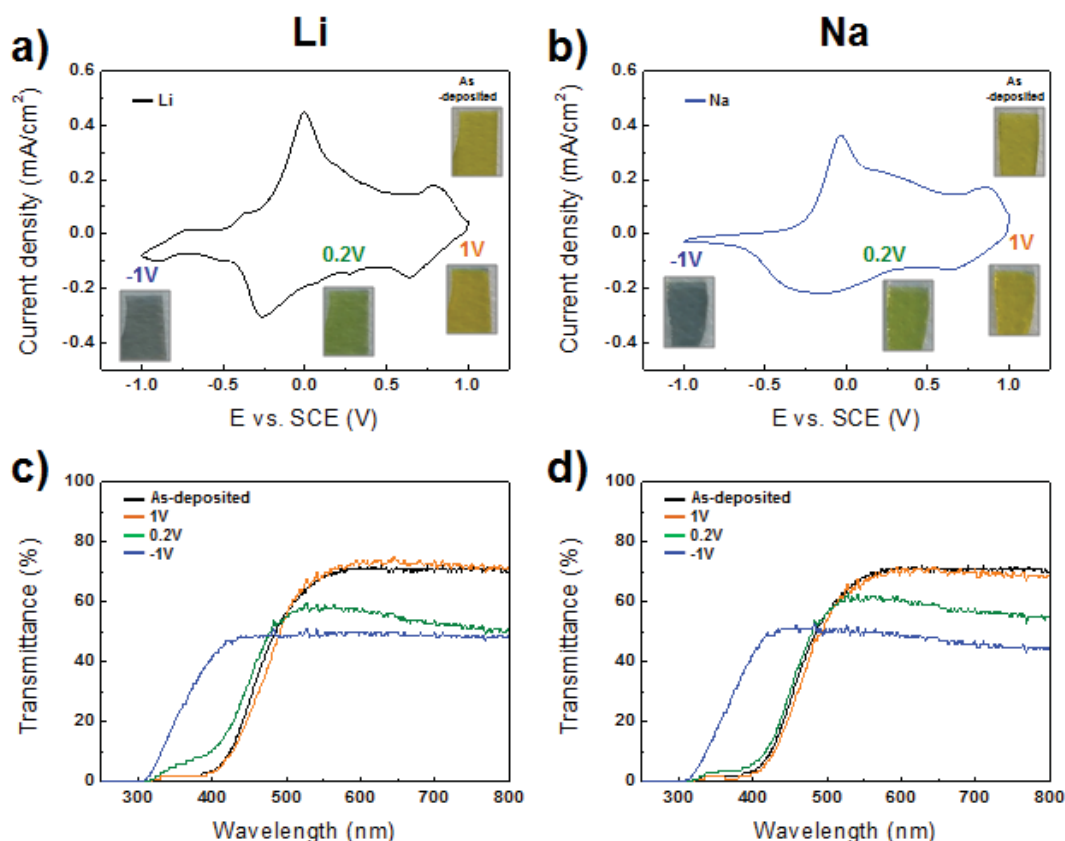


Figure 60. Cyclic voltammograms and *ex-situ* optical transmittance spectra of 200 nm V_2O_5 RF-oxide thin films in Li (a, c) and Na (b, d) based electrolyte after 20 cycles. The electrochemical chain is V_2O_5 /electrolyte/Pt vs SCE.

Table 14 summarizes the coloration efficiency of the films in two wavelengths corresponding to 420 nm and 650 nm, exhibiting values of $27.5 \text{ cm}^2/\text{C}$ and $7.0 \text{ cm}^2/\text{C}$ in Li electrolyte. In Na electrolyte, the coloration efficiency of the films exhibit value of $28.2 \text{ cm}^2/\text{C}$ and $6.4 \text{ cm}^2/\text{C}$.

Table 14. Coloration efficiency, transmittance variation ΔT , and optical density ΔOD of 200 nm V_2O_5 RF-oxide thin films in Li and Na based electrolyte.

Electrolyte	Charge density (mC/cm^2)	$\lambda = 420\text{nm}$			$\lambda = 650\text{nm}$		
		ΔT	ΔOD	$CE(\text{cm}^2/\text{C})$	ΔT	ΔOD	$CE(\text{cm}^2/\text{C})$
Li	27.8	39	0.77	27.5	27	0.20	7.0
Na	26.4	41	0.74	28.2	23	0.17	6.4

5.3 Durability

Cyclic voltammetry (CV) measurements were performed with a scan rate of 10 mV/s at potential range of -1 V to +1 V over 1000 cycles in Li and Na electrolytes. The cyclic voltammograms show that the V_2O_5 RF-oxide thin films possessed sustainability and limitations during cycling (Figure 61). In Li electrolyte, the degradation (i.e. strong decrease in capacity) appears as soon as after 100 cycles. After 250 cycles, the one characteristic peak shown in the first 20 cycles is greatly reduced. After several tens of cycles, CV measurement was stopped because the disappearance of the films was visually observed. In the Na electrolyte, thin film was observed to start modification after 100 cycles. Subsequently, the deterioration of the film was continued until 1000 cycles.

Figure 61 (c, d) shows the corresponding evolution of the coulombic capacity of the V_2O_5 RF-oxide thin films upon cycling. A short activation period occurs from the initial cycle to $\sim 100^{\text{th}}$ cycle. It corresponds to the gradual participation of the bulk of the films in the electrochemical process. Beyond 100^{th} cycle the capacity decreases continuously. The decrease is much more pronounced for Li electrolyte. The capacity of thin film is reduced by 25% after 1000 cycles in Na electrolyte, whereas in Li it is by more than 50% after 250 cycles (Figure 62 d). Related to this result, SEM images show a more pronounced decohesion and peeling-off for V_2O_5 thin film in Li and Na after cycles (Figure 62). Several cracks are observed on the film surface after 20 cycles in Li electrolyte. After 250 cycles, the disappearance of the thin film can be clearly seen. In the Na electrolyte, small cracks and dilatableness occur on the thin film surface after 250 cycles, and several cracks are visible after 1000 cycles. Therefore, we suggest that the decrease of the capacity is also correlated to the progressive loss of mechanical adhesion of the thin films from the ITO substrates, which is more pronounced in Li based electrolyte.

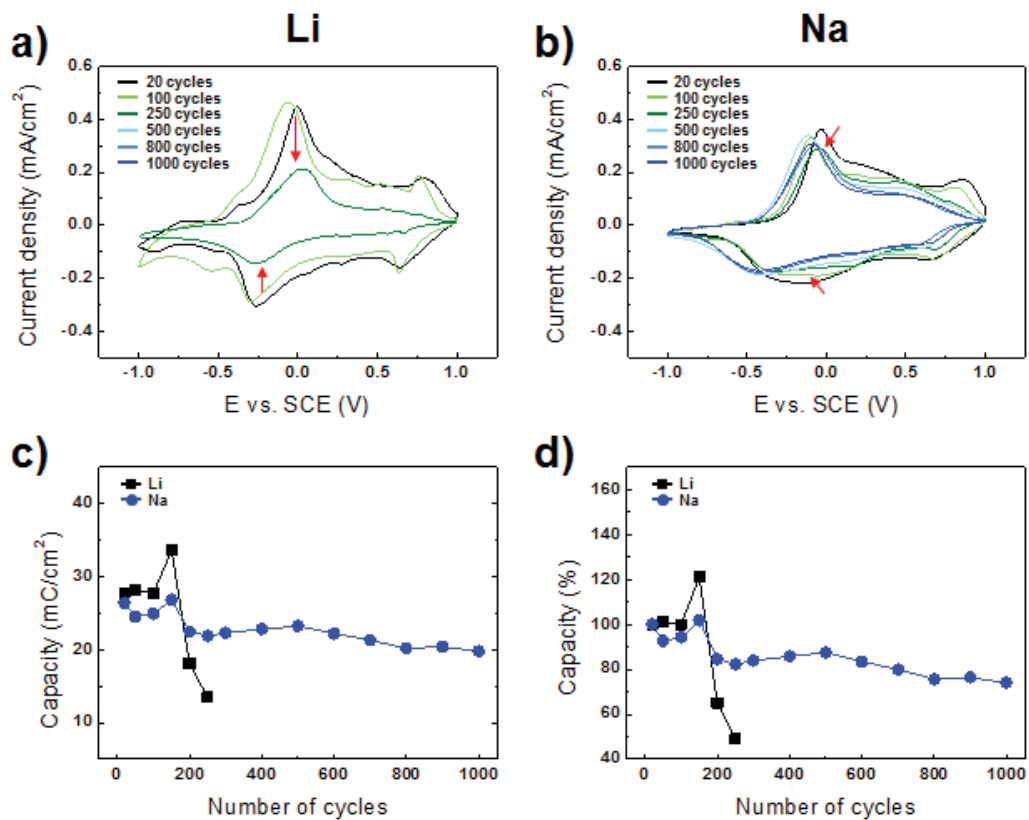


Figure 61. Cyclic voltammograms and evolution of the capacity versus the number of cycles of 200 nm V_2O_5RF -oxide in Li (a, c, d) and Na (b, c, d) electrolyte until 1000 cycles. The electrochemical chain is V_2O_5 /electrolyte/Pt vs SCE.

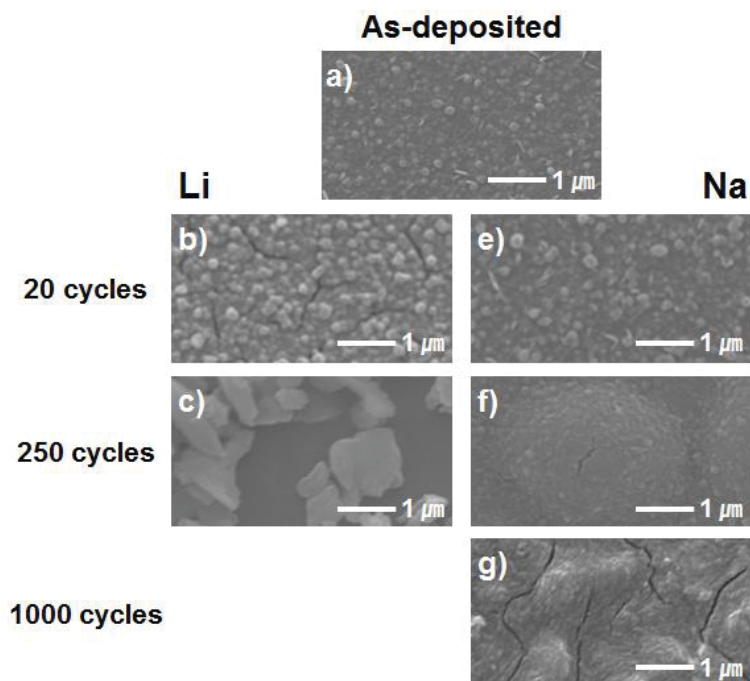


Figure 62. SEM images of 200 nm V_2O_5RF -oxide in Li (b, c) and Na (e, f, g) based electrolyte after 20, 250 and 1000 cycles.

5.4 Switching time

Chronoamperograms of 200 nm V_2O_5 RF-oxide films recorded applying voltage in reduction of -1 V and in oxidation of +1 V with a pulse duration of 40 s in Li and Na electrolytes are shown in Figure 63. The switching time for the insertion and deinsertion of V_2O_5 films was defined as the time interval for the value to reach 90% of its full contrast. In Li electrolyte, switching time is 4.4 s in insertion and 8.0 s in deinsertion (Figure 63 a). In Na electrolyte, switching time is 5.8 s in insertion and 2.3 s in deinsertion (Figure 63 b). The insertion reaction is faster than deinsertion reaction in both electrolytes. It is considered that deinsertion reaction in which ions are deinserted from thin films is more difficult than insertion reaction in which ions are inserted into thin films. The switching time in Na is faster than in Li. These results are similar to the phenomenon of V_2O_5 RF-metal thin films (Figure 49, p 80). However, the V_2O_5 RF-oxide film shows twice faster switching time than the crystalline V_2O_5 RF-metal film in the Li electrolyte.

We measured chronoamperograms using a non-ions electrolyte (EMITFSI) and compared electrochemical response behavior in Li and Na electrolytes. Figure 63 (c) shows the anodic chronoamperogram for EMITFSI (non-ions), Li and NaTFSI-EMITFSI electrolytes. In EMITFSI electrolyte, electrochemical response corresponding to electrical double layer charge is shown. In the Na based electrolyte, anodic chronoamperogram corresponding to electrical double layer charge and oxidation-relaxation are shown. On the other hand, electrochemical response corresponding to oxidation-relaxation and oxidation-diffusion for a very long time is shown in Li based electrolyte. This curve is similar with previous V_2O_5 RF-metal films (Figure 49 c). As a result, cycles in non-ions electrolytes exhibit very fast switching time due to capacitive components, while the ones in Li based electrolytes exhibit very slow switching time due to faradic components. In the case of Na based electrolyte, the switching time is intermediate between the two electrolytes, and the oxidation-diffusion reaction is shorter than Li and showing more capacitive component characteristics. More details on the capacitive and faradic contributions on the electrochemical behavior will be discussed later in Part C (Chapter 1).

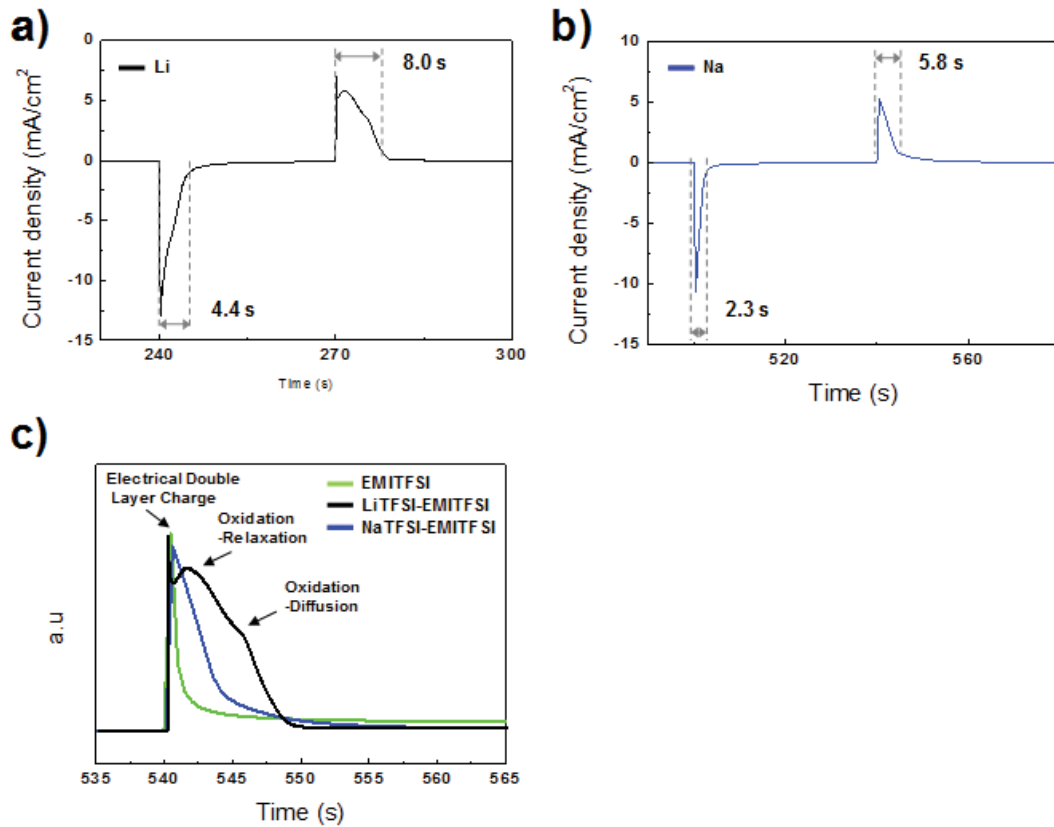


Figure 63. Chronoamperograms of V_2O_5 /RF-oxide thin films in Li (a, c), Na (b, c) based and non-ions (EMITFSI) (c) electrolyte at potential range of -1V to 1V after 10 cycles.

In conclusion, the amorphous V_2O_5 /RF-oxide thin films deposited with V_2O_5 oxide target exhibit good EC characteristics when cycled in Li and Na electrolytes. However, a very fast degradation and film detachment after few hundred CV cycles are observed. One explanation may be that the mechanical adhesion of V_2O_5 film to the substrate is weak. Using “regular” RFMS sputtering, we observe a very strong degradation of the morphology upon cycling. To prevent such degradation, we investigated the HiPIMS (High Power Impulse Magnetron Sputtering) deposition technique to deposit V_2O_5 thin films aiming at improved adhesion.

Chapter 2. Deposition of vanadium oxide thin films by HiPIMS

1. High Power Impulse Magnetron Sputtering (HiPIMS)

High power impulse magnetron sputtering (HiPIMS), or sometimes referred to as high power pulsed magnetron sputtering (HPPMS), is an ionized PVD method based on conventional direct current magnetron sputtering (DCMS).

High fluxes of ions allowing favourable tailoring of the film structure and properties is beneficial for film quality [201]. In the DCMS process, increased ion flux can be achieved by unbalancing the magnetron or by increasing the applied substrate bias. The latter however mainly increases the ion energy, which can lead to undesired implantation of Ar^+ ions and deterioration of the film structure [202]. Efforts have therefore been made to increase the total ion flux, and to ionize the deposition species [203]. Some of these approaches require substantial modifications of existing deposition systems, such as the use of external RF coils for post-ionization of the sputtered material [204]. The approach demonstrated by Kouznetsov [205] now known as HiPIMS, requires in principle only the sputtering power supply to be replaced in an existing magnetron sputtering setup. In the original paper, using HiPIMS from a Cu cathode, a high degree of ionization of sputtered material, as well as void-free trench filling, due to the possibility to direct the deposition flux, was demonstrated. Because of the many evident similarities between DCMS and HiPIMS, the two methods are often compared.

1.1 Principle of HiPIMS

The foremost reason for employing the HiPIMS technique is that it permits turning a conventional magnetron into a source for ionization of sputtered material. Approximately twice the voltage used in a conventional DCMS process is applied in short discharge pulses to the target, resulting in power densities of kWcm^{-2} in the peak of the pulse [206]. The resulting substrate current peak densities are in the order of Acm^{-2} , which is more than two orders of magnitude higher than for DCMS [207]. By applying this very high power to the sputtering source, a high plasma density is generated in front of the target. In a HiPIMS

discharge, the electron densities obtained can be in the order of 10^{18} m^{-3} [208, 209], i.e. 2-4 orders of magnitude higher than for DCMS [210]. Such plasma densities reduces the mean ionization distance to a few cm, i.e. the dimensions of the intense plasma close to the target, while the corresponding figure for DCMS can be several tens of cm [211]. Thus, the probability for the sputtered species to be ionized is higher in a HiPIMS discharge. The amount of ionization depends mainly on the discharge characteristics [212] and the target material. Values ranging from ~5% for C [213] to 90% for Ti [214] have been reported. In order to avoid overheating of the target, the power is applied in short, repeated pulses, with resulting duty factors in the order of a few percent. Thereby the average power is kept similar to that of a DCMS process, thus circumventing the need for enhanced target cooling. The discharge is typically operated with pulse widths ranging from a few tens up to several hundreds of microseconds, with repetition frequencies of tens of Hz to several kHz. An example of HiPIMS waveforms recorded from an oscilloscope is shown in figure 65. Modulated pulse power sputtering magnetron sputtering (MPP) techniques is a derivative of high power pulsed magnetron sputtering during the power pulse. Different from these middle frequency pulsed dc magnetron sputtering, high power pulsed magnetron sputtering (HiPIMS) has been developed as a new ionized physical vapor deposition technique featuring very high peak power density at the target (typically in the range of $500\sim 3000 \text{ W/cm}^2$) with low frequency ($<10 \text{ kHz}$) and low duty factors ($<10\%$) to avoid melting the target.

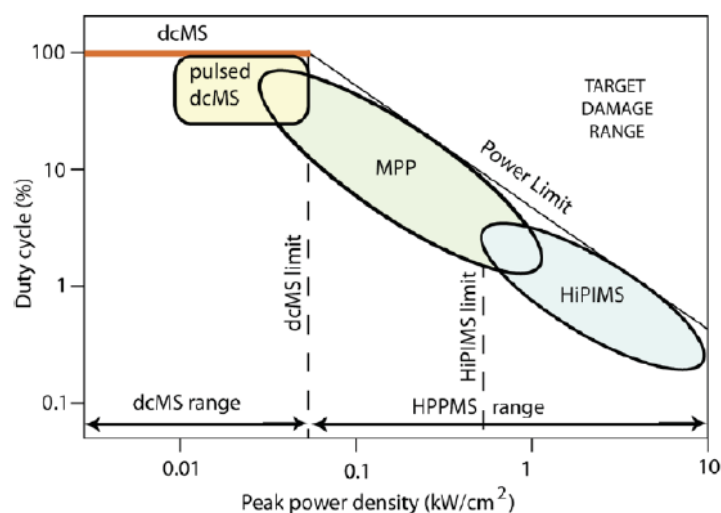


Figure 64. Graphical representation of the classification of magnetron sputtering process as a function of the power delivered. Due to thermal ceiling limitations of the magnetron, increase of the plasma density is obtained through an increase of the instantaneous power [215].

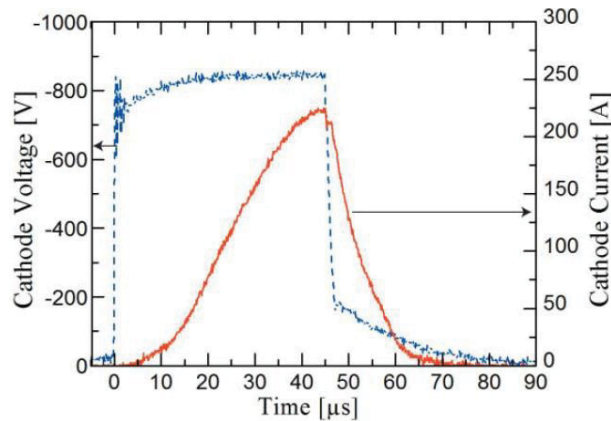


Figure 65. Voltage and current waveforms recorded from an oscilloscope during a HiPIMS discharge [216].

Typically, the amplitude of the applied voltage pulse is in the range of 400–2000 V. Substantially, the current densities of 3~4 A/cm², peak power densities of 0.5–10 kW/cm², repetition frequency in the range of 50–5000 Hz, and duty cycle of 0.5–5 % are used for operation of a HiPIMS discharge [217]. Elevated ionization of sputtered species improves the film quality. Improved properties are film density [218] adhesion to other materials [219], surface roughness [220, 221, 222] and hardness [223, 224]. Better control of the reactivity during reactive sputtering can be achieved while the growth temperature is lowered and film quality is maintained [225]. Moreover, the instant deposition rate is relatively high because of the pulsed nature of the growth flux, hence increasing the super saturation of adatoms on the substrate [226]. As a result the altered growth condition leads to the deposition of dense films with flat surfaces.

1.2 Advantages of HiPIMS

The main advantage of the HiPIMS technique is that with very little modification, existing magnetron sputtering systems can be converted to ionized magnetron sputtering. As previously discussed, an ionized deposition flux can be controlled in terms of direction and energy of the film forming species by electric and magnetic fields. The implications for the deposition process and film growth due to higher ion content present in the HiPIMS process, has been demonstrated in several publications. Bohlmark et al. showed that the deposition flux could be directed by applying an external magnetic field, thus greatly altering the spatial

distribution of sputtered species [227]. Moreover, since ions will be accelerated through the plasma sheath to impinge practically normal to any surface immersed in the plasma, HiPIMS is a less pronounced line of sight process as compared to DCMS. By applying a negative bias potential to the substrates, a more homogeneous coating of complex shaped objects is possible. This was demonstrated by Bobzin et al. showing that for HiPIMS, the deposition rate for surfaces perpendicular to the target surface was 71% of that for surfaces facing the deposition source, while the corresponding number for DCMS was ~45% [228]. Coating of trenches in the μm dimensions was demonstrated by Kouznetsov et al [229], and on the cm scale by Alami et al. The latter found no tilted columnar growth in HiPIMS grown films although the substrate was oriented perpendicular to the target surface [230]. The high ion flux towards the substrate also favours adatom surface diffusion processes during film growth [231], and can cause renucleation [232] and knock-on effects. As a consequence, films deposited by HiPIMS often appear strikingly dense, featureless with a smooth surface [233], as seen in figure 67 for Ti. Furthermore, studies have shown that the coating density increase when using HiPIMS as compared to DCMS is between 6-30% for different target materials [231, 234, 235] Since the aforementioned studies were performed under widely separated experimental conditions, it is difficult to draw any general conclusions from the findings.

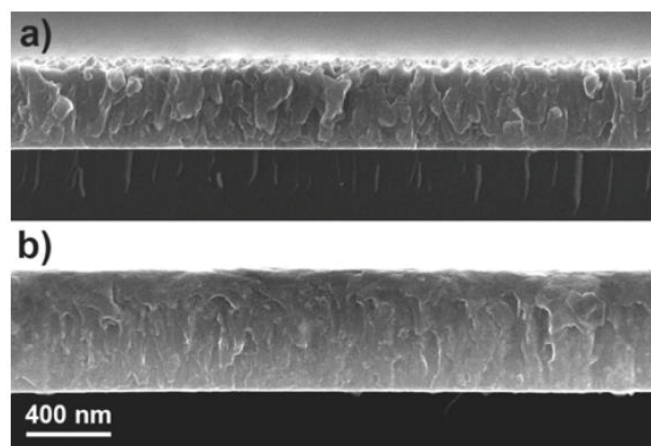


Figure 66. Cross sectional SEM micrographs of Ti thin films deposited using a) DCMS, and b) HiPIMS under otherwise identical experimental conditions [233].

The source material ionic content present in the HiPIMS flux can also be used for

pretreatment of substrates prior to deposition, typically during a plasma etch where a high voltage is applied to the substrate. Thereby, film forming species are implanted in the substrate, forming a gradient towards the surface [236]. This allows for interface engineering and increases adhesion of the coatings. In addition, as reported in the original HiPIMS paper by Kouznetsov et al., the target utilisation can be improved and thereby also the coating uniformity in front of the deposition source [237].

2. Deposition conditions : experimental methodology

The HiPIMS discharge experiments were performed in a stainless steel vacuum system turbo-molecularly pumped to a base pressure of 10^{-5} mTorr. The total gas pressure during operation was kept at 2 Pa. Argon (99.999% purity) and oxygen (99.995% purity) were admitted to the chamber at a total flow rate of 20 sccm, while the oxygen partial pressure $P(O_2) = O_2/(Ar+O_2)$ was varied between 2, 10 and 20%. A magnetron head supported a 50 mm diameter vanadium target (99.99% purity, Neyco). The magnetron was powered from a HiPIMS power supply (Effitech) providing a cathode voltage of 588~600 V and a discharge current of up to 26~80 mA, while using a 45 μ s long pulse duration and a repetition rate of 1200 Hz.

3. Thin film deposition of V_2O_5 with HiPIMS at various pulse durations and a repetition rate conditions

3.1. Using various pulse durations and a repetition rate conditions

Vanadium oxide films by HiPIMS with V metallic target will be replaced later in the manuscript by V_2O_5 HiPIMS to simplify the writing.

V_2O_5 HiPIMS thin films were deposited under different pulse durations (20, 45 μ s), repetition rates (500, 1200 Hz) and powers (19, 23, 51 W) at total pressure of 2 Pa and $P(O_2)$ of 2%. The conditions, a,b,c are gathered in Table 15. Thin films deposited during 90~180 min were about 200 nm. Figure 67 shows the cyclic voltammograms of V_2O_5 HiPIMS thin films deposited with different pulse durations and repetition rates in LiTFSI-EMITFSI

electrolyte at applied voltage between -1 V and 1 V after 200 cycles. V₂O₅HiPIMS thin films deposited by conditions (a) and (b) show degradation after 100 cycles associated with a poor adhesion to the substrate during cycling. On the contrary, V₂O₅HiPIMS thin films deposited at pulse duration of 45 μs, repetition rate of 1200 Hz and power of 51 W (conditions c), show no degradation at least up to 200 cycles. From the above results, V₂O₅HiPIMS thin films deposited with condition (c), exhibiting better cycling stability, were used for subsequent study.

Table 15. Deposition conditions of different V₂O₅HiPIMS thin films

	Pulse duration (μs)	Repetition rate (Hz)	Power (W)	Thickness (nm)	Deposition time (min)
a)	20	1200	19 W	199	180
b)	45	500	23 W	187	180
c)	45	1200	51 W	204	90

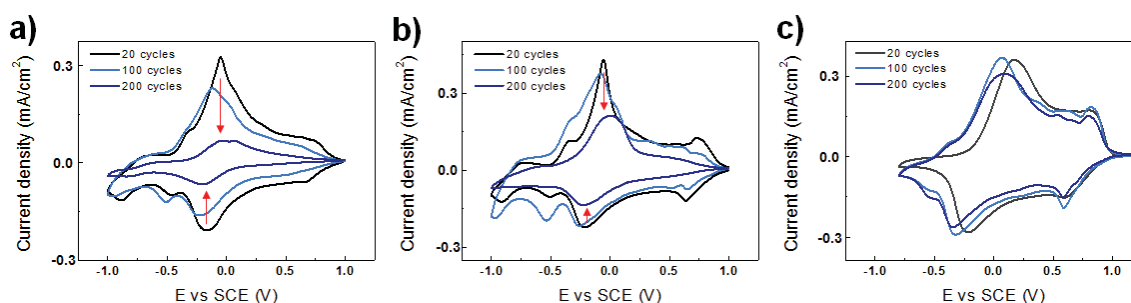


Figure 67. Cyclic voltammograms of 200 nm V₂O₅HiPIMS thin films deposited by different pulse durations and repetition rates in LiTFSI-EMITFSI electrolyte at applied voltage between -1 V and 1 V after 200 cycles. The electrochemical chain is V₂O₅/electrolyte/Pt vs SCE.

3.2 Using various oxygen partial pressure conditions

We first characterized the deposition process by analyzing the HiPIMS discharge current and voltage with different oxygen partial pressure. Figure 68 shows time-dependent waveforms of discharge current and discharge voltage for the HiPIMS conditions under P(O₂)

of 0% in metal mode and P(O₂) of 10% in oxide mode. In the metal mode, discharge current exhibits an initial increase, reaching a maximum at 36 μs and then decays until the end of the pulse (Figure 68 a). In the oxide mode, on the other hand, discharge current continues to increase until the end of the pulse (Figure 68 a). The peak value of discharge current is similar in the metal and oxide mode. The discharge voltage is 363 V in P(O₂) of 0% at metal mode and 494 V in P(O₂) of 10% at oxide mode (Figure 68 b). The peak value of discharge voltage is 36% higher in the oxide mode more than in the metal mode.

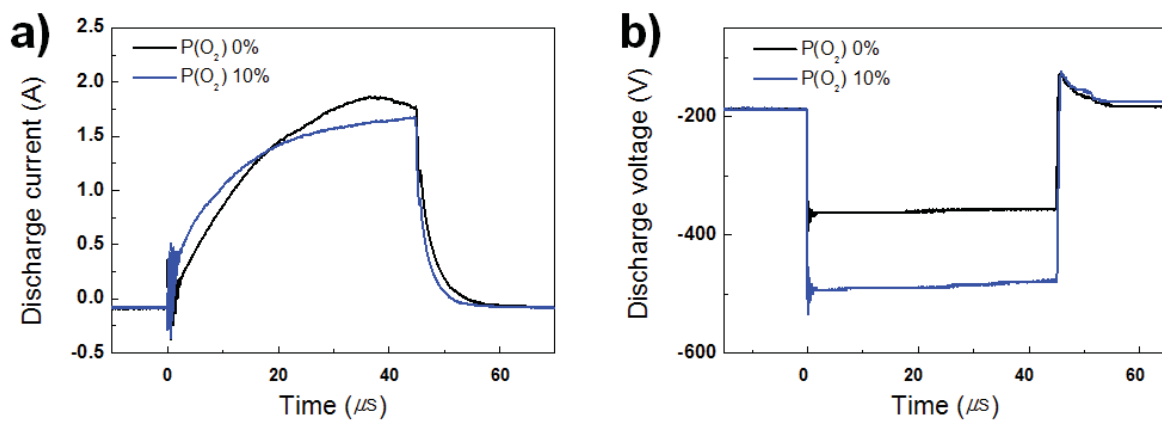


Figure 68. Discharge current (a) and voltage (b) waveforms vs. time for P(O₂) of 0% at metal mode and P(O₂) of 10% at oxide mode of vanadium oxide HiPIMS discharges.

3.2.1. Visual aspect

Figure 69 shows the visual appearance of the V₂O₅HiPIMS thin films in their as-deposited states as a function of P(O₂). All as-deposited films are 200 nm and yellow color at P(O₂) of 2, 10, 20%.

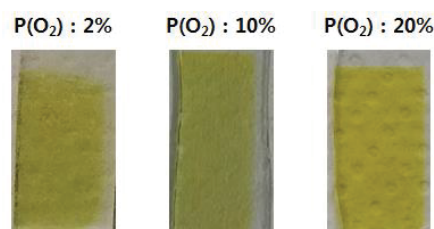


Figure 69. Visual image of as-deposited V₂O₅HiPIMS thin films of 200 nm thickness with different P(O₂).

3.2.2 Optical transmittance

Figure 70 describes the evolution of optical transmission spectra and optical band gap of V_2O_5 HiPIMS thin films as a function of $P(O_2)$. The transmittance is slightly different depending on the $P(O_2)$ condition. The transmittance at 650 nm wavelength increases with increasing oxygen partial pressure (Figure 70 a). The thin film deposited under $P(O_2)$ of 10% and 20% show overall higher transmittance than 2% and a slight shift towards lower wavelength of the edge. The optical band gap of film can be evaluated by the relations equation 17 and 18 (p 61). Figure 70 (b) shows the plot of $(\alpha h\nu)^{1/2}$ versus $h\nu$ of V_2O_5 HiPIMS thin films. We found that experimental data fit better when n took value of 2 is used, suggesting the indirect allowed transition. The calculated value of the E_g were was 2.29 eV at $P(O_2)$ 2%, 2.25 eV at $P(O_2)$ 10% and 2.15 eV at $P(O_2)$ 20%, respectively.

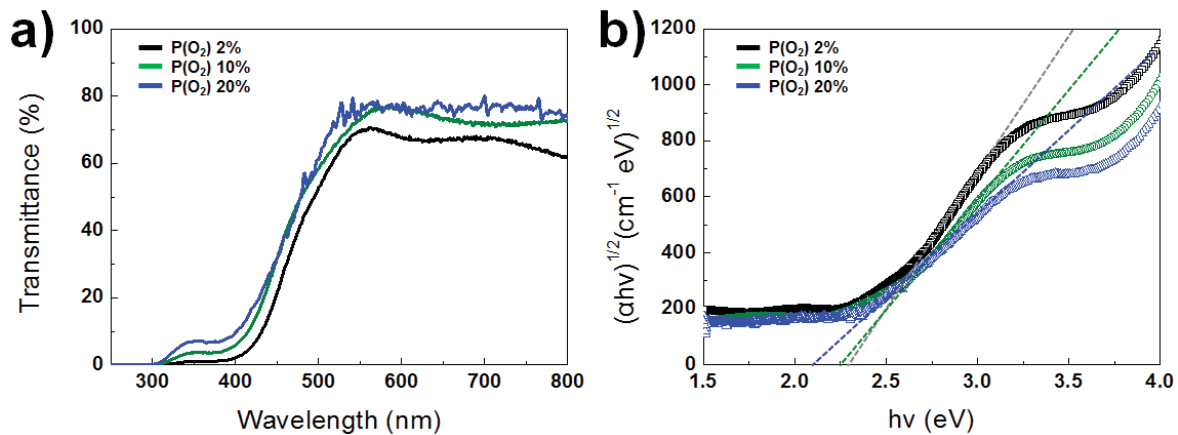


Figure 70. Transmittance (a) and plot of $(\alpha h\nu)^{1/2}$ versus $h\nu$ (b) of as-deposited V_2O_5 HiPIMS thin films of 200 nm thickness with different $P(O_2)$.

3.2.3 Morphology

Figure 71 shows the SEM images of the V_2O_5 HiPIMS thin films deposited with different oxygen partial pressures. At a 2% oxygen partial pressure, the film shows very smooth and homogeneous surface. As the oxygen partial pressure increases, the surface of the thin film gradually shows some “asperities”. Nevertheless in comparison with previous V_2O_5 RF-metal (Figure 37) and V_2O_5 RF-oxide thin films (Figure 54), the surface of V_2O_5 HiPIMS films, at all different oxygen partial pressures, is much smoother.

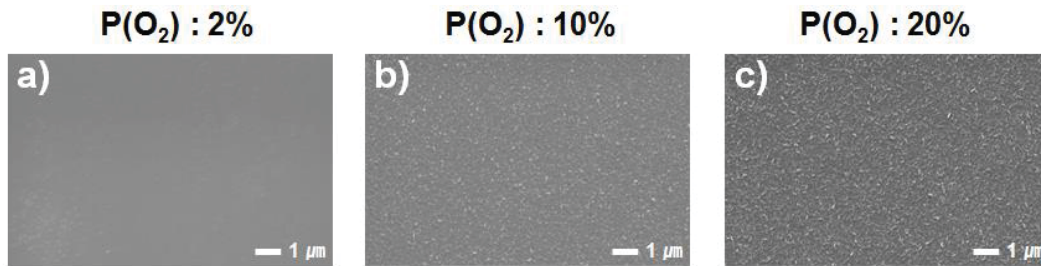


Figure 71. SEM images of surface of 200 nm V_2O_5 HiPIMS thin films deposited by $P(O_2)$ of (a) 2%, (b) 10% and (c) 20%.

3.2.4 Structural characterization

Figure 72 shows the grazing incidence X-ray diffraction pattern (incidence degree 0.5 degree) of V_2O_5 HiPIMS thin film according to oxygen partial pressures. No diffraction patterns are visible except the ITO peaks for the vanadium oxide thin films deposited under 2, 10 and 20% oxygen partial pressure. Whatever the oxygen partial pressure, all thin films are amorphous. This trend is different from the one observed on thin film of V_2O_5 RF-metal and V_2O_5 RF-oxide, in which the crystallinity increases as the oxygen content increases. In the literature, vanadium oxide films deposited by HiPIMS were reported to be amorphous when the substrate temperature was below 200 °C [238]. In our case, all vanadium oxide thin films are deposited without any heating or annealing of the substrate.

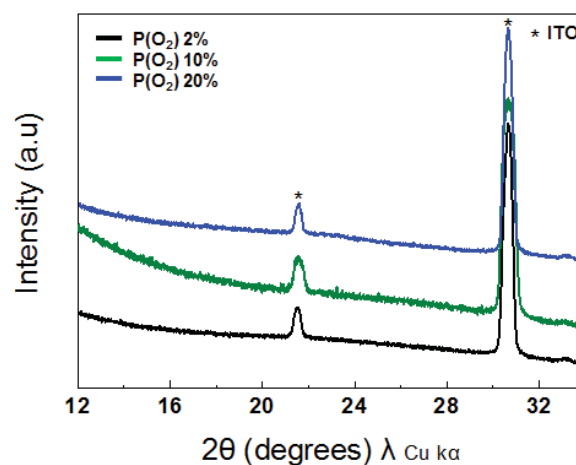


Figure 72. GIXRD pattern of 200 nm V_2O_5 HiPIMS thin films deposited under $P(O_2)$ of 2, 10 and 20%

3.2.5 Electrochemical properties

Figure 73 shows the cyclic voltammograms of 200 nm V_2O_5 HiPIMS thin films deposited under $P(O_2)$ 2, 10 and 20% cycled using a V_2O_5 /electrolyte/Pt vs SCE cell. The cycling was done at a fixed scan rate of 10 mV/s in the range of -1.0 to 1.0 V in LiTFSI-EMITFSI electrolyte. Whatever the oxygen partial pressure, the CV curves are characterized by a pair of redox peak located around 0 V in oxidation and -0.2 V in reduction. The peak in oxidation appear thinner and of higher intensity for the $P(O_2)$ 10%.

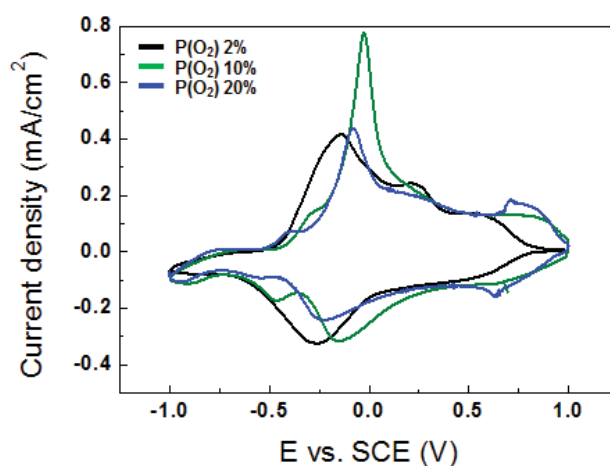


Figure 73. Cyclic voltammograms of 200 nm V_2O_5 HiPIMS films by deposited by $P(O_2)$ 2, 10 and 20% in LiTFSI-EMITFSI electrolyte after 20 cycles. The electrochemical chain is V_2O_5 /electrolyte/Pt vs SCE.

3.2.6 Optical properties

V_2O_5 HiPIMS thin films deposited under $P(O_2)$ 2%, 10%, and 20% are yellowish. The optical properties of the thin film were measured after cycling. Figure 74 shows *ex-situ* optical transmittance data under applied potential. In Li based electrolyte, films were gray/blue in the reduced state (-1 V) and orange in the oxidized state (+1 V). The difference in transmittance ΔT in between the gray color (-1 V) and the orange color (+1 V) measured at 650 nm are of 15%, 28% and 25%, for 2%, 10% and 20% oxygen partial pressure, respectively. Conclusively, V_2O_5 HiPIMS thin film deposited by $P(O_2)$ 10% shows the highest contrast ratio.

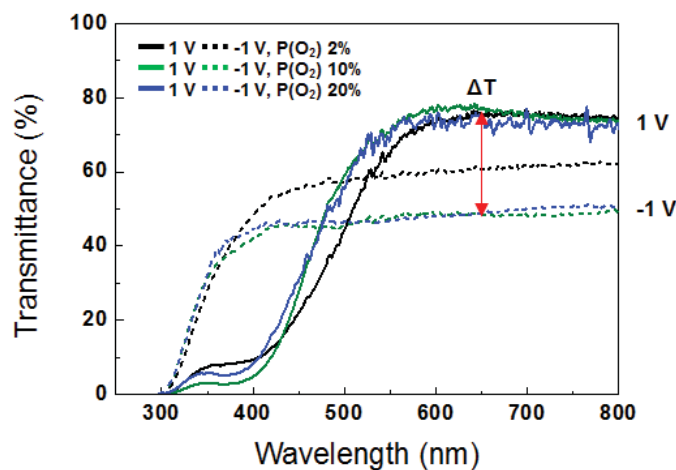


Figure 74. *Ex-situ* optical transmittance spectra of 200 nm V_2O_5 HiPIMS films deposited under $P(O_2)$ 2%, 10% and 20% in LiTFSI-EMITFSI electrolyte at -1 V to 1 V potential range after 20 cycles. The electrochemical chain is V_2O_5 /electrolyte/Pt vs SCE

3.2.7 Cycling stability

Figure 75 shows SEM images and cyclic voltammograms of V_2O_5 HiPIMS thin films deposited in 10% and 20% oxygen partial pressure in Li electrolyte after 250 cycles. Several cracks are observed on the film surface deposited at 20% oxygen partial pressure after 250 cycles. On the other hand, the surface of the thin film deposited at 10% maintains a smooth surface even after cycling. The better EC properties of $P(O_2)$ 10% thin films are confirmed looking at the cycling life. The decrease in capacity (i.e decrease in current density) observed for the $P(O_2)$ 20% thin film (Figure 75 d) is associated with a strong evolution of the film morphology (Figure 75 c).

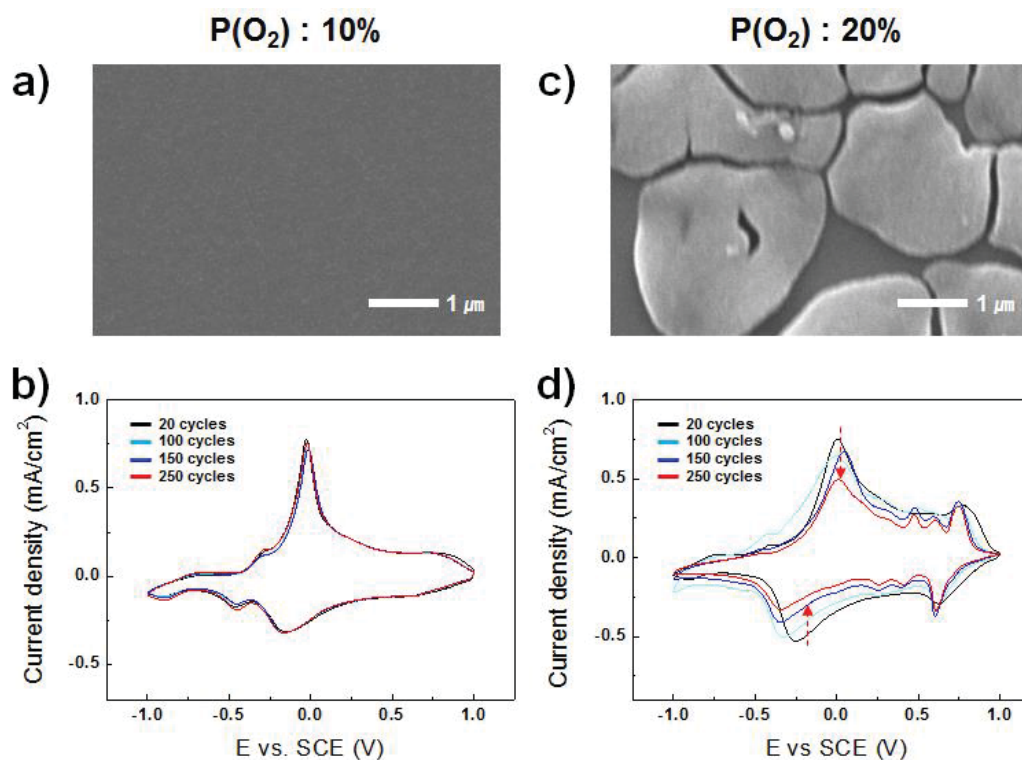


Figure 75. SEM image and cyclic voltammograms of 200nm V_2O_5 HiPIMS thin films deposited under 10% (a, c) and 20% (b, d) oxygen partial pressure in Li based electrolyte at -1 V to 1 V potential range after 250 cycles. The electrochemical chain is V_2O_5 /electrolyte/Pt vs SCE

From the above results, the thin film deposited at 45 μ s, 1200 Hz, total pressure of 2 Pa and $P(O_2)$ of 10% by HiPIMS with V metallic target showed amorphous V_2O_5 and showed better electrochromic properties and adhesion with substrate. Those films were chosen for conducting further experiments.

4. Electrochromic properties of V_2O_5 HiPIMS in Li and Na based electrolytes

4.1 V_2O_5 HiPIMS thin films

4.1.1 Thickness and morphology

We deposited thin films of various thicknesses using the previously selected optimized deposition conditions. Figure 76 shows the surface morphology and GIXRD pattern for each

thin film thickness. Previous thin films deposited by V_2O_5 RF-metal and V_2O_5 RF-oxide show fibrous texture of the needle or flake type grows on the surface as the thickness increases. On the other hand, the thin films deposited with HiPIMS show a smooth surface even though the thickness increases. We selected a 200 nm thick film for comparison with the previous thin films deposited by V_2O_5 RF-metal and V_2O_5 RF-oxide and studied the electrochromic characteristics.

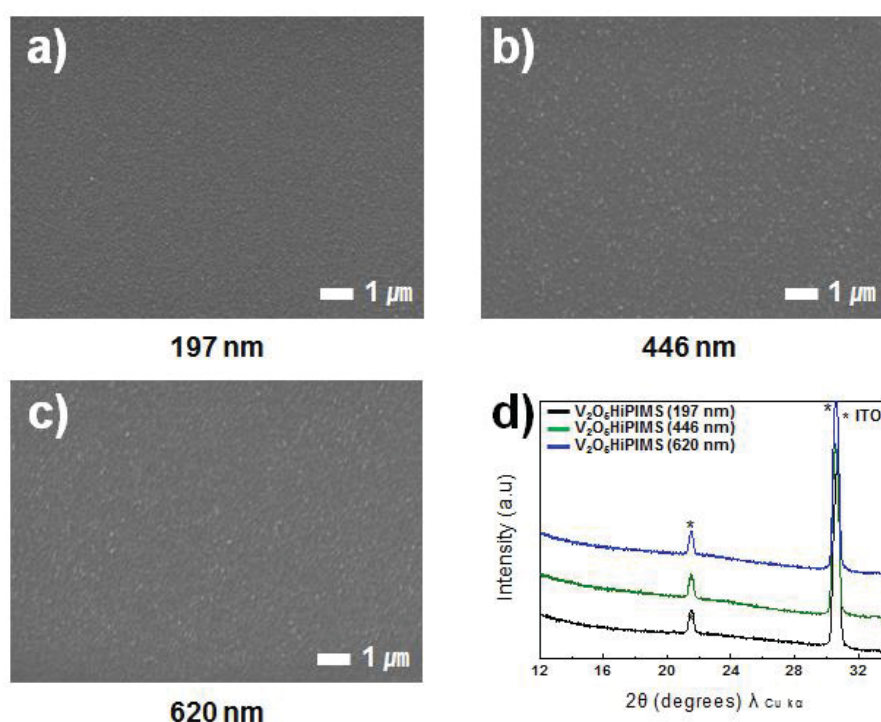


Figure 76. SEM images and GIXRD pattern for 197 nm (a, d), 446 nm (b, d) and 620 nm (c, d) of V_2O_5 HiPIMS thin films.

Figure 77 shows the deposition rate of V_2O_5 HiPIMS thin film compared with V_2O_5 RF-metal and V_2O_5 RF-oxide. The thickness of all thin films is 200 nm. The deposition rate of V_2O_5 HiPIMS is about twice smaller than that of V_2O_5 RF-metal and V_2O_5 RF-oxide. In the literature, a deposition rate reduction using HiPIMS has already been reported. In HiPIMS deposition of copper and titanium, the deposition rate was about 50% lower than that of DC sputtering [239]. HiPIMS rates are reduced to 15% for TiO_2 deposition and about 25% for Al_2O_3 and for ZrO_2 coatings [240]. One of the reasons for deposition rate reduction was the

decrease in the pulse length [241]. In addition, the deposition rates are closely related to sputtering yields, target surface conditions, and many other factors [242].

Hereafter, we evaluate the electrochromic properties using the 200 nm thickness V_2O_5 HiPIMS thin film for comparison with V_2O_5 RF-metal and V_2O_5 RF-oxide thin films.

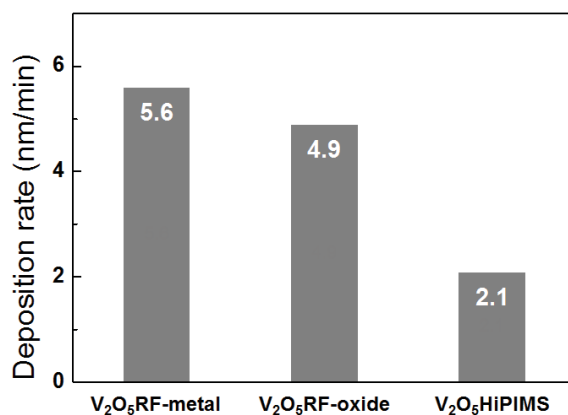


Figure 77. Deposition rate of V_2O_5 RF-metal, V_2O_5 RF-oxide and V_2O_5 HiPIMS. The thickness of all thin films is 200 nm.

4.1.2 Composition

EELS spectroscopy was carried out to characterize the 200 nm V_2O_5 HiPIMS thin film. Figure 78 (a) presents the observed energy loss spectra of the V_2O_5 HiPIMS thin film. It is seen that the characteristic edges of V shift significantly towards lower values comparison with V_2O_5 RF-metal and V_2O_5 RF-oxide thin films. The value of ΔE , which is the distance between the vanadium (VL_3) and oxygen (O_k) edges, was measured. Oxidation state of V_2O_5 HiPIMS can be derived directly from the position at this calibration line using VO_2 and V_2O_5 pure powder as demonstrated in figure 78 (b). V_2O_5 HiPIMS thin film shows oxidation state of +4.2. Table 16 summarizes the respective quantitative data on the chemical shift and the derived oxidation states for V_2O_5 RF-metal, V_2O_5 RF-oxide and V_2O_5 HiPIMS thin films.

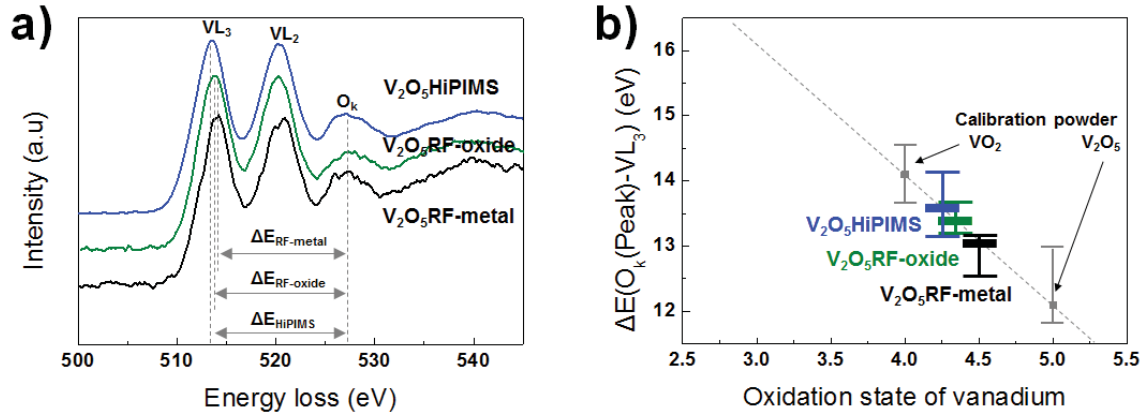


Figure 78. EELS (a) and quantitative determination of the V-oxidation state (b) of 200 nm V_2O_5 HiPIMS thin films.

Table 16. Quantitative determination of the V-oxidation state of 200 nm V_2O_5 HiPIMS thin films.

Sample	O_k Peak (eV)	VL_3 Peak (eV)	ΔE (O- VL_3) (eV)	V-oxidation state
V_2O_5 Powder	526.7	514.4	12.3	5
VO_2 Powder	527.9	513.4	14.5	4
V_2O_5 HiPIMS	527.1	513.4	13.6	4.2 ± 0.2
V_2O_5 RF-oxide	527.1	513.6	13.5	4.3 ± 0.2
V_2O_5 RF-metal	527.2	514.1	13.1	4.5 ± 0.2

Elemental composition analyses of the films were carried out using RBS (Rutherford backscattering spectroscopy) / NRA (Nuclear reaction analysis) analyses. Analysis was carried on AIFIRA facility (CENBG, France). Unfortunately due to experimental limitation, thicker films than 200 nm had to be tested, The 400 nm V_2O_5 HiPIMS thin films deposited on ITO substrates were analyzed. The concentration of V and O found by RBS/NRA was 28.4 at% and 71.6 at% on ITO. Table 17 summarizes the respective quantitative data of V_2O_5 HiPIMS thin films.

Table 17. V₂O₅HiPIMS thin films (400 nm) and oxygen to vanadium atomic ratio.

Thickness	Atomic %		Stoichiometry V _x O _y
	V	O	
400 nm	28.4	71.6	V _{1.98} O ₅

Hereafter, we evaluate the electrochromic properties using the 200 nm thickness V₂O₅HiPIMS thin film for comparison with V₂O₅RF-metal and V₂O₅RF-oxide thin films.

4.2 Electrochromic properties

4.2.1 Electrochemical and optical properties

V₂O₅HiPIMS thin films of 200 nm thickness were electrochemically and optically characterized using V₂O₅/electrolyte/Pt vs SCE. Figure 79 (a) and (c) show the 20th typical cyclic voltammograms in Li(LiTFSI-EMITFSI) and Na(NaTFSI-EMIFTSI) based electrolytes, respectively with a sweep rate of 10 mV/s. In Li electrolyte, cyclic voltammogram exhibits one pair of reversible peaks of higher intensity in oxidation. The CV curve in Na electrolyte shows in very first approximation a similar shape with however, a much lower peak intensity than in Li. The V₂O₅HiPIMS film, initially yellow, goes through distinct color changes as green at 0.2 V, blue at -0.4 V and gray at -1 V upon reduction/oxidation. The orange color is recovered at the end of the oxidation. The reversible electrochromism with 4 color states was demonstrated for both electrolytes. Figure 79 (c) and (d) show *ex-situ* optical transmittance data under applied potential. In Li electrolyte, transmittance modulation ΔT of 36% at 420 nm and 29% at 650 nm are determined between reduced gray state (-1 V) and the oxidized orange state (+1 V). In Na electrolyte, the transmittance modulation ΔT are 44% and 25% at 420 nm and 650 nm respectively (Table 17). The absorption edge is shifted to lower wavelength in reduction for both electrolytes. In conclusion, V₂O₅HiPIMS thin films exhibit reversible multi-color electrochromic characteristics under applied voltage in Li and Na electrolytes. The similarity in the value of difference in transmittance ΔT and current density in Na electrolyte and Li electrolyte is a similar phenomenon than observed for amorphous V₂O₅RF-oxide thin films, but different

phenomenon with crystalline V_2O_5 RF-metal thin films.

As a result, the amorphous thin films deposited by V_2O_5 HiPIMS and V_2O_5 RF-oxide show better electrochromic properties in not only Li ions but also Na ions than crystalline V_2O_5 RF-metal thin films. This remark is limited to the initial stage of cycling. It is noteworthy that the thin films deposited by HiPIMS show larger capacities than films deposited by RFMS. This is probably due to the fact that the films deposited by HiPIMS have a higher density than the films deposited by RFMS [231, 234, 235].

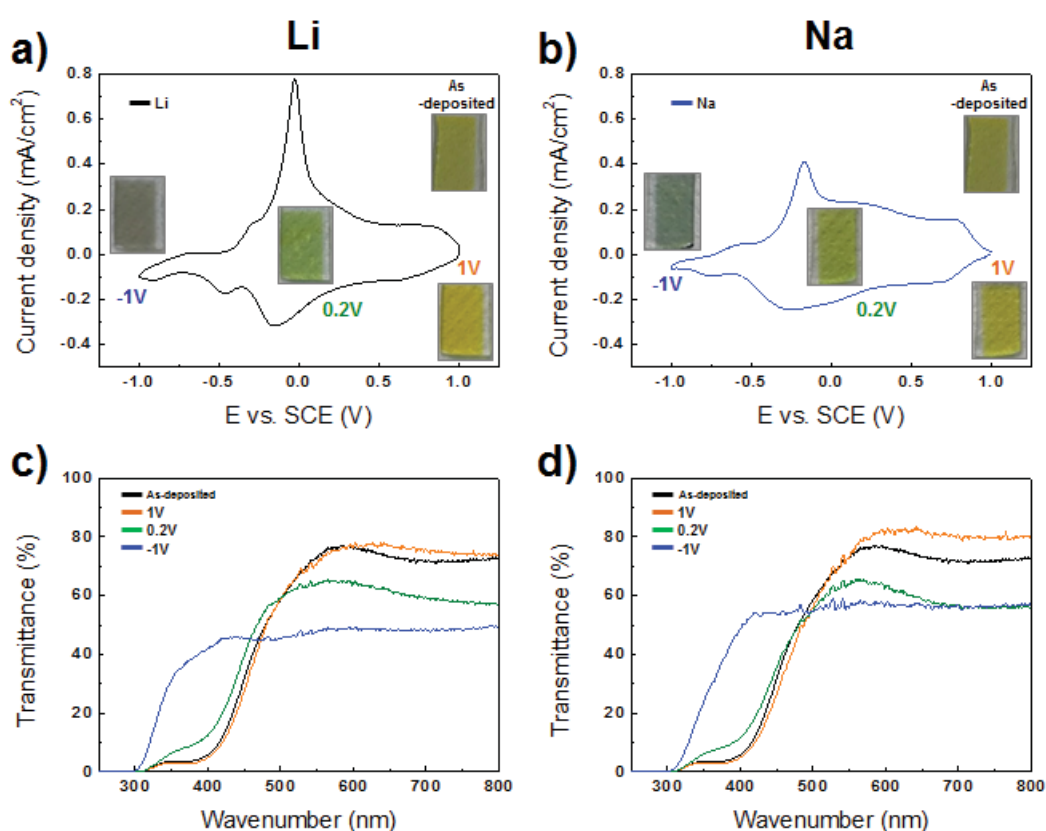


Figure 79. Cyclic voltammograms and *ex-situ* optical transmittance spectra of 200 nm V_2O_5 HiPIMS thin films in Li (a, c) and Na (b, d) based electrolyte after 20 cycles. The electrochemical chain is V_2O_5 /electrolyte/Pt vs SCE.

Table 17 summarizes the coloration efficiency of the films in two wavelengths corresponding to 420 nm and 650 nm, exhibiting value of $22.6 \text{ cm}^2/\text{C}$ and $6.9 \text{ cm}^2/\text{C}$ in Li electrolyte. In Na electrolyte, the coloration efficiency of the films exhibit value of $26.9 \text{ cm}^2/\text{C}$ and $5.9 \text{ cm}^2/\text{C}$.

Table 17. Coloration efficiency, transmittance variation ΔT , and optical density ΔOD of 200 nm V_2O_5 HiPIMS thin films in Li and Na based electrolyte.

Electrolyte	Charge density (mC/cm ²)	$\lambda = 420\text{nm}$			$\lambda = 650\text{nm}$		
		ΔT	ΔOD	CE(cm ² /C)	ΔT	ΔOD	CE(cm ² /C)
Li	29.3	36	0.66	22.6	29	0.20	6.9
Na	27.2	44	0.73	26.9	25	0.16	5.9

4.3 Durability

Cyclic voltammetry (CV) measurements were performed with a scan rate of 10 mV/s at potential range of -1 V to +1 V over 1000 cycles in Li and Na electrolytes. The cyclic voltammograms show that the V_2O_5 HiPIMS thin films possessed sustainability during cycling (Figure 80). Thin film show good cycling stability until 1000 cycles in both electrolytes, while slight CV shape modification appears after 500 cycles in both electrolytes. Figure 80 (c) shows steady trend of the evolution of the coulombic capacity of the V_2O_5 HiPIMS thin films upon cycling. Figure 80 (d) shows that the capacity trend remains constant as increasing cycles. After 1000 cycles, the capacity of thin film is 112 % in Li and 106 % in Na of the capacity in first few 20 cycles. The cyclic voltammograms and coulombic capacity upon cycling of the V_2O_5 HiPIMS thin films show very less modification or deterioration in comparison with films by V_2O_5 RF-metal (Figures 47, 48, p 78) and V_2O_5 RF-oxide (Figures 61, 61, p 84).

Related to this result, SEM images show surface of V_2O_5 HiPIMS thin film in Li and Na after cycles (Figure 81). Cracks are observed on the thin film surface after 1000 cycles in Li electrolyte. In the Na electrolyte, dilatation occurs on the thin film surface after 1000 cycles. This is a very different phenomenon than previous observed for V_2O_5 RF-metal and V_2O_5 RF-oxide films exhibiting visible cracks and severe deterioration after 100 cycles or 250 cycles.

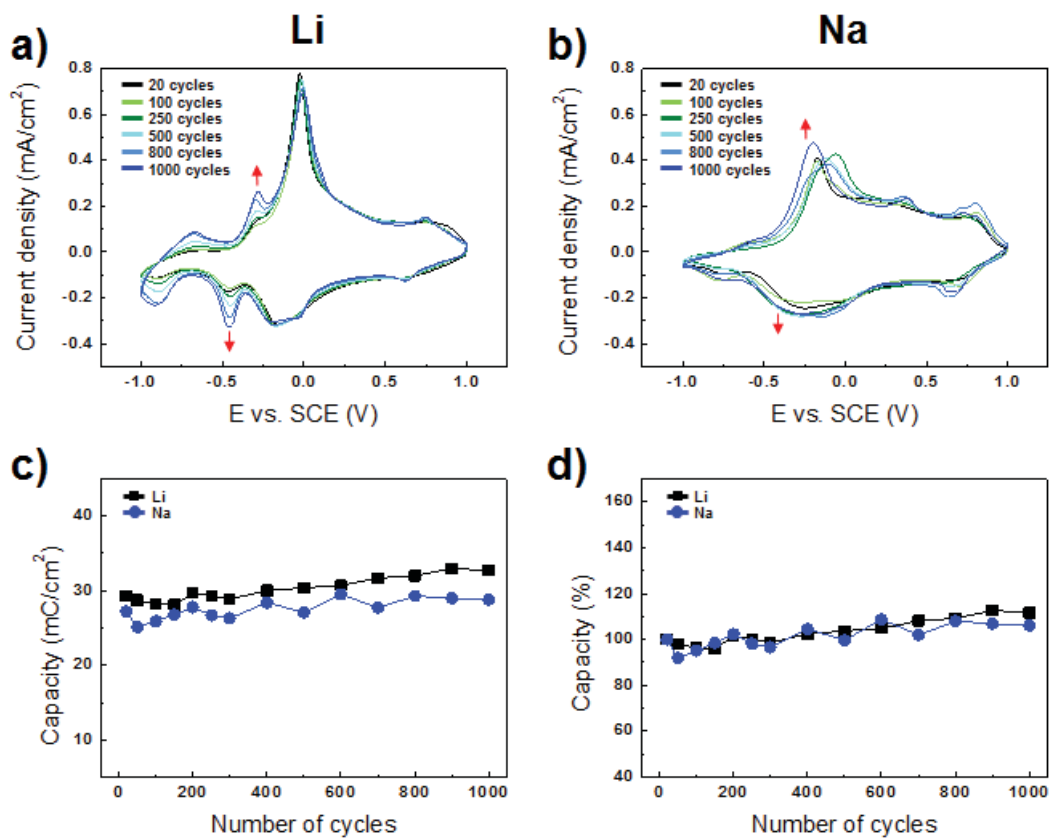


Figure 80. Cyclic voltammograms, evolution of the capacity versus the number of cycles of 200 nm V_2O_5 /HiPIMS in Li (a, c, d) and Na (b, c, d) electrolyte until 1000 cycles. The electrochemical chain is V_2O_5 /electrolyte/Pt vs SCE

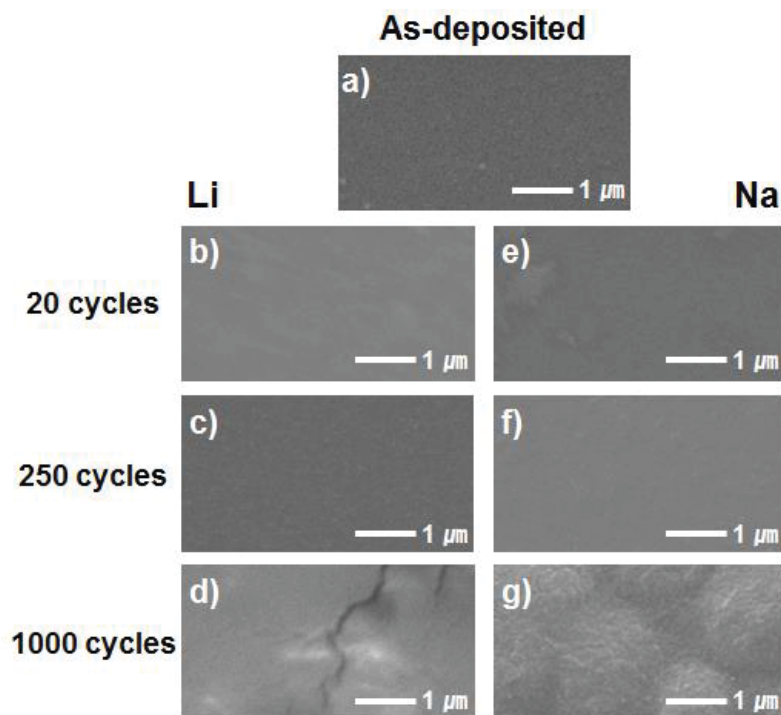


Figure 81. SEM images of 200 nm V_2O_5 HiPIMS in Li (b, c, d) and Na (e, f, g) based electrolyte after 20, 250 and 1000 cycles.

4.4 Switching time

Chronoamperograms of 200 nm V_2O_5 HiPIMS films were recorded applying voltage in reduction of -1 V and in oxidation of +1 V with a pulse duration of 40 s in Li and Na electrolytes (Figure 82). As previously observed, insertion reaction was faster than the deinsertion in both electrolytes and the switching times in Na are shorter than in Li. A comparison of the values show however that amorphous V_2O_5 HiPIMS film exhibit faster switching time than the crystalline V_2O_5 RF-metal film particularly, in Li electrolyte and higher than the one of amorphous V_2O_5 RF-oxide film (Table 18).

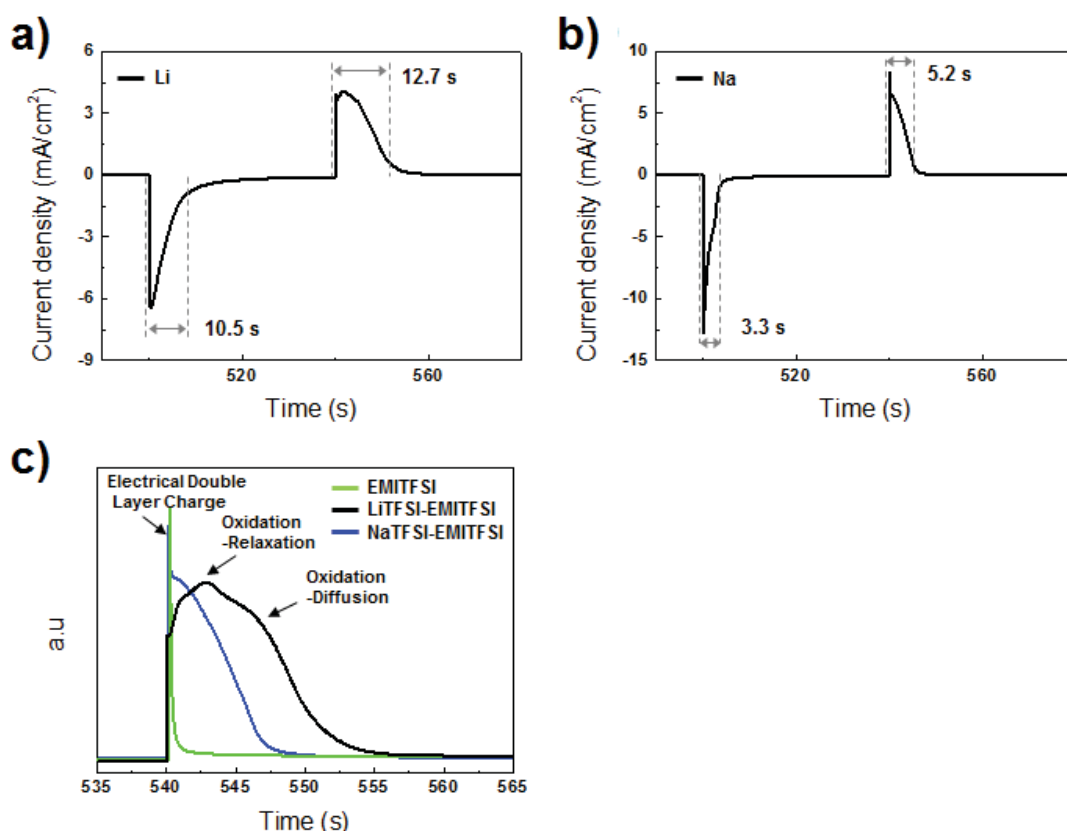


Figure 82. Chronoamperograms of 200 nm V_2O_5 HiPIMS thin films in Li (a) and Na (b) based electrolyte after 20 cycles. The electrochemical chain is V_2O_5 /electrolyte/Pt vs SCE.

Table 18. Switching time of 200 nm V₂O₅RF-metal, V₂O₅RF-oxide and V₂O₅HiPIMS thin films in Li and Na based electrolytes.

Switching time (s)						
Electrolyte	V ₂ O ₅ RF-metal		V ₂ O ₅ RF-oxide		V ₂ O ₅ HiPIMS	
	Reduction	Oxidation	Reduction	Oxidation	Reduction	Oxidation
Li	13.0	16.8	4.4	8	10.5	12.7
Na	2.5	4.5	2.3	5.8	3.3	5.2

Table 19. Summary of electrochromic properties of 200 nm V₂O₅RF-metal, V₂O₅RF-oxide and V₂O₅HiPIMS thin films in Li and Na based electrolytes.

◎ : Good ○ : Average ● : Poor

		V ₂ O ₅ RF-metal	V ₂ O ₅ RF-oxide	V ₂ O ₅ HiPIMS
Morphology		Disturbed		Smooth
Structure		Orthorhombic		Amorphous
Li	Capacity	○	◎	◎
	CE	◎	○	○
	Durability	○	●	◎
Na	Capacity	●	◎	◎
	CE	○	○	○
	Durability	◎	○	◎

The amorphous V₂O₅HiPIMS film also shows CA curves of Li and Na electrolytes similar to the crystalline V₂O₅RF-metal film and amorphous V₂O₅RF-oxide film, which are considered to be due to capacitive and faradic components characteristics in Li and Na based electrolytes. More details of behavior for capacitive and faradic components will be discussed in Part C (chapter 1).

Conclusion

Vanadium oxide thin films were deposited on ITO coated glass substrate at room temperature using three different deposition conditions, namely radio frequency magnetron sputtering (RFMS) with V metallic target (V_2O_5 RF-metal) or V_2O_5 oxide target (V_2O_5 RF-oxide) and High Power Impulse Magnetron Sputtering (HiPIMS) with V metallic target (V_2O_5 HiPIMS), respectively. Significant difference in structure and morphologies are reported. V_2O_5 RF-metal films are crystalline and dense with a disturbed surface which is thickness dependent, while V_2O_5 RF-oxide and V_2O_5 HiPIMS films are amorphous and porous or dense respectively. V_2O_5 thin films show reversible electrochromism with 4 colors, which are orange, green, blue and gray, in reduction/oxidation states when cycled in Li and Na based electrolytes. However, depending on the deposition method, V_2O_5 films show different cycling stability, recorded up to 1000 cycles, that is attributed to a modification of the morphology (i.e. increase of the surface area due to cracks and increase porosity).

As a result, V_2O_5 thin film deposited by HiPIMS shows higher EC performance than the one deposited by RFMS, linked to a stronger adhesion to the substrate, a smooth and dense morphology and an amorphous structure.

PART C : ELECTROCHROMIC MECHANISM

In this part, a deeper investigation of the EC mechanism taking place in V_2O_5 thin films was carried out. In chapter 1, initial comparisons in between the three different types of films, namely V_2O_5 RF-metal, V_2O_5 RF-oxide and V_2O_5 HiPIMS, will be discussed in terms of faradic to capacitive contributions. In the second chapter, focusing on the V_2O_5 RF-metal, several characterizations including, XRD, XPS, TOFSIMS, AES and RBS/NRA will be combined.

Chapter 1. Comparison of the EC behavior of V₂O₅ thin films : capacitive to faradic contributions

Recent investigation in the group on EC mechanisms taking place in oxides showed us that considering a simple insertion mechanism was not sufficient. Indeed Mathias Da Rocha, characterizing the electrochromic behavior of sputtered Ni_{1-x}O thin films reported an EC mechanism associating both faradic and capacitive contributions [243]. A close observation of the various CVs recorded from cycling V₂O₅ films in Li and Na based electrolytes, as described in the previous chapter, concluded on a much more complex CV shape than a well-resolved double peak usually reported for well-crystallized V₂O₅ films. This observation raised the question of what would be the part of capacitive and faradic contributions and would the EC mechanism in V₂O₅ better described as pseudo-capacitance, corresponding to a faradaic process involving surface or near surface redox reactions. The distinction between the faradaic and capacitive contributions in battery or electrochromic systems, has been recently discussed for different materials including TiO₂ [244, 245] and WO₃ [246]. Indeed, the current (*i*) at a fixed potential (*V*) can be quantitatively separated into a diffusion contribution and a capacitive contribution as shown by the following equation:

$$i(V) = k_1 v + k_2 v^{1/2} \quad (19)$$

For analytical purposes, this equation is slightly rearranged to

$$i(V)/v^{1/2} = k_1 v^{1/2} + k_2 \quad (20)$$

In eq 18, $k_1 v$ and $k_2 v^{1/2}$ correspond to the current contributions from the surface capacitive phenomena and the diffusion-controlled insertion process, respectively. Thus the determination of k_1 and k_2 , allows, at specific potentials, one to quantify the fraction of the current due to each of the two contributions.

To characterize the contribution of capacitive and faradic reaction, cyclic voltammetry at different scan rates from 2 to 50 mV/s were carried out. Figure 83 shows cyclic voltammograms of different scan rates of 200 nm V₂O₅RF-metal thin film in LiTFSI-EMITFSI in the potential range between -1 V and 1 V after 20 cycles. For the scan rate of 2

and 50 mV/s, the curve $i = k_1v = f(V)$ (black curve), corresponding to the capacitive contribution and the blue curve corresponding to the experimental curve are plotted $i = k_1v + k_2v^{1/2} = f(V)$. A large part of the current is attributed to surface phenomena and those despite a slow scan rate of 2 mV/s (Figure 83 b), usually favoring insertion phenomena. Indeed, the low scan rate is illustrated by well defined peaks. Figure 83 (c) shows that at a scan rate of 50 mV/s the current is mainly associated with surface phenomena.

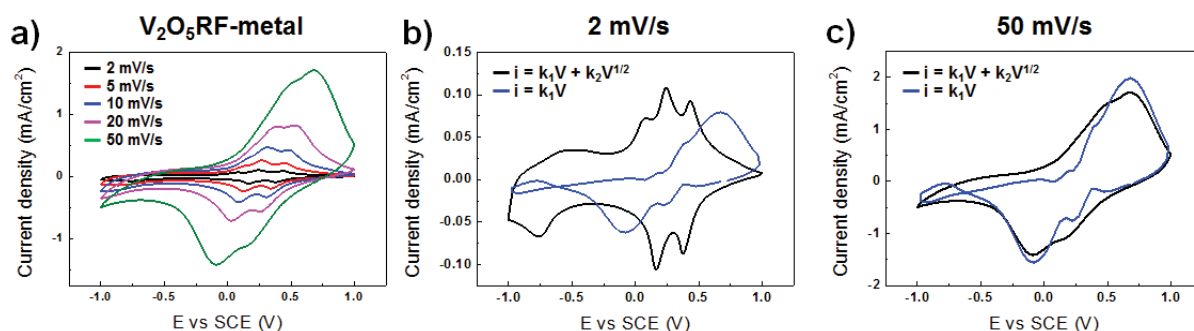


Figure 83. Cyclic voltammograms (a) of 200 nm V_2O_5RF -metal thin film / LiTFSI EMITFSI / Pt vs SCE as a function of the scan rate from 2 to 50 mV/s and in a potential range -1 V / 1 V. Calculated curves $i = k_1v$ (black) and experimental (blue) for V_2O_5RF -metal thin film at scan rate of 2 mV/s (b) and 50 mV/s (c).

Figure 84 shows the evolution of the capacitive and faradic contributions of 200 nm V_2O_5RF -metal thin films as a function of the scan rate in Li based electrolyte. At the slow scan rate, the current is associated with a slightly higher faradic contribution. At fast scan rate over 10 mV/s, the current is essentially associated with a capacitive contribution as high as 77 % for the 50 mV/s scan rate.

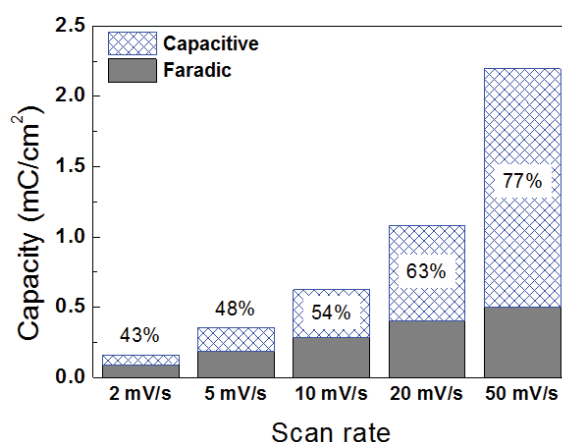


Figure 84. Evolution of the capacitive and faradic contributions of 200 nm V_2O_5RF -metal thin film /

LiTFSI/EMITFSI / Pt vs SCE as a function of the scan rate from 2 to 50 mV/s and in a potential range -1 V / 1 V.

In order to evaluate the influence on the capacitive to faradic contributions of the V_2O_5 thin films characteristics in terms of crystallinity and morphology, cyclic voltammetry of 200 nm V_2O_5 RF-metal, V_2O_5 RF-oxide and V_2O_5 HiPIMS thin films were performed at different scan rates from 2 to 50 mV/s in LiTFSI-EMITFSI in the potential range between -1 V and 1 V. Figure 85 shows the 20th cycles. The capacitive contribution increases with increasing scan rates in all films. The higher faradic contribution observed for V_2O_5 RF-metal thin film as compared to the others well agree with its higher crystallinity. At 2 mV, it decreases from 57 % to 30-35 % for amorphous V_2O_5 RF-oxide and V_2O_5 HiPIMS films while at 50 mV/s it is only of 23 % (V_2O_5 RF-metal) down to about 10 % (V_2O_5 RF-oxide and V_2O_5 HiPIMS). As an interesting observation, despite very different morphologies, V_2O_5 RF-oxide and V_2O_5 HiPIMS thin films show similar capacitive and faradic contributions.

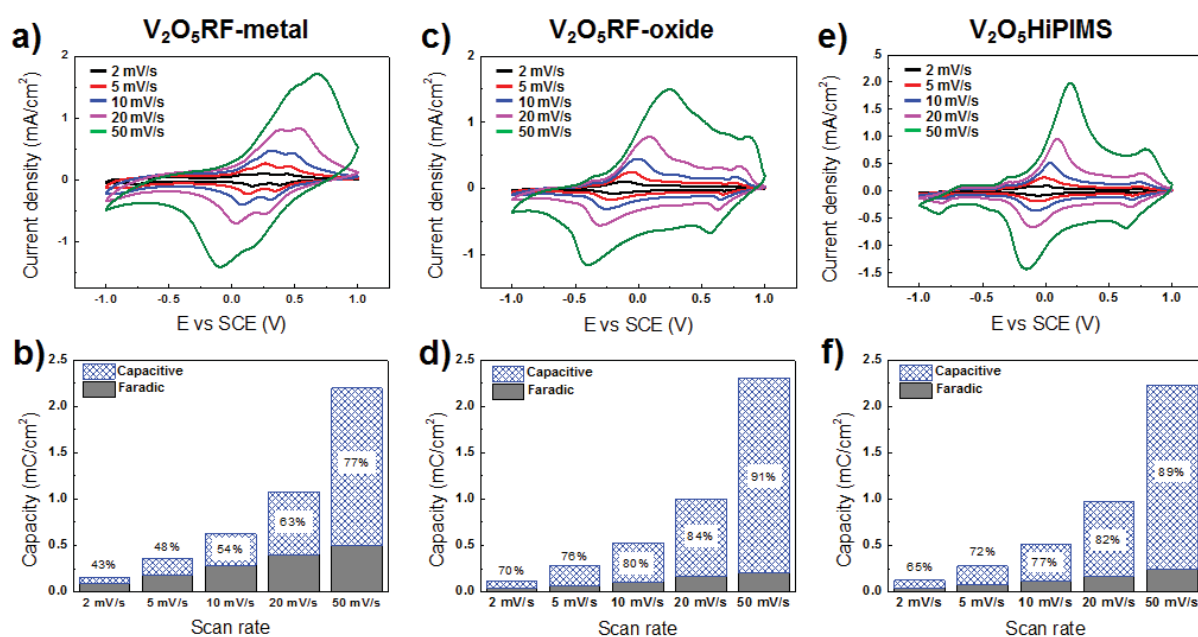


Figure 85. Cyclic voltammograms and evolution of the capacitive and faradic contributions of 200 nm V_2O_5 RF-metal (a, b), V_2O_5 RF-oxide (c, d) and V_2O_5 HiPIMS (e, f) thin film / LiTFSI-EMITFSI / Pt vs SCE as a function of the scan rate from 2 to 50 mV/s and in a potential range -1 V / 1 V.

The trends observed in lithium based electrolyte were confirmed in Na electrolyte. In a similar method, to characterize the contribution of capacitive and faradic reaction of V_2O_5 thin films in Na based electrolyte, cyclic voltammetry of 200 nm V_2O_5 RF-metal, V_2O_5 RF-oxide and V_2O_5 HiPIMS thin films was performed at different scan rates from 2 to 50 mV/s in NaTFSI-EMITFSI in the potential range between -1 V and 1 V. Figure 86 shows the 20th cycles. In all films, capacitive contribution increases with increasing scan rate reaching for all films values of about 90 %. Indeed from a general point of view, the difference in the CV shapes for cycles in Na electrolytes are much less than in Li electrolytes. However, it is worth mentioning the higher intensity for V_2O_5 RF-metal films (Figure 86 a, b). The proportion of capacitive and faradic contribution in Na electrolyte was similar in the three V_2O_5 thin films contrary to Li electrolyte. The capacitive and faradic contributions of V_2O_5 RF-oxide and V_2O_5 HiPIMS thin films in Na electrolyte were similar to Li at all scan rate. On the other hand, the capacitive contribution of V_2O_5 RF-metal thin film in Na electrolyte compared to Li was larger. This result is the same as the previous results of electrochemical response in non-ions , Na and Li electrolytes of V_2O_5 RF-metal thin film (Figure 49 (c)). Non-ions and Na electrolytes exhibit very fast switching time due to higher capacitive components, while Li based electrolytes exhibit slow switching time due to faradic components.

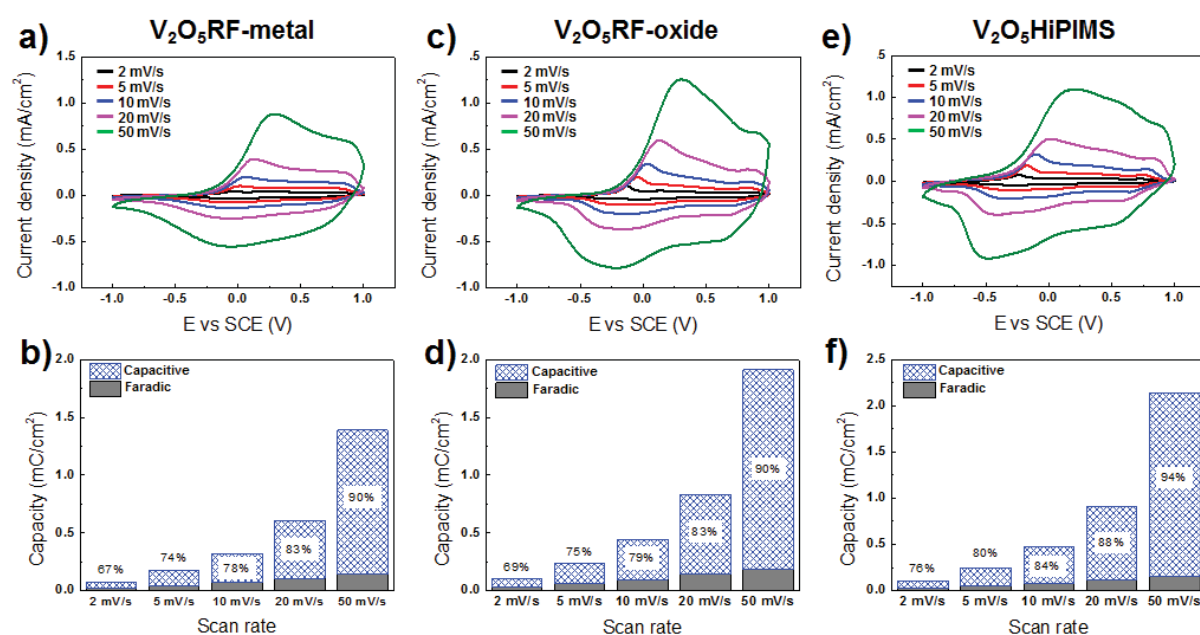


Figure 86. Cyclic voltammograms and Evolution of the capacitive and faradic contributions of 200 nm V_2O_5 RF-metal (a, b), V_2O_5 RF-oxide (c, d) and V_2O_5 HiPIMS (e, f) thin film / NaTFSI-EMITFSI / Pt vs SCE as a function

of the scan rate from 2 to 50 mV/s and in a potential range -1 V / 1 V.

To complete our approach of the mechanism required to correlate the electrochemical observations to techniques of characterization, The limited time of the thesis did not allow us to perform characterizations on all films. In respect of their EC performances, V₂O₅RF-metal thin films were chosen. Their characterization upon cycling using tools, “commonly” available in the laboratory such as X-ray diffraction or in collaboration for what we could described as more sophisticated, X-ray Photoelectron Spectroscopy, TOFSIMS, Rutherford Back Scattering were carried out. This study is detailed in the following chapter.

Chapter 2. EC mechanism in V₂O₅RF-Metal thin films

Cyclic Voltammetry Behavior

As a reminder of the cycling behavior of V₂O₅RF-metal films in Li and Na based electrolyte the 20th cycle in three electrodes cell is recalled in figure 46 (a) and (b).

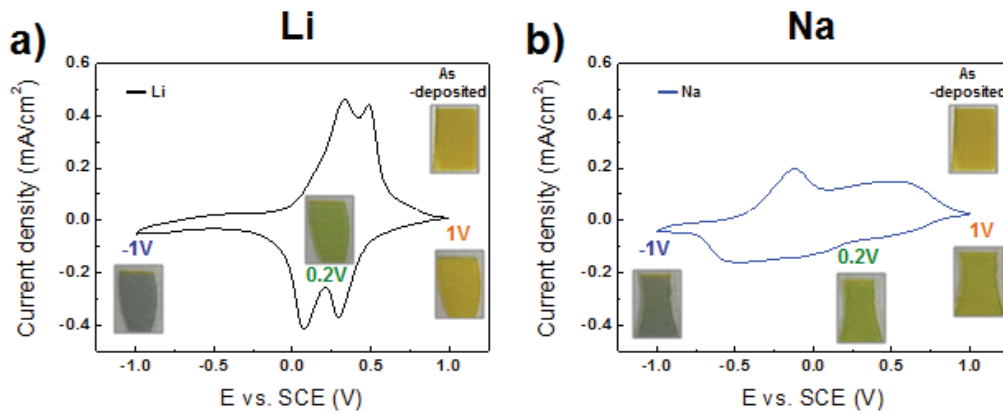
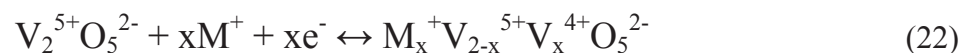


Figure 46. Cyclic voltammograms of V₂O₅RF-metal thin films in Li (a) and Na (b) based electrolytes after 20 cycles. V₂O₅/electrolyte/Pt vs SCE chain is cycled with a scan rate of 10 mV/s.

From the CV curve the number of electrons exchanged (NEE) can be easily calculated using the following formula (equation 21):

$$NEE = \frac{Q \cdot M}{F \cdot \rho \cdot e} \quad (21)$$

Q is the capacity (0.023 C/cm²), M is molar mass of V₂O₅ (181.88 g/mol), F is Faraday's constant (96485 C/mol), ρ is the density of V₂O₅ (3.36 g/cm³), e is the thickness of the cycled film (200 nm). For the calculation, 75% of the density has been arbitrarily considered. Assuming initially an insertion/deinsertion mechanism, the number of electrons exchanged is equal to the number of Li⁺/(equal to the number of V⁴⁺) following the equation : .



The various x values, from 1V to +0.2 V (Green state) and from 1 V to -1 V (Blue state) are gathered in Table 20. x increases from 0.35 to 0.84 in Li electrolyte and from 0.17 to 0.65 in Na based electrolyte. As expected from the lower capacity in Na based electrolyte, the x values remain smaller with a value lower than one whatever the nature of the electrolyte cations suggesting that at most one V⁵⁺ will be fully reduced to V⁴⁺.

Table 20. The x value at Li and Na insertion states of as-deposited 200 nm V₂O₅RF-metal thin film at the applied voltage at 0.2 and -1 V in Li, NaTFSI-EMITFSI after 20 cycles.

Electrolyte (ions)	0.2 V (insertion)		-1 V (insertion)	
	color	x (Mx)	color	x (Mx)
Li		0.35		0.84
Na		0.17		0.65

1. Structural modification upon cycling by XRD

One way to follow *ex-situ* the structural behavior of the film upon cycling was to run XRD after stopping the CV at 0.2 V, -1 V and in re-oxidation at 1 V. Cycled V₂O₅ films were washed with ethanol prior to XRD measurements. Such *ex-situ* experiments were possible due to the property of V₂O₅ film to retain the colour at least for several hours. This so-called memory effect (i/e. ability of the material to retain the color after the potential is being cut) was indeed confirmed in our group making similar characterizations on V₂O₅ thick films [247]. No change in the optical properties (i.e; chromaticity parameters) was observed after 30 days in the green and blue states while no potential was being applied.

Figure 87 (a), (b) presents the XRD patterns of the 200 nm V₂O₅RF-metal thin film in the as-deposited state, reduced at 0.2 V and -1 V and after oxidation at 1 V in Li and NaTFSI-EMITFSI after 20 cycles, respectively. XRD pattern of as-deposited V₂O₅RF-metal thin film show (001) and (200) orientation of V₂O₅ orthorombic structure (S.G : Pmmn, JCPDS 41-1426). From the position of the (001) peak located at 19.93° (2θ), we calculate a c cell

parameter of 4.45 Å corresponding to the interlayer distance. As later discussed in figure 91, this value is slightly higher than the values reported in the literature for DC sputtered ($c = 4.42$ Å) and electrodeposited ($c = 4.38$ Å) films.

In Li electrolyte (Figure 87 a), upon reduction the (001) peak shifts progressively to lower angles, namely to 18.89° (0.2 V) and to 18.49° (-1 V) while it returns to 19.78° (+1V) upon oxidation. In the mean time the (200) completely disappears. The shifts correspond to an increase in the c parameter to 4.70 Å. (+0.2 V) and 4.78 Å. (-1.0 V). Those values are consistent with the reported ones [248, 249, 250]. If the film retains the orthorhombic structure after 20 redox cycles, in each colored state in first approximation, the lower XRD peak intensity of the 0.2 V suggests a decrease in crystallinity for this specific state. The reason for this difference in crystallinity is not yet understood but it was observed for all films. In addition, the slight difference in the (001) peak position between the as-deposited state and the oxidized one may illustrate a small irreversibility corresponding to a small amount of trapped lithium ions. Among the defects sites where this is expected to occur, grain boundaries are likely the best candidates. It is interesting to note that the intensity of (001) peak decreases during cycling, indicating the crystalline structure of the film gets more disordered during cycling [251].

In Na electrolyte (Figure 87 b), in first approximation, one can consider the evolution of the XRD pattern as summarized in the shift of the (001) peak to lower angle to 18.74° (0.2 V), and to lower angle to 18.52° -1 V. The shifts correspond to an increase in the c parameter to 4.70 Å (+0.2 V) and 4.78 Å (-1.0 V). The significant discrepancy with cycling in Na based electrolyte comes from the presence of irreversibility illustrated by the position of the (001) peak at 18.90° (1 V) lower than the one in the deposited state. However, the evolution appears more complex as the XRD peak can be deconvoluted in two peaks as shown in figure 88 (b). One of the peak located at 19.93° and corresponding to the (001) of the as-deposited state does not move but appears to decrease in intensity while a second peak appear in the cycled film.

Table 21 gathers the x values calculated from the electrochemical measurements and from the change in the lattice parameters c during cycling of 200 nm V_2O_5 RF-metal thin film in Na based electrolyte. Upon insertion of Na ions, the interlayer spacing c increases from 4.45 Å (as-deposited) to 4.73 Å ($x=0.17$ (0.2 V)) and 4.79 Å ($x=0.65$ (-1 V)). Upon oxidation, c

decreases to 4.69 Å (1 V). After oxidation (1 V), the most intense peak does not go back to the initial position but the XRD pattern still consists of two peaks, an intense peak located at 18.89° and a broad one at 19.92° such as in as-deposited film. Such behavior may be interpreted as an insertion/deinsertion mechanism taking place in some part of the films and not in the full thickness of it while some V₂O₅ films remains unchanged upon cycling. Any how, as the main peak does not return to the initial value, we can reasonably assume some irreversibility phenomenon correlated with trapped Na ions in V₂O₅ film during cycling. This trend well agrees with the larger size of Na⁺ as compared to Li⁺ ($r_{Li^+} + 0.74 \text{ \AA} < r_{Na^+} + 1.02 \text{ \AA}$).

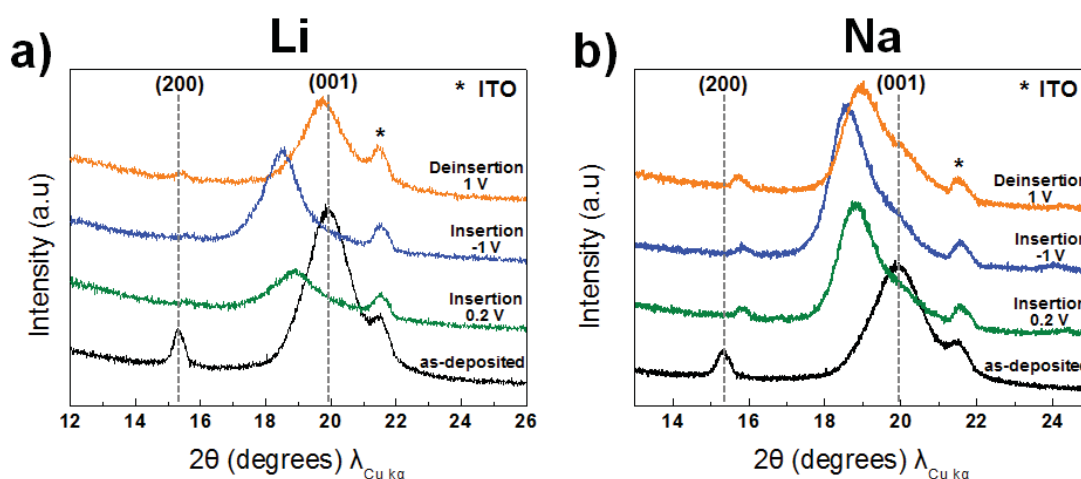


Figure 87. XRD patterns of as-deposited 200 nm V₂O₅RF-metal thin film and Li (a) and Na (b) at the applied voltage at 0.2, -1 V and 1 V in Li, NaTFSI-EMITFSI after 20 cycles.

Table 21. Li and Na insertion coefficient x and interlayer spacing of as-deposited 200 nm V₂O₅RF-metal thin film and Li (a) and Na (b) at the applied voltage at 0.2, -1 V and 1 V in Li, NaTFSI-EMITFSI after 20 cycles.

As-deposited V ₂ O ₅ RF-metal		Electrolyte (ions)	0.2 V (insertion)			-1 V (insertion)			1 V (deinsertion)	
color	c		color	c	x (Mx)	color	c	x (Mx)	Color	c
	4.45 Å	Li		4.70 Å	0.35		4.78 Å	0.84		4.49 Å
		Na		4.73 Å	0.17		4.79 Å	0.65		4.69 Å

In Na medium, the initial (001) peak may be indeed further splitted in two peaks of each area was calculated (Figure 88). The peak A is originated from as-deposited film, and the peak B is shifted according to Na insertion. The peak A shows a portion of 26% at 0.2 V ($x=0.17$), 28% at -1 V ($x=0.65$) and 32% at 1 V, respectively. As a result, it can be seen that the Na insertion/deinsertion reaction takes place in some (approximately 70%) but not all of V_2O_5 thin film. We assume that Na ions being larger than Li ions it will be therefore more difficult to insert into the V_2O_5 film during cycling. Such behavior well agrees with a mechanism more complex than a simple insertion/deinsertion.

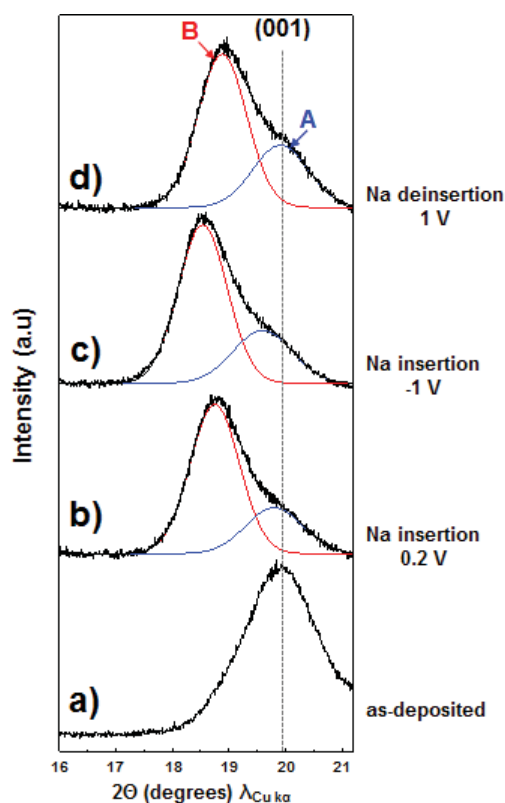


Figure 88. XRD patterns of as-deposited (a) 200 nm V_2O_5 /RF-metal thin film in NaTFSI-EMITFSI at the applied voltage at 0.2 (b), -1 V (c) and 1 V (d) after 20 cycles.

Figure 89 shows the evolution of the interlayer spacing (crystallographic c parameter) of as-deposited 200 nm V_2O_5 /RF-metal thin film and cycled in Li and Na applied potential between -1 V to 1 V. The values reported by Talledoa et al. on sputtered films and Andmkaitis et al on electrodeposited ones are added for comparison [248, 249]. Whatever the technique of

deposition, the interlayer spacing increases with insertion. The presence of Li or Na leads to an increase in repulsion in between the VO₅ planes as x increases.

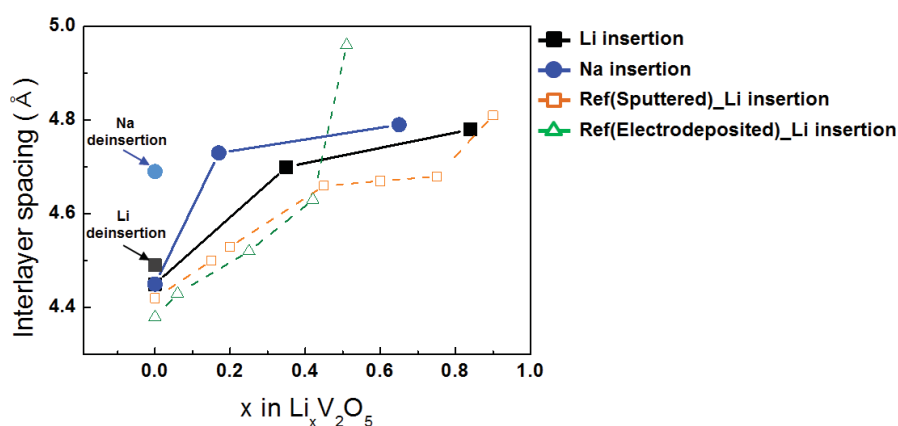


Figure 89. Interlayer spacing (crystallographic c parameter) of as-deposited 200 nm V₂O₅RF-metal thin film and Li and Na insertion state at the applied voltage between -1 V to 1 V. Results from A. Talledoa et al. and Andmkaitis et al. are shown as open squares and open triangles, respectively [248, 249].

* Structure analysis during long cycling

Figure 90 shows the XRD patterns recorded on as-deposited 200 nm V₂O₅RF-metal thin film and Li and Na insertion/deinsertion in the potential range between -1 V and 1 V in Li and NaTFSI-EMITFSI until 250 cycles. As the cycle increases in Li electrolyte, the (001) XRD peak intensity decreases gradually and after 250 cycles the peak is no more visible, suggesting a complete amorphization. In Na electrolyte, considering two peaks (as discussed in Fig. 88), the (001) as-deposited peak progressively disappears while the second one remains visible even after 250 cycles. In addition, a similar shift in between -1 V and +1V ($\Delta 2\theta$) persists upon cycling suggesting a constant irreversibility upon cycling.

As a result, it can be concluded that the crystalline V₂O₅RF-metal thin film becomes amorphous during cycling and that the amorphization occurs more rapidly in the Li than in the Na based electrolyte. Such phenomenon was already reported in the literature [252].

J. Swiatowska-Mrowiecka et al. presented the amorphisation of the structure initiated at the grain boundaries after cycling [252].

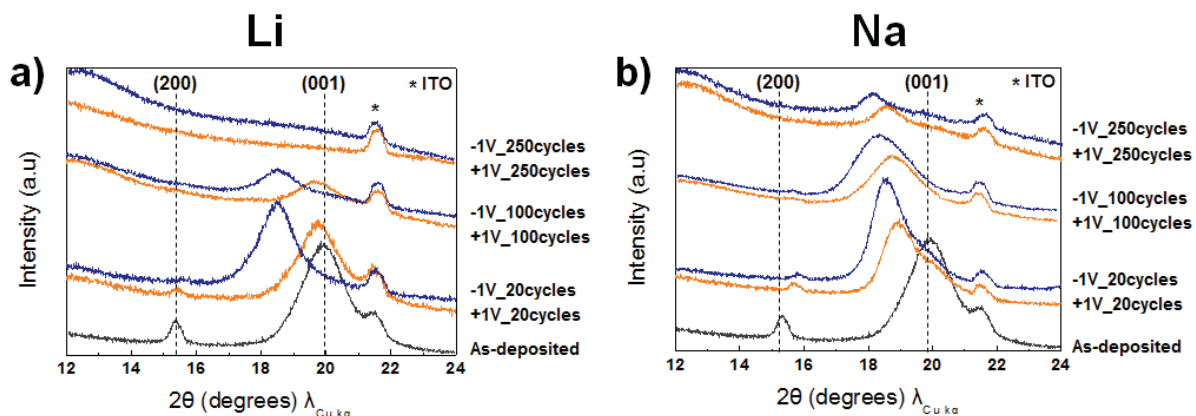


Figure 90. XRD patterns of as-deposited 200 nm V_2O_5 RF-metal thin film and Li (a) and Na (b) at the applied voltage at -1 V and 1 V in Li, NaTFSI-EMITFSI until 250 cycles.

2. XPS analysis

The multi-step electrochromism from orange to green and green to blue, during the reduction of V_2O_5 films (with reverse phenomenon during oxidation) was previously observed by several authors [253-256]. In the literature, it can be associated, to come from a double oxidation number change (V^{5+} to V^{4+} and then V^{4+} to V^{3+}) [253].

Recently ascribed the color change to olive green to the presence of V^{3+} ions, associating the multiple colors in V_2O_5 to the presence of V^{3+}/V^{4+} and V^{5+} . Such observations well agree with the color of V^{3+} , V^{4+} , and V^{5+} in aqueous solutions: i.e., in an octahedral ligand field with aqua ligands. In the meantime, those observations are not well correlated to the low x values determined from electrochemical behavior or from X-ray diffraction. Similarly multicolor electrochromism has been detected on amorphous VO_x films, with x between 1.5 and 2. Nonetheless some authors [257, 258, 259] have shown that the occurrence of a single V^{5+}/V^{4+} redox couple, can explain the green intermediate coloration by a potential range where the vanadium ions with the two oxidation numbers coexist with a well-defined ratio. Also, the electrochemical capacities we have measured, close to 1 electron only per cycle, tend to show that (i) a redox process with only oxidation numbers involving a change of only one unit occurs, or (ii) only a fraction about 50% of the film is submitted to the redox process. To study, in our case, the oxidation number really implied in the color changes observed in V_2O_5 films, i.e. to investigate what are the different amount mixtures of V^{5+} and V^{4+} ions, during cycling, *ex-situ* XPS spectroscopy, for different applied voltages, was performed in

collaboration with Christine Labrugère from PLACAMAT. Cycled films were washed using the same manner as for the XRD measurements.

The experiment protocole was as follow : A ThermoFisher Scientific K-Alpha spectrometer was used for surface XPS analysis of thin films. The monochromatized $AlK\alpha$ source ($h\nu=1486.6$ eV) was activated with a spot size $200\ \mu\text{m}$ in diameter. The full spectra (0-1320 eV) were obtained with a constant pass energy of 200 eV and high resolution spectra with a constant pass energy of 40 eV. High resolution XPS spectra were quantified and fitted using the AVANTAGE software provided by Thermo Fisher Scientific.

Figure 91 shows the XPS survey spectra, recorded on as-deposited 200 nm V_2O_5 RF-metal thin film in the potential range between -1 V and 1 V in LiTFSI-EMITFSI after 20 cycles. In addition of the expected visible peaks assigned to O and V, the survey spectrum shows the presence of carbon contamination (24 at.%) at the surface evidenced by low intensity peak of C1s. Additional F contamination is detected on the cycled films (-1.0 V) probably due to the traces of unwashed electrolyte.

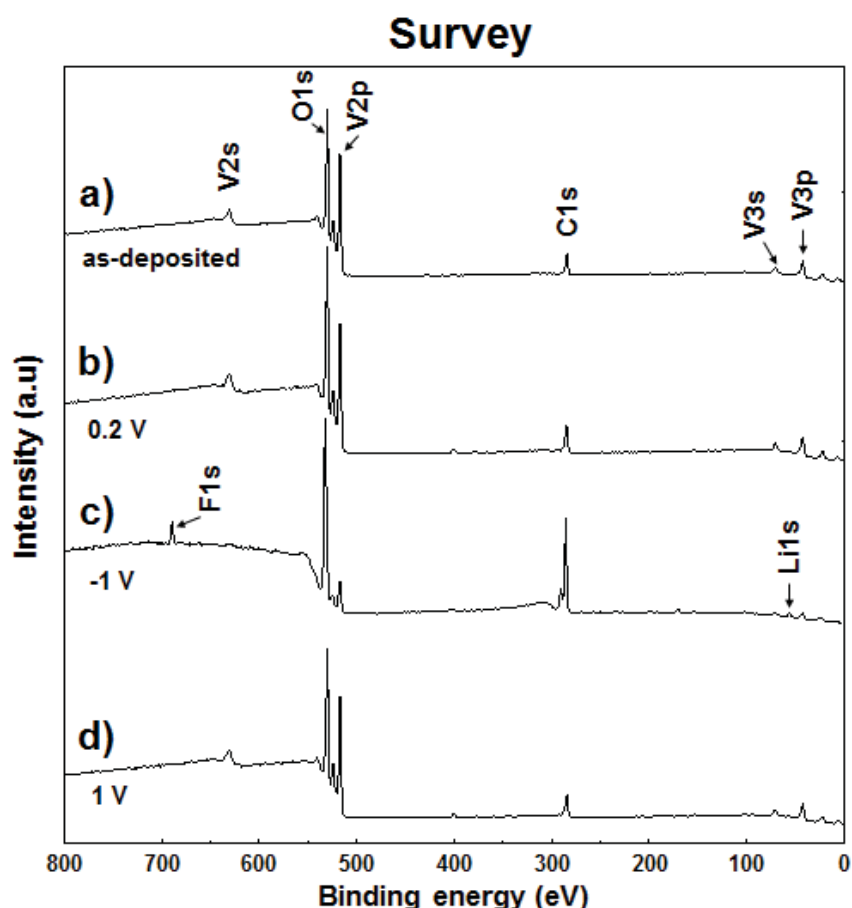


Figure 91. XP spectra of survey spectrum for 200 nm as-deposited V_2O_5 RF-metal thin film (a), in reduction at 0.2 V (b) and at -1 V (c) and oxidation state at 1 V (d) in LiTFSI-EMITFSI after 20 cycles.

Figure 92 shows the XPS spectra of C1s, O1s and F1s core levels carried out at the different applied voltage in LiTFSI-EMITFSI after 20 cycles. The oxygen signal of as-deposited V₂O₅RF-metal thin film at E_B = 529.9 eV corresponds to the oxygen ions of the oxide layer [260]. At -1 V, a new component is observed at E_B = 532.0 eV. Aware of possible electrolyte contamination, the XPS spectrum of the electrolyte alone was recorded showing a similar peak located at 532.0 eV.

The decomposition of the C1s peak shows three components (Figure 92 e). The main one, set at E_B = 284.3 eV, is assigned to hydrocarbons CH_x, always detected at the extreme surface. The second one at E_B = 285.4 eV can be assigned to C–O bonds. The third C1s peak at E_B = 288.3 eV corresponds to O=C–O [260, 261]. After reduction at -1 V, a new component at E_B = 290.3 eV is observed consistent with the C-F_x bonding of the electrolyte [262, 263, 264] (as well as F1s located at 689 eV (Figure 92 k) [265]). The component observed on the as-deposited film at E_B = 288.3 eV is shifted to the higher binding energy at E_B = 288.9 eV after reduction at -1 V.

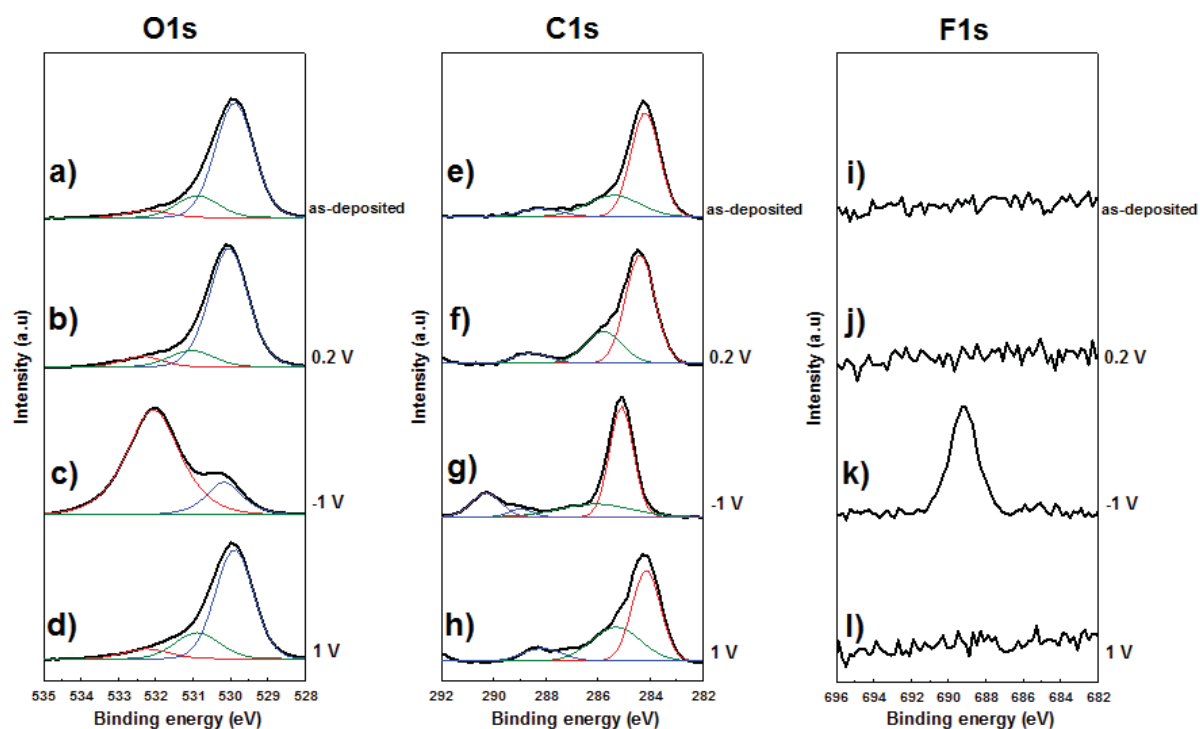


Figure 92. C1s, O1s and F1s XPS high resolution spectra for the as-deposited V₂O₅RF-metal thin film (a,e,i), in reduction at 0.2 V (b,f,j) and at -1V (c,g,k) and oxidized state at 1V (d,h,l) in LiTFSI-EMITFSI after 20 cycles.

Figure 93 shows the XPS spectra of V2p_{3/2} and Li1s. For the later, a Li bump or peak of higher intensity are only observed for the 0.2 V and -1 V reduction states. The Li quantification was indeed too difficult as also in the case of the -1 V sample, the presence of Li and of F may be assigned to the electrolyte. Having the electrolyte for the paper, we could quantify which Li % is associated with F. A more obvious observation of the reduction/oxidation process comes from the XPS spectra of V2p_{3/2} showing upon reduction the appearance at lower energy of a second component assigned to the presence of vanadium cation at a lower oxidation state. More precisely, two peaks of V2p_{3/2} region at 517.1 and 515.7 eV corresponding to the V⁵⁺ and V⁴⁺ oxidation states were measured on V₂O₅ thin films [266-269]. In case of as-deposited V₂O₅ film, the presence of 100% of V⁵⁺ indicates that thin film as expected contain mostly V⁵⁺ species (Figure 93 e) [267, 268, 269]. At 0.2 V of Li insertion state (Figure 93 f), the spectra can be fitted into two peaks with the appearance of a peak at lower binding energy. The second peak is due to a partial reduction of V⁵⁺ ions into V⁴⁺ ions. It corresponds to 18% of V to 82% of V⁵⁺. At -1 V upon further reduction (Figure 93 g), a significant increase in V⁴⁺ (35%) peak intensity was observed, while the one corresponding to V⁵⁺ population (65%) further decreases. On re-oxidation at 1V (Figure 93 h), an increase of the V⁵⁺ ions comparatively to the insertion state at -1 V is observed from 65 to 100% with concomitant decrease in V⁴⁺ ions from 35 to 0%. This result indicates that the surface of the V₂O₅ film consists mostly of V⁵⁺ and that the reaction is fully reversible. In first approach, we can assume that these changes in the V⁴⁺/ V⁵⁺ ratio illustrate some lithium insertion/deinsertion into the V₂O₅ structure. Such observations are consistent with the ones of other groups [267, 268, 269].

Besides, the FWHM values of the V2p_{3/2} components increase from 1.0 eV (V⁵⁺) for the as-deposited film up to 1.3 eV (V⁵⁺) and 1.5 eV (V⁴⁺) after Li insertion (-1 V) and decreases down to 1.0 eV (V⁵⁺) after the Li deinsertion (1 V). The V2p_{3/2} peaks of Li inserted film present higher FWHM than that for Li deinserted film as a response to a more disordered system [260]. This phenomenon was already observed in the case of intercalation of Li into V₂O₅ prepared by plasma vapour deposition (PVD) [270] and physical deposition [262]. The evolution of the V2p_{3/2} binding peak is contributed to the appearance of a Li peak (E_B around 56 eV) to confirm the previous results. At 0.2 V as Li was inserted, Li1s peak appeared. And the Li peak increased significantly at -1 V as further Li insertion state. On the other hand, after Li deinsertion at 1 V, Li1s peak disappeared. The XPS data obtained after deinsertion

also evidence that the process of Li insertion is fully reversible on the surface of V_2O_5 RF-metal thin film.

The binding energies (BE), full-widths at half-maximum (FWHM) values of Li insertion/deinsertion state at each applied potential for the $V2p_{3/2}$ peak (V^{5+} , V^{4+}) and the relative ratio of V^{4+} / V^{5+} are reported in Table 22. The proportion of vanadium oxidation state V^{5+} and V^{4+} changes significantly with the states of Li insertion, and can be calculated from the $V2p_{3/2}$ (V^{5+}) and $V2p_{3/2}$ (V^{4+}) peak areas.

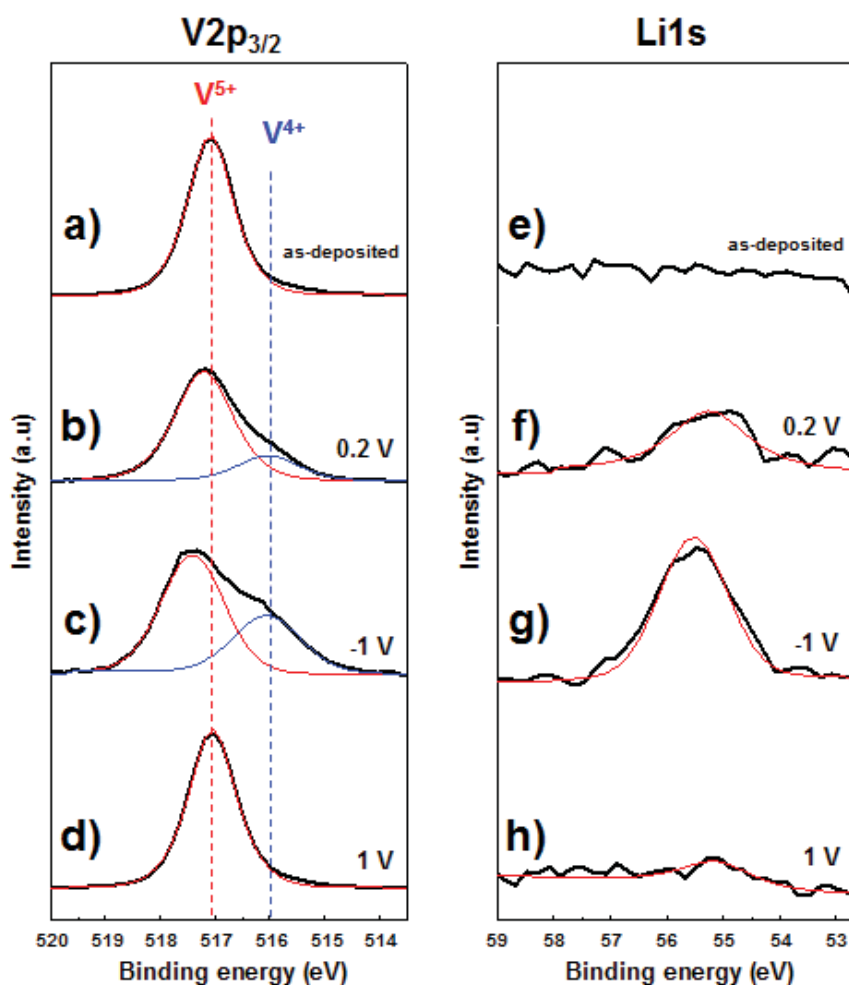


Figure 93. $V2p_{3/2}$ and $Li1s$ XPS high resolution spectra for the as-deposited V_2O_5 RF-metal thin film (a,e), Li insertion state at 0.2 V (b,f), at -1 V (c,g) and deinsertion state at 1 V (d,h) in LiTFSI-EMITFSI after 20 cycles.

Table 22. Binding energy (BE), full-width at half-maximum (FWHM) and fractional intensity (I) ratio of the V^{4+} and V^{5+} components of the $V2p_{3/2}$ fitted spectrum for the as-deposited, at 0.2 V, -1 V and 1 V in LiTFSI-EMITFSI after 20 cycles.

	BE (eV)				FWHM (eV)				V^{4+} / V^{5+} ratio			
	As-deposited	0.2 V	-1 V	1 V	As-deposited	0.2 V	-1 V	1 V	As-deposited	0.2 V	-1 V	1 V
$V2p_{3/2}(V^{5+})$	517.1	517.2	517.4	517.1	1.0	1.2	1.3	1.0	0.00	0.23	0.55	0.00
$V2p_{3/2}(V^{4+})$	-	516.0	516.1	-	-	1.3	1.5	-				

XPS results show modifications of the oxide composition with a V^{4+} / V^{5+} ratio increasing from 0.00 prior to 0.55 at applied potential. We calculated the corresponding Li content assuming a $Li_xV_2O_5$ formula compare the results of electrochemical measurement and XPS. Table 23 shows the comparison of the estimated x values from XPS and electrochemical measurements. The x values are not so far. This result is similar with results of A.M Salvi group [271]. As a result, the surface composition of the vanadium oxide thin film is a mixed state of V^{5+} and V^{4+} upon insertion. It can be seen that vanadium oxide thin film show completely reversible reaction in the applied voltage on the surface of the V_2O_5 RF-metal thin film. This is somewhat different from the XRD results showing that some of Li ions were trapped in the V_2O_5 thin film. It is presumed that Li insertion / deinsertion behaviors are different between the whole thin film (i.e. XRD analysis) and its surface (i.e. XPS analysis). We conducted a depth profile analysis using TOF-SIMS and NRA to better understand this phenomenon.

Table 23. The Li intercalation coefficient x obtained from electrochemistry and XPS measurements, and comparison with extent of reduction of vanadium

	Electrochemistry	XPS
Li insertion, at 0.2 V	$Li_{0.35}V_2O_5$	$Li_{0.24}V_2O_5$
Li insertion, at -1 V	$Li_{0.84}V_2O_5$	$Li_{0.70}V_2O_5$

3. Depth profile using TOF-SIMS

The TOF-SIMS analyses were performed using a TOF-SIMS IV (ION-TOF GmbH, Münster, Germany) at Technical University of Denmark, in collaboration with Eugen Stanmate and Kion Norman. 25-ns pulses of 25 keV Bi⁺ (primary ions) were bunched to form ion packets with a nominal temporal extent of < 0.9 ns at a repetition rate of 10 kHz, yielding a target current of 0.7 pA. These primary ion conditions were used to obtain mass spectra and depth profiles. For the depth profiling an analysis area of 200×200 μm² centered in a sputter area of 300×300 μm² was used. 28 nA of 3 keV Xe⁺ was used as sputter ions. For all analyses electron bombardment (20 eV) was used to minimize charge built-up at the surface. Desorbed secondary ions were accelerated to 2 keV, mass analyzed in the flight tube, and post-accelerated to 10 keV before detection.

SIMS profiles have been performed from the outer surface, and all the way across the film down to ITO substrate, in order to check the Li concentration in the various film regions vs. the concentration of V, taken as an internal reference. ToF-SIMS analysis was carried out for the V₂O₅RF-metal, V₂O₅RF-oxide, V₂O₅HiPIMS thin films in the as-deposited state and after cycling 20 times in LiTFSI-EMITFSI in the potential range between -1 V and 1 V. The thickness of all thin films was 200 nm.

Figure 94 shows the ToF-SIMS depth profiles for the intensities of V⁺, Li⁺ and In⁺ ions from as-deposited V₂O₅ thin films, the sample after reduction (i.e. Li insertion) at 0.2 V and -1 V, in oxidation (Li deinsertion) at 1 V, respectively. All profiles were recorded in the same conditions mentioned above In⁺ ions come from the ITO substrate.

The spectra of as-deposited V₂O₅RF-metal, V₂O₅HiPIMS thin films show a stable intensity of V ion profile before reaching the ITO substrate region (Figure 94 a, i). It can be attributed to a continuous and compact V₂O₅ layer without significant porosity. On the other hand, the intensity of V ion profile of V₂O₅RF-oxide film exhibits a change in the curve before reaching the ITO substrate region (Figure 94 d) suggesting a higher porosity for this V₂O₅ film. It may also indicate same artifacts occurring at the interface.

For the reduction state at 0.2 V, the increased intensity of Li profile can be easily observed in three V₂O₅ films (Figure 94 b, f, j). At -1 V upon further Li insertion (Figure 94 c, g, k), a significant enlargement in Li profile was observed. Upon re-oxidation at 1 V (i.e. Li

deinsertion state), the Li ion signal becomes very narrow in the three V_2O_5 films (Figure 94 d, h, l). The evolution of the Li signal appears to be reversible illustrating a reversible EC mechanism. The most striking feature was the occurrence of the Li signal at the interface with the substrate and no lithium at the film surface. A first hypothesis could be that the Lithium diffusion within the film occurs faster than the electron conduction.

Li concentration in the V_2O_5 thin films was evaluated by calculating the Li/V ratio. Figure 95 displays the Li/V intensity ratio of V_2O_5 RF-metal, V_2O_5 RF-oxide, V_2O_5 HiPIMS thin films in Li insertion at 0.2 V and -1 V and Li deinsertion at 1 V. The Li ions seem to distribute more not only at interface with ITO but also in the ITO film than at the surface of the V_2O_5 thin film. This accumulation of lithium at the internal interfaces was found on all V_2O_5 thin films and at Li insertion/deinsertion state. This phenomenon was observed in the literature and was the same as the other studies and is explained in several ways. Y. Fujita et al. presented that the reason for this is not clear at present, but light Li^+ ions may be pushed into the interior by Ar^+ ion sputtering [272]. Franco Decker et al presented that it can be explained with the formation of new Li-rich phases at the film boundaries, in contrast to the bulk of the V_2O_5 film with a more or less uniform Li concentration. The negative dip in this profile could arise from an electric field in the sub-surface region, consequence of a space charge layer, which would tend to remove the mobile charges (the Li ions) by migration [273]. Luis Santos et al [274] presented that these results indicate that, during intercalation, the Li ions were able to migrate through the vanadium oxide layers to the oxide/metal interface. The same observation was made by Swiatowska et al. for the intercalation of lithium in thin V_2O_5 layers, generated by thermal oxidation of a vanadium substrate, in presence of a conventional organic electrolyte ($LiClO_4$ -PC) [267]. At the deinsertion state, the Li ion signal shows a low intensity, which can be attributed to some lithium trapped in the oxide structure. The lithium accumulation at the oxide/metal interface can be evidenced by the high Li intensity. After cycling, irreversible changes caused by repeated processes of lithium-ion insertion and deinsertion may be created, trapping lithium in the oxide film preferentially at its inner interface. The same phenomenon of Li trapping occurring preferentially at the interfacial region between the active electrode thin film material and metallic substrate (current collector) confirms the previous results obtained on the V_2O_5 thermal oxide [267] and other electrode materials such as thin films of iron oxide [275] iron sulfide [276] and Si [277, 278].

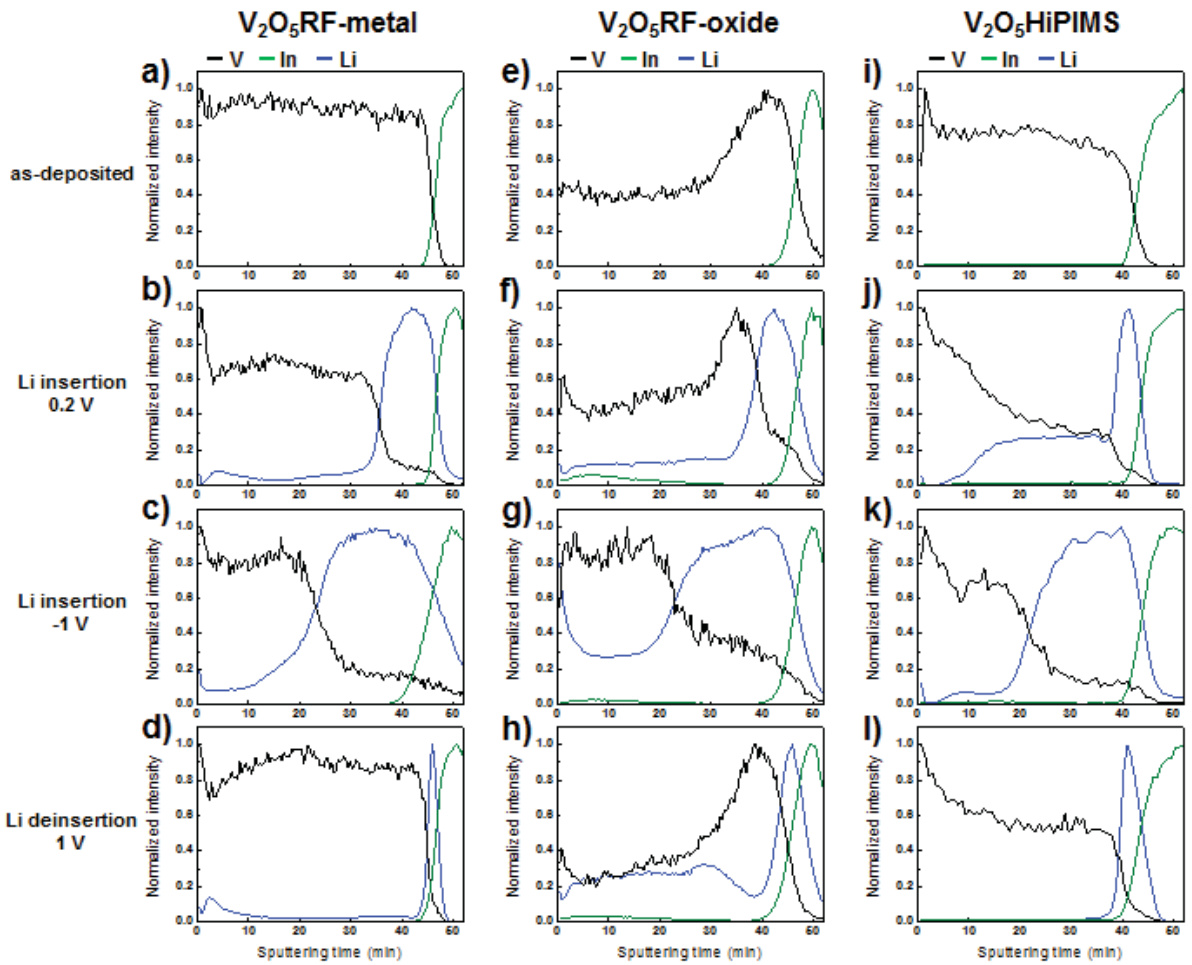


Figure 94. SIMS depth profile normalized intensity to maximum 1 of V, Li and In ions of as-deposited, Li insertion at 0.2 V and -1 V and Li deinsertion at 1 V of V_2O_5 RF-metal, V_2O_5 RF-oxide, V_2O_5 HiPIMS thin films in LiTFSI-EMITFSI in the potential range between -1 V and 1 V after 20 cycles

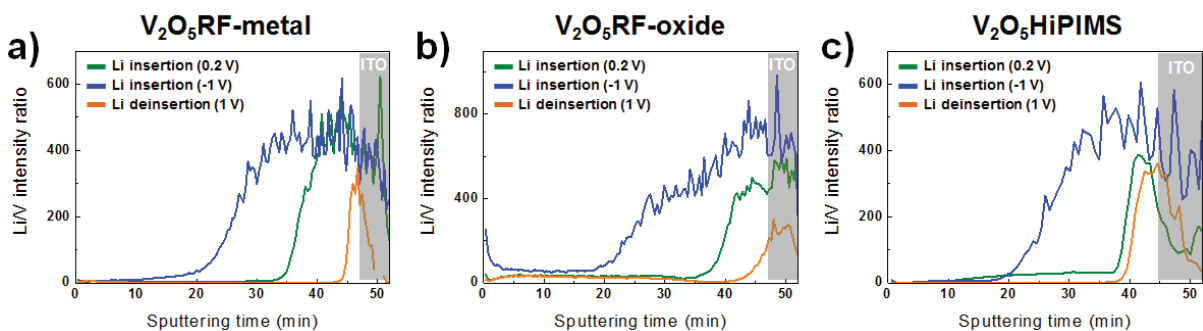


Figure 95. Li/V intensity ratio of V_2O_5 RF-metal, V_2O_5 RF-oxide, V_2O_5 HiPIMS thin films in Li insertion at 0.2 V and -1 V and Li deinsertion at 1 V

4. Depth profiles using Auger Electron Spectroscopy (AES)

Another mean to determine, the relative Li distribution in V_2O_5 thin film, was to perform AES (Auger electron spectroscopy) depth profiles in collaboration with Michel Lahaye at UMS PLACAMAT. Figure 96 shows Li contents as a function of the thickness of 200 nm V_2O_5 RF-metal thin film in Li insertion at 0.2 V and -1 V and Li deinsertion at 1 V in LiTFSI-EMITFSI in the potential range between -1 V and 1 V after 20 cycles. At Li insertion state of 0.2 V, Li concentration increases as increasing sputtering until reaching the detection of In (Figure 96 a). At further Li insertion state of -1 V, during the first ten of seconds sputtering, Li concentration is high (Figure 96 b). This indicates the presence of Li on the surface of the thin film, which is the same as the result of the previous XPS result (Li and carbon compounds were detected on the thin film surface) (Figure 92, 93). Between 10 and 100 seconds of sputtering, Li concentration decreases. With further sputtering, Li concentration increases as increasing sputtering until reaching to the detection of In. After Li deinsertion of 1 V, Li was not detected or very low (Figure 96 c). At Li insertion of 0.2 and -1 V, Li increases as increasing sputtering. This observation indicates that Li is inserted in the inner part of the thin film. This is same result with previous ToF-SIMS depth profiles (Figure 94, 95).

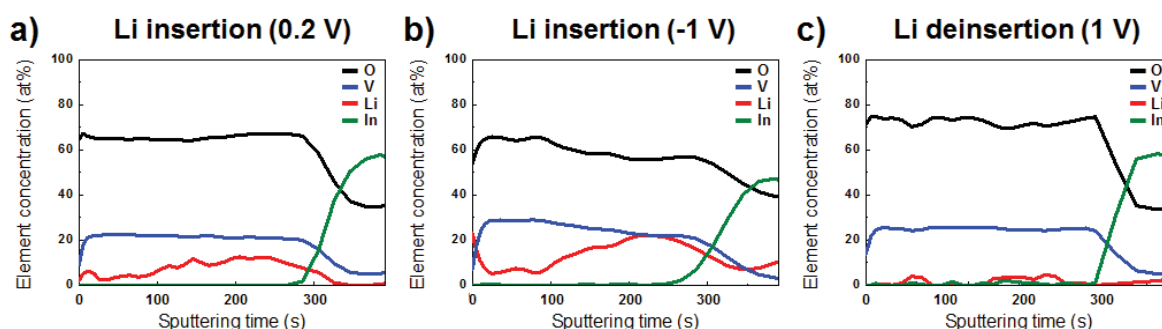


Figure 96. Depth profile of 200 nm V_2O_5 RF-metal in Li insertion at 0.2 V and -1 V and Li deinsertion at 1 V

5. Li content analysis using RBS/NRA(AIFIRA)

In order to investigate the Li content as a function of depth, RBS (Rutherford backscattering spectroscopy) / NRA (Nuclear reaction analysis) analyses were performed. Analysis were

carried on AIFIRA facility (CENBG, France) with a 2.8 MeV proton beam in collaboration with Stéphanie Sorieul. RBS and NRA were both performed with the same Si-detector (PIPS, Canberra) mounted at 140° with a solid angle of 25 msr. PIXE analysis were done with a HPGe detector (GUL0110P, Canberra) mounted at 135° and equipped with a Funny Filter (180 μm polyester, hole : 500 μm). The beam current was adjusted in order to keep the dead time below 10%. Each analysis lasted 30 minutes with a beam current of 2 nA which is enough to have a good statistic below the Li NRA-peak. Data treatment was done respectively with SIMNRA and its add-on MultiSIMNRA for RBS/NRA, and GUPIX for PIXE. RBS and PIXE results were used in order to have a proper characterization of the samples. A thin film of LiCoO_2 was used for Li-quantification [279]. Figure 97 shows Li contents as a function of the thickness of 400 nm V_2O_5 RF-metal thin film in Li insertion at 0.2 V and -1 V and Li deinsertion at 1 V in LiTFSI-EMITFSI in the potential range between -1 V and 1 V after 20 cycles. Li content is continuously increased in the V_2O_5 RF-metal thin film upon Li insertion at 0.2 V and further Li insertion at -1 V. Li ions seem to be distributed in the inner part of V_2O_5 film and at the interface with ITO substrate and not at the surface of V_2O_5 film. This result is supported by previous ToF-SIMS and Auger depth profiles results (Figure 94, 95, 96).

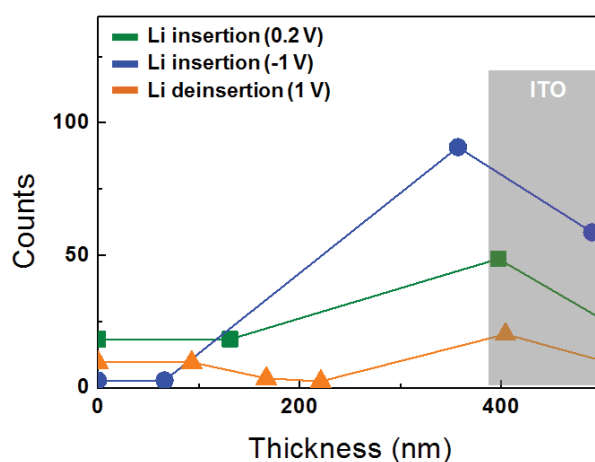


Figure 97. Li contents as a function of the thickness of V_2O_5 RF-metal in Li insertion at 0.2 V and -1 V and Li deinsertion at 1 V

Conclusion

Through the combination of different characterization techniques and cycling behavior, we perform preliminary investigation of the EC mechanism.

Scanning using various scan rates allows us to separate the faradic to the capacitive contributions. V_2O_5 RF-oxide and V_2O_5 HiPIMS thin films show higher capacitive contributions than V_2O_5 RF-metal thin films in Li electrolyte. On the contrary, in Na electrolyte, the capacitive contributions are similar for the three types of V_2O_5 thin films. This result can explain that cycling in Na electrolytes is associated to fast switching time due to higher capacitive components, while in Li based electrolytes films exhibit slow switching time due to faradic components.

V_2O_5 RF-metal thin films show upon reduction that the (001) peak shifts progressively to lower angles. The shifts correspond to an increase in the c parameter from 4.45 Å (as-deposited) to 4.70 Å (0.2 V, ion insertion coefficient $x=0.35$) and 4.78 Å (-1.0 V, $x=0.84$) in Li electrolyte, to 4.70 Å (0.2 V, $x=0.17$) and 4.78 Å (-1.0 V, $x=0.65$) in Na electrolyte, respectively. The interlayer spacing of V_2O_5 RF-metal thin films increases with insertion. The presence of Li or Na leads to an increase in repulsion in between the VO_5 planes as x increases. The evolution of the GIXRD patterns upon cycling would favor a simple insertion/desinsertion mechanism. During 1000 cycles, the crystalline V_2O_5 RF-metal thin film becomes amorphous during cycling and that the amorphisation occurs more rapidly in the Li than in the Na based electrolytes. The different cycling stability of V_2O_5 films is attributed to a modification of the morphology (i.e. increase of the surface area due to cracks and increase porosity), as well as a progressive amorphization particularly in lithium electrolyte. As expected the average film oxidation state decreases upon reduction with a significant amount of V^{4+} as detected by XPS. The V^{4+} / V^{5+} ratio reaches a value of 0.55 at -1V. From depth profile using ToF-SIMS, AES and RBS/NRA, the continuous increase of the Li content with reduction appears not fully homogeneous in the full thickness of the films but to occur preferentially at the interface.

PART D : ELECTROCHROMIC DEVICES (ECDs)

As stated in the state of the art, Electrochromic Devices, ECDs, are still very often described as a battery type architecture consisting in a five layers stack, schematized by the TCO/EC1/Electrolyte/EC2/TCO chain in which TCO stands for Transparent Conducting Oxides layer, EC1 and EC2 for Electrochromic layers and Electrolyte for electrolyte. In our work V_2O_5 films were combined either to WO_3 using a transparent electrolyte or in a more novel architecture to V_2O_5 films using an opaque electrolyte. Thus, this part is divided in two chapters. The first one concerns the conception and EC characterization of more “common” $WO_3/(Li,Na)$ electrolyte/ V_2O_5 device while in the second chapter the utilization of an opaque electrolyte has allowed the conception of a symmetrical V_2O_5/V_2O_5 device. In addition of its role of ionic conductor in the later, the opaque nature of the electrolyte makes it possible to distinguish the color of each face of an electrochromic device. This study is a new approach in our group [101]. The schematic of the two types of ECDs is described in Figure 98. ECD with V_2O_5 and WO_3 thin films are considered for smart window application. In case of double-sided device, ECD with V_2O_5/V_2O_5 thin films aim at display application. The color changes expectations for the combination of the WO_3/V_2O_5 films is a switch from orange to green and blue (V_2O_5 , side) at the applied voltage, from colorless to blue (WO_3 side). With opaque type of electrolyte, when $U < 0$ V or > 0 V, the ECD with double sides V_2O_5 films has two colored faces, with side 1 colored orange and side 2 colored blue.

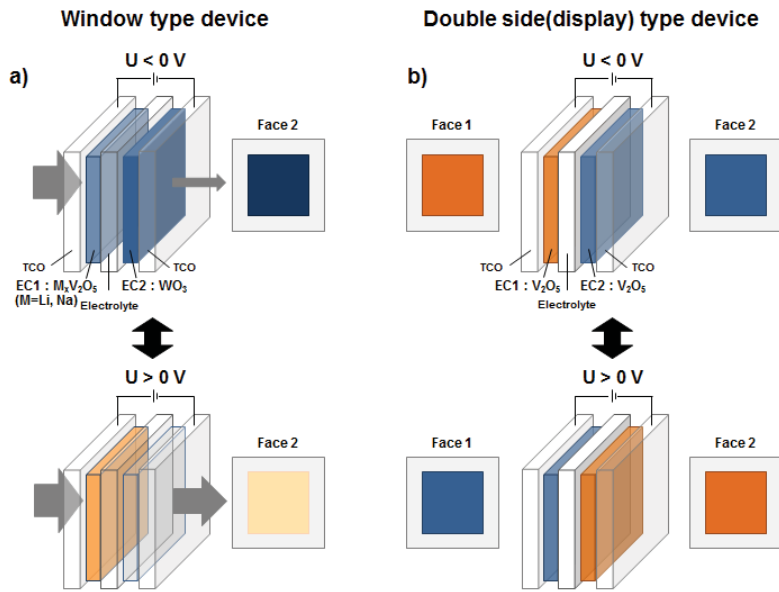


Figure 98. Principle of electrochromic devices with transparent electrolyte (a) and opaque electrolyte (b).

Chapter 1. Full devices of V_2O_5/WO_3 films for smart window application

1. V_2O_5/WO_3 with Li and Na based electrolytes

1.1 Fabrication method

To fabricate the V_2O_5/WO_3 device, we first prepared a V_2O_5 RF-metal single thin film and WO_3 single thin film. V_2O_5 and WO_3 single thin film were deposited by RF reactive magnetron sputtering.

1.1.1 EC behavior of WO_3 single thin films

WO_3 thin films were deposited on $2.5 \times 2.5 \text{ cm}^2$ $In_2O_3: Sn$ coated glasses (ITO glass, $\sim 30 \Omega/sq$) by reactive RF magnetron sputtering. The target was 100 mm diameter tungsten oxide (99.99%). The distance from the substrate to the target fixed at 8 cm. Such conditions led to the production of uniform thin films. The gas-flow ratio of Ar (99.99%) to O_2 (99.99%) was fixed by mass flow controllers at $P(O_2)$ of 2 %, corresponding working pressure of 2 Pa. The power was maintained at 90 W. A deposition rate of 10.4 nm/min was recorded. WO_3 films appeared rather smooth. The deposition parameters are gathered in Table 24.

Table 24. The deposition parameters of tungsten oxide thin films

Parameters	WO_3 target
Power (W)	90
Total pressure (Pa)	2
$P(O_2)$ %	2
Distance of target-substrate (mm)	80

1.1.2 Pre-cycling of single thin films

Figure 99 shows the cyclic voltammograms and the *ex-situ* optical transmittance spectra of the 470 nm WO₃ thin films cycled in LiTFSI-BMITFSI (a) and in NaTFSI-BMITFSI (b) in the bleached (1.2 V) and colored (-0.8 V) states after 20 cycles. In the bleached state W⁶⁺O₃ is colorless while the film is blue in the colored state thanks to the presence of W⁵⁺. In WO₃, It is well accepted that an insertion/deinsertion mechanism takes place : $WO_3 + xLi^+/(Na^+) + xe^- = (Li_xW^{5+}_xW^{6+}_{1-x}O_3)$. From the CV shape and corresponding electrochemical capacity, cycling in Na electrolyte leads to limited color change illustrated by a small variation of the transmittance.

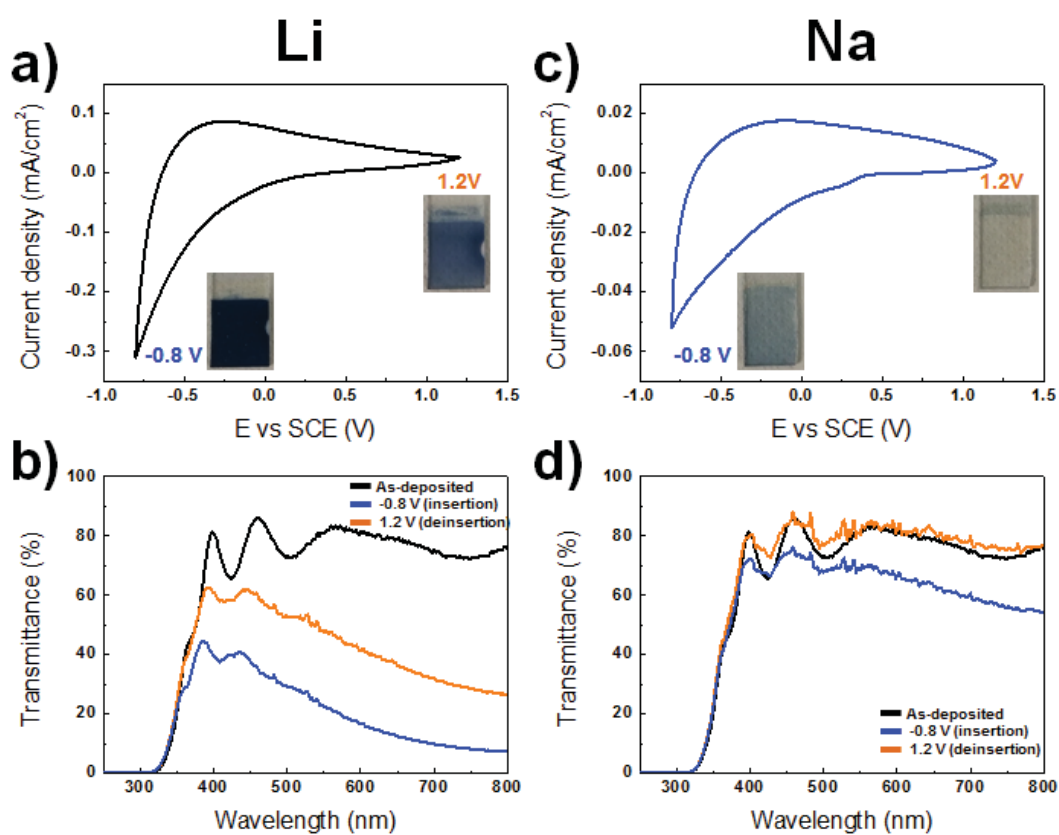


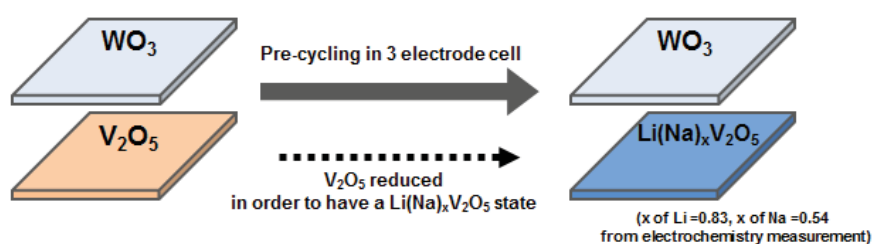
Figure 99. Cyclic voltammograms and *ex-situ* optical transmittance spectra of 470 nm WO₃ thin films at the bleached (1.2 V) and colored (-0.8 V) state in Li(a,b) and Na(c,d) based electrolyte after 20 cycles. WO₃/Li,NaTFSI-BMITFSI/Pt vs SCE.

1.1.3 Fabrication of V_2O_5 /Li and Na gel liquid electrolytes/ WO_3

In order to well-balanced the charge when building the device, the thickness of each thin film was selected considering its capacity. We used 93 nm V_2O_5 RF-metal thin film (Q : 10.3 mC/cm^2) and 470 nm WO_3 thin film (Q : 11.0 mC/cm^2) in lithium based electrolyte. However, in Na based electrolyte, due to thickness issues, we could not properly balance the charge, the capacity of 470 nm WO_3 was three times lower ($Q_{WO_3} \approx 1/3 Q_{V_2O_5}$).

Prior to device assembly, V_2O_5 and WO_3 thin films were pre-cycled separately in a three electrodes cell containing a liquid Li and NaTFSI-EMITFSI electrolyte. WO_3 was pre-cycled to the bleached state after 20 cycles, V_2O_5 was stopped in the reduced ($Li_xV_2O_5$ ($x=0.83$)), ($Na_xV_2O_5$ ($x=0.54$)) state after 20 cycles. A few drops of a Li/NaTFSI-BMITFSI containing 40% PMMA (Poly (methymethacrylate)) transparency electrolyte were homogeneously deposited on one of the two thin films. The film covered with electrolyte was then deposited on a hot plate with a minimum temperature of 80 °C to allow the butanone to evaporate and to remove the bubbles in the electrolyte. Once the electrolyte membrane is formed, the second V_2O_5 thin film is then positioned above it. After a few hours at room temperature, the electrolytic membrane provides the mechanical cohesion between the two V_2O_5 thin films. The process is schematized in figure 100.

a) Pre-cycling of single films



b) Fabrication of the full device

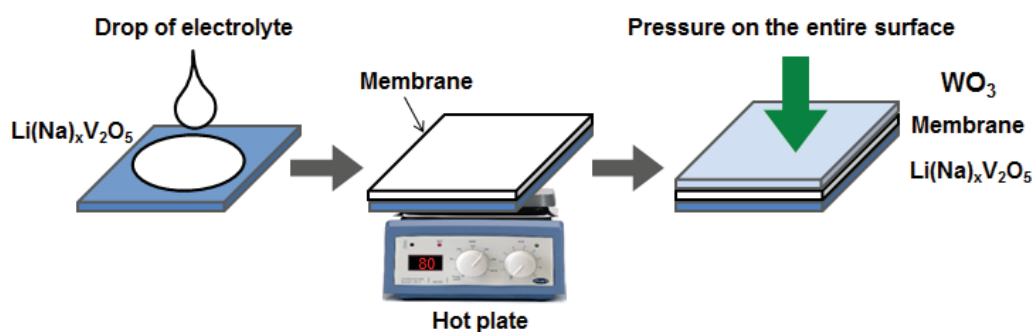


Figure 100. The various fabrication steps of the $WO_3 / Li(Na)_xV_2O_5$ device.

1.2 Electrochromic properties of V₂O₅/ Li and Na gel liquid electrolytes / WO₃

1.2.1 Electrochemical and optical properties

Figure 101 shows the 20th typical cyclic voltammograms of V₂O₅/ Li (a) and Na (b) electrolyte/ WO₃ in Li based electrolyte at applied voltage with -1 and +2 V and in Na based electrolyte at applied voltage with -1.6 and +2.4 V with a sweep rate of 10 mV/s. In both electrolytes, the CVs show good reversibility while significant difference in shape is visible. EC device shows much more symmetrical cyclic voltammogram in Li based electrolyte, consisting of two visible peaks in oxidation and reduction than in Na based electrolyte in which a large intense peak is mostly seen in oxidation. Charge density of EC device in Li electrolyte (Q: 17.9 mC/cm²) is much larger than in Na electrolyte (Q: 4.5 mC/cm²). In Li electrolyte, V₂O₅/WO₃ device exhibits distinct color changes as bleached at -1 V, colored at 2 V. In Na electrolyte, V₂O₅/WO₃ device show color changes as yellowish bleached at -1.6 V, dark-greenish colored at 2.4 V, respectively.

Figure 101 (c,d) shows the optical switching behavior of *in-situ* transmittance under relatively operational conditions over an extended time ~50000 s in Li (85 cycles) based electrolyte at applied voltage with -1 and +2 V and in Na (140 cycles) based electrolyte at applied voltage with -1.6 and +2.4 V at 650 nm wavelength. In Li electrolyte, reduced state (-1 V) and the oxidized state (2 V) are associated with transmittance values of T_R 75.5% and T_O 26.7% at 650nm, corresponding to a transmittance modulation ΔT of 48.9% (Table 25). In Na electrolyte, transmittance modulation ΔT are 29.1% at 650 nm (Table 25). CE values of EC devices with Li and Na based electrolytes are summarized in Table 25. EC device with Na electrolyte shows relatively low transmittance modulation compared to the one cycled in Li electrolyte, but the coloration efficiency was about twice as high as that of the Li electrolyte due to larger charge capacity of EC device with Li electrolyte.

In summary, EC device shows a good durability and a higher contrast and a difference of transmittance of ~50% without performance deterioration in Li medium (Figure 101 c). In Na electrolyte, EC device shows a good durability with difference of transmittance of ~30% (Figure 101 d).

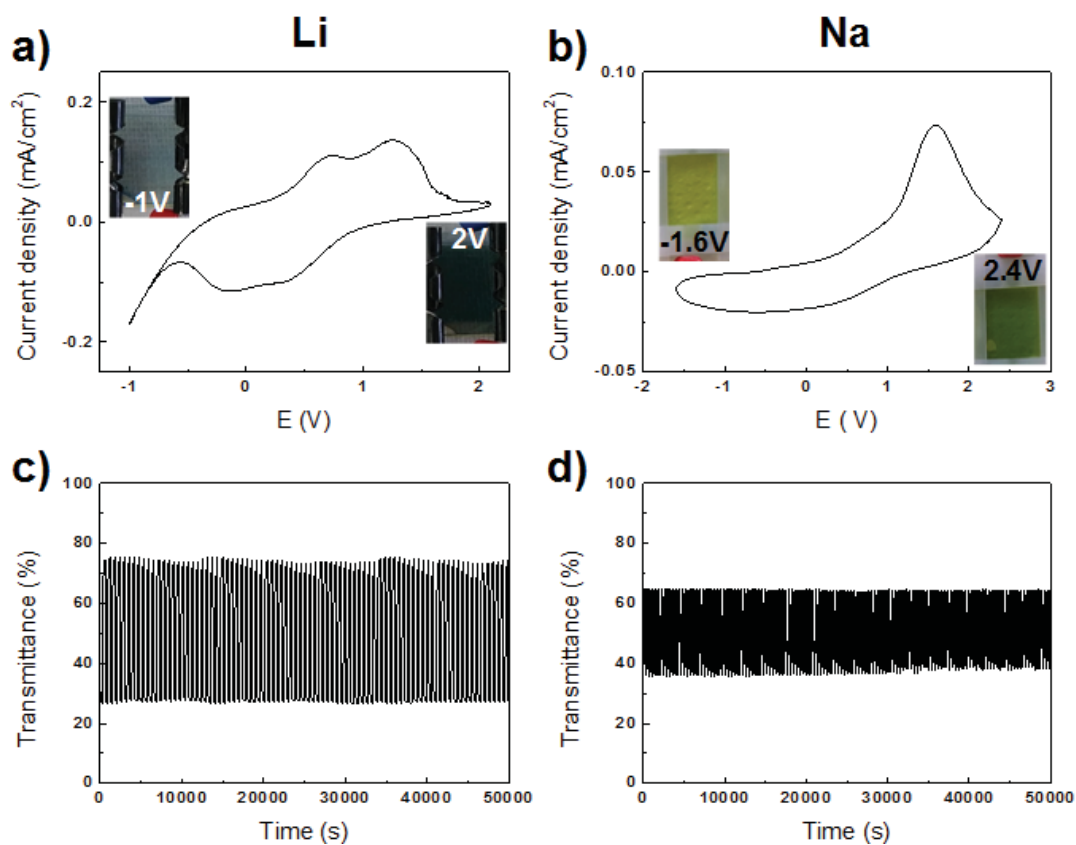


Figure 101. Cyclic voltammograms of V_2O_5/ Li (a) and Na (b) based electrolyte $/WO_3$ device after 20 cycles. *In-situ* optical transmittance spectra at 650 nm wavelength of V_2O_5/ Li (c) and Na (d) based electrolyte $/WO_3$ device until 50000s.

Table 25. Coloration efficiency of V_2O_5/ Li (a) and Na (b) based electrolyte $/WO_3$ device. ΔT , ΔOD and CE from Part A, 1.4, equation (1), (3) and (4), respectively.

Electrolyte	Charge density (mC/cm ²)	$\lambda = 650\text{nm}$		
		ΔT	ΔOD	$CE(\text{cm}^2/\text{C})$
Li	17.9	48.9	0.45	25.3
Na	4.5	29.1	0.26	57.4

1.2.2 Switching time

The switching time was calculated as the time to reach 90% of the total contrast from *in-situ* optical transmittance spectra at 650 nm wavelength in Li based electrolyte at applied voltage with -1 and +2 V and in Na based electrolyte at applied voltage with -1.6 and +2.4 V (Figure 101 c, d). Figure 102 shows the switching time of V₂O₅/ Li (a) and Na (b) based electrolyte /WO₃ device. Switching time of ECD in Li based electrolyte is $t_{90}=10.7$ s in coloration and $t_{90}=110.7$ s in the bleached state. The switching time of the oxidized state is about 10 times slower than the switching time of the reduced state. In case of ECD with Na electrolyte, switching time were $t_{90}=65.0$ s in coloration and $t_{90}=45.0$ s oxidized state contrasting with the behavior in Li electrolyte as the the switching time of the oxidized state was faster than the reduced state in the Na electrolyte. The reasons of those different behaviors still remain to be understood.

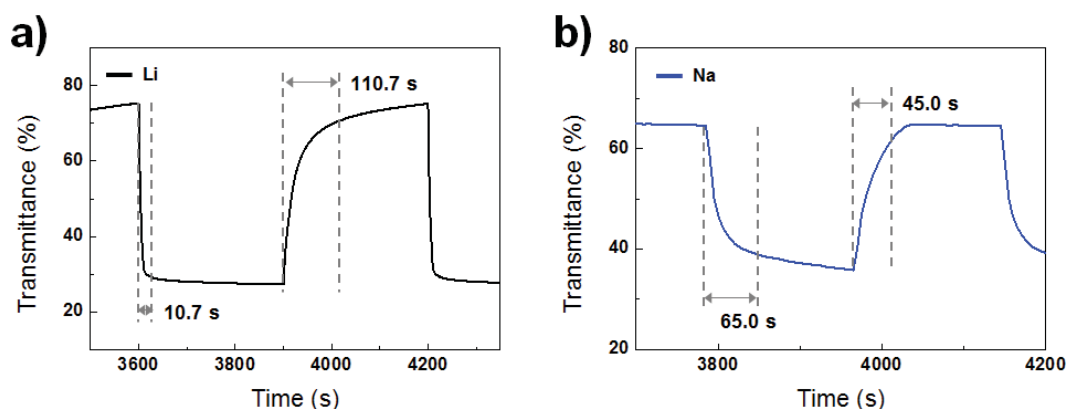


Figure 102. Switching time of V₂O₅/ Li (a) and Na (b) based electrolyte /WO₃ device.

Interestingly, in collaboration with the group of Padilla [280], we perform a careful study on the determination of the switching time as no real standard method exists meaning that no real comparison in between different materials or different systems can be made. Javier Padilla's group proposed a standard method for reporting electrochromic switching times, based on straightforward experimental fittings resulting in an analytical expression that can directly correlate obtainable optical contrast values with their corresponding switching times. We calculated and compared the switching times using the conventional and proposed methods

for V₂O₅/WO₃ device with Javier Padilla group. We summarized the comparison results of t₉₀ values calculated from proposed method, and the conventional method in Table 26.

Table 26. Comparison of t₉₀ values calculated from proposed method, and the conventional one.

ECD	Proposed method		Conventional Method (t ₉₀)	
	Symmetrical variable steps	Asymmetrical variable steps	Coloration	Bleaching
V ₂ O ₅ / Li electrolyte / WO ₃	37.9 s	Coloration 11.5 s Bleaching 51.2 s	Coloration 10.7 s	Bleaching 110.7 s

Significant difference in switching time appears in particular in the bleaching step. We are not able to explain such discrepancies, but this comparison between the two methods for the determination of the switching time point out the need for a standard calculation.

In conclusion, the fabricated double sides V₂O₅/transparent Li and Na gel liquid electrolyte/WO₃ devices shows electrochromic color change with durability in Li electrolyte as well as in Na electrolyte. Our study confirms that they are well driven and applicable to smart window.

Chapter 2. Full devices of V_2O_5/V_2O_5 films for display application

1. V_2O_5/V_2O_5 with Li and Na based electrolytes

1.1 Fabrication method

The first step was the development of a white-opaque electrolyte. For this, a small amount of TiO_2 submicronic powder (Aldrich) was mixed with the ionic liquid.

1.1.1. Preparation of white-opaque gel electrolyte

An optimization of the mixture of TiO_2 powder and ionic gel was carried out in the following way:

0.85 grams of TiO_2 powder ($\phi = 200$ nm) purchased from Sigma-Aldrich were mixed with 2 grams of the commercial 0.3M Li and Na-TFSI electrolyte in EMITFSI + 40% PMMA (Poly (methylmethacrylate)), and the electrolyte obtained was stirred for 3 hours at room temperature.

1.1.1.1 Transmittance and reflectance of white-opaque gel electrolyte

Figure 103 shows the spectrum of optical transmission and reflection of the white-opaque electrolyte composed of TiO_2 and Li/NaTFSI-EMITFSI-40% PMMA. The optical transmittance has a value of 0% while the value of reflectance varies from 58 to 48% over the entire spectrum of visible wavelengths.

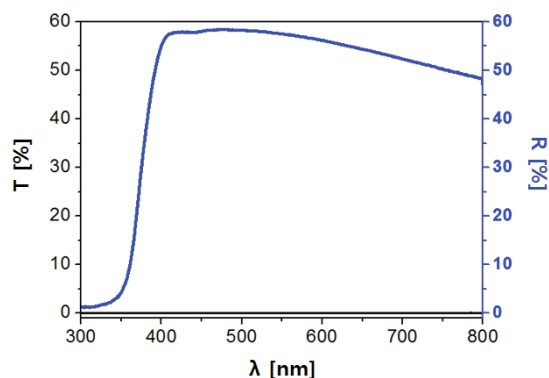


Figure 103. The spectrum of optical transmission and reflection of the white-opaque electrolyte composed of TiO_2 and LiTFSIEMITFSI, 40% PMMA.

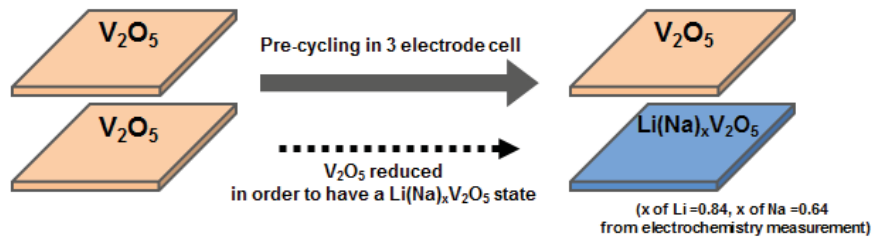
1.1.1.2 Conductivity of white-opaque gel electrolyte

The conductivity of the white and opaque electrolyte was determined by impedance spectroscopy by placing the electrolyte between two platinum plates. The white and opaque electrolyte has an electronic conductivity of 1.4×10^{-4} S/cm whereas the conventional electrolyte 0.3M LiTFSI-EMITFSI, 40% PMMA has a conductivity of 1.9×10^{-4} S/cm. More details on the white electrolyte may be found in the paper of Danine et al from our group [281].

1.1.2 Fabrication of $\text{V}_2\text{O}_5/\text{Li}$ and Na- white-opaque gel electrolyte/ V_2O_5

Due to their good performance, the 200 nm V_2O_5 RF-metal thin films, were used. Prior to device assembly, the V_2O_5 RF-metal thin films were cycled separately in a cell with three electrodes containing a liquid Li, Na electrolyte. The purpose of this step was to stabilize one thin film in the reduced state and the other one in the oxidized state. A few drops of prepared white-opaque liquid gel electrolyte was homogeneously deposited on one of the two V_2O_5 thin films. This was then deposited on a hot plate with a minimum temperature of 80 °C to allow the butanone to evaporate and to remove the bubbles in the electrolyte. Once the electrolyte membrane was formed, the second V_2O_5 thin film is then positioned above it. After a few hours at room temperature, the electrolytic membrane provided the mechanical cohesion between the two V_2O_5 thin films.

a) Pre-cycling of single films



b) Fabrication of the full device

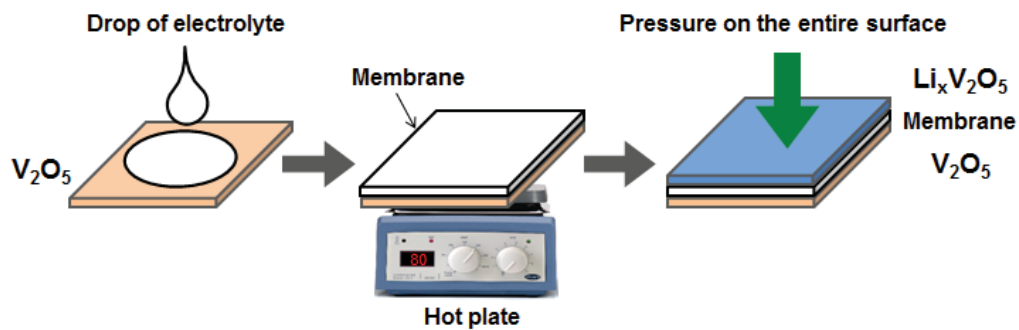


Figure 104. The various fabrication steps of the $V_2O_5 / Li(Na)_xV_2O_5$ device.

1.2 Electrochromic properties of V_2O_5/Li and Na-white-opaque gel electrolyte/ V_2O_5

1.2.1 Electrochemical properties

Figure 105 shows the cyclic voltammogram of $V_2O_5/Li_xV_2O_5$ device after 20 cycles with a sweep rate of 10 mV/s in -1.5 V~1.5 V voltage window in Li electrolyte and in Na electrolyte, respectively. They show reversible behavior in both electrolytes. In Li electrolyte, the voltammogram is composed of two merged peaks in reduction, at -0.2 V and -0.4 V and two merged peaks also in oxidation at 0.2 V and 0.4 V. In Na electrolyte, the voltammogram is composed of two poorly visible very broad peaks in reduction, at 0.4 V and -1 V and two broad peaks/waves also in oxidation at -0.4 V and 1.1 V. The charge capacity was 25.7 mA/cm² in Li electrolyte and 11.0 mA/cm² in Na electrolyte, respectively.

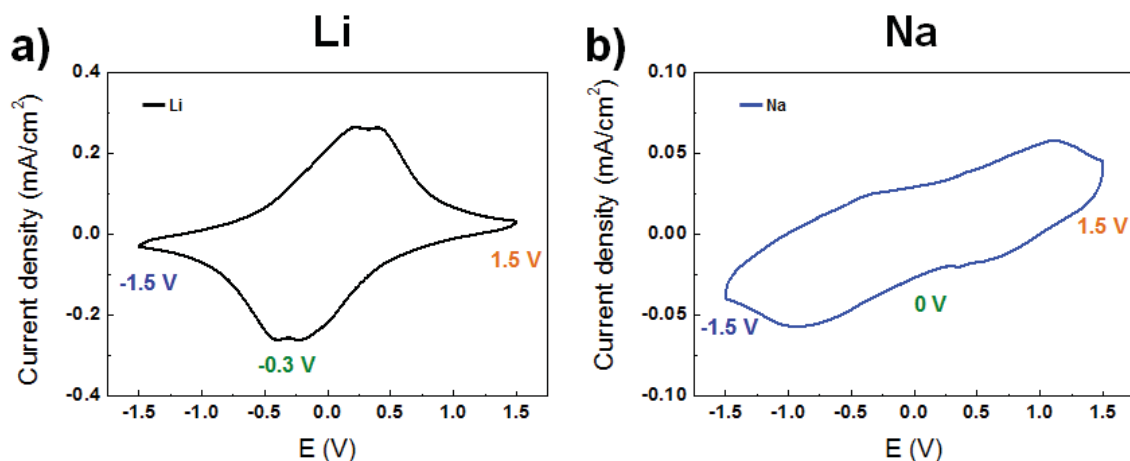


Figure 105. Cycle voltammograms of EC device V_2O_5/ Li (a,c) and Na (b,d) TFSI-EMITFSI-40% PMMA(70wt%)- TiO_2 (30wt%) / $Li_xV_2O_5$ after 20 cycle with a sweep rate of 10 mV/s.

1.2.2 Optical properties

The CIELAB color space (also known as CIE $L^*a^*b^*$ or sometimes abbreviated as simply "Lab" color space) is a color space defined by the International Commission on Illumination (CIE) in 1976. It expresses color as three numerical values, L^* for the lightness and a^* and b^* for the green–red and blue–yellow color components. It is used to indicate the level of clarity L^* , which varies between 0 (black) and 100 (white), as well as the two components of chromaticity a^* and b^* . These constitute a two-dimensional plane for which the a^* axis has the magnitude of the red and the green, perpendicular to the axis b^* which signifies the magnitude of the yellow with the blue (Figure 106). The color contrast between the oxidation state and reduction state can be calculated using the following equation 23:

$$\Delta E = \sqrt{(L_{oxidation} - L_{reduction})^2 + (a_{oxidation} - a_{reduction})^2 + (b_{oxidation} - b_{reduction})^2} \quad (23)$$

V_2O_5/V_2O_5 device shows multi-color of yellow, green and blue at applied potential in Li electrolyte. Each face of device at applied voltage has a different color (Figure 107 a). In Na electrolyte, V_2O_5/V_2O_5 device shows different color at applied potential (Figure 107 b). It can be seen that the color change observed in a single thin film in Li and Na based liquid electrolyte is well implemented in the device.

The CIE Lab values and the color contrast (ΔE) calculations show that both sides of the device exhibit almost the same color (Table 27).

The color contrast (ΔE) value in lithium electrolyte is about 6 times higher than in Na electrolyte (Table 27). This confirmed previous difference value of charge capacity. The charge capacity in lithium electrolyte is about 3 times higher than in Na electrolyte (Figure 101, Table 25).

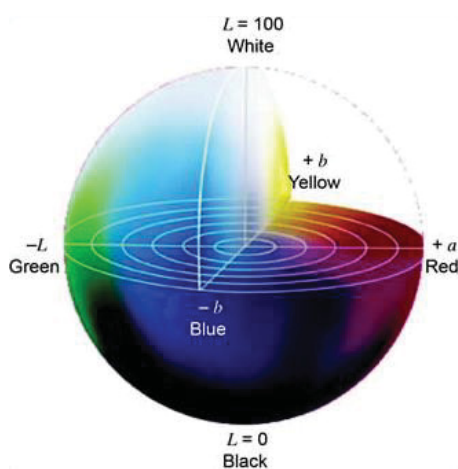


Figure 106. Diagram description of the chromaticity parameters $L^* a^* b^*$ in the CIE space

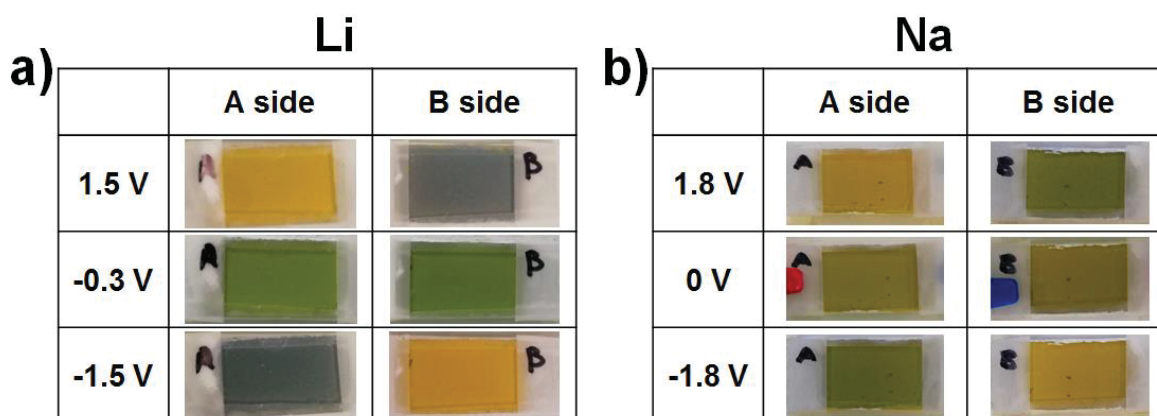


Figure 107. Color images at applied potential of EC device V_2O_5/Li (a,c) and Na (b,d)TFSI-EMITFSI-40% PMMA(70wt%)- TiO_2 (30wt%)/ V_2O_5

Table 27. CIE L*, a*, b* and color contrast(ΔE) values of V_2O_5/V_2O_5 device in Li and Na based electrolytes at applied potential.

Electrolyte	Device face	Voltage	Charge capacity (mA/cm ²)	Color	L*	a*	b*	ΔE
Li	Face A	1.5 V	30.1	Yellow	66.8	-4.8	51.3	60.5
		-1.5 V		Gray	50.6	-4.7	-7.2	
	Face B	1.5 V	29.2	Gray	51.3	-4.4	-5.0	58.1
		-1.5 V		Yellow	66.5	-3.7	51.0	
Na	Face A	1.5 V	9.2	Yellow	63.0	1.9	23.7	8.6
		-1.5 V		Green	59.9	-5.3	15.9	
	Face B	1.5 V	9.1	Green	59.7	-1.9	16.8	8.4
		-1.5 V		Yellow	61.6	0.9	21.4	

1.2.3 Switching time

Chronoamperograms of $V_2O_5/Li(Na)_xV_2O_5$ device were recorded at the -1.5 V and 1.5 V with a pulse duration of 120 s in Li and Na electrolytes (Figure 108). The switching time of the V_2O_5/V_2O_5 device was similar to that of a single V_2O_5 thin film. And also switching times using Na electrolyte are faster than in Li as seen in single thin films (Figure 49, p.79). This is due to the faradic contribution of V_2O_5 RF-metal thin film in Li electrolyte as compared to Na. (Figure 85 a, 86 a, p.119,120).

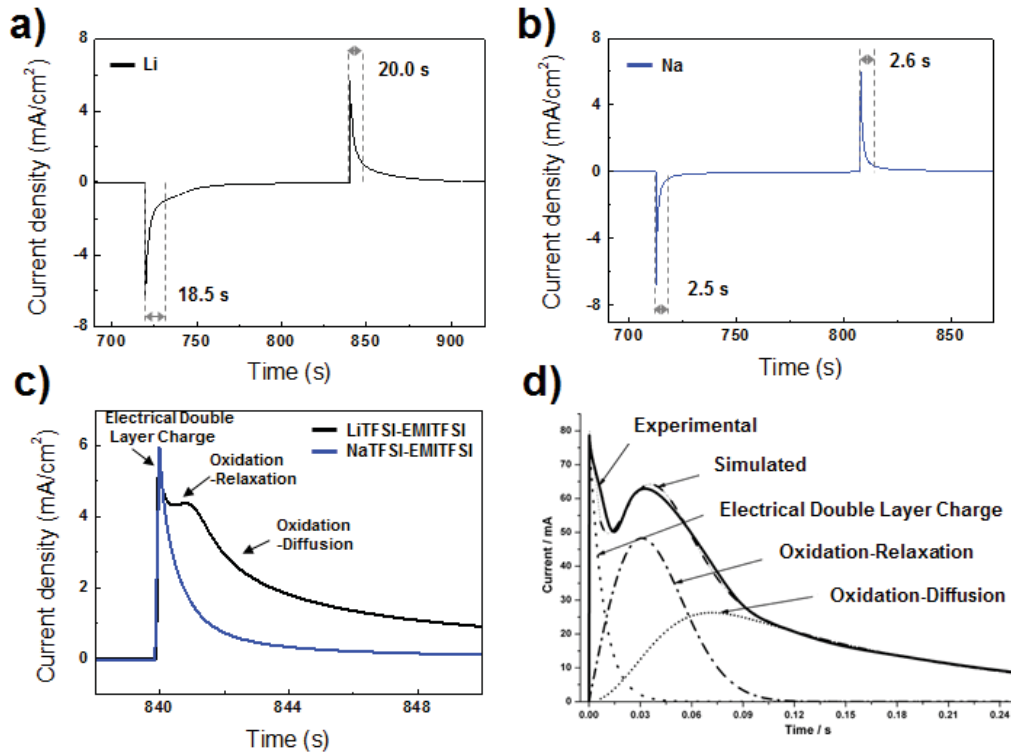


Figure 108. The evolution of chronoamperogram of V_2O_5/V_2O_5 devices, performed with the potential -1.5 V (120 s) / 1.5 V (120 s) in Li electrolyte and Na electrolyte, respectively.

From the results described above, we suggest that the phenomenon of insertion/deinsertion of cations in the single thin film occurs in the same way in full device. In conclusion, the fabricated double sides V_2O_5 /white-opaque gel liquid electrolyte/ V_2O_5 devices show multi-color electrochromism in Li electrolyte as well as in Na electrolyte and confirm that they are well driven and applicable to displays.

We also fabricated a double side full device labelled with ICMCB and U-BDX (University of Bordeaux). Figure 109 shows a full device that works well in Li based electrolyte.



Figure 109. Color images at applied potential of EC device represented the labels for ICMCB and U-BDX. $V_2O_5/LiTFSI-BMITFSI-40\% PMMA(70wt\%)-TiO_2(30wt\%)/V_2O_5$

Conclusion

Two types of ECDs using either transparent electrolyte membrane or opaque where fabricated coupling V_2O_5 thin films to WO_3 or to V_2O_5 in a symmetrical device aiming at application in smart windows and displays, respectively. V_2O_5/WO_3 EC device with transparent electrolyte membrane shows a good durability and a higher contrast associated with a difference of transmittance of $\sim 50\%$ in Li medium and $\sim 30\%$ in Na medium without performance deterioration. V_2O_5/V_2O_5 symmetrical device with an opaque white electrolyte shows multi-color of yellow, green and blue at applied potential. Each face of the device at applied voltage exhibits a different color.

General conclusion and perspectives

Vanadium oxide thin films were deposited with three different deposition conditions which are radio frequency magnetron sputtering (RFMS) with V metallic target (V_2O_5 RF-metal), V_2O_5 oxide target (V_2O_5 RF-oxide) and High Power Impulse Magnetron Sputtering (HiPIMS) with V metallic target (V_2O_5 HiPIMS), respectively. Vanadium oxide films of a constant thickness (200 nm) were deposited upon ITO coated glass substrate at room temperature (without substrate annealing).

Our initial step consists in the determination of the deposition conditions leading to higher electrochromic properties and better adhesion to the substrate. In addition, structure and morphology depends on the deposition conditions. V_2O_5 RF-metal thin film deposited at RF power of 200 W, total pressure of 2 Pa and $P(O_2)$ of 20% by RFMS shows crystalline orthorhombic structure, while V_2O_5 RF-oxide thin film deposited at RF power of 150 W, total pressure of 2 Pa and $P(O_2)$ of 2% by RFMS and V_2O_5 HiPIMS thin film deposited at 45 μ s, 1200 Hz, total pressure of 2 Pa and $P(O_2)$ of 10% by HiPIMS are amorphous. All as-deposited films were yellowish. Surface morphology of 200 nm V_2O_5 HiPIMS thin films is smooth, whereas 200 nm V_2O_5 RF-metal and 200 nm V_2O_5 RF-oxide thin films are rough.

V_2O_5 thin films were electrochemically characterized using V_2O_5 /electrolyte/Pt vs SCE galvanostatic chain. The current - potential curve was measured at a fixed scanning rate of 10 mV / sec in the range of -1.0 to 1.0 V in Li (LiTFSI-EMITFSI) and Na(NaTFSI-EMITFSI) electrolytes.

Cyclic voltammograms of V_2O_5 RF-metal thin films shows better resolution with the presence of two well defined peaks located at 0.3 V and 0.1 V in reduction and at 0.3 V and 0.5 V in oxidation in Li electrolyte, while a rather rectangular shape is observed in Na electrolyte. The V_2O_5 RF-metal film, initially yellow, goes through distinct and reversible color changes as green at 0.2 V, blue at -0.4 V and gray at -1 V upon reduction/oxidation. The reversible electrochromism with 4 color states was demonstrated for both electrolytes. However, the color of the thin film remains slightly green at 1 V in Na electrolyte suggesting a limited reversibility. *Ex-situ* optical transmittance shows different transmittance and color under applied potential. In Li electrolyte, transmittance modulation ΔT of 39% at 420 nm and 27% at 650 nm is determined between reduced gray state (-1 V) and the oxidized orange state

(+1 V). In Na electrolyte, the CV curves of V_2O_5 RF-oxide film exhibits one pair of reversible peaks located around 0 V in oxidation and -0.2 V in reduction. V_2O_5 RF-oxide thin films exhibit reversible multi-color as green at 0.2 V, blue at -0.4 V and gray at -1 V upon reduction/oxidation. The transmittance modulation ΔT are 41% and 23% at 420 nm and 650 nm respectively.

The CV curves of V_2O_5 RF-oxide film are characterized by a pair of redox peak located around 0 V in oxidation and -0.25 V in reduction in Li based electrolyte. The V_2O_5 RF-oxide film, initially yellow, goes through distinct and reversible color changes as green at 0.2 V, blue at -0.4 V and gray at -1 V upon reduction/oxidation. The transmittance modulation ΔT of 39% at 420 nm and 27% at 650 nm was determined between reduced gray state (-1 V) and the oxidized orange state (+1 V) in Li electrolyte. In Na electrolyte, the CV curves of V_2O_5 RF-oxide film show one pair of reversible peaks located around 0 V in oxidation and -0.2 V in reduction. V_2O_5 RF-oxide thin films exhibit reversible multi-color as green at 0.2 V, blue at -0.4 V and gray at -1 V upon reduction/oxidation. The transmittance modulation ΔT are 41% and 23% at 420 nm and 650 nm respectively.

The CV curves of V_2O_5 HiPIMS film are characterized by a pair of redox peak located around 0 V in oxidation and -0.2 V in reduction in Li based electrolyte. The V_2O_5 HiPIMS film, initially yellow, goes through distinct and reversible color changes as green at 0.2 V, blue at -0.4 V and gray at -1 V upon reduction/oxidation. *Ex-situ* optical transmittance shows different transmittance and color under applied potential. In Li electrolyte, transmittance modulation ΔT of 36% at 420 nm and 29% at 650 nm was determined between reduced gray state (-1 V) and the oxidized orange state (+1 V). In Na electrolyte, the CV curves of V_2O_5 HiPIMS film show one pair of reversible peaks located around -0.1 V in oxidation and -0.25 V in reduction. V_2O_5 HiPIMS thin films exhibit reversible multi-color as green at 0.2 V, blue at -0.4 V and gray at -1 V upon reduction/oxidation. The transmittance modulation ΔT are 44% and 25% at 420 nm and 650 nm respectively.

The amorphous thin films V_2O_5 HiPIMS and V_2O_5 RF-oxide show better electrochromic properties in not only Li medium but also in Na electrolyte than crystalline V_2O_5 RF-metal thin films. However, this behavior remains limited to the initial stage of cycling. It is noteworthy that the thin films deposited by HiPIMS show larger capacities than films deposited by RFMS. This is probably due to the fact that the films deposited by HiPIMS has

a higher density than the films deposited by RFMS.

During 1000 CV cycles, in Li based electrolyte, V₂O₅RF-metal thin films show continuously capacity increase with the decrease of the two well defined peaks and appearance of extra peaks. V₂O₅RF-oxide thin films show poor stability after 150 cycles with capacity decrease rapidly, while V₂O₅HiPIMS thin films show stable capacity trend as increasing CV cycles. In Na based electrolyte, similar cyclic voltammograms with one peak located in reduction and in oxidation are observed for V₂O₅RF-metal, V₂O₅RF-oxide and V₂O₅HiPIMS. The continuous capacity increase of V₂O₅RF-metal thin film is attributed to the increase of the surface area due to the crack and the change to the porous form

In Na based electrolyte, V₂O₅RF-metal films show stable capacity trend as increasing CV cycles during 1000 cycles. V₂O₅RF-oxide films show 20% decrease of capacity, while V₂O₅HiPIMS films show stable capacity trend as increasing CV cycles during 1000 cycles. These results follow the same phenomenon as in Li based electrolyte. The amorphous V₂O₅RF-oxide and V₂O₅HiPIMS films show larger capacity than crystalline V₂O₅RF-metal in Na based electrolyte. This trend well agrees with the fact that a large amount of distorted structures and defects (as compared to crystalline V₂O₅), is suitable to facilitate the insertion/deinsertion mechanism.

The determination of the EC mechanism was addressed by various means. From GIXRD analysis, V₂O₅RF-metal thin films show upon reduction that the (001) peak shifts progressively to lower angles, namely to 18.89° (0.2 V) and to 18.49° (-1 V,) while it returns to 19.78° (1 V) upon oxidation in Li electrolyte. The shifts correspond to an increase in the c parameter to 4.70 Å. (0.2 V, ion insertion coefficient x=0.35) and 4.78 Å. (-1.0 V, x=0.84). V₂O₅RF-metal thin films show the shift of the (001) peak to lower angle to 18.74° (0.2 V), and to 18.52° (-1 V). The shifts correspond to an increase in the c parameter to 4.70 Å (0.2 V, x=0.17) and 4.78 Å (-1.0 V, x=0.65). The significant discrepancy with cycling in Na based electrolyte comes from the presence of irreversibility illustrated by the position of the (001) peak at 18.90° (1V) lower than the one in the deposited state. The interlayer spacing of V₂O₅RF-metal thin films increases with insertion. The presence of Li or Na leads to an increase in repulsion in between the VO₅ planes as x increases. The evolution of the GIXRD patterns upon cycling would favor a simple insertion/desinsertion mechanism associated to the : $x\text{Li}^+ + xe^- + \text{V}_2\text{O}_5 \rightarrow \text{Li}_x\text{V}_2\text{O}_5$, Such mechanism with x values of 0.70 is supported by

XPS characterization and the distribution of V^{4+}/V^{5+} vanadium cations. During longer cycling conditions (1000 cycles), the XRD peak intensity of V_2O_5 RF-metal thin film decreases gradually. It means that the continuous capacity increase of V_2O_5 RF-metal thin film is attributed to the increase of the surface area as well as to change in the structure from crystalline to amorphous states. Getting away from a pure insertion/deinsertion mechanism, the evaluation of the scan rates on the CV shape tends to demonstrate that the mechanism is more complex and that it can be splitted in two contributions, namely faradic and capacitive.

In agreement with their amorphous character, V_2O_5 RF-oxide and V_2O_5 HiPIMS thin films show higher capacitive contributions than V_2O_5 RF-metal thin films in Li electrolyte. On the contrary, in Na electrolyte, the capacitive contributions are similar for the three types of V_2O_5 thin films. This result can explain that Na electrolytes exhibit very fast switching time due to higher capacitive components, while Li based electrolytes exhibit slow switching time due to faradic components.

From depth profile using ToF-SIMS, AES and RBS/NRA, the continuous increase of the Li content with reduction appears not fully homogeneous in the full thickness of the films but to occur preferentially at the interface.

Finally two types of electrochromic devices were fabricated; the first one combines Li and Na based ionic liquid transparent electrolyte to V_2O_5/WO_3 aiming at smart window application. EC device shows a good durability and a higher contrast associated with a difference of transmittance of ~50% without performance deterioration in Li medium. In Na electrolyte, EC device shows a good durability with difference of transmittance of ~30%. The second combination uses an opaque white electrolyte in a V_2O_5 symmetrical device for displays applications. V_2O_5/V_2O_5 device shows multi-color of yellow, green and blue at applied potential. Each face of device at applied voltage exhibit a different color.

In conclusion, three kinds of V_2O_5 thin films show multi-color and reversible electrochromic properties in Li and Na based electrolyte. Depending on the deposition method and conditions, different characteristics of the thin films were observed, which were related to the electrochromic properties. The different behaviors and mechanisms of the ionic species during the electrochromic process were investigated. In this study, it is possible to fabricate EC films with good performance in Li as well as Na electrolytes by using vanadium oxide, which can be applied to EC devices.

In the future, preliminary investigation of the mechanism needs to be completed. In our group, the comparison with thick V_2O_5 films coated from nanopowders shows similar multichromism from orange, green and blue, while the mechanism appears completely different. Upon cycling, V_2O_5 thick film goes through an amorphization-rechristallization process. Considering devices and application, a future direction lies in the combination of V_2O_5 with polymers, namely PEDOT, for the optimization of composite EC materials showing higher properties.

Finally, one can think of taking advantages of the very good memory effect of V_2O_5 for targeting new applications.

Appendix

Characterization Techniques of Structure

1. X-ray diffraction (XRD)

Film structures were determined by XRD. If the material is perfectly crystallized, the atoms should be continuous and infinite in three dimensions, forming regularly repeating atomic planes with a certain distance, d . When the distance d is close to the x-ray wavelength (λ_x), the X-rays are diffracted by the repeated atomic planes. As shown in Figure 110, a beam of parallel x-rays incident at angle θ to perfect atomic planes and the x-rays are reflected at θ from the planes. The path difference for the two reflected x-rays from the atomic planes is $2d \cdot \sin\theta$. If the path difference consists of a whole number of wavelengths, then the reflected x-ray waves interfere constructively. This rule is described by Bragg's law :

$$n\lambda_x = 2d \cdot \sin\theta \quad (24)$$

where n is an integer. Structure, phase composition, orientation of the planes and crystallinity information can be obtained from the diffraction peak position and intensity.

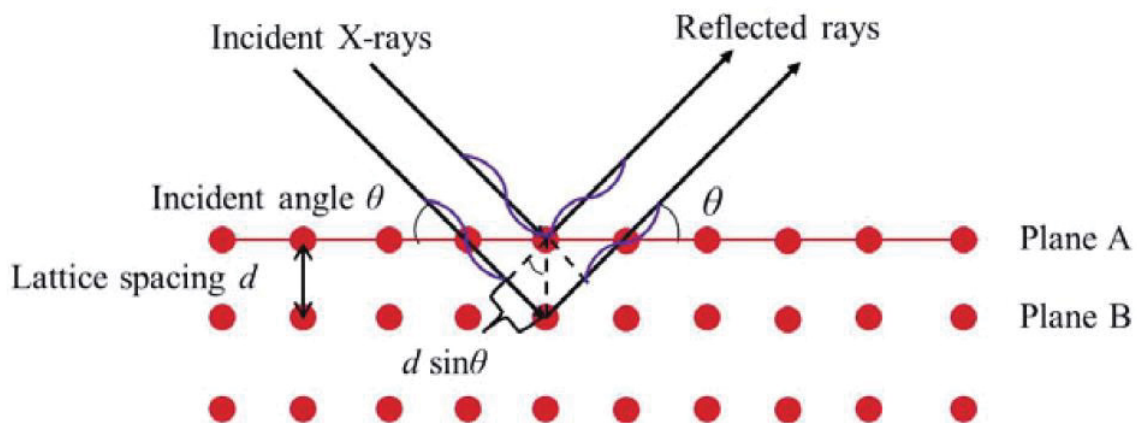


Figure 110. Principles of x-ray diffraction

2. Grazing Incidence X-Ray Diffraction (GIXRD)

X-ray techniques hold a leading role as a tool for material characterization. In this connection, X-ray powder diffraction (XRD) generally employs the conventional $\theta - 2\theta$ (or Bragg-Brentano) “reflection” geometry, in which the incidence angle equals the angle of the diffracted beam with respect to the inspected sample surface (Figure 111 a). The device configuration ensures that a high intensity beam diffracted from any particular set of crystalline planes of the sample will be focused onto a slit in front of the rotating detector. However, X-rays with large glancing angles of incidence will go through a few to several hundred micrometers inside the material under investigation, depending on its “radiation” density, so that when it comes to thin film analysis the beam penetration depth may be much greater than the sample thickness. Hence, conventional XRD is rather not suitable for detailed study of sub-micrometric layers in thin film specimens. For instance, in the case of a multilayer electrodeposited film, conventional XRD would only allow for tracing the complete structure after deposition, while the large number of overlapping peaks indicating the different crystallographic phases would make the spectrum interpretation difficult. Grazing incidence configurations have been developed to overcome such limitations, e.g., to render the XRD measurement more sensitive to the near surface region of the sample and minimize the substrate contribution on the diffraction response. Grazing Incidence X-Ray Diffraction (GIXRD) technique, the Bragg-Brentano geometry is modified to provide an “asymmetric” diffraction result, which allows access to small depths in the sample by varying the incidence angle. A parallel mono-chromatic X-ray beam falls on the sample surface at a fixed, low glancing angle, α (larger than the critical angle for total reflection, α_c , but usually smaller than 10°) and the diffraction profile is recorded by detector-scan only (Figure 111 b); non-rotating sample). GIXRD makes possible the use of X-rays for the characterization of surfaces, buried interfaces, and ultra thin films. By means of this technique, valuable information can be obtained regarding the thickness and phase crystallography of the sample [282-285] and its microstructure (stress, preferred orientation, etc.) [286].

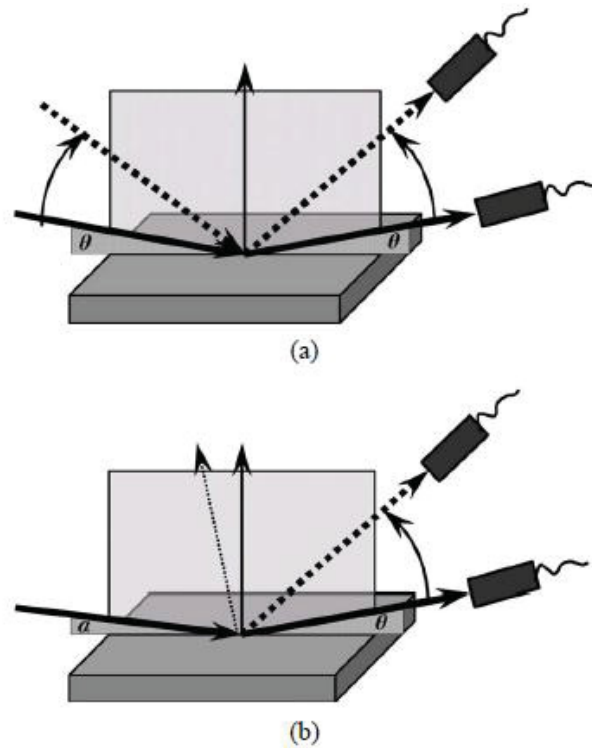


Figure 111. Schematic diagrams of (a) symmetric $\theta - 2\theta$, and (b) asymmetric glancing angle XRD geometry [286].

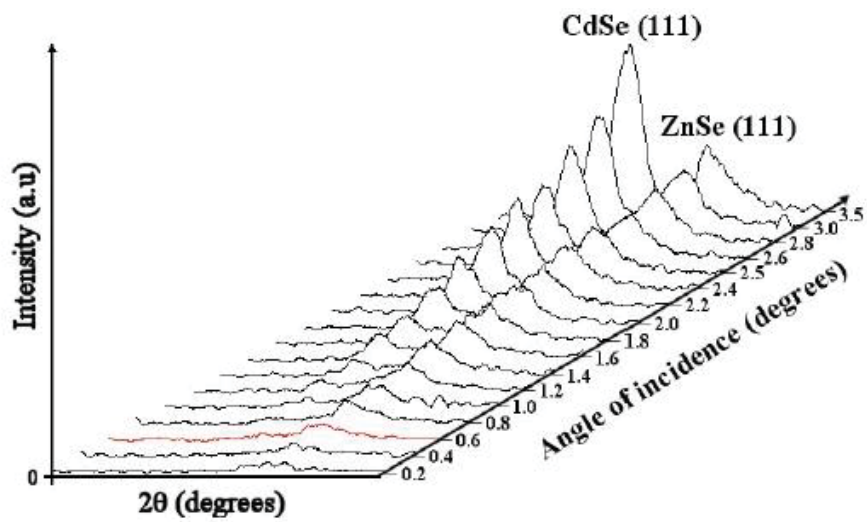


Figure 112. GAXRD diagrams of a ZnSe/CdSe bilayer electrodeposited on Ni from acidic electrolyte. ZnSe (111) and CdSe (111) reflections are indicated [287].

3. X-ray photoelectron spectroscopy (XPS)

X-ray photoelectron spectroscopy is a technique that uses an X-ray beam (photons) that will interact with the surface of a sample. X-rays are generated by high-energy electrons that strike a metal anode (commonly known as Al or Mg). The atoms present in the sample, receive a quantity of energy $h\nu$. This received energy allows the electrons (photoelectrons) which gravitate around the nucleus of the atom to break their bonds with the atom, Figure 113. During the ejection of the photoelectrons, they acquire a kinetic energy EC which will be read by the XPS spectrometer. Incident photons generally have energy of 1 to 2 keV. The photoelectrons then come only from the upper layers of the sample (<10 nm) because their energies are relatively low (20-2000 eV). Incident rays of low energies are favored, because they make it possible to obtain a good resolution of the order of the electron-volt. It is then possible to go back to the binding energies of the elements present in the sample. h corresponds to the Planck constant, ν is the frequency.

$$EL = h\nu + EC \quad (25)$$

The link energy (EL) of the photoelectrons has characteristic values, which make it possible to identify the elements. An XPS spectrum illustrates the intensity of photoelectrons (number of electrons input) as a function of the link energy (eV). At first, an ultra-vacuum is used to prevent the surface from becoming contaminated and to reduce the number of collisions that may occur with the gas present in the enclosure. Low-energy photoelectrons are easily dispersed by the gas and this can reduce the signal intensity by increasing the background noise of the spectrum. The set of orbitals is identified on a spectrum covering the range of energy of the source then each element is identified with analysis not on one of its orbitals.

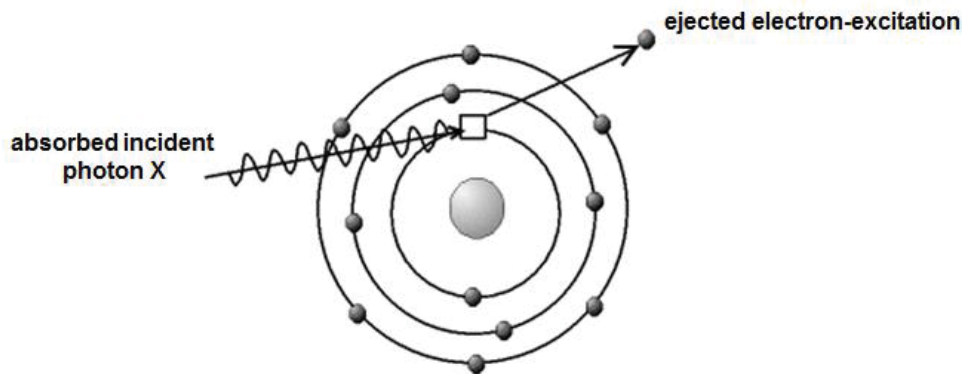


Figure 113. Schematic of the principle of the photoelectric effect, absorption of a photon with the emission of an electron from an atom

XPS spectra can have 3 types of peaks : photo-emission from the electrons of the orbitals closest to the nucleus, photo-emission from valence levels, and Auger emissions excited by X-ray. The XPS spectrum may also include satellite peaks that correspond to the interaction between a photoelectron and a valence electron. A photoelectron can excite a valence electron to a higher energy level and thus lose some electrons-volts of its kinetic energy. This will create satellite peaks close to the main photoemission peaks. The peaks are then fractionated into multiplet for chemical analysis. The position of the peaks of the elements in the spectrum is sensitive to their chemical environments but also to the degree of oxidation. Depth profile of surface chemistry can be generated using an ion gun, which provides a positively charged argon ion. These ions will spray the surface of the sample and a crater will form. A surface profile can be achieved by examining the crater at different depths. The chemical shift of peak binding energy for one element is caused by the chemical environment of the element. To quantize in XPS, a sensitivity factor for each element is used which may vary according to the conditions of the instrument.

4. Spectroscopy of energy loss of electrons (EELS)

When using a transmission electron microscope (TEM), high energy electrons pass through a thin film, and elastic and elastic disruptions occur, Figure 114. The electrons can then lose energy when they pass through the sample (elastic scattering). This elastic distribution will

depend essentially on the energy of the electrons, the thickness of the film and the atomic number of the excited atom. The loss of energy of these electrons can be used for detailed information such as the chemical composition of the material, the electronic structure, chemical bonds, and so on. The elastic distribution is the consequence of the direct interaction between the primary electrons of energy E_0 from the electron gun and the electrons heart of the atom, or those of the valence or conduction band. An EELS spectrometer consists of a dispersive analyzer and an electron gun. An electric field is created inside the dispersive analyzer that will disperse the electrons according to their energy.

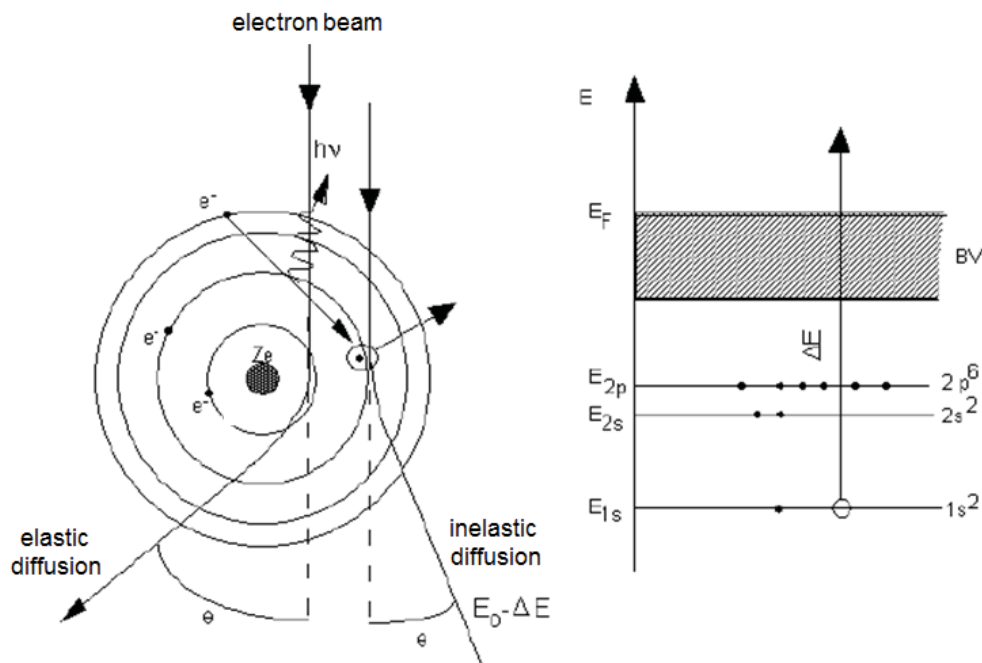


Figure 114. Elastic and inelastic deletion of electrons

5. Rutherford Backscattering Spectrometry (RBS)

The composition, element distribution and density of the sample can be determined by RBS by measuring the backscattering of a beam with high energetic light ions (typically 4He^+). The collision between the beam ions and near-surface atoms of the investigated sample is considered elastic. The energy of the elastically backscattered ions is measured at different backscattering angles by a detector, which can be adjusted based on the direction of the

incident beam ions. The measured energy depends on the mass of the investigated sample atoms and on the depth where the collision and scattering happen. The depth can be obtained by measuring the ion energy loss. This allows profiling the element concentration, composition and thickness of the thin film samples. The RBS measurements were carried out at the Uppsala Tandem Laboratory, specifically using 2MeV 4He ions back scattered at an angle of 170 degrees for nickel oxides and 172 degrees for iridium oxides. The RBS data were fitted to a model of the film–substrate system by use of the SIMNRA program. The film density ρ was computed from

$$\rho = \frac{MN_s}{n_{\text{atoms}}N_A d_i} \quad (26)$$

where M is molar mass, N_s is the areal density of atoms (atoms/cm²), n_{atoms} is number of atoms in a molecule, N_A is Avogadro's constant, and d_i is the film thickness in centimeters. Figure 115 (a) shows the RBS working principles and how to identify the elements and thickness; Figure 115 (b) shows a fitted RBS spectrum of Ir-Ni oxide to determine the compositions by SIMNRA.

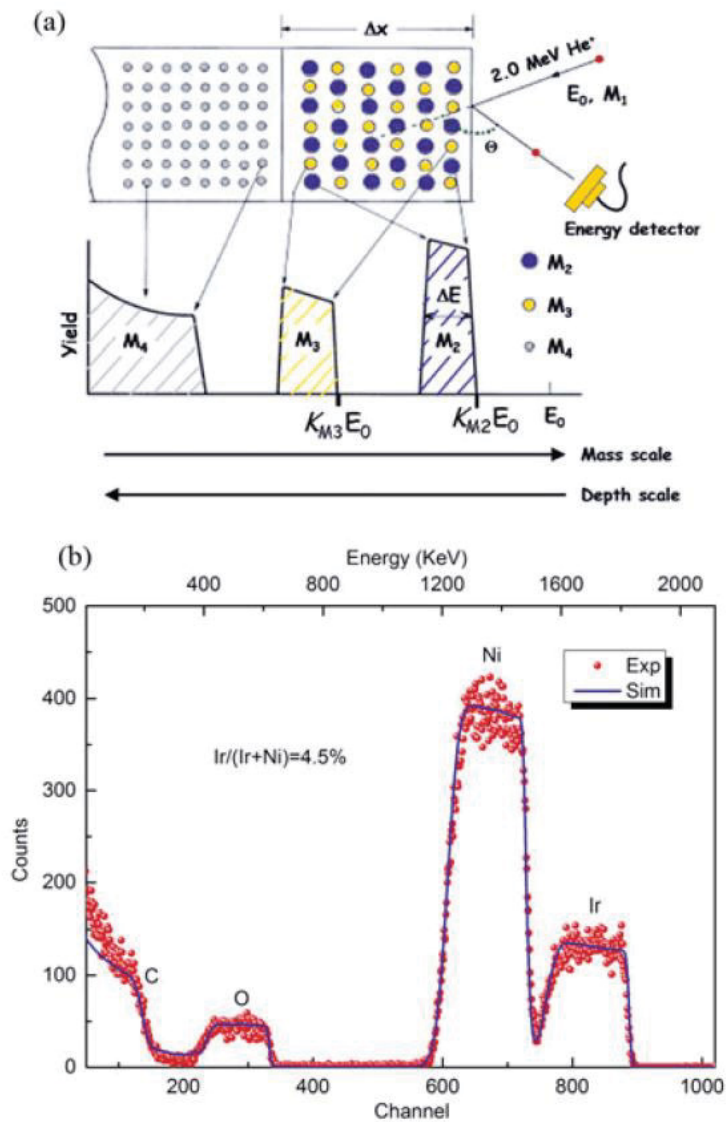


Figure 115. Working principle of RBS. (a) Schematic illustration of the backscattering spectrum of ions of mass M_1 impinging on a thin film containing two different masses (M_2 , M_3) deposited on a low-mass (M_4) elemental substrate. Energies of backscattered ions from various depths and various atoms are marked by arrows. The film thickness (Δx) is determined from the measured energy with ΔE . (b) A fitted RBS spectrum of Ir-Ni oxide thin film on a carbon substrate. Ir/(Ir+Ni) ratio was determined to be 4.5%.

Reference

- [1] N.L. Sbar, L. Podbelski, H.M. Yang, B. Pease, *Int. J. Sustainable Built Environ*, 1 (2012) 125~139.
- [2] J.S. Svensson, C.G. Granqvist, *Proc. SPIE Int. Soc. Opt. Eng. Proceedings of SPIE*, 502 (1984) 3037.
- [3] M. casini, *Renewable energy*, 119 (2018) 923.
- [4] www.suntuitive.com.
- [5] www.sageglass.com/fr/produits.
- [6] www.chromogenics.com.
- [7] www.viewglass.com.
- [8] www.econtrolglas.de.
- [9] E.L. Runnerstrom, A. Llordes, S.D. Lounis, D.J. Milliron, *Chem. Commun*, 50 (2014) 10555-10572.
- [10] www.gentex.com
- [11] Lawrence Berkeley National Laboratory. A design guide for early-market electrochromic windows. 2006.
- [12] <https://www.ynvisible.com>
- [13] M.A. Invernale, Y. Ding, G.A. Sotzing, *ACS Appl. Mater. Interfaces*, 2 (2010) 296-300.
- [14] Market reports electrochromic glass and film markets 2014-2021, www.ntechresearch.com.
- [15] A.F. Diaz, J.I. Castillo, J.A. Logan, W.Y. Lee, *J. Electroanal. Chem*, 129 (1981) 115-132.
- [16] T. Kobayashi, H. Yoneyama, H. Tamura, *J. Electroanal. Chem. Interfacial Electrochem*, 177 (1984) 281-291.
- [17] Q. Pei, G. Zuccarello, M. Ahlskog, O. Inganäs, *Polymer*, 35 (1994) 1347-1351.

- [18] A. Kumar, D.M. Welsh, M.C. Morvant, F. Piroux, K.A. Abboud, J.R. Reynolds, *Chem. Mater.*, 10 (1998) 896-902.
- [19] H.W. Heuer, R. Wehrmann, S. Kirchmeyer, *Adv. Funct. Mater.*, 12 (2002) 89-94.
- [20] J. Roncali, *Macromol. Rapid Commun.*, 28 (2007) 1761-1775.
- [21] Y.Z. Long, M.M. Li, C. Gu, M. Wan, J.L. Duvail, Z. Liu, Z. Fan, *Prog. Polym. Sci.*, 36 (2011) 1415-1442.
- [22] M. Mastragostino, C. Arbizzani, A. Bongini, G. Barbarella, M. Zambianchi, *Electrochim. Acta*, 38 (1993) 135-140.
- [23] F. Vidal, C. Plesse, P.H. Aubert, L. Beouch, F. Tran-Van, G. Palaprat, P. Verge, P. Yammine, J. Citerin, A. Kheddar, L. Sauques, C. Chevrot, D. Teyssie, *Polym. Int.*, 59 (2010) 313-320.
- [24] S. Lagoutte, P.H. Aubert, F. Tran-Van, X. Sallenave, C. Laaiteur, C. Sarrazin, C. Chevrot, *Electrochim. Acta*, 106 (2013) 13-22.
- [25] F. Tran-Van, M. Carrier, C. Chevrot, *Synth. Met.*, 142 (2004) 251-258.
- [26] P.R. Somani, S. Radhakrishnan, *Mater. Chem. Phys.*, 77 (2003) 117-133.
- [27] H.J. Byker, *Solution-Phase Electrochromic Devices and Systems*. 2015.
- [28] P.M.S. Monk R.J. Mortimer, D.R. Rosseinsky, *Electrochromic Materials and Devices*, 2015.
- [29] K. Itaya, K. Shibayama, H. Akahoshi, S. Toshima, *J. Appl. Phys.*, 53 (1982) 804-805.
- [30] A. Roig, J. Navarro, J.J. Garcia, F. Vicente, *Electrochim. Acta*, 39 (1994) 437-442.
- [31] G. Beni, L.M. Schiavone, J.L. Shay, W.C. Dautremont-Smith, B.S. Schneider, *Nature*, 282 (1979) 281~283.
- [32] S. Gottesfeld, *J. Electrochem. Soc.*, 127 (1980) 272-277.
- [33] S. Lee, P. Liu, H.M. Cheong, C.E. Tracy, S.K. Deb, *Solid State Ionics*, 165 (2003) 217-221.

- [34] C.G Granqvist, *Sol. Energy Mater. Sol. Cells*, 60 (2000) 201-262.
- [35] M. Chigane, M. Ishikawa, *J. Electrochem. Soc*, 147 (2000) 2246-2251.
- [36] T. Maruyama, S. Arai, *J. Electrochem. Soc*, 143 (1996) 1383-1386.
- [37] X.H. Xia, J.P. Tu, J. Zhang, X.L. Wang, W.K. Zhang, H. Huang, *Sol. Energy Mater. Sol. Cells*, 92 (2008) 628-633.
- [38] J. Livage, *Solid State Ionics*, 86-88 (1996) 935-942.
- [39] S.K. Deb, *Philos. Mag*, 27 (1973) 801822.
- [40] E. Washizu, A. Yamamoto, Y. Abe, M. Kawamura, K. Sasaki, *Solid State Ionics*, 165 (2003) 175-180.
- [41] A. Rougier, F. Portemer, A. Quede, M.E. Marssi, *Appl. Surf. Sci*, 153 (1999) 1-9.
- [42] K. Shimanoe, M. Suetsugu, N. Miura, N. Yamazoe, *Solid State Ionics*, 113-115 (1998) 415-419.
- [43] P.M.S. Monk, T. Ali, R.D. Partridge, *Solid State Ionics*, 80 (1995) 75-85.
- [44] K. Yoshimura, T. Miki, S. Iwama, S. Tanemura, *Thin Solid Films*, 281 (1996) 235-238.
- [45] M. Ottaviani, S. Panero, S. Morzilli, B. Scrosati, M. Lazzari, *Solid State Ionics*, 20 (1986) 197-202.
- [46] C. G. Granqvist, *Thin Solid Films*, 564 (2014) 1-38.
- [47] R. Wen, G.A. Niklasson, C.G. Granqvist, *Sol. Energy Mater. Sol. Cells*, 120 (2014) 151-156.
- [48] M. Bernard, A.H. Go, *J. Electrochem. Soc*, 140 (1993) 3065-3070.
- [49] P. Liu, S. Lee, C.E. Tracy, J.A. Turner, J.R. Pitts, S.K. Deb, *Solid State Ionics*, 165 (2003) 223-228.
- [50] Y. Shigesato, *Jpn. J. Appl. Phys*, 30 (1991) 1457.
- [51] S. Lee, H.M. Cheong, C.E. Tracy, A. Mascarenhas, A.W. Czanderna, S.K. Deb, *Appl. Phys. Lett*, 75 (1999) 1541-1543.

- [52] S.H. Lee, R. Deshpande, P.A. Parilla, K.M. Jones, B. To, A.H. Mahan, A.C. Dillon, *Adv. Mater.*, 18 (2006) 763-766.
- [53] T. Brezesinski, D.F. Rohlmg, S. Sallard, M. Antonietti, B.M. Smarsly, *Small*, 2 (2006) 1203-1211.
- [54] B. Gerand, L. Seguin, *Solid State Ionics*, 84 (1996) 199-204.
- [55] L. Seguin, M. Figlarz, J. Pannetier, *Solid State Ionics*, 63-65 (1993) 437-441.
- [56] M. Figlarz, *Prog. Solid State Chem*, 19 (1989) 1-46.
- [57] M. Kitao, H. Akram, K. Urabe, S. Yamada, *J. Electron. Mater.*, 21 (1992) 419-422.
- [58] K.K. Purushothaman, G. Muralidharan, *J. Sol-Gel Sci. Technol*, 46 (2007) 190-194.
- [59] X. Song, G. Dong, F. Gao, Y. Xiao, Q. Liu, X. Diao, *Vacuum*, 111 (2015) 48-54.
- [60] R.B. Goldner, G. Seward, K. Wong, T. Haas, G.H. Foley, R. Chapman, S. Schulz, *Sol. Energy Mater. Sol. Cells*, 19 (1989) 17-26.
- [61] S.A. Agnihotry, N. Pradeep, S.S Sekhon, *Solid State Ionics*, 136-137 (2000) 573-576.
- [62] O. Bohnke, C. Rousselot, P.A. Gillet, C. Truche, *J. Electrochem. Soc*, 139 (1992) 1862-1865.
- [63] R. Marcilla, F. Alcaide, H. Sardon, J.A. Pomposo, C. Pozo-Gonzalo, D. Mecerreyes, *Electrochem. Commun*, 8 (2006) 482-488.
- [64] A. Fericola, B. Scrosati, H. Ohno, *Solid State Ionics*, 12 (2006) 95-102.
- [65] H. Moulki, D.H. Park, B.K. Min, H. Kwon, S.J. Hwang, J.H. Choy, T. Toupance, G. Campet, A. Rougier, *Electrochim. Acta*, 74 (2012) 46-52.
- [66] W. Lu, A.G. Fadeev, B. Qi, B.R. Mattes, *J. Electrochem. Soc*, 151 (2004) H33-H39.
- [67] M. Deepa, A. Awadhia, S. Bhandari, *Phys. Chem. Chem. Phys*, 11 (2009) 5674-5685.
- [68] K.L. Chopra, S. Major, D.K. Pandya, *Thin Solid Films*, 102 (1983) 1-46.
- [69] B.G. Lewis, D.C. Paine, *MRS Bulletin*, 25 (2000) 22-27.

- [70] J.C. Manificier, *Thin Solid Films*, 90 (1982) 297-308.
- [71] W. Tang, D.C. Cameron, *Thin Solid Films*, 238 (1994) 83-87.
- [72] X. Yu, J. Ma, F. Ji, Y. Wang, X. Zhang, C. Cheng, H. Ma, *J. Cryst. Growth*, 274 (2005) 474-479.
- [73] P.C. Lansaker, J. Backholm, G.A. Niklasson, C.G. Granqvist, *Thin Solid Films*, 518 (2009) 1225-1229.
- [74] G. Leftheriotis, S. Papaefthimiou, P. Yianoulis, *Sol. Energy Mater. Sol. Cells*, 61 (2000) 107-112.
- [75] R. Yu, C. Zhang, Q. Meng, Z. Chen, H. Liu, Z. Guo, *ACS Appl. Mater. Interfaces*, 5 (2013) 12394-12399.
- [76] X. Li, C. Liu, C. Zhang, H. Fu, X. Nan, W. Ma, Z. Li, K. Wang, H. Wu, G. Cao, *ACS Appl. Mater. Interfaces*, 8 (2016) 24629-24637.
- [77] Y. Tang, X. Rui, Y. Zhang, T.M. Lim, Z. Dong, H.H. Hng, X. Chen, Q. Yan, Z. Chen, *J. Mater. Chem. A*, 1 (2013) 82-88.
- [78] S. Caes, J.C. Arrebola, N. Krins, P. Eloy, E.M. Gaigneaux, C. Henrist, R. Cloots, *J. Mater. Chem. A*, 2 (2014) 5809-5815.
- [79] I. Mjejri, N. Etteyeb, F. Sediri, *J. Alloys Compd.* 611 (2014) 372-380.
- [80] S. Tepavcevic, H. Xiong, V.R. Stamenkovic, X. Zuo, M. Balasubramanian, V.B. Prakapenka, C.S. Johnson, T. Rajh, *ACS Nano*, 6 (2012) 530-538.
- [81] L.L. Zhang, G. Liang, A. Ignatov, M.C. Croft, X.Q. Xiong, I.M. Hung, Y.H. Huang, X.L. Hu, W.X. Zhang, Y.L. Peng, *J. Phys. Chem. C*, 115 (2012) 13520-13527.
- [82] M. Simões, Y. Mettan, S. Pokrant, A. Weidenkaff, *J. Phys. Chem. C*, 118 (2014) 14169-14176.
- [83] L. Yu, J. Xi, *ACS Appl. Mater. Interfaces*, 8 (2016) 23425-23430.
- [84] Y. Wang, T. Katsunori, H.L. Kyoungcho, G.Z. Cao, *Adv. Funct. Mater.*, 16 (2016) 1133-1144.

- [85] R. Baddour-Hadjean, A. Boudaoud, S. Bach, N. Emery, J.P. Pereira-Ramos, *Inorganic Chemistry*, 53 (2014) 1764-1772.
- [86] R. Baddour-Hadjean, M.S. Renard, N. Emery, L.T.N. Huynh, M.L.P. Le, J.P. Pereira-Ramos, *Electrochim. Acta*, 270 (2018) 129-137.
- [87] A. Dhayal Raj, T. Pazhanivel, P. Suresh Kumar, D. Mangalaraj, D. Nataraj, N. Ponpandian, *Curr. Appl. Phys.* 10 (2010) 531-537.
- [88] J. Liu, X. Wang, Q. Peng, Y.D. Li, *Adv. Mater*, 17 (2005) 764-767.
- [89] K.S. Karimov, M. Saleem, M. Mahroof-Tahir, R. Akram, M.T. Saeed Chane, A.K. Niaz, *J. Semicond*, 9 (2014) 094001.
- [90] Y. Iida, Y. Kaneko, Y. Kanno, *J. Mater. Process. Technol*, 197 (2008) 261-267.
- [91] M. Kovendhan, D.P. Joseph, P. Manimuthu, A. Sendilkumar, S.N. Karthick, S. Sambasivam, K. Vijayarangamuthu, H.J. Kim, B.C. Choi, K. Asokan, C. Venkateswaran, R. Mohan, *Curr. App. Phys*, 15 (2015) 622-631.
- [92] Y. Yang, D. Kim, P. Schmuki, *Electrochem. Commun*, 13 (2011) 1021-1025.
- [93] Y. Wei, J. Zhou, J. Zheng, C. Xu, *Electrochim. Acta*, 166 (2015) 277-284.
- [94] W. Kang, C. Yan, X. Wang, C.Y. Foo, A.W.M. Tan, K.J.Z. Chee, P.S. Lee, *J. Mater. Chem. C*, 2 (2014) 4727-4732.
- [95] Z. Tong, H. Yang, L. Na, H. Qu, X. Zhang, J. Zhao, Y. Li, *J. Mater. Chem. C*, 3 (2015) 3159-3166.
- [96] L. Ottaviano, A. Pennisi, F. Simone, A.M. Salvi, *Opt. Mater*, 27 (2014) 307-313.
- [97] Y. Fujita, K. Miyazaki, C. Tatsuyama, *Jpn J Appl Phys*, 24 (1985) 1082-1084.
- [98] Z. Wang, J. Chen, X. Hu, *Thin Solid Films*, 375 (2000) 238.
- [99] I. Mjejri, M. Gaudon, G. Song, C. Labrugère, A. Rougier, *ACS Appl. Energy Mater*, 1 (2018) 2721-2729.
- [100] G. Salek, B. Bellanger, I. Mjejri, M. Gaudon, A. Rougier, *Inorg. Chem*, 55 (2016) 9838-9847.

- [101] I. Mjejri, L.M. Manceri, M. Gaudon, A. Rougier, F. Sediri, *Solid State Ionics*, 292 (2016) 8–14.
- [102] S. Kumar, A. Qadir, F. Maury, N. Bahlawane, *ACS Appl. Mater. Interfaces*, 9 (2017) 21447-21456.
- [103] D.H. Qiu, Y.Q. Wen, Q.H. Yang, Z. Chen, Y.L. Jing, H.W. Zhang, *Mater. Sci. Semicond. Process*, 27 (2014) 140-144.
- [104] M.M. Seyfour, R. Binions, *Sol. Energy Mater. Sol. Cells*, 59 (2017) 52- 65.
- [105] W. Li, S. Ji, K. Qian, P. Jin, *J. Colloid Interface Sci*, 456 (2015) 166-173.
- [106] H. Zhang, X. Xiao, X. Lu, G. Chai, Y. Sun, Y. Zhan, G. Xu, *J. Alloys Compd*, 636 (2015) 106-112.
- [107] Z. Liu, F. Guojia, W. Youqing, B. Yandong, Y. Kai-Lun, *J. Phys. D: Appl. Phys*, 33 (2000) 2327-2332.
- [108] C. Wu, F. Feng, Y. Xie, *Chem. Soc. Rev*, 42 (2013) 5157-5183.
- [109] I. Mjejri, A. Rougier, M. Gaudon, *Inorg. Chem*, 56 (2017) 1734-1741.
- [110] M. Kang, I. Kim, S. Kim, J. Ryu, H. Park, *Appl. Phys. Lett*, 98 (2011) 131907.
- [111] E.E. Chain, *Appl. Opt*, 30 (1991) 2782-2787.
- [112] C. Wu, F. Feng, Y. Xie, *Chem. Soc. Rev*, 42 (2013) 5157-5183.
- [113] Z. Zhang, Y. Gao, Z. Chen, J. Du, C. Cao, L. Kang, H. Luo, *Langmuir*, 26 (2010) 10738-10744.
- [114] S. Andersson, *J. Phys. Chem. Solids*, 28 (1967) 1613-1621.
- [115] D. Wruck, *Thin Solid Films*, 182 (1989) 79-85.
- [116] A.A. Akl, *Appl. Surf. Sci*, 253 (2007) 7094-7099.
- [117] Y. Yue, H. Liang, *Adv. Energy Mater*, 7 (2017) 1602545.
- [118] N.A. Chernova, M. Roppolo, A.C. Dillon, M.S. Whittingham, *J. Mater. Chem*, 19 (2009) 2526-2552.

- [119] P. Balog, D. Orosel, Z. Cancarevic, C. Schon, M. Jansen, *J. Alloys Compd*, 429 (2007) 87.
- [120] S. Beke, *Thin Solid Films*, 512 (2011) 1761-1771.
- [121] A.M. Lejus, D. Ballutaud, C.R. Kha, J. Livage, *Mat. Res. Bull.* 15 (1980) 95-102.
- [122] L.C. Tien, Y.J. Chen, *Appl. Surf. Sci.*, 274 (2013) 64-70.
- [123] Y. Yue, H. Liang, *Adv. Energy Mater.*, 7 (2017) 1602545.
- [124] C.G. Granqvist, *Handbook of Inorganic Electrochromic Oxides*, Elsevier, Amsterdam, (1995)
- [125] Y. Iida, Y. Kaneko, Y. Kanno, *J. Mater. Process. Technol.*, 197 (2008) 261-267.
- [126] M. Kovendhan, D.P. Joseph, P. Manimuthu, A. Sendilkumar, S.N. Karthick, S. Sambasivam, K. Vijayarangamuthu, H.J. Kim, B.C. Choi, K. Asokan, C. Venkateswaran, R. Mohan, *Curr. App. Phys.*, 15 (2015) 622-631.
- [127] Z. Tong, H. Yang, L. Na, H. Qu, X. Zhang, J. Zhao, Y. Li, *J. Mater. Chem. C*, 3 (2015) 3159-3166.
- [128] Z. Tong, X. Zhang, H. Lv, N. Li, H. Qu, J. Zhao, Y. Li, X.Y. Liu, *Adv. Mater. Interfaces*, 2 (2015) 1500230.
- [129] Z. Tong, H. Lv, X. Zhang, H. Yang, Y. Tian, N. Li, J. Zhao, Y. Li, *Sci. Rep.*, 5 (2015) 16864.
- [130] Z. Tong, J. Hao, K. Zhang, J. Zhao, B.L. Su, Y. Li, *J. Mater. Chem. C*, 2 (2014) 3651-3658.
- [131] I. Quinzeni, S. Ferrari, E. Quartarone, P. Mustarelli, *J. Power Sources*, 196 (2011) 10228-10233.
- [132] I. Mjejri, L.M. Mancieru, M. Gaudon, A. Rougier, F. Sediri, *Solid State Ionics*, 292 (2016) 8-14.
- [133] X. Peng, X. Zhang, L. Wang, *Adv. Funct. Mater.*, 26 (2016) 784.
- [134] C. Petitjean, M. Grafoute, J.F. Pierson, C. Rousselot, O. Banakh, *J. Phys. D: Appl. Phys.*,

39 (2006) 1894-1898.

[135] D. Horwat, M. Jullien, F. Capon, J.F. Pierson, J. Andersson, *J. Phys. D: Appl. Phys.*, 43 (2010) 132003.

[136] R. Lucio-Porto, S. Bouhtiyya, J.F. Pierson, A. Morel, F. Capon, *Electrochim. Acta*, 141 (2014) 203-211.

[137] B. Laik, S. Bourg, J.P. Pereira-Ramos, S. Bruyere, J.F. Pierson, *Electrochim. Acta*, 164 (2015) 12-20.

[138] M. Grafouté, C. Petitjean, A. Diama, J.F. Pierson, J.M. Greneche, *Surf. Coat. Technol.*, 272 (2015) 158-164.

[139] M. Fenker, O. Banakh, H. Kappl, N. Martin, J.F. Pierson, *Surf. Coat. Technol.*, 201 (2006) 4152-4157.

[140] Y. Wang, J. Ghanbaja, F. Soldera, S. Migot, P. Boulet, *Appl. Surf. Sci.*, 335 (2015) 85-91.

[141] A. Sreedhar, M. Hari Prasad Reddy, S. Uthanna, J.F. Pierson, *Adv. Sci. Lett.*, 20 (2014) 946-952.

[142] J.E. Mahan, *Physical vapor deposition of thin films*, Wiley inter-science, 2000.

[143] B.A. Movchan, A.V. Demchishin, *Phys. Met. Metalogr.*, 28 (1969) 83.

[144] J.A. Thornton, *J. Vac. Sci. Technol.*, 11 (1974) 666-670.

[145] A. Anders, *Thin Solid Films*, 518 (2010) 4087-4090.

[146] Y. Liu, M. Clark, Q. Zhang, D. Yu, D. Liu, J. Liu, G. Cao, *Adv. Energy Mater.*, 1 (2011) 194.

[147] C. Niu, J. Li, H. Jin, H. Shi, Y. Zhu, W. Wang, M. Cao, *Electrochim. Acta*, 182 (2015) 621.

[148] K.E. Swider-Lyons, C.T. Love, D.R. Rolison, *Solid State Ionics*, 152 (2002) 99.

[149] Z. Chen, V. Augustyn, J. Wen, Y. Zhang, M. Shen, B. Dunn, Y. Lu, *Adv. Mater.*, 23 (2011) 791.

- [150] B. Saravanakumar, K.K. Purushothaman, G. Muralidharan, *ACS Appl. Mater. Interfaces*, 4 (2012) 4484.
- [151] C.G. Granqvist, *Sol. Energy Mater. Sol. Cells*, 99 (2012) 1.
- [152] D. Louloudakis, D. Vernardou, E. Spanakis, N. Katsarakis, E. Koudoumas, *Surf. Coat. Technol*, 230 (2013) 186.
- [153] O. Berezina, D. Kirienko, A. Pergament, G. Stefanovich, A. Velichko, V. Zlomanov, *Thin Solid Films*, 574 (2015) 15.
- [154] J. Huotari, R. Bjorklund, J. Lappalainen, A.L. Spetz, *Sens. Actuators. B*, 217 (2015) 22-29.
- [155] S. Tepavcevic, H. Xiong, V.R. Stamenkovic, X. Zuo, M. Balasubramanian, V.B. Prakapenka, C.S. Johnson, T. Rajh, *ACS nano*, 6 (2012) 530-538.
- [156] W. Luo, J. Gaumet, L. Mai, *MRS Communications*, 7 (2017) 152-165
- [157] E. Hollands, D.S. Campbell, *J. Mater. Sci*, 3 (1968) 544552.
- [158] H. Miyazaki, H. Sakamura, M. Kamei, I. Yasui, *Solid State Ionics*, 122 (1999) 223-229.
- [159] E. Mandouh, MS. Selim, *Thin Solid Films*, 371 (2000) 259.
- [160] K. Melghit, S.P. Pillai, V.G. Kumar Das, *J. Mater. Sci. let*, 18 (1999) 661.
- [161] N. Elkadry, A. Ashour, M.F. Ahmed, K. Abdel-Hady, *Thin Solid Films*, 229 (1995) 194.
- [162] L. Ottaviano, A. Pennisi, F. Simone, A.M. Salvi, *Opt. Mater*, 27 (2004) 307-313.
- [163] K.M. Park, S. Yi, S. Moon, S. Im, *Opt. Mater*, 17 (2001) 311.
- [164] S. Thiagarajan, M. Thaiyan, R. Ganesan, *New J. Chem*, 39 (2015) 9471.
- [165] Z. Luo, Z. Wu, X. Xu, M. Du, T. Wang, Y. Jiang, *Vacuum*, 85 (2010) 145-150.
- [166] C.R. Aita, Y.L. Liu, M.L. Kao, S.D. Hansen, *J. Appl. Phys*, 60 (1986) 749.
- [167] M.S.B. Castro, C.L. Ferreira, R.R. Avillez, *Infrared Phys. Technol*, 60 (2013) 103-107.
- [168] L. Ottaviano, A. Pennisi, F. Simone, A.M. Salvi, *Optical Materials*, 27 (2004) 307-313.

- [169] M.S.B. Castro, C.L. Ferreira, R.R. Avillez, *Infrared Phys. Technol*, 60 (2013) 103-107.
- [170] P. Singh, D. Kaur, *J. Appl. Phys*, 4 (2008) 103.
- [171] A.A. Akl, *Appl. Surf. Sci*, 253 (2007) 7094-7099.
- [172] H. Miyazaki, H. Sakamura, M. Kamei, I. Yasui, *Solid State Ionics*, 122 (1999) 223-229.
- [173] S. Oukassi, R. Salot, J.P. Pereira-Ramos, *Appl. Surf. Sci*, 256 (2009) 149-155.
- [174] M. Benmoussa, E. Ibnouelghazi, A. Bennouna, E.L. Ameziane, *Thin Solid Films*, 265 (1995) 22-28.
- [175] S. Oukassi, R. Salot, J.P. Pereira-Ramos, *Appl. Surf. Sci*, 256 (2009) 149-155.
- [176] I. Mjejri, A. Rougier, M. Gaudon, *Inorg. Chem*, 56 (2017) 1734-1741.
- [177] G. Van der Laan, I.W. Kirkman, *J. Phys.: Condens. Matter*, 4 (1992) 4189-4204.
- [178] L. Laffont, M.Y. Wu, F. Chevallier, P. Poizot, M. Morcrette, J.M. Tarascon, *Micron*, 37 (2006) 459-464.
- [179] T. Gallasch, T. Stockhoff, D. Baither, G. Schmitz, *J. Power Sources*, 196 (2011) 428-435.
- [180] S. Sorieul, P. Alfaut, L. Daudin, L. Serani, P. Moretto, *Nucl. Instrum. Methods Phys. Res., Sect. B*, 332 (2014) 68-73.
- [181] C. Navone, R. Baddour-Hadjean, J.P. Pereira-Ramos, R. Salot, *J. Electrochem. Soc*, 152 (2005) A1790-A1796.
- [182] M. Zhi, W. Huang, Q. Shi, B. Peng, K. Ran, *J. Electrochem. Soc*, 163 (2016) H891.
- [183] M. Benmoussa, A. Outzourhit, A. Bennouna, A. Ihlal, *Eur. Phys. J. Appl. Phys*, 48 (2009) 10502.
- [184] K. Nagase, Y. Shimizu, N.Miura, N. Yamazoe, *Appl. Phys. Lett*, 60 (1992) 802.
- [185] Z. Wang, J. Chen, X. Hu, *Thin Solid Films*, 375 (2000) 238.
- [186] W. He, Y. Liu, Z. Wan, C. Ji, *RSC Adv*, 6 (2016) 68997.

- [187] K.C. Cheng, F.R. Chen, J.J. Kai, *Sol. Energy Mater. Sol. Cells*, 90 (2006) 1156.
- [188] H.K. Koduru, H.M. Obili, G. Cecilia, *Int. Nano Lett*, 3 (2013) 24.
- [189] C.E. Patil, N.L. Tarwal, P.S. Shinde, H.P. Deshmukh, P.S. Patil, *J. Phys. D: Appl. Phys*, 42 (2009) 025404.
- [190] Z.C. Wang, Z.Y. Li, X.F. Chen, X.F. Hu, *Acta Phys. Sin*, 8 (1999) 57.
- [191] S.F. Cogan, N.M. Nguyen, S.J. Perrotti, R.D. Rauh, *J. Appl. Phys*, 66 (1989) 1333.
- [192] Y.S. Lin, C.W. Tsai, P.W. Chen, *Solid State Ionics*, 179 (2008) 290.
- [193] M. Panagopoulou, *Electrochim. Acta*, 232 (2017) 54-63.
- [194] W. Yong, H.L. Zhang, H.T. Cao, T. Tian, J.H. Gao, L.Y. Liang, F. Zhuge, *J Sol-Gel Sci Technol*, 77 (2016) 604-609.
- [195] C.E. Patil, N.L. Tarwal, P.R. Jadhav, P.S. Shinde, H.P. Deshmukh, M.M. Karanjkar, A.V. Moholkar, M.G. Gang, J.H. Kim, P.S. Patil, *Curr. Appl Phys*, 14 (2014) 389-395.
- [196] Y. Tezuka, K. Aoki, *J. Electroanal. Chem*, 273 (1989) 161.
- [197] Y. Tezuka, S. Ohyama, T. Ishii, K. Aoki, *Bull. Chem. Soc. Jpn*, 64 (1991) 2045.
- [198] T.F. Otero, H.J. Grande, J. Rodriguez, *J. Phys. Chem. B*, 101 (1997) 3688.
- [199] P. Gimenez, K. Mukai, K. Asaka, K. Hata, H. Oike, T.F. Otero, *Electrochim. Acta*, 60 (2012) 177-183.
- [200] T.F. Otero, J.G. Martinez, K. Asaka, *Front. Mater*, 3 (2016) 3.
- [201] I. Petrov, P.B. Barna, L. Hultman, J.E. Greene, *J. Vac. Sci. Technol., A*, 21 (2003) S117.
- [202] J. Robertson, *Mater. Sci. Eng., R*, 37 (2002) 129.
- [203] U. Helmersson, M. Lattemann, J. Bohlmark, A. Ehiasarian, J. Gudmundsson, *Thin Solid Films*, 513 (2006) 1.
- [204] S. Konstantinidis, C. Nouvellon, J.P. Dauchot, M. Wautelet, M. Hecq, *Surf. Coat. Technol*, 174 (2003) 100.

- [205] V. Kouznetsov, K. Macák, J.M. Schneider, U. Helmersson, I. Petrov, *Surf. Coat. Technol*, 122 (1999) 290.
- [206] K. Sarakinos, J. Alami, S. Konstantinidis, *Surf. Coat. Technol*, 204 (2010) 1661.
- [207] V. Kouznetsov, K. Macák, J.M. Schneider, U. Helmersson, I. Petrov, *Surf. Coat. Technol*, 122 (1999) 290.
- [208] J. Bohlmark, J.T. Gudmundsson, J. Alami, M. Latteman, U. Helmersson, *IEEE Trans. Plasma Sci*, 33 (2005) 346.
- [209] J.T. Gudmundsson, P. Sigurjonsson, P. Larsson, D. Lundin, U. Helmersson, *J. Appl. Phys*, 105 (2009) 123302.
- [210] C. Christou, Z.H. Barber, *J. Vac. Sci. Technol., A*, 18 (2000) 2897.
- [211] J.T. Gudmundsson, *Vacuum*, 84 (2010) 1360.
- [212] J. Alami, K. Sarakinos, F. Uslu, M. Wuttig, *J. Phys. D: Appl. Phys*, 42 (2009) 015304
- [213] B.M. DeKoven, P.R. Ward, R.E. Weiss, D.J. Christie, R.A. Scholl, W.D. Sproul, F. Tomasel, A. Anders, *46th Annual Technical Conf. Proc*, (2003) 158.
- [214] J. Bohlmark, J. Alami, C. Christou, A.P. Ehiasarian, U. Helmersson, *J. Vac. Sci. Technol., A*, 23 (2005) 18.
- [215] J.T. Gudmundsson, N. Brenning, D. Lundin, U. Helmersson, *J. Vac. Sci. Technol., A*, 30 (2012) 30801.
- [216] S. Loquai, J.P. Fortier, M. Hála, O. Zabeida, J.E. Klemberg-Sapieha, *SVC Bulletin*, (2014) 46-49.
- [217] U. Helmersson, M. Lattemann, J. Bohlmark, A.P. Ehiasarian, J.T. Gudmundsson, *Thin Solid Films*, 513 (2006) 1-24.
- [218] M. Samuelsson, D. Lundin, J. Jensen, M.A. Raadu, J.T. Gudmundsson, U. Helmersson, *Surf. Coat. Technol*, 202 (2010) 591-596.
- [219] A.P. Ehiasarian, A. Vetushka, Y.A. Gonzalvo, G. Sáfrán, L. Székely, P.B. Barna, *J. Appl. Phys*, 109 (2011) 104314.

- [220] F. Magnus, A.S. Ingason, O.B. Sveinsson, S. Olafsson, J.T. Gudmundsson, *Thin Solid Films*, 520 (2011) 1621.
- [221] J. Alami, K. Sarakinos, F. Uslu, M. Wuttig, *J. Phys. D: Appl. Phys*, 42 (2009) 015304.
- [222] S. Shayestehaminzadeh, T.K. Tryggvason, F. Magnus, S. Olafsson, J.T. Gudmundsson, *Thin Solid Films*, 549 (2013) 199-203.
- [223] A.P. Ehiasarian, J.G. Wen, I. Petrov, *J. Appl. Phys*, 101 (2007) 054301.
- [224] J. Paulitch, M. Schenkel, T. Zafrass, P.H. Mayrhofer, W.D. Münz, *Thin Solid Films*, 518 (2010) 5558-5564.
- [225] J.M. Schneider, W.D. Sproul, A.A. Voevodin, A. Matthews, *J. Vac. Sci. Technol., A*, 15 (1997) 1084.
- [226] M. Lattemann, U. Helmersson, J.E. Greene, *Thin Solid Films*, 518 (2010) 5978.
- [227] J. Bohlmark, M. Östbye, M. Lattemann, H. Ljungcrantz, T. Rosell, U. Helmersson, *Thin Solid Films*, 515 (2006) 1928.
- [228] K. Bobzin, N. Bagcivan, P. Immich, S. Bolz, J. Alami, R. Cremer, *J. Mater. Process. Technol*, 209 (2009) 165.
- [229] V. Kouznetsov, K. Macák, J.M. Schneider, U. Helmersson, I. Petrov, *Surf. Coat. Technol*, 122 (1999) 290.
- [230] J. Alami, P.O. Å Persson, D. Music, J.T. Gudmundsson, J. Bohlmark, U. Helmersson, *J. Vac. Sci. Technol., A*, 23 (2005) 278.
- [231] J. Alami, K. Sarakinos, F. Uslu, M. Wuttig, *J. Phys. D: Appl. Phys*, 42 (2009) 015304.
- [232] A.P. Ehiasarian, P.Eh Hovsepien, L. Hultman, U Helmersson, *Thin Solid Films*, 457 (2004) 270.
- [233] K. Sarakinos, J. Alami, S. Konstantinidis, *Surf. Coat. Technol*, 204 (2010) 1661.
- [234] B.M. DeKoven, P.R. Ward, R.E. Weiss, D.J. Christie, R.A. Scholl, W.D. Sproul, F. Tomasel, A. Anders, *46th Annual Technical Conf. Proc*, (2003) 158.
- [235] S. Konstantinidis, A. Hemberg, J.P. Dauchot, M. Hecq, *J. Vac. Sci. Technol., B*, 25

(2007) L19.

[236] A.P. Ehiasarian, J.G. Wen, I. Petrov, *J. Appl. Phys*, 101 (2007) 054301.

[237] V. Kouznetsov, K. Macák, J.M. Schneider, U. Helmersson, I. Petrov, *Surf. Coat. Technol*, 122 (1999) 290.

[238] A. Aijaz, Y.X. Ji, J. Montero, G.A. Niklasson, C.G. Granqvist, *Sol. Energy Mater. Sol. Cells*, 149 (2016) 137-144.

[239] P. Bugaev, N.N. Koval, N.S. Sochugov, A.N. Zakharov, *Proceedings of the 17th International Symposium on Discharges and Electrical Insulation in Vacuum*, (LBNL, Berkeley, CA, 1996) 1074-1076.

[240] D.A. Glocker, M.M. Romach, D.J. Christie, W.D. Sproul, *47th Annual Technical Conference of Society of Vacuum Coaters, Dallas*, 24-29 (2004) 183-186.

[241] S. Konstantinidis, J.P. Dauchot, M. Ganciu, A. Ricard, M. Hecq, *J. Appl. Phys*, 99 (2006) 013307.

[242] A. Anders, *J. Vac. Sci. Technol. A*, 28 (2010) 783.

[243] M. Da Rocha, A. Rougier, *Appl. Phys. A*, 122 (2016) 370.

[244] J. Wang, J. Polleux, J. Lim, B. Dunn, *J. Phys. Chem. C*, 111 (2007) 14925-14931.

[245] V. Augustyn, P. Simon, B. Dunn, *Energy Environ. Sci*, 7 (2014) 1597-1614.

[246] P. Yang, P. Sun, L. Du, Z. Liang, W. Xie, X. Cai, L. Huang, S. Tan, W. Mai, *J. Phys. Chem. C*, 119 (2015) 16483-16489.

[247] I. Mjejri, M. Gaudon, G. Song, C. Labrugère, A. Rougier, *ACS Appl. Energy Mater*, 1 (2018) 2721-2729.

[248] A. Talledo, C.G. Granqvist, *J. Appl. Phys*, 77 (1995) 4655.

[249] P. Andrukaitis, W.M. Jacobs, J.W. Lorimer, *Solid State Ionics*, 27 (1988) 19.

[250] V. Vivier, J. Farcy, J.P. Pereira-Ramos, *Electrochim. Acta*, 44 (1998) 831-839.

[251] Y. Wang, G. Cao, *Electrochim. Acta*, 51 (2006) 4865-4872.

- [252] J. Swiatowska-Mrowiecka, V. Maurice, S. Zanna, L. Klein, E. Briand, I. Vickridge, P. Marcus, *J. Power Sources*, 170 (2007) 160-172.
- [253] Z. Tong, X. Zhang, H. Lv, N. Li, H. Qu, J. Zhao, Y. Li, X.Y. Liu, *Adv. Mater. Interfaces*, 2 (2015) 1500230.
- [254] Z. Tong, H. Lv, X. Zhang, H. Yang, Y. Tian, N. Li, J. Zhao, Y. Li, *Sci. Rep.*, 5 (2015) 16864.
- [255] Z. Tong, J. Hao, K. Zhang, J. Zhao, B.L. Su, Y. Li, *J. Mater. Chem. C*, 2 (2014) 3651-3658.
- [256] Y.R. Lu, T.Z. Wu, C.L. Chen, D.H. Wei, J.L. Chen, W.C. Chou, C.L. Dong, *Nanoscale Res. Lett.*, 10 (2015) 387.
- [257] J. Livage, *Coord. Chem. Rev.* 190-192 (1999) 391-403.
- [258] M. Alsawafta, A. Almoabadi, S. Badilescu, V.V. Truong, *J. Electrochem. Soc.*, 162 (2015) H466-H472.
- [259] C. Costa, C. Pinheiro, I. Henriques, C.A.T. Laia, *ACS Appl. Mater. Interfaces*, 4 (2012) 5266-5275.
- [260] J. Swiatowska-Mrowiecka, V. Maurice, S. Zanna, L. Klein, P. Marcus, *Electrochim. Acta*, 52 (2007) 5644-5653.
- [261] G. Beamson, D. Briggs, *High Resolution XPS of Organic Polymers*, The Scienta ESCA 300 Database, John Wiley & Sons (1992).
- [262] A. Benayad, H. Martinem, A. Gies, B. Pecquenard, A. Lavasseur, D. Gonbeau, *J. Electron Spectrosc.*, 150 (2006) 1.
- [263] G.R. Zhuang, K. Wang, Y. Chen, P.N. Ross Jr, *J. Vac. Sci. Technol. A*, 16 (1998) 3041.
- [264] D. Aurbach, B. Markovsky, A. Shechter, Y. Ein-Eli, H. Cohen, *J. Electrochem. Soc.*, 143 (1996) 3809.
- [265] M. Tulodziecki, J.M. Tarascon, P.L. Taberna, C. Guéry, *Electrochemistry Communications*, 77 (2017) 128-132.

- [266] C. Delmas, S. Brethes, M. Menetrier, *J. Power Sources*, 34 (1991) 113.
- [267] J. Swiatowska-Mrowiecka, F. Martin, V. Maurice, S. Zanna, L. Klein, J. Castle, P. Marcus, *Electrochim. Acta*, 53 (2008) 4257.
- [268] R. Lindstrom, V. Maurice, H. Groult, L. Perrigaud, S. Zanna, C. Cohen, P. Marcus, *Electrochim. Acta*, 51 (2006) 5001.
- [269] L. Santos, J. Swiatowska, V. Lair, S. Zanna, A. Seyeux, A. Melendez-Ceballos, P. Tran-Van, M. Cassir, P. Marcus, *J. Power Sources*, 364 (2017) 61-71
- [270] Q.H. Wu, A. Thißen, W. Jaegermann, *Surf. Sci.* 578 (2005) 203.
- [271] A.M Salvi, M.R Guascito, A. DeBonis, F. Simone, A. Pennisi, F. Decker, *Surf. Interface Anal*, 35 (2003) 897-905.
- [272] Y. Fujita, K. Miyazaki, C. Tatsuyama, *Jpn. J. Appl. Phys*, 24 (1985)1082-1086.
- [273] F. Decker, F. Donsanti, A.M. Salvi, N. Ibris, J.E. Castle, F. Martin, D. Alamarguy, A.S. Vuk, B. Orelid, A. Lourenco, *J. Braz. Chem. Soc*, 19 (2008) 667-671.
- [274] L. Santos, J. Swiatowska, V. Lair, S. Zanna, A. Seyeux,, A. Melendez-Ceballos, P. Tran-Van, M. Cassir, P. Marcus, *J. Power Sources*, 364 (2017) 61-71.
- [275] B. Tian, J. Swiatowska, V. Maurice, S. Zanna, A. Seyeux, L.H. Klein, P. Marcus, *Langmuir*, 30 (2014) 3538.
- [276] F. Liao, J. Swiatowska, V. Maurice, A. Seyeux, L.H. Klein, S. Zanna, P. Marcus, *Electrochim. Acta*, 120 (2014) 359.
- [277] C. Pereira-Nabais, J. Swiatowska, M. Rosso, F. Ozanam, A. Seyeux, A. Gohier, P. Tran-Van, M. Cassir, P. Marcus, *ACS Appl. Mater. Interfaces*, 6 (2014) 13023.
- [278] C. Pereira-Nabais, J. Swiatowska, A. Chagnes, F. Ozanam, A. Gohier, P. Tran-Van, C.eS. Cojocar, M. Cassir, P. Marcus, *ACS Appl. Mater. Interfaces*, 266 (2013) 5.
- [279] S. Sorieul, Ph. Alfaut, L. Daudin, L. Serani, Ph. Moretto, *Nucl. Instrum. Methods Phys. Res., Sect. B*, 332 (2014) 68-73.
- [280] S. Hassab, D.E. Shen, A M. Österholm, M. Da Rocha, G. Song, Y. Alesanco, A.

- Viñuales, A. Rougier, J.R. Reynolds, J. Padilla, *Sol. Energy Mater. Sol. Cells*, 185 (2018) 54-60.
- [281] A. Danine, L. Manceri, A. Fargues, A. Rougier, *Electrochim. Acta*, 258 (2017) 200-207.
- [282] M. Nauer, K. Ernst, W. Kautek, M. Neumann-Spallart, *Thin Solid Films*, 489 (2005) 86-93.
- [283] K. Wang, C. Steimer, D. Wamwangi, S. Ziegler, M. Wuttig, *Appl. Phys. A*, 80 (2005) 1611-1616.
- [284] P. Colombi, P. Zanola, E. Bontempi, R. Roberti, M. Gelfi, L.E. Depero, *J. Appl. Crystallogr.*, 39 (2006) 176- 179.
- [285] S. Debnath, P. Predecki, R. Suryanarayanan, *Pharm. Res.*, 21 (2004) 149-159.
- [286] A.A. Williams, J.M.C. Thornton, J.E. Macdonald, R.G. Vansilfhout, J.F. Vanderveen, M.S. Finney, A.D. Johnson, C. Norris, *Phys. Rev. B: Condens. Matter*, 43 (1991) 5001-5011.
- [287] M. Bouroushian, T. Kosanovic, *Crystal Structure Theory and Applications*, 1 (2012) 35-39.